The role of zinc on the chemistry of complex intermetallic compounds

by

Weiwei Xie

A dissertation submitted to the graduate faculty

in partial fulfilment of the requirements for the degree of

DOCTOR OF PHILOSOPHY

Major: Chemistry

Program of Study Committee:
Gordon J. Miller, Major Professor
Mark S. Gordon
Klaus Schmidt-Rohr
Xueyu Song
Vitalij K. Pecharsky

Iowa State University

Ames, Iowa

2014

TABLE OF CONTENTS

ACKNOWLEDGMENTS

I would like to sincerely thank my Ph.D advisor, Prof. Gordon J. Miller, for teaching me in both my professional and personal life. I have learned how to do a critical and creative research. After four-year working with him, I maintain a strong interest and continue to engage in solid state chemistry in the future. I would also like to thank Prof. John D. Corbett not only for teaching a lot about solid state synthesis and generating ideas, but also educate me to be strong and never give up. Many thanks to Prof. Robert McQueeney, Prof. Klaus Schmidt-Rohr, Prof. Vitalij Pecharsky, Prof. Paul Canfield, Prof. Mark Gordon, Prof. Xueyu Song, Prof. Mei Hong and Prof. Robert Angelici for teaching me knowledge and help me in my personal life.

I would also like to thank Dr. Irmi Schewe-Miller, who made me feel warm like home in ISU. I deeply appreciate all the help from group members in the Miller and Corbett groups, especially from Dr. Srinivasa Thimmaiah, Dr. Fei Wang, Dr. Qisheng Lin and Dr. Jakoah Brgoch who trained me in both experimental and computational techniques. I would also like to thank our collaborators, Prof. Susan Kauzlarich and her student, Nasrin Kazem, in UC-Davis and Prof. Aaron Sadow and his student, Regina Reinig in ISU. I also owe my gratitude to my friends in Ames: Yi, Fanghao, Jean, Chen, Tai, Zhiyuan, Min, Yu and Hongwei, Yuemei, Marilu, Jing, Xinle and so on. They made my life in Ames so beautiful. Also thanks AmesLab for funding support. (Contract No. DE-AC02-07CH11358)

Finally, I would like to thank my parents, who love me more than their own lives. And I really appreciate deep understanding and strong support from my husband, Tuo Wang. He is with me all the time in the past 7 years and helped me overcome many difficulties. Right now, my little daughter, Felicity, gives me more motivation to do research.

ABSTRACT

Combining experiments and electronic structure theory provides the framework to design and discover new families of complex intermetallic phases and to understand factors that stabilize both new and known phases. Using solid state synthesis and multiple structural determinations, ferromagnetic β-Mn type $Co_{8+x}Zn_{12-x}$ was analyzed for their crystal and electronic structures. Inspection of the atomic arrangements of $Co_{8+x}Zn_{12-x}$ reveals that the β-Mn aristotype may be derived from an ordered defect, cubic Laves phase ($MgCu_2$-type) structure. Structural optimization procedures using the Vienna Ab-initio Simulation Package (VASP) and starting from the undistorted, defect Laves phase structure achieved energy minimization at the observed β-Mn structure type, a result which offers greater insights into the β-Mn structure type and establishes a closer relationship with the corresponding α-Mn structure (*cI*58). Continuously, our research moved on Zn-rich γ-brasses Co-Zn system which has a homogeneity range $Co_{2+x}Zn_{11-y}\square_{y-x}$ including a small concentration of vacancies as the Co content increased as well as clear site preference of Co atoms in the structure. Inspired by the electronic structure calculated for Co_2Zn_{11}, substituting Pd atoms for Zn or Co atoms in the Co-Zn system leads to the discovery of a ferromagnetic (erromagnetic) $Co_{2.5}Pd_{2.5}Zn_8$ γ-brass compound. To extend the research on Hume-Rothery phases, γ-brasses Fe-Pd-Zn system was also investigate to study the site preference of transition metals in Hume-Rothery phases.

Additionally, establishing structure-property relationships for complex metal-rich materials, e.g., thermoelectric, magnetic and superconductors is related to both practical as well as fundamental issues. $Cr_{22}Sn_{24}Zn_{72}$ and $V_{23.3(1)}Sn_{26.3(1)}Zn_{68.4(1)}$ crystallize in space

group $Fm\bar{3}c$, Z = 8, Pearson symbol *Cf*944, with unit cell parameters, respectively, a = 25.184(4) Å and 25.080(3) Å. Their structures can be described as a cubic $NaZn_{13}$-type packing of two distinct, yet condensed intermetallic clusters, or a simple cubic packing of I13 clusters condensed via extreme Zn sites with rhombic dodecahedra in the voids. Instead of using transition metals Cr/V, rare earth element, Ce, was also used to react with Zn and Sn. The new cerium-based ternary intermetallic phase, $Ce(Sn_{1-x}Zn_x)_6$ ($0.45(1) < x < 0.49(1)$) adopted to $CeCu_6$-type structure. It exhibits a structural transition from orthorhombic to monoclinic around 150 K. Moreover, the magnetic properties of a sample analyzed as $CeSn_{3.33(6)}Zn_{2.67}$ shows it to be Langegin paramagnetic above 2K.

CHAPTER 1

Introduction

1.1 The Specialties of Intermetallic Compounds

Intermetallic compounds [1] as solid phases contain two or more metallic or semi-metallic elements, with optionally one or more non-metallic elements as minority components, and adopt crystal structure differ from one of the other constituents. For molecules, the principles of covalent bonding lead to a deeper understanding of compositions and structures. However, intermetallic compounds cannot often be interpreted in a simple and effective way like molecules because of itinerant nature of the valence electrons as a characteristic feature of the metallic state. Moreover, most of conventional molecules are fully ordered and stoichiometric, but usually intermetallic compounds are not perfectly stoichiometric always containing defects and mixtures as the result of self-diffusion. [2] The defects and mixtures in intermetallic compounds are common and used to control the physical properties of materials, for example, high-temperature unconventional superconductor, $Ba_{1-x}K_xFe_2As_2$ ($1>x>0$). [3] Recent research also illustrates complex intermetallic compounds with large unit cells and distortions (defects and mixtures) low the lattice thermal conductivities and enable themselves potentially good thermoelectric materials. [4]

1.2 Zinc Metal in Intermetallics

Among the late transition metals, the zinc group elements are widely studied on both experimental and theoretical aspects. Experimentally, they form diverse crystal structures from Laves phases like $MgZn_2$ [5], to quasicrystals such as Cd-Yb, [6] Zn-Mg-Ho [7] and Zn-Mg-Sc [8]; Theoretically, zinc group elements have more localized *d*-electrons than other

transition metals, which plays a significant role in controlling the chemical and physical properties like structural anomalies and melting points. [9]

1.2.1 Structural Anomalies of Zinc [10]

For metallic elements, the assumption of itinerant, electron-gas-like valence electrons forming no directed bonds, and virtually spherical atomic cores suggests a structural classification based on geometrical arrangements. Indeed, most of the metallic elements can be related to sphere packings, body centered cubic (*bcc*), face centered cubic (*fcc*), hexagonal close packed (*hcp*) or double hexagonal close packed (*dhcp*), the latter three being close sphere packings. Usually the metals in one group show the same structure, suggesting that the electronic structure of atoms plays a role in determining the packing of the atoms. The ideal *c/a* ratio in *hcp* crystal systems is 1.633. But most of the elements have a *c/a* ratio which is slightly smaller than the ideal value. These variations may be regarded as first indications for interactions between partially filled valence and even semi-core shells of the atoms. Elements with closed electronic shells are expected to be closer to the ideal value, as there are weak interactions between partially filled valence shells of atoms. [10] Indeed, magnesium is in accordance with this expectation, but two other elements with filled valence and core (sub)shells, zinc ([Ar]3d^{10}4s^2) and cadmium ([Kr]4d^{10}5s^2), actually show spectacular deviations from the ideal *c*/*a* ratio of 14% and 16%, respectively. Results from experimental and theoretical calculations [11-12] indicate that the anomalies of *c/a* ratios come from 4*s*-3*d* electron interactions but not an effect of anisotropy in thermal expansion.

Zinc does not only exhibit a structurally unusual *c*/*a* ratio, it also has lower melting point than other 3*d* transition metals, which makes it possible to react at relative low temperature (lower than 1000°C, most tube furnace can reach.) with elements, like Mo [13] , Nb [13] , and Ir,

[14] that have high melting points. Furthermore, previous research indicates melting and boiling points of elements are relative with the thermodynamic properties of entropy and enthalpy. [15]

1.2.2 Enthalpy of atomization for *d*-block metals and their related properties

The enthalpy of atomization [16] is the energy required to divide the solid metal into separate, gaseous atoms, and it appears in nearly every thermochemical cycle involving the metals and their compounds. As one of the most important physical properties of a metal for chemists, the enthalpy of atomization is a direct measure of the binding energy of the solid metal, although it depends also on the electronic configuration of the gas-phase atoms. Many other physical properties, like melting and boiling points, Young's modulus of elasticity, hardness and thermal conductivity, would be related to the enthalpy of atomization. [17]

For the *s*-block metals, the enthalpy of atomization rises with increasing group number, and the nearly-free electron approach works well to explain electronic structures and stabilities of *s*-block atoms. It is observed that the energies of phase transitions in *s*-block metals are smaller than *p*- and *d*-block elements, which means that the energy of the lattice is insensitive the details of the structures.

It is much more difficult to simply use nearly-free-electron approximation for *d*-block metals. The nearly-free-electron model is a modification of the free-electron gas model which includes a weak periodic perturbation meant to model the interaction between the conduction electrons and the ions in a crystalline solid. This model, like the free-electron model, does not take into account electron-electron interactions. For *s*- and *p*-block metals, the overlap of wave functions is exceedingly small and negligible, so the nearly-free-electron approximation works well. However, for *d*-shelled transition metal atoms, the overlap of

atomic wave function is enough to require corrections to the picture of isolated atoms, but not so much as to render the atomic description completely irrelevant. Thus, *d*-electrons have to be treated by the tight-binding method. The tight-binding method is an approximation to calculate the electronic band structure of tightly bound electrons in solids, for example, *d* electrons in transition metals. The enthalpies of atomization are much larger than *s*- and *p*-block metals, indicating that the *d*-electrons make a great contribution to the binding. For a metal with few *d*-electrons, the lower part of the band is filled. As orbitals are filled, the metallic bonding energy increases, as a result, the melting points would increase as well. After about five *d* electrons per atom have been filled in, the bonding levels are full and further electrons must go into the antibonding parts. The antibonding occupancy in orbitals destabilizes the system and the metallic bonding energy decreases, so the melting points of metals decrease. Even when the *d*-band is completely filled, some cohesion is obtained from the *s*-electrons and from hybridization of *s*- and *d*- levels. The rough trend of enthalpy of atomization increases in each period, reaching a maximum in Group V or VI, then decreases from Group VII. Within each group, the enthalpy of atomization usually increases with increasing atomic number in Figure 1.2.2(*a*). Corresponding to the enthalpy of atomization, the melting points and boiling points in Figure 1.2.2(*b*) and 1.2.2(*c*) have the similar trend with enthalpy of atomization. [18]

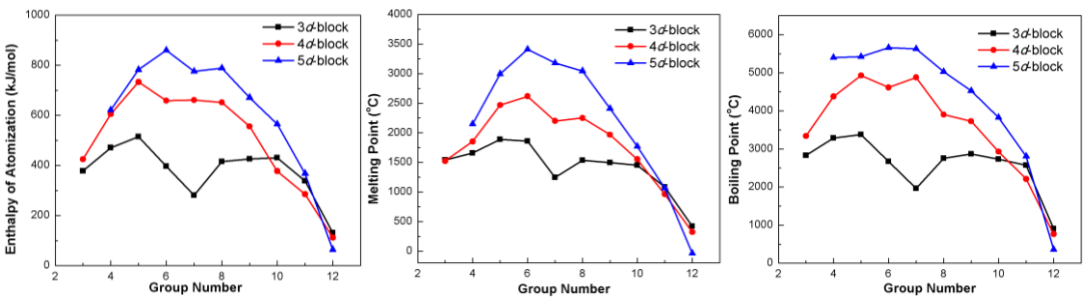

Figure 1.2.2 (*a*) Enthalpies of atomization of *d*-block metals (*b*) Melting points of *d*-block metals (c) Boiling points of *d*-block metals

The low melting point of zinc makes it possible to react with different types of elements from alkali, transition metals to main group elements. Mostly, they are likely to form polar intermetallic phases when active elements like alkali, alkali earth or rare earth elements react with zinc, for example, AZn_{13} (A=Li, Na, K, Rb, Cs, Be, Ca, Sr and Ba) ($NaZn_{13}$-type).[19-23] For early transition metals, like group IV and V elements, they could form Laves phases with Zn.[24-26] However, as electronegativity increases until similar with zinc, the late transition metals prefer to form typically Hume-Rothery phases with Zn, like α-brass, β-brass, γ-brass and ε-brass.[27-30] Particularly, when zinc reacts with some main group elements like In and Sn, they would form eutectic phases instead of any compound.[31- 32] The eutectic phase has the lower melting point than Zn and main group elements, which is ideal for the high-temperature solid reactions or flux method to grow intermetallic compounds.

1.2.3 Specialties of Zinc Group Elements

As mentioned above, the enthalpies of atomization and melting points are much lower for zinc group elements than other *d*-block metals. Zinc group elements have a ground state electronic configuration in which electrons fill up all the available subshells. According to Hund's rules, this configuration strongly resists removal of an electron, so the elements behave similarly to noble gas elements, which form weak bonds and become solids that melt easily at relatively low temperatures compared with other *d*-block metals. Especially for mercury, the stability of the 6*s* shell is due to the presence of a filled 4*f* shell, which poorly screens the nuclear charge that increases the attractive Coulomb interaction of the 6*s* shell and the nucleus. The absence of a filled inner *f* shell is the reason for the somewhat higher

melting temperature of cadmium and zinc, although both these metals still melt easily and, in addition, have unusually low boiling points. [33]

Mercury can dissolve many other metals such as gold and silver to form amalgams.[34] Similarly, zinc can also dissolve many metals to form eutectic phases and form solid solutions for solid state reactions, like Zn-Sn and Zn-In binary phases.[31-32]

1.3 Rationalizing Structures and "Coloring" Problem

1.3.1 Rationalizing Structures

The questions to answer when we seek to rationalize the structures of intermetallic compounds are, given a chemical composition, at certain external conditions, among several possible structures, which one will it adopt and why. To answer these, we can build up iso-compositional models according to these possible structures, carry out quantum mechanical calculations using them, and analyze the results. The process of analysis is principally the same as the process of analyzing a simple solid metal element, for instance, Co, as briefly discussed below.

Cobalt is ferromagnetic with hexagonal-closed-packing (*hcp*) at room temperature. Above 673 K, cobalt will undergo a structural phase transition from *hcp* to *fcc* while remaining ferromagnetic. Here, we examine why it is not *fcc* at low temperature or *hcp* at high temperature. Calculations using the Tight-Binding Linear-Muffin-Tin-Orbital Atomic-Sphere-Approximation (TB-LMTO-ASA) [35-36] upon the two models provide us with the total energy (E_{tot}) for the *hcp* and *fcc* volumes (11.115 $Å^3$/atom for *hcp*; 11.130 $Å^3$/atom for *fcc*)[37], shown in Table 1.3.1. On increasing temperature, the volume of cobalt extends to 11.288 $Å^3$/atom at 673K according to the thermal expansion coefficient of cobalt at 20°C [38], in this volume, the E_{tot} of *fcc* is slightly lower (~20meV) than E_{tot} of *hcp*, and the phase

would transform from *hcp* to *fcc*. From the Table 1.1, it is shown that for the same volume in room temperature (experimental results) the total energy of *hcp* is lower than total energy of *fcc*. As volume rises at high temperature, the *fcc* structure becomes more favorable instead of *hcp*, which matches the experiments well. However, E_{tot} is not so informative. To obtain energy-resolved visualization of chemical bonding on stability, as well as possible magnetic properties of cobalt, TB-LMTO-ASA calculations were carried out to evaluate and analyze the electronic structures of cobalt in the two models.

Table 1.3.1 Energy terms of Cobalt in different structure models

Structure	Energy/atom in R.T. volume	Energy/atom in H.T. volume
E_{tot}(*hcp*)	0	44.94 meV
E_{tot}(*fcc*)	51.17 meV	7.87 meV

In accordance with Born-Oppenheimer approximation, the electronic structure is given primary emphasis onto analyzing computational results, as electronic structure is the significant step to study quantum mechanical motion of a molecular or non-molecular (like intermetallic) system. [39] The DOS (density of states) and COHP (crystal orbital Hamilton population) of *hcp*-Co and *fcc*-Co without spin polarization are shown in Figure 1.3.1. The calculation corresponds to 0K. For *hcp*-Co in Fig. 1.3.1(*a*), the Fermi level locates on the sharp peak in DOS, and falls in the strong Co-Co antibonding region in –COHP, which indicate the electronic instability of *hcp*-Co in local density approximation (LDA). Consequently, one would expect some kind of structural change—which here does not occur: *hcp*-Co stays *hcp*-Co. The answer to that puzzle is that nonmagnetic cobalt does undergo a distortion, but instead of the atoms rearranging themselves, the electrons do. Nonmagnetic *hcp*-Co is unstable with respect to an electronic structure distortion, which makes the two spin wavefunctions inequivalent, thereby lowering the energy and giving rise, upon ordering,

to ferromagnetism; these are the corresponding spin-polarized results in Figure 1.3.2(*a*). The theoretical magnetic moment (1.58 μ_B) is very close to the experimental one (1.6-1.7μ_B). Upon spin-polarization, the total energy lowers by ~31 meV. The shifts in the majority and minority have removed the antibonding states at the Fermi level, thereby maximizing the Co–Co bonding as far as possible. [40] Similarly, the electronic calculations imply *fcc*-Co ferromagnetic. The Curie temperature for cobalt is 1388K, much higher than structural transition temperature from *hcp* to *fcc*, so cobalt in *fcc* is still ferromagnetic experimentally. [41] The theoretical calculations match with experimental results very well.

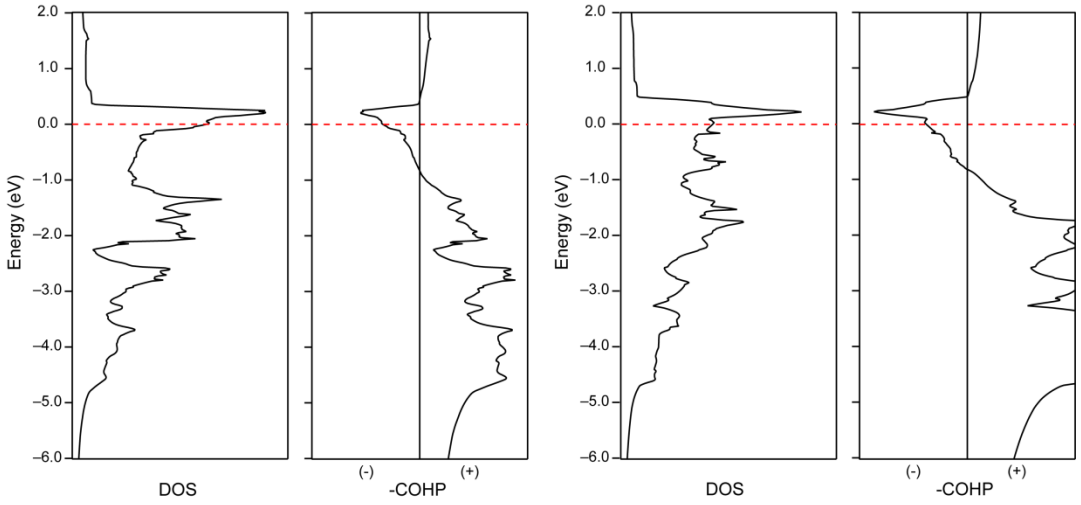

(a) (b)

Figure 1.3.1 DOS and –COHP in LDA for (*a*) *hcp*-Co and (*b*) *fcc*-Co

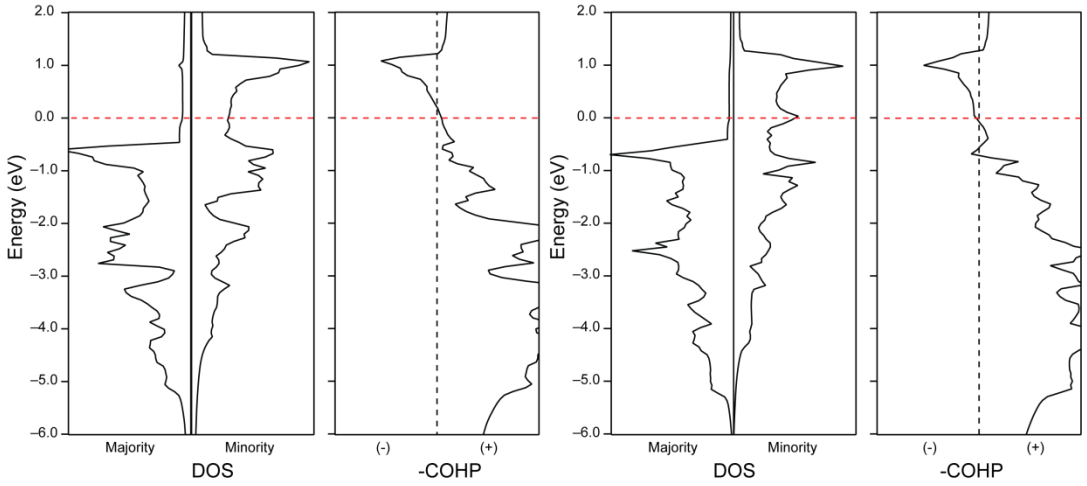

Figure 1.3.2 DOS and –COHP in LSDA for (*a*) *hcp*-Co and (*b*) *fcc*-Co

1.3.2 "Coloring" Problem

A "coloring" problem occurs when there is more than one element constructing the framework of an intermetallic phase. [42] Finding out how to distribute different atoms on the sites of a framework is essential for rationalizing its structure. The criterion of a preferred distribution of different atoms (or "coloring scheme") is that it provides the lowest total energy. One efficient way to determine which coloring scheme is favorable over the others is accomplished by a population analysis upon a "uniform reference frame". To study a certain framework, we can construct a hypothetical model of the structure with only one element, execute quantum mechanical calculations upon such a uniform reference frame, and analyze the valence electron population on each site. When constructing the same framework with more than one element, the sites with higher populations favor the more electronegative element. This is because the valence orbitals of the more electronegative atoms have lower energy. Positioning such atoms onto the site(s) with higher electron population(s) means more electrons are filling the lower energy orbitals and this will lower the electronic energy.

Another structural aspect to consider about the "coloring" problem is to compare the numbers of heteroatomic and homoatomic contacts in competing coloring schemes. [43-44]We can calculate several tentative coloring schemes with different numbers of heteroatomic and homoatomic contacts and see which one gives the lowest total energy. For example, if more heteroatomic than homoatomic contacts leads to lower total energy, then, with the help of a computer, we can then generate all possible coloring schemes and find the one(s) with the most heteroatomic contacts.

1.4 Layout of the Dissertation

Chapter 2 summarizes the experimental and computational methods we employed in all work included in this dissertation. With these techniques, we addressed the questions raised in Sections 1.2 and 1.3 by investigating the projects described in the following chapters.

In Chapter 3, we studied the β-Mn type Co-Zn system in both experimental and theoretical methods. We showed that β-Mn Co-Zn phases may be expressed as $Co_{8+x}Zn_{12-x}$, ($1.7(2) < x < 2.2(2)$) and establish clear preferences for Co atoms in the 8*c* sites and Zn atoms in the 12*d* sites with all additional Co atoms replacing some Zn atoms. Moreover, inspection of the atomic arrangements of $Co_{8+x}Zn_{12-x}$ reveals that the β-Mn aristotype may be derived from an ordered defect, cubic Laves phase ($MgCu_2$-type) structure. This work has been published on *Inorganic Chemistry*.

In Chapter 4, we studied γ-brass Co-Zn system with and without Pd doping. After doping Pd, the magnetic properties of γ-brass changes from a Curie-Weiss paramagnetic in Co-Zn system to dilute ferrimagentic with Co-Pd-Zn system. A giant magnetic moment on Co atom is induced by the Pd atoms. This work has been submitted to *Chemistry of Materials*.

Chapter 5 reports our work in the Fe-Pd-Zn ternary systems. Experimentally we observed how the structures of the systems switch between two competing structure types, $(Fe_{1-x}Pd_x)_4Zn_9$ and $(Fe_{1-x}Pd_x)_5Zn_8$-type, in response to a change in composition. We then theoretically explained our experimental observations. Site preferences and site sharing between Fe and Pd atoms and the coloring problem are investigated in detail.

Chapter 6 includes experimental work on TM-Sn-Zn systems, where TM includes Cr and V. These complex intermetallic materials feature similar structural clusters. Chapter 7 includes experimental work on RE-Sn-Zn systems, where TM includes Ce, Nd, and Gd. These complex intermetallic materials feature with interesting magnetic and heat capacities properties.

Appendix includes the collaborative works with other research groups. First part is the computational work on $Eu_{11}Cd_6Sb_{12-x}As_x$, which has been under review by *Chemistry of Materials*. Second part is our work on refining the structure and identifying the physical properties of complex intermetallic compound, $Tb_{117}Fe_{54.7}Ge_{112}$. The last part is the summary of all the experiments I did in my Ph.D life.

1.5 Reference

[1] Westbrook, J. H.; Fleischer, R. L. *Intermetallic Compounds: Principles and Practice*, Wiley, 2002.

[2] Zhang, S. B.; Northrup, J. E. *Phys. Rev. Lett.* **1991**, *67*, 2339.

[3] Rotter, M.; Pangerl, M.; Tegel, M.; Johrendt, D. *Angew. Chem. Int. Ed.*, **2008**, *47*, 7949.

[4] Snyder, G. J.; Toberer, E. S. *Nat. Mater.* **2008**, *7*, 105.

[5] Stein, F.; Palm, M.; Sauthoff, G. *Intermetallics*, **2004**, *12*, 713.

[6] Guo, J. Q.; Abe, E.; Tsai, A. P. *Phys. Rev. B* **2000**, *62*, R14605.

[7] Sato, T. J.; Takakura, H.; Tsai, A. P.; Shibata, K. *Phys. Rev. Lett.* **1998**, *81*, 2364.

[8] Kaneko, Y.; Arichika, Y.; Ishimasa, T. *Philos. Mag. Lett.* **2001**, *81*, 777.

[9] Bhargava, R. N.; Gallagher, D.; Hong, X.; Nurmikko, A. *Phys. Rev. Lett.* **1994**, *72*, 416.

[10] Wedig, U.; Nuss, H.; Nuss, J.; Jansen, M.; Andrae, D.; Paulus, B.; Kirfel, A.; Weyrich, W. *Z. Anorg. Allg. Chem.* **2013**, *639*, 2036.

[11] Nuss, J.; Wedig, U.; Kirfel, A.; Jansen, M. *Z. Anorg. Allg. Chem.***2010**, *636*, 309.

[12] Skelton, E. F.; Katz, J. L. *Phys. Rev.* **1968**, *171*, 801.

[13] Nasch, T.; Jeitschko, W. *J. Solid State Chem.* **1999**, *143*, 95.

[14] Hornfeck, W.; Thimmaiah, S.; Lee, S.; Harbrecht, B. *Chem. Eur. J.* **2004**, *10*, 4616.

[15] Parish, R.V. *The Metallic Elements*, Longman, 1977.

[16] Cotton, F. A. *Advanced Inorganic Chemistry*; Wiley, 1988.

[17] Tyson, W. R.; Miller, W. A. *Surf. Sci.***1977**, *62*, 267.

[18] Hofmann, P. *Solid State Physics: an Introduction.* Wiley-VCH, 2008.

[19] Wendorff, M.; Roehr, C. *J. Alloys Compd.* **2006**, *421*, 24.

[20] Fischer, D.; Jansen, M. *Z. Anorg. Allg. Chem.* **2010**, *636*, 1917.

[21] Zhang, Y.; Kevorkov, D.; Liu, X.; Bridier, F.; Chartrand, P.; Medraj, M. *J. Alloys Compd.* **2012**, *523*, 75.

[22] Bruzzone, G.; Ferretti, M.; Merlo, F. *J. Less-Common Met.* **1985**, *114*, 305.

[23] Saparov, B.; Bobev, S. *J. Alloys Compd.* **2008**, *463*, 119.

[24] Brown, P.J.; Ziebeck, K.R.A.; Mattocks, P.G. *J. Magn. Magn. Mater.* **1984**, *42*, 12.

[25] Rossteutscher, W.; Schubert, K. *Z. MetaIlkd.* **1965**, *56*, 730.

[26] Vold, C.L. *Acta Crystallogr.* **1961**, *14*, 1289.

[27] Miettinen, J.; Vassilev, G. *Cryst. Res. Technol.* **2011**, *46*, 1122.

[28] Okamoto, H. *J. Phase Equilib.* **2003**, *24*, 280.

[29] Mizutani, U. *Hume-Rothery Rules for Structurally Complex Alloy Phases*. Taylor & Francis, US, 2010.

[30] Bostroem, M.; Lidin, S. *J. Solid State Chem.* **2002**, *166*, 53.

[31] Kim, Y. S.; Kim, K. S.; Hwang, C. W.; Suganuma, K. *J. Alloys Compd.* **2003**, *352*, 237.

[32] Dutkiewicz, J.; Zakulski, W. *J. Phase Equilib.* **1984**, *5*, 284.

[33] Kleppner, D. *Rev. Mod. Phys.* **1999**, *71*, S78.

[34] O'Shea, T. J.; Lunte, S. M. Analytical Chemistry, **1993**, *65*, 247.

[35] Tank R.; *et al*, *TB-LMTO-ASA program*, Germany,

[36] Jepsen O.; *et al*, *Z. Phys.***1995**, *B97*, 35.

[37] Owen, E.A.; Madoc Jones, D. *Proc. Phys. Soc. London* **1954**, *67*, 459.

[38] Lide, D. R. *CRC Handbook of Chemistry and Physics*, 84th Edition. CRC Press, Boca Raton, Florida, 2003.

[39] Born, M.; Oppenheimer, J. R. *Ann. Phys.* **1927**, *84*, 457.

[40] Dronskowski, R.; Bloechl, P. E. *J. Phys. Chem.***1993***, 97*, 8617.

[41] Schneider, C. M.; Bressler, P.; Schuster, P.; Kirschner, J.; De Miguel, J. J.; Miranda, R. *Phys. Rev. Lett.* **1990**, *64*, 1059.

[42] Miller G. J. *Eur. J. Inorg. Chem.* **1998,** 523.

[43] Kohn, W.; Sham, L. J. *Phys. Rev.* **1965,** *140*, A1133.

[44] Gimarc, B. M. *J. Am. Chem. Soc.* **1983**, *105,* 1979.

CHAPTER 2

Experimental and Theoretical Techniques, in General

In this chapter, we describe the experimental and theoretical techniques in general. This includes what techniques and theories were employed, what purposes they were serving, and what their advantages and disadvantages are. The specific details for each problem can be found in each of the following chapters.

2.1 Synthesis

2.1.1 Starting Materials. High purity elements, listed in Table 2.1.1, were used as starting materials for all synthetic preparations. All elements were used as received from the manufacturer. The starting materials except Mn or rare earth elements were stable in air at room temperature as pieces; Mn and rare earth elements were stable in Argon-filled glove box at room temperature as pieces.

Table 2.1.1. The starting materials used for all synthetic preparations. (Purity of a specific element as a ratio based on other metallic elements; purity of a specific rare earth element as a ratio based on other rare earths)

Element	Source	Melting Point (K)	Purity	Form
Cr	MPC-Ames Lab	2130	99.9%	Chunks
Mn	Sigma Aldrich	1518	99.9%	Pieces
Fe	MPC-Ames Lab	1808	99.9%	Pieces
Co	MPC-Ames Lab	1768	99.9%	Pieces
Ni	MPC-Ames Lab	1726	99.9%	Pieces
Cu	MPC-Ames Lab	1358	99.99%	Pieces
Zn	MPC-Ames Lab	693	99.99%	Chunks
Ga	MPC-Ames Lab	303	99.999%	Chunks
Nb	MPC-Ames Lab	2750	99.99%	Pieces
Mo	MPC-Ames Lab	2896	99.99%	Pieces
Ru	MPC-Ames Lab	2523	99.99%	Chunks

Table 2.1.2 continued

Rh	MPC-Ames Lab	2239	99.9%	Chunks
Pd	MPC-Ames Lab	1828	99.99%	Chunks
Ag	MPC-Ames Lab	1235	99.99%	Chunks
In	MPC-Ames Lab	430	99.99%	Chunks
Sn	MPC-Ames Lab	505	99.99%	Chunks
Sb	MPC-Ames Lab	904	99.99%	Chunks
Te	Sigma Aldrich	723	99.99%	Chunks
RE(La) elements	MPC-Ames Lab	1068-1909	99.9%	Chunks

2.1.2 Selecting Sample Containers. For solid state reactions at high temperatures, it is necessary to choose a suitable container material that is chemically inert to the reactants under the heating conditions used. Considering the reactivity, costs, strength, and heat-resistance, Table 2.1.2 lists the usual types of sample containers and their temperature and reactivity limits.

Table 2.1.2. The usual types of sample containers and their temperature and reactivity limits

Container	Temperature limits	Elements attacking the container
Silica	1200 °C	Rare earth, Alkali, Alkali earth, Al [1]
Alumina	1800 °C	Rare earth, Alkali, Alkali earth. (Thermite) [2]
Ta	3250 °C	Alkali, non-metals(halogen, chalcogen), Al, Pt [3]
Ni	1455 °C	Alkali resistance, use to melt Fe and clay [4]

2.1.3 Tube Furnace Heating. The high purity elements used as starting materials are typically sealed in evacuated silica tubes ($<10^{-5}$ torr) as the reaction vessel if the elements do not attack the container. Whenever required, other reaction vessels are considered, for example, precleaned tantalum tubes ($\phi \approx 0.9$cm), used for reactions involving elements like Mg and Al are weld-sealed under Ar, or alumina crucibles in which Ga, Sn and Cd metals are used as flux materials.[5] The Ta tubes or alumina crucibles are also sealed in evacuated silica

tubes ($<10^{-5}$ torr) as double-jackets. With tube furnaces, we are able to program the temperature profiles and thus control the reacting/annealing temperatures and the rate of heating and cooling. Mostly, we use either quenching or slow-cooling to get final products. Quenching is the rapid cooling to prevent low-temperature processes, such as phase transformations, from occurring by only providing a narrow window of time in which the reaction is both thermodynamically favorable and kinetically accessible. However, quenching can reduce crystallinity and thereby increase toughness of products, because there is not enough time for the solid to crystallize. Instead, slow-cooling is applied to gain better crystalline products. Both procedures usually yield single crystals suitable for subsequent X-ray diffraction experiments.

2.2 Characterization Techniques and Analysis

2.2.1 Powder X-ray Diffraction Analysis. For powder XRD, we ground about 0.1 g samples and took several milligrams for diffraction. So, the refinement results, especially to determine the lattice parameters, are a course-grained average over the bulk. The three-dimensional diffraction space can be described with reciprocal axes x^*, y^*, and z^* or, alternatively, in spherical coordinates q, φ^*, and χ^*. In powder diffraction, intensity is homogeneous over φ^* and χ^*, and only q remains as the important measurable quantity. The three-dimensional reciprocal space that is studied in single crystal diffraction is projected onto a single dimension by averaging the oriented results. Moreover, one-dimensional powder patterns, although less informative than single crystal diffraction patterns, can be used for “fingerprint” identification of the phases present in samples. Moreover, we still apply powder X-ray diffraction for crystallographic structural analysis and unit cell calculations by interpreting the intensity of patterns, quantitative determination of amounts of

different phases in multi-phase mixtures by peak-ratio calculations [6], and determination of crystallite size from analysis of peak broadening by Scherrer equation [7].

All samples were finely ground and examined by powder X-ray diffraction for identification and phase purity on a STOE WinXPOW powder diffractometer employing Cu radiation ($\lambda_{K\alpha}$= 1.5406 Å) for all the samples. The scattered intensity was recorded as a function of Bragg angle (2θ) using a scintillation detector with a step of 0.03° 2θ in step scan mode, ranging from 0° to 130°. Phase identification was accomplished using the program *PowderCell* [8].

Because X-ray fluorescence can create high background for Cr-, Mn-, Fe-, Co- and Ni-containing samples examined using Cu *K*α radiation [9], the samples containing Co were also examined on a Philips PANalytical X'pert-Pro powder diffractometer using Co radiation ($\lambda_{K\alpha}$ =1.7903Å). The scattered intensities were recorded in step scan mode with 0.008° steps over a 2θ range from 5°-100°. For these measurements, phase identification and the lattice parameters were refined by full-profile Rietveld [10] refinements using *LHPM RIETICA* [11].

2.2.2 Single Crystal X-ray Diffraction Analysis. Single crystal XRD provides three-dimensional diffraction patterns, so it offers more effective than powder XRD for solving and refining crystal structures. It is especially able to determine the occupancies of crystallographic sites by different atoms or mixtures of atoms in complex structures. However, its results largely depend on the availability and quality of the single crystals. Moreover, the mass of the single crystal is on the scale of a microgram, so it does not give the average information, such as lattice parameters, of the whole sample, which is around 0.5 g. To get more accurate information, several crystals from the sample are picked and examined.

Crystals from each reaction sample were mounted on the tips of glass fibers. Room temperature intensity data were collected on a Bruker Smart Apex CCD diffractometer using Mo Kα radiation (λ = 0.71073 Å). Data were collected over a full sphere of reciprocal space flexible scans in ω with an exposure time of 10s per frame. If the crystal structure is complex or the intensity of scattering is not strong enough to be indexed or integrated, the crystal would be exposed for as long as 20s per frame. The 2θ range could be extended up to 60°. The *SMART* software was used for data acquisition. Intensities were extracted and corrected for Lorentz and polarization effects using the *SAINT* program. Empirical absorption corrections were accomplished with *SADABS*, which is based on modeling transmission by spherical harmonics employing equivalent reflections with $I > 3\sigma(I)$ [12-13]. With the *SHELXTL* package [14], the crystal structures were solved using direct methods and refined by full-matrix least-squares on F^2. All crystal structure drawings were produced using the program *Diamond* [15].

2.2.3 Neutron Powder Diffraction. Neutrons as quantum particle interact with matters differently from X-ray that is electromagnetic radiation in many ways. These differences arising primarily from quite different scattering process make neutron scattering complementary to X-ray diffraction. First of all, the scattering length of neutron diffraction is not atomic number dependent, so the visibility of light elements like H is good, and the adjacent elements in the periodic table are often readily distinguished. Secondly, the neutron diffraction can defect different isotopic behaviors (e.g. hydrogen and deuterium) because the isotopes have different scattering lengths. Additionally, the interaction between neutron and atomic magnetic moments due to unpaired electrons makes neutron diffraction able to

measure magnetic structures as well as crystal structures. However, as the scattering is weak, neutron diffraction needs much larger quantity of samples than X-ray.

In the measurement of neutron scattering, vanadium containers (L≈7.5cm; ϕ≈3.0mm) are used to hold the sample, because vanadium has a negligible coherent scattering cross section and hence does not contribute observable peaks to the diffraction pattern.[16] Since our sample contains cobalt that is radiated after neutron scattering, the sample could not be recycled any more. Finally, we refined the neutron powder diffraction data by the Rietveld method [10] using the program *FullProf* [17].

2.2.4 Scanning Electron Microscopy. A scanning electron microscope (SEM) produces images of a sample by scanning it with a focused beam of electrons. The electrons interact with atoms in the sample, producing various signals that can be detected and that contain information about the sample's surface topography and composition. A SEM image can offer us the direct visual information on the phase identification of the sample. For conventional imaging in the SEM, specimens must be electrically conductive, at least at the surface, and electrically grounded to prevent the accumulation of electrostatic charge at the surface.

Characterization was completed using a variable pressure scanning electron microscope (Hitachi S-2460N) and Energy-Dispersive Spectroscopy (EDS) (Oxford Instruments Isis X-ray analyzer). Scanning electron microscopy and energy-dispersive spectroscopy were utilized to check the homogeneity and measure the compositions of the samples. Samples were mounted in epoxy, carefully polished, and then sputter-coated with a thin layer of carbon prior to loading into the SEM chamber. The samples were examined at 20 kV. Spectra were collected for 100 seconds. An Oxford Instruments Tetra backscattered electron (BSE) detector was used to image the samples using the BSE signal. Multiple points were

examined in each phase within multiple grains of a specimen. Compositional estimates were calculated using Oxford's SEM *Quant* software to correct intensities for matrix effects.

2.3 Physical Property Measurements

2.3.1 Magnetic Measurement. The magnetization measurements were performed using a superconducting quantum interference device (SQUID) magnetometer MPMS XL-7, and Vibrating Sample Magnetometer (VSM) EV11 manufactured by Quantum Design, Inc. were employed to measure the magnetic properties on pieces of samples. The SQUID operates over a temperature range of 1.8-400 K (He^3 cooling to 0.4K) and in applied fields of up to 70 kOe. The VSM can be operated till 1000K. The samples were placed in glass capsules for measurement. SQUID that can detect the magnetic field as low as 5×10^{-18}T is more sensitive than VSM. However, VSM can measure the magnetic properties above room temperature, as high as 1000K. The Curie temperature was approximated by the intersection of a linear fit the maximum *dM/dT* of the magnetization vs temperature curve, and the effective magnetic moments (μ_{eff}) and Weiss temperature (Θ) were determined according to equation 2.3.1(*a*):

$$\chi^{-1} = \frac{T-\Theta}{(\frac{N\mu_{eff}^2}{3k_B})} \qquad \text{Eq. 2.3.1}(a)$$

For some cases that could not be fitted by the Curie-Weiss relation, instead, a modified Curie-Weiss relation is applied to calculate the effective magnetic moments according to the equation 2.3.1(*b*):

$$\chi^{-1} = \frac{T-\Theta}{(\frac{N\mu_{eff}^2}{3k_B})} + C \qquad \text{Eq. 2.3.1}(b)$$

C is the temperature-independent constant. [18]

2.3.2 Specific Heat Capacity Measurement. The heat capacity is measured by Physical Property Measurement System (PPMS) manufactured by Quantum Design, Inc. The temperature ranges from 2K to room temperature (300K) with non-applied field and pressure at 9.40×10^{-6} Torr. The Dulong–Petit law [19] states the classical expression for the molar specific heat capacity of a crystal at room temperature, expressed as equation 2.3.2(*a*):

$$C^* = \frac{C}{nR} = 3 \qquad \text{Eq. 2.3.2}(a)$$

However, at low temperature, heat capacity (C_P) consists of the specific heat of the electrons $C_{P,el}$ which depends linearly on temperature T, and of the specific heat of the crystal lattice vibrations (phonons) $C_{P,ph}$ which depends cubically on temperature T^3 in equation 2.3.2(*b*),

$$C_P = C_{P,el} + C_{P,ph} = \gamma T + \beta T^3 \qquad \text{Eq. 2.3.2}(b)$$

γ is the Sommerfield parameter; β is proportionality constant. We can also write in format of Cp/T, that is equation 2.3.2(*c*),

$$\frac{C_P}{T} = \gamma + \beta T^2, \text{ with } \gamma = \frac{\pi^2}{2}\frac{k_B}{\varepsilon_F} n k_B,\ \varepsilon_F = \frac{h^2 k_F^2}{4\pi^2 m} \qquad \text{Eq. 2.3.2}(c)$$

For $C_P/T\sim T^2$ plot, if T= 0K, we can figure out the γ value. For normal metals, γ is around $(0.1\sim1)\times10^{-3}$ J/mol•K^2, if γ becomes large, ε_F would become small, and the effective *m* becomes large. The materials with large effective mass can be called *heavy fermion* materials. [20]

2.4 Theory and Electronic Structure Calculations

2.4.1 Extended Hückel Theory (EHT) Calculation. Extended Hückel Theory (EHT) is a semi-empirical approach rather than using first-principles to solve the Schrödinger equation for molecules and solids. [21] The construction of the Hamiltonian matrix and the solution of the eigenfunctions and eigenvalues are completed only once, without self-consistent

iterations. So, it takes much shorter time than first-principles calculations. Also, it employs Slater-type atomic orbitals with double zeta functions for transition metals and single zeta functions for the main group elements. Extended Hückel theory provides convenient electron population analysis and it is successful to determine the molecular orbitals and the relative energy of different geometrical configurations. The disadvantage of EHT calculations is that it involves significant approximations by ignoring the electron-electron repulsions.

2.4.2 TB-LMTO-ASA Calculation. We employed two techniques for first-principles calculations. The first one is Tight Binding Linear Muffin Tin Orbital with Atomic Spheres Approximation (TB-LMTO-ASA). [22] The tight-binding model (TB model) is an approach to the calculation of electronic band structure using an approximate set of wave functions based upon superposition of wave functions for isolated atoms located at each atomic site. The electrons in this model should be tightly bound to the atom to which they belong and they should have limited interaction with states and potentials on surrounding atoms of the solid. As a result the wave function of the electron will be rather similar to the atomic orbital of the free atom to which it belongs. In the tight-binding approximation, the wave functions of electrons can be written as the sum of Bloch wave functions (equation 2.4.2(*a*)):

$$\varphi_k^i = \frac{1}{\sqrt{N}} \sum_{\boldsymbol{n}} e^{i\boldsymbol{k}\boldsymbol{R_n}} \varphi_i(r - R_n) = \frac{1}{\sqrt{N}} \sum_{\boldsymbol{n}} e^{i\boldsymbol{k}\boldsymbol{R_n}} \varphi_i W_n\,(r - R_n) \qquad \text{Eq. 2.4.2}(a)$$

For mathematical convenience, the crystal is divided up into regions inside muffin-tin spheres, where Schrödinger's equation is solved numerically, and an interstitial region. In all LMTO methods the wave functions in the interstitial region are constant.

TB-LMTO method is a self-consistent calculation, so it takes more time than EHT, which also means that it has higher accuracy. TB-LMTO is an extremely efficient method for band structure calculations utilizing large number of *k*-points. However, the Atomic Spheres

Approximation really imposes limitations upon this LMTO calculation by neglecting the contributions from currents in the interstitial regions between the atomic spheres. It makes an atomic sphere around each atom in the unit cell and ensures that the total volume of the atomic spheres is equal to the volume of the unit cell. In simple systems, it is possible to optimize the Wigner-Seitz radii to build the atomic spheres. For the complex systems, it can be difficult to maintain the constant radii when comparing hypothetical structures.

2.4.3 VASP Calculation. We also did first-principles calculations using the Vienna *ab initio* simulation package (VASP). [23-26] VASP employs pseudopotentials or the projector-augmented wave method and a plane wave basis set to handle electrons. So the electron densities are independent of the atomic positions, as a result, structural optimizations and the total energy calculations on many hypothetical structures converge with relative ease. Although pseudopotentials are not as straightforward as the atomic orbital basis set, Blochl's description of projector-augmented wave (PAW) pseudopotentials provides a means of retaining information about the correct behavior of the valence electron wavefunctions. This allows pseudopotentials to be analyzed based on orbital descriptions, similar to the linear combinations of atomic orbitals (LCAO) method that is familiar to chemists.

A few of key uses for VASP in the research are: (*a*) total energy calculations with or without spin polarization, (*b*) structural optimizations with or without spin polarization, (*c*) determining electron localization through charge-density plots. The main disadvantage of VASP is the requirement to input size cutoffs to calculate integrated values. These values are often rather arbitrary and require a keen chemical sense to substantiate their sizes.

2.5 Reference

[1] Gschneidner, K. A.; Bünzli, J. C.; Pecharsky, V. K. *Handbook on the Physics and Chemistry of Rare Earths*, Elsevier, 2004.

[2] Mei, J.; Halldearn, R. D.; Xiao, P. *Scripta Mater.***1999**, *41*, 541.

[3] Petrov, I.; Mojab, E.; Powell, R. C.; Greene, J. E.; Hultman, L.; Sundgren, J. E. *Appl. Phys. Lett.* **1992**, *60*, 2491.

[4] Cai, F. S.; Zhang, G. Y.; Chen, J.; Gou, X. L.; Liu, H. K.; Dou, S. X. *Angew. Chem. Int. Ed.* **2004**, *43*, 4212.

[5] Scheel, H. J.; Schulz-Dubois, E. O. *J. Cryst. Growth* **1971**, *8*, 304.

[6] Pecharsky, V. K.; Zavalij, P. Y. *Fundamentals of Powder Diffraction and Structural Characterization of Materials*. Springer, 2004.

[7] Klug, H. P.; Alexander, L. E. *X-Ray Diffraction Procedures: For Polycrystalline and Amorphous Materials,* Wiley-VCH*,* 1974.

[8] *PowderCell*, version 2.3, Federal Institute for Materials Research and Testing: Unter den Eichen, Berlin, Germany, 2000.

[9] Nordgren, J.; Bray, G.; Cramm, S.; Nyholm, R.; Rubensson, J. E.; Wassdahl, N. *Rev. Sci. Instrum.*, **1989**, *60*, 1690.

[10] Rietveld, H.M. *J. Appl. Crystallogr.* **1969**, *2*, 65.

[11] Hunter, B.A.; Howard, C.J. *LHPM-Rietica*, version 1.71: Australian Nuclear Science and Technology Organization: Menai, Australia, 2000.

[12] Sheldrick, G. M. *SADABS*, University of Gottingen: Gottingen, Germany, 2001.

[13] Sheldrick, G. M. *Acta Crystallogr. A* **2008**, *64*, 112.

[14] *SHELXTL*, version 6.10, Bruker AXS Inc.: Madison, WI, 2000.

[15] *Diamond*, version 3.2; Crystal Impact: Bonn, Germany, 2010.

[16] Lovesey, S. W.; Lovesey, S. W. *Theory of Neutron Scattering from Condensed Matter*, Oxford: Clarendon Press, 1984.

[17] Rodriguez Caravajal, J. *Fullprof*, version 3.2; Laboratoire Léon Brilloui, 1997.

[18] O'handley, R. C. *Modern Magnetic Materials: Principles and Applications*, Wiley, New York, 2000.

[19] Kittel, C.; McEuen, P. *Introduction to Solid State Physics*, Wiley, New York, 1996.

[20] Stewart, G. R. *Rev. Mod. Phys.***1984**, *56*, 755.

[21] Hoffmann, R. J. *Chem. Phys.* **1963**, *39*, 1397.

[22] Jepsen, O.; Andersen, O.K. *TB-LMTO*, version 47; Max-Planck-Institut für Festkörperforschung: Stuttgart, Germany, 2000.

[23] (a) Kresse, G.; Hafner, J. *Phys. Rev. B* **1993**, *47*, 558. (b) Kresse, G.; Hafner, J. *Phys. Rev. B* **1994**, *49*, 14251.

[24] Kresse, G.; Furthmüller, J. *Comput. Mat. Sci.* **1996**, *6*, 15.

[25] Kresse, G.; Furthmüller, J. *Phys. Rev. B* **1996**, *54*, 11169.

[26] Kresse, G.; Joubert, D. *Phys. Rev. B*. **1999**, *59*, 1758.

CHAPTER 3

β-Mn type $Co_{8+x}Zn_{12-x}$ as a Defect Cubic Laves Phase: Site Preferences, Magnetism, and Electronic Structure

Modified from a publication in the Inorganic Chemistry
(*Inorg. Chem.* **2013**, *52*, 9399)

Weiwei Xie,[a] *Srinivasa Thimmaiah,*[a] *Jagat Lamsal,*[b], *Jing Liu,*[c] *Thomas W. Heitmann,*[d] *Dante Quirinale,*[b] *Alan I. Goldman,*[b] *Vitalij Pecharsky,*[c] *Gordon J. Miller*[a]*

[a] Department of Chemistry, Iowa State University and Ames Laboratory, US Department of Energy, Ames, IA, USA 50011
[b] Department of Physics and Astronomy, Iowa State University and Ames Laboratory, US Department of Energy, Ames, IA, USA 50011
[c] Department of Material Science and Engineering, Iowa State University and Ames Laboratory, US Department of Energy, Ames, IA, USA 50011
[d] The Missouri Research Reactor, University of Missouri, Columbia, MO, USA 65211

3.1 Abstract

Results of a crystallographic analysis, magnetic characterization, and theoretical assessment of β-Mn type Co-Zn intermetallics prepared using high temperature methods are presented. These β-Mn Co-Zn phases crystallize in the space group $P4_132$ (Pearson symbol *cP*20; a = 6.3555(7)-6.3220(7)) and their stoichiometry may be expressed as $Co_{8+x}Zn_{12-x}$, ($1.7(2) < x < 2.2(2)$). According to a combination of single crystal X-ray diffraction, powder neutron diffraction, and scanning electron microscopy, atomic site occupancies establish clear preferences for Co atoms in the 8*c* sites and Zn atoms in the 12*d* sites with all additional Co atoms replacing some Zn atoms, a result which can be rationalized by electronic structure calculations. Magnetic measurements and powder neutron diffraction of an equimolar Co:Zn sample confirm ferromagnetism in this phase with a Curie temperature of ~420 K. Neutron powder diffraction and electronic structure calculations using the local spin density

approximation indicate that the spontaneous magnetization of this phase arises exclusively from local moments at the Co atoms. Inspection of the atomic arrangements of $Co_{8+x}Zn_{12-x}$ reveals that the β-Mn aristotype may be derived from an ordered defect, cubic Laves phase ($MgCu_2$-type) structure. Structural optimization procedures using the Vienna Ab-initio Simulation Package (VASP) and starting from the undistorted, defect Laves phase structure achieved energy minimization at the observed β-Mn structure type, a result which offers greater insights into the β-Mn structure type and establishes a closer relationship with the corresponding α-Mn structure (*cI*58).

3.2 Introduction

Understanding the relationships among structure, composition, bonding, and properties of complex intermetallic compounds remains both fascinating and challenging because few general predictive strategies have emerged that allow targeted synthesis of novel compounds with specific properties. For compounds involving the late- and post-transition metals, the Hume-Rothery electron counting rules, [1] which emphasize the valence *s* and *p* electrons in the compound, can be used to rationalize crystal structure. However, if a system exhibits partially filled *d*-bands, then these rules to predict crystal structures typically incorporate negative valences for the transition metals, but cannot rationalize some subtle structural distortions nor element distributions.[2] Electronic structure calculations have successfully identified some patterns of band structure and occupancies in γ-brass Fe-Zn,[3] Ni-Zn,[3] and M-Ga (M = Cr-Fe)[4-6] cases, yet no reports have examined the noncentrosymmetric cubic β-Mn type systems in any systematic way. For example, unlike Fe or Ni, which reacts with Zn in 1:1 molar ratio to form a β-brass, Co is reported to form a β-Mn type structure with Zn.[7-9] However, other than a lattice constant, no other structural details have been reported.[10]

Therefore, investigating the Co-Zn system may help us to understand how 3*d* transition metals control the crystal structures within the framework of Hume-Rothery rules.

The Co-Zn system shows some anomalies in its phase equilibria arising, in part, from the magnetic transition associated with Co.[8] Ferromagnetism in elemental Co certainly influences its anomalous ground state structure, which is hexagonal close packed and not cubic close packed like Rh and Ir, by breaking the degeneracy between spin-up and spin-down electronic states. Ferromagnetic "$Co_{0.5}Zn_{0.5}$", which is the Co-richest intermetallic in the Co-Zn system and has been assigned the cubic β-Mn type (Strukturbericht designation *A*13), was explored for its magneto-optical properties several decades ago.[10] In recent years, the Zn-rich region of the Co-Zn diagram has been reinvestigated for two brass-like structures, δ-Co_2Zn_{15} and δ_1-$CoZn_{7.8}$,[11,12] the first of which shows an interesting double-helix of icosahedra. However, there are only a few reports of Co-rich Co-Zn phases,[8,10] and even any characterization of β-Mn type Co-Zn phases remains limited other than a lattice constant (a = 6.319 Å), its room temperature magnetization (39 $A \cdot m^2 \cdot kg^{-1}$) and polar Kerr rotation angle (–0.25° at 633 and 830 nm).[10] The recent observation of skyrmions, which are described as vortex-like spin structures, in noncentrosymmetric cubic magnetic solids like MnSi and FeGe provide additional impetus for a closer examination of the noncentrosymmetric β-Mn type systems that contain magnetically active metals.[13-15] In particular, Nuclear Quadrupole Resonance (NQR) studies[16] on β-Mn itself show that inequivalent Mn atoms contribute differently to its overall magnetism. Moreover, there is a close structural relationship between octagonal quasicrystals and the β-Mn structure.[17-20]

With these magnetic and structural features in mind, we report herein a thorough structural characterization and investigation of the magnetic properties and theoretical electronic structures of β-Mn type Co-Zn phases, with an emphasis on elemental distribution throughout the unit cell, local magnetic moments, and chemical bonding. In a subsequent study, we will examine the electronic states and bonding features with respect to other related intermetallic phases.

3.3 Experimental Section

3.3.1 Synthesis. β-Mn type Co-Zn phases were obtained by fusion of mixtures of Co pieces (99.9%, Ames Laboratory) and Zn particles (99.99%, Alfa Aesar), combinations that ranged from 35-65 mole percent Zn. Each reactant mixture, about 500 mg total, was sealed into an evacuated silica tube ($<10^{-5}$ Torr), heated to 1000 °C for 12 hr, followed by cooling to 925 °C at a rate of 1 °C/hr and annealed at this temperature for 3 days, after which the container was quenched into water or slowly cooled in the furnace. Seven different Co-Zn samples were prepared (see Table 1). Of these, the three Zn-rich loadings yielded a mixture of β-Mn type and γ-brass Co_2Zn_{11}. The two Co-rich samples contained β-Mn type compounds and Co particles. Only the two intermediate loadings, i.e., 50 and 55 mole percent Zn, led to single-phase β-Mn type compounds. Using an optical microscope, the β-Mn type crystals adopt tetragonal block shapes, whereas γ-brass Co_2Zn_{11} crystals have elongated rectangular morphologies. All products are stable toward decomposition in air and moisture, but react with dilute acid at room temperature.

3.3.2 Phase Analyses. All samples were finely ground and examined by powder X-ray diffraction for identification and phase purity on a STOE WinXPOW powder diffractometer employing Cu radiation ($\lambda_{K\alpha}$= 1.5406 Å) for all the samples. The scattered intensity was

recorded as a function of Bragg angle (2θ) using a scintillation detector with a step of 0.03° 2θ in step scan mode, ranging from 0° to 130°. Phase identification was accomplished using the program *PowderCell*, [21] and lattice parameters from manually selected β-Mn type crystals were refined by Bragg's law using a silicon 640*b* powder X-ray diffraction position standard (NIST; $a = 5.430940 \pm 0.000035$ Å).

Because X-ray fluorescence can create high background for Co-containing samples examined using Cu *K*α radiation, X-ray powder diffraction patterns of three samples showing high yields of a β-Mn phase, i.e., those loaded with 40, 50, and 60 atomic percent Zn, were also collected on a Philips PANalytical X'pert-Pro powder diffractometer using Co radiation ($\lambda_{K\alpha}$=1.7903Å). The scattered intensities were recorded in step scan mode with 0.008° steps over a 2θ range from 5°-100°. For these measurements, phase identification and the lattice parameters were refined by full-profile Rietveld [22] refinements using *LHPM RIETICA*[23].

3.3.3 Structure Determination. Crystals from each reaction sample were mounted on the tips of glass fibers. Room temperature intensity data were collected on a Bruker Smart Apex CCD diffractometer using Mo Kα radiation (λ = 0.71073 Å). Data were collected over a full sphere of reciprocal space by taking three sets of 606 frames with 0.3° scans in ω with an exposure time of 10s per frame. The 2θ range extended from 8° to 60°. The *SMART* software was used for data acquisition. Intensities were extracted and corrected for Lorentz and polarization effects using the *SAINT* program. Empirical absorption corrections were accomplished with *SADABS*, which is based on modeling transmission by spherical harmonics employing equivalent reflections with $I > 3\sigma(I)$.[24-25] With the *SHELXTL* package,[26] the crystal structures were solved using direct methods and refined by full-matrix

least-squares on F^2. All crystal structure drawings were produced using the program *Diamond*.[27]

3.3.4 Neutron Powder Diffraction (NPD). Neutron powder diffraction (NPD) measurements on a polycrystalline sample with nominal composition of $Co_{50.15(1)}Zn_{49.85(1)}$, which produced the highest yield of β-Mn type compound, were performed on the high resolution powder diffractometer at the University of Missouri Research Reactor (MURR) using a double focusing Si (511) crystal monochromator to select neutrons with a wavelength, λ = 1.4803Å. To obtain sufficient sample for NPD measurements, ~1.3 grams of polycrystalline $Co_{50.01(1)}Zn_{49.99(1)}$ were loaded in a vanadium sample holder (7.5 cm long; 3.0 mm diameter). A set of five linear position sensitive detectors was employed to collect a series of 19° sections of the diffraction pattern; the full diffraction pattern was measured in five steps to a $2\theta_{max}$ value of 108°. This powder diffractometer uses a radial oscillating collimator that averages the shadow of the collimator blades at every channel. The large detector areas allow very weak magnetic peaks to be detected by neutrons with high statistical accuracy. The NPD pattern at 293K was taken in air, whereas the pattern at 500K was collected using a high-temperature furnace. We note that the large amount of material contained with the high temperature furnace results in a high background in the low-angle segment of the patterns. Therefore, the empty furnace background was subtracted from the powder diffraction pattern collected for the sample in the high temperature furnace to represent the diffraction pattern from the sample only. Analysis of the NPD data was performed by the Rietveld method using the program *FULLPROF*.[28]

3.3.5 Scanning Electron Microscopy (SEM). Characterization was completed using a variable pressure scanning electron microscope (Hitachi S-2460N) and Energy-Dispersive

Spectroscopy (EDS) (Oxford Instruments Isis X-ray analyzer). Samples were mounted in epoxy, carefully polished, and then sputter-coated with a thin layer of carbon prior to loading into the SEM chamber. The samples were examined at 20 kV. Spectra were collected for 100 seconds. An Oxford Instruments Tetra backscattered electron (BSE) detector was used to image the samples using the BSE signal. Multiple points were examined in each phase within multiple grains of a specimen. Compositional estimates were calculated using Oxford's SEM *Quant* software to correct intensities for matrix effects.

3.3.6 Magnetization Measurements. The magnetization measurements were performed using a superconducting quantum interference device (SQUID) magnetometer MPMS XL-7, and Vibrating Sample Magnetometer (VSM) EV11 manufactured by Quantum Design, Inc. on pieces of β-Mn type single crystals that were manually selected from the product obtained from the loading with 49.85(1) atomic percent Zn. The SQUID operates over a temperature range of 2-300 K and in applied fields of up to 70 kOe. The samples were placed in glass capsules for measurement. The VSM was operated from 300K to 900K.

NPD at 293K also gives magnetic contribution to nuclear Bragg reflections, which facilitates refinement of magnetic moments on each atom.

3.3.7 Electronic Structure Calculations

Tight-Binding, Linear Muffin-Tin Orbital-Atomic Spheres Approximation (TB-LMTO-ASA)[29]: Calculations of the electronic and possible magnetic structures were performed by TB-LMTO-ASA using the Stuttgart code. Exchange and correlation were treated by the local density approximation (LDA) and the local spin density approximation (LSDA).[30] In the ASA method, space is filled with overlapping Wigner-Seitz (WS) spheres. The symmetry of the potential is considered spherical inside each WS sphere and a combined correction is

used to take into account the overlapping part. The WS radii are: 1.34 Å for Co; and 1.52 Å for Zn. No empty spheres are necessary, and the overlap of WS spheres is limited to no larger than 16%. The basis set for the calculations included Co 4*s*, 4*p*, 3*d* and Zn 4*s*, 4*p*, 3*d* wavefunctions.[31] The convergence criterion was set to 0.1 meV. A mesh of 60 *k* points in the irreducible wedge of the first Brillouin zone was used to obtain all integrated values, including the density of states (DOS) and Crystal Orbital Hamiltonian Population (COHP) curves.

Vienna ab-initio Simulation Package[32-35] (VASP): Structure optimization and charge density calculations[36-38] were completed using VASP, which employs projector augmented-wave (PAW) pseudopotentials that were adopted with the Perdew-Burke-Ernzerhof generalized gradient approximation (PBE-GGA), in which scalar relativistic effects are included. For structural optimization, the conjugate gradient algorithm was applied. The energy cutoff was 346.1 eV. Reciprocal space integrations were completed over a 9×9×9 Monkhorst-Pack k-points mesh[39] with the linear tetrahedron method.[40] With these settings, the calculated total energy converged to less than 0.1 meV per atom.

3.4 Results and Discussion

According to the Co-Zn phase diagram,[8] β-Mn type phases exist between ~49 and 58 atomic percent Zn, but this range narrows significantly to ~50 atomic percent Zn above ~920°C. Although the phase diagram indicates the existence of a "high-temperature ZnCo" phase, which may adopt the β-brass[7] (*cP*2 or *cI*2-type) structure in the range 820-870°C, our synthetic approach did not yield anything other than crystalline β-Mn type product. Because this structure type involves two sites with different multiplicities, i.e., 8*c* and 12*d*, elucidation of the Co/Zn distribution is warranted. This aspect of the structural chemistry may also

influence the bulk magnetic properties. In the course of investigating this Co-Zn phase, we identified an exceptional relationship between the structure of β-Mn and an extremely common intermetallic structure, the cubic Laves phase $MgCu_2$-type.

3.4.1 Phase Analyses: In accordance with the reported Co-Zn phase diagram, synthetic attempts to prepare β-Mn type Co-Zn phases yielded mixtures of phases for Co-rich or Zn-rich loadings. Only those reactant mixtures that were loaded approximately 50 and 55 atomic percent Zn yielded single phase, crystalline products. Co-rich loadings produced hcp-Co particles, which could contain significant fractions of Zn as a substitutional solid solution. On the other hand, Zn-rich reactions yielded a γ-brass Co-Zn phase in addition to a β-Mn type product. Table 1 summarizes the synthetic results; the powder X-ray diffraction patterns and electron micrographs of selected samples are illustrated in Figures S1 and S2 in Supporting Information.

Table 1. Compositions, phase analyses, lattice constants, and refined compositions for β-Mn type $Co_{8+\delta}Zn_{12-\delta}$ phases. PXRD = powder X-ray diffraction; SCXRD = single crystal X-ray diffraction.

Atomic % Zn Loaded	Phases (PXRD)	---------- *a* (Å) ---------- (PXRD)[a]	(SCXRD)[a]	(NPD)	---------- Composition ---------- (SCXRD)	(SEM)	(NPD)
35.04(1)	β-Mn; hcp-Co	6.315(5)					
40.33(1)	β-Mn; hcp-Co	6.319(2)	6.322(1)		$Co_{10.2(4)}Zn_{9.}$	$Co_{10.1(2)}Zn_{9.9(2)}$	
45.06(1)	β-Mn; hcp-Co	6.327(4)					
49.85(1)	β-Mn	6.329(7)	6.337(6)	6.3342(1)[b] 6.3547(2)[c]	$Co_{10.0(4)}Zn_{10}$	$Co_{9.8(2)}Zn_{10.2(2)}$	$Co_{10.4(2)}Zn_{9.6(2)}$
55.01(1)	β-Mn	6.331(6)					
60.03(1)	β-Mn; γ-brass	6.339(7)	6.341(2)		$Co_{9.9(4)}Zn_{10.}$	$Co_{9.5(2)}Zn_{10.5(2)}$	
65.10(1)	β-Mn; γ-brass	6.344(7)	6.356(3)		$Co_{9.7(2)}Zn_{10.}$		

[a] 293 K; Numbers in ( )'s are standard uncertainties using at least two different measurements of similar loadings.
[b] 293 K; Numbers in ( )'s are standard uncertainties in the last given digit from standard deviation of Rietveld fits.
[c] 500 K; Numbers in ( )'s are standard uncertainties in the last given digit from standard deviation of Rietveld fits.

For the X-ray powder diffraction patterns, all scale factors and lattice parameters were refined, whereas the displacement parameters of all atoms were assumed to be isotropic at B = 0.6 according to NPD measurement and were not refined. The resulting profile residuals Rp varied between ca. 1.6-2.8 with weighted profile residuals R_{wp} between ca. 2.2-4.0. The refined lattice parameters for β-Mn type Co-Zn phases showed a 0.46(8)% increase according to X-ray powder diffraction as the Zn loading increased from 35 to 65 atomic percent. Single crystals extracted from four reaction products showed a similar trend, +0.54(6)%. Analysis of samples, whether by refinements from single crystal or neutron powder diffraction, or by SEM, all fall within two standard deviations of an equimolar ratio of Co:Zn in this phase. Therefore, β-Mn type Co-Zn phases exhibit a small homogeneity region centered at 50 mol.% Zn when quenched from 925°C. From our powder diffraction results, the lower bound for Zn content lies between 40-45 atomic percent, whereas the upper bound is 55-60 atomic percent. Results from single crystal diffraction suggest an even narrower range (see discussion below).

Because the published phase diagrams[7,8,41] from the last 25 years show various homogeneity widths of this Co-Zn phase region toward lower temperatures, three samples loaded with 40, 50, and 60 atomic percent Zn were heated to 1000°C at a rate of 1 C°/min, kept for 12 hr, then cooled to 600 °C at 1 C°/min, at which point they were annealed for 3 weeks. Upon cooling to room temperature, PXRD patterns showed β-Mn type Co-Zn phases in all three, with increasing lattice constants (6.3526(1)Å, 6.3570(1)Å, and 6.3601(1)Å) with

increasing loaded Zn content. Moreover, the Zn-richest sample also contained γ-brass-type phase; the Co-richest sample indicated hcp-Co; and 50:50 sample was essentially single phase. These results confirm that the β-Mn-type Co-Zn phase exists over a broad range of concentrations as temperature is lowered to 600 °C.

3.4.2 Structure Determination and Site Preferences. To obtain further insights into the structural features of these β-Mn type Co-Zn phases, single crystals were investigated to extract elemental distributions and accurate determination of interatomic distances and coordination environments. The results of single crystal diffraction on specimens extracted from four distinct loadings are summarized in Tables 2 and 3. Corresponding anisotropic displacement parameters and significant interatomic distances are summarized in Tables S1 and S2 in Supporting Information. All structures crystallize in the noncentrosymmetric cubic space group $P4_132$ (No. 213) with atoms located at the 8*c* (C_3 symmetry) and 12*d* (C_2 symmetry) sites. Regardless of refined compositions, the 8*c* sites are fully occupied by Co atoms, whereas the 12*d* sites accommodate a mixture of Co and Zn atoms. Therefore, a formulation of these phases is $Co_{8+x}Zn_{12-x}$, in which x ranges from ~1.7(2)-2.2(2), to reflect this pattern of site occupation. Before embarking on a discussion of the structural subtleties of this Co-Zn phase, however, we have identified an interesting relationship between the complex β-Mn type structure and that of the cubic Laves phase, $MgCu_2$-type.

Table 2. Single crystal crystallographic data for β-Mn type Co-Zn phases at 293(2) K.

Load. Comp. (at. % Zn)	40.33(1)	49.85(1)	60.03(1)	65.10(1)
Refined Formula	$Co_{10.2(2)}Zn_{9.8}$	$Co_{10.0(2)}Zn_{10.0}$	$Co_{9.8(2)}Zn_{10.2}$	$Co_{9.7(2)}Zn_{10.3}$
F.W. (g/mol)	1241.39	1242.94	1244.48	1244.88
F(000)	1138	1140	1142	1142
a (Å)	6.3220(7)	6.3358(14)	6.3450(7)	6.3555(7)

Table 2. continued

V (Å^3)	252.68(5)	254.33(10)	255.44(5)	256.71(5)
d_{calc} (Mg/m^3)	8.158	8.115	8.093	8.041
Abs. Corr.	Empirical	Empirical	Empirical	Empirical
Ext. Coeff.	0.018(2)	0.004(1)	0.014(4)	0.003(1)
μ (mm^{-1})	38.879	38.800	38.856	38.656
θ range (deg)	4.56–28.05	4.55–27.99	4.54–27.94	4.54–28.32
hkl ranges	$-8 \le h,k,l \le 8$	$-8 \le h,k,l \le 8$	$-8 \le h,k,l \le 8$	$-8 \le h,k,l \le 8$
No. Refl. (R_{int})	1572 (0.0467)	1570 (0.0376)	2216 (0.0287)	2205 (0.0245)
No. Indep. Refl.	110	109	110	111
No. Par.	12	12	12	12
R_1; wR_2 (all I)	0.0170; 0.337	0.0167; 0.0280	0.0115; 0.0278	0.0146; 0.0290
Goodness of fit	1.285	1.180	1.358	1.321
Peak; Hole (e$^-$/Å^3)	0.432; –0.463	0.320; –0.353	0.407; –0.388	0.405; –0.442

Table 3. Atomic coordinates, site occupancies, and equivalent isotropic displacement parameters of β-Mn type Co-Zn phases at 293(2) K. U_{eq} is defined as one-third of the trace of the orthogonalized U_{ij} tensor (Å^2).

$Co_{10.2(2)}Zn_{9.8}$

Atom	Wyckoff Site	Occupancy	x	y	z	U_{eq}
Zn/Co	12*d*	0.81(3)/0.19	1/8	0.2031(1)	0.4531(1)	0.0100(3)
Co	8*c*	1	0.0649(1)	0.0649(1)	0.0649(1)	0.0072(3)

$Co_{10.0(2)}Zn_{10.0}$

Atom	Wyckoff Site	Occupancy	x	y	z	U_{eq}
Zn/Co	12*d*	0.83(3)/0.17	1/8	0.2030(1)	0.4530(1)	0.0108(3)
Co	8*c*	1	0.0648(1)	0.0648(1)	0.0648(1)	0.0081(3)

$Co_{9.8(2)}Zn_{10.2}$

Atom	Wyckoff Site	Occupancy	x	y	z	U_{eq}
Zn/Co	12*d*	0.86(2)/0.14	1/8	0.2030(1)	0.4530(1)	0.0099(2)
Co	8*c*	1	0.0648(1)	0.0648(1)	0.0648(1)	0.0073(2)

$Co_{9.7(2)}Zn_{10.3}$

Atom	Wyckoff Site	Occupancy	x	y	z	U_{eq}

Table 3. continued

Zn/Co	12*d*	0.86(2)/0.14	1/8	0.2028(1)	0.4528(1)	0.0095(2)
Co	8*c*	1	0.0648(1)	0.0648(1)	0.0648(1)	0.0075(3)

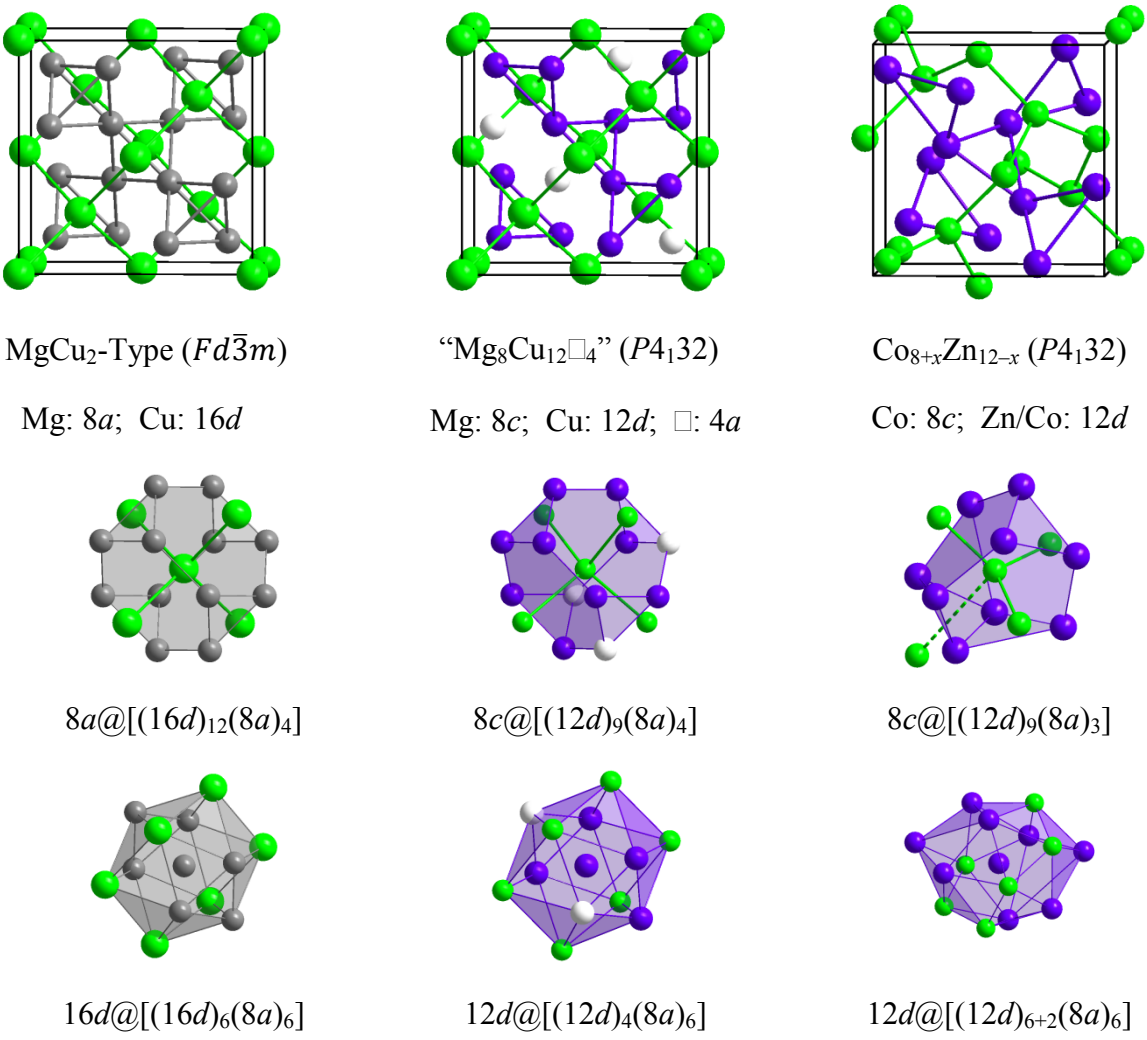

Figure 1. Unit cell and atomic coordination environments showing the relationship between the $MgCu_2$-type, cubic Laves phase structure and the β-Mn type, $Co_{8+x}Zn_{12-x}$. (Left) $MgCu_2$-type (Mg, green; Cu, gray); (Middle) hypothetical $Mg_8Cu_{12}\square_4$ (Mg, green; Cu, purple; □, white); (Right) β-Mn type $Co_{8+x}Zn_{12-x}$ (Co, green; Zn/Co, purple).

β-Mn as an Ordered Defect Cubic Laves Phase. In a tantalizing description of the analogies between the structures of β-Mn and the molecular solid P_4S_3, as well as between those of α-Mn and white phosphorus, Nesper intimated possible relationships between the structures of

α-Mn and β-Mn and tetrahedral structures.[42] As it turns out, the structure of β-Mn type $Co_{8+x}Zn_{12-x}$ (space group $P4_132$; Pearson symbol cP20) can be derived from the cubic Laves phase $MgCu_2$ (space group $Fd\bar{3}m$; Pearson symbol cF24), both of which exhibit some close relationships with the diamond structure. In particular, the Mg atom sites (Wyckoff designation 8a) in the cubic Laves phase $MgCu_2$ form precisely a three-dimensional (3-d) diamond network. Within the voids, Cu atoms (Wyckoff designation 16d) form a 3-d framework of vertex-sharing tetrahedra, as emphasized in Figure 1. The formulation of the complete cubic unit cell of this cubic Laves phase is, therefore, Mg_8Cu_{16}. After transforming the unit cell of the Laves phase from (***a***, ***b***, ***c***) to (–***b***, ***a***, ***c***) and orderly removal of 4 atoms from the 16d (Cu) sites, one from each tetrahedron located around the (revised) coordinates (¼, ¼, ¼), (¾, ¾, ¼), (¼, ¾, ¾), and (¾, ¼, ¾), a cubic "Mg_8Cu_{12}" unit cell can be created with space group $P4_132$ (see also Figure 1). Here, the Mg and Cu sites become, respectively, 8c and 12d, and the 4-fold vacant positions are 4a in the non-centrosymmetric space group. Relaxation of this hypothetical ordered defect cubic Laves phase structure yields the β-Mn structure type for $Co_{8+x}Zn_{12-x}$. We note that the vacant 4a sites are occupied by C atoms in Mo_3Al_2C[45] or N atoms in Mo_3Ni_2N.[43]

To study further this relationship between the cubic Laves phase (cF24) and β-Mn (cP20) structure types, a series of hypothetical "Co_8Zn_{12}" structures was constructed starting with "Co_8Zn_{16}" in space group $Fd\bar{3}m$ and following the algorithm discussed in the previous paragraph. The question becomes, how many distinct ways can one atomic site be removed from each of the four tetrahedra formed by the 16d sites? Because there are 4 tetrahedra, each with 4 atomic sites, it might appear that there are $4^4 = 256$ different possibilities. However, rotations, reflections, and translations will cause many of these options to be

equivalent. This counting problem can be solved by using Burnside's lemma,[44] which allows enumeration of distinct isomers ("orbits") in a set of structures that is permuted by a group. For this problem, it turns out that there are 9 distinct solutions, labeled α-ι,[44] which are listed and illustrated in Figure S3 of Supporting Information. For each ordered vacancy structure, "Co_8Zn_{12}," a complete structural optimization was carried out using VASP. Table 4 lists the total energies per atom relative to the lowest energy case before and after the structural relaxation. The arrangement of vacancies that gives the lowest energy before relaxation is model η, the one most closely related to the β-Mn type structure, space group $P4_132$. Upon relaxation, the atoms at the 8*c* sites shift from (0, 0,0) along body diagonals to final coordinates (x, x, x; x = 0.0649), whereas the atoms at the 12*d* sites shift from (⅛, ⅛, ⅜) along face diagonals to final coordinates (⅛, y, y+¼; y = 0.2029). Comparison with the crystallographic results in Table 3 indicates excellent agreement between the calculated ground state of the ordered defect structure and the experimentally determined parameters of β-Mn type $Co_{8+x}Zn_{12-x}$.

Table 4. Pearson symbols, volume (Å^3/atom) after relaxation, relative total energies (eV/atom) before and after relaxation, and relative electrostatic ("metallic") energies (eV/atom) before relaxation for the nine ordered defect models of "Co_8Zn_{12}". The labels of the models follow the assignment of an analogous problem in Ref. 45.

Model	Pearson Symbol	Volume/atom (Å^3)	ΔE_{TOT}/atom (eV)(before)	ΔE_{TOT}/atom (eV)(after)	ΔE_{ES}/atom (eV)(before)
α	*hR*15	12.20	0.4504	0.2292	39.7767
β	*mS*40	11.59	0.2255	0.2118	15.2145
γ	*oP*10	12.64	0.2130	0.1919	19.4932
δ	*mS*20	12.01	0.3631	0.4215	13.4378
ε	*aP*20	11.71	0.4180	0.1131	56.3823
θ	*cI*40	13.21	0.2349	0.2682	61.3661
η	*cP*20	11.51	0	0	0
ζ	*mS*40	12.43	0.1827	0.1301	17.5775

Table 4. continued

ι	*tP*20	12.27	0.1809	0.2374	15.7561

Assessment of the total energies after relaxation reveals that a major driving force for the ordering of defects comes from the electrostatic energy between the conduction electrons and the arrangement of atomic cores,[46] which gives its lowest value for model η (the β-Mn arrangement). This effect also leads to the lowest atomic volume for model η. Further analysis suggests that two-center orbital interactions prefer the alternative models ε and θ, both of which show the two highest electrostatic energies. Since these energy values can be dependent on valence electron count, i.e., energy band filling, we are examining the variation in defect ordering as a function of electron count, and other structural alternatives to the β-Mn structure type in the Co-Zn and related systems, and will report these results in a forthcoming paper.

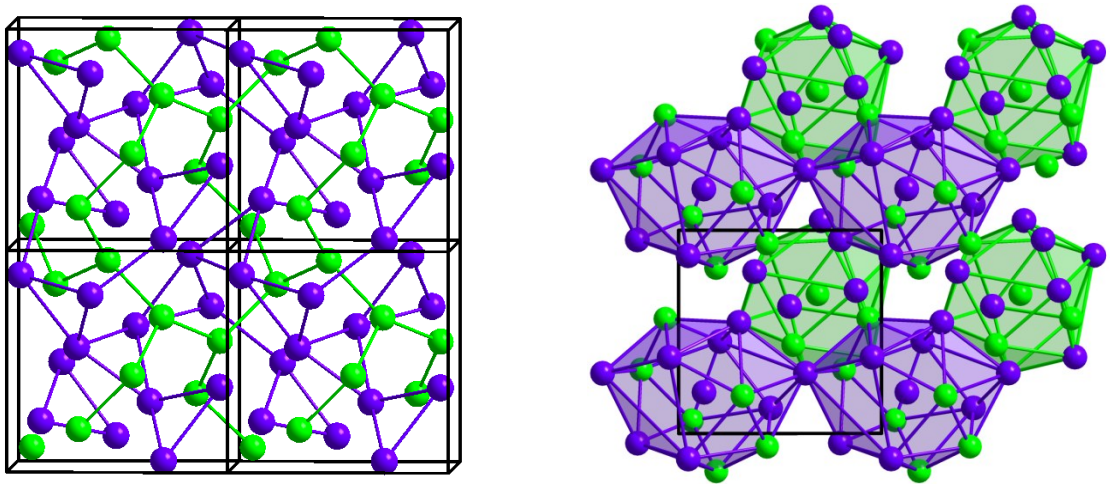

Figure 2. The crystal structure of β-Mn type $Co_{8+x}Zn_{12-x}$ showing (left) four unit cells with 8*c*–8*c* and 12*d*–12*d* connections emphasized and (right) a (001) view emphasizing the coordination polyhedra surrounding the 8*c* (green) and 12*d* (purple) sites.

Site Preferences in β-Mn type Co-Zn Phases. An expanded view of the unit cell and coordination polyhedra for β-Mn type $Co_{8+x}Zn_{12-x}$ is shown in Figure 2. The polyhedral

environments for each site in $Co_{8+x}Zn_{12-x}$ are Frank-Kasper polyhedra. The 8*c* (Co) site is surrounded by a distorted icosahedron consisting of 3 other 8*c* (Co) sites and 9 12*d* (Zn/Co) sites. On the other hand, each 12*d* (Zn/Co) site is coordinated by a 14-vertex polyhedron of 6 8*c* (Co) and 8 12*d* (Zn/Co). Thus, given the refined site occupancies for the 12*d* sites, each 8*c* Co atom is coordinated, on average, by 4.2(2)-4.7(2) Co atoms and 7.8-7.2 Zn atoms, whereas each 12*d* site is surrounded by 7.0(2)-7.5(2) Co atoms and 7.0-6.5 Zn atoms. Such Frank-Kasper polyhedra are signature building blocks of tetrahedrally close packed (*tcp*) solids, which are common among transition metal intermetallics.[47,48] Examples of *tcp* solids include the cubic $MgCu_2$-type and hexagonal $MgZn_2$-type Laves phases as well as the structure of α-Mn, which is also called the χ-phase. These structures, which are influenced by their valence electron concentrations or valence electron-to-atom ratios,[49] are composed of densely packed tetrahedra. The β-Mn type may also be assigned among the *tcp* solids, as each unit cell contains four distinct $[(8c)_2(12d)_3]$ trigonal bipyramids (two face-sharing tetrahedra) that are linked to each other via additional tetrahedra. In the series of $Co_{8+x}Zn_{12-x}$ crystals, the shortest distances occur between neighboring 8*c* (Co) sites; these are ~2.37 Å, which is ~5% shorter than the nearest neighbor Co–Co distances in hcp-Co (~2.50 Å). The 8*c*–12*d* (Co–Zn/Co) interatomic distances range from 2.59 to 2.70 Å, whereas the 12*d*–12*d* (Zn/Co–Zn/Co) distances are more uniform, viz., 2.65-2.68 Å. Both of these distance ranges are in line with the six shorter Zn–Zn distances (~2.66 Å) in hcp-Zn. Moreover, these structural features of the $Co_{8+x}Zn_{12-x}$ series are similar to the distance relationships in β-Mn (Mn_{20}), itself, and Re_3Fe_2.[43,50-52] Other related phases, e.g., Mg_3Ru_2[50] and Mo_3Ni_2N[43] have somewhat different distance relationships (see Table S3 in Supporting Information),

which is part of the detailed structural/computational investigation that is currently underway for these complex intermetallics.

Because Co and Zn differ by only approximately 10% in X-ray scattering functions, a sample loaded with an equimolar mixture of Co and Zn was prepared for NPD experiments as described above. The neutron scattering length for Co (2.49 fm) and Zn (5.68 fm) differ significantly. However, since neutron diffraction is also sensitive to magnetic ordering, data were taken both above and below the Curie point, i.e., ~420 K (see Figure 3 and subsequent section on Magnetic Characterization), yielded structural parameters that concur with the results of single crystal X-ray diffraction; these results are summarized in Table 5. Again, the 8*c* site refined to be fully occupied by Co. Refinement of the 12*d* site yielded ~80% Zn for an overall composition that is slightly Co-rich, i.e., $Co_{10.4(2)}Zn_{9.6}$. Furthermore, as part of this refinement, the 12*d* site was constrained to be fully occupied by a mixture of Co and Zn. The average of ten readings from this sample using SEM-EDS is $Co_{10.0(4)}Zn_{10.0(4)}$, which agrees well with the NPD refinement, and is consistent with results of single crystal XRD on crystalline specimens extracted from a similarly loaded sample. As expected, the unit cell constant and isotropic displacement parameters for the 8*c* and 12*d* sites are larger at 500 K than at 293 K. NPD refinement also indicated that polycrystalline β-Mn type $Co_{10.0(4)}Zn_{10.0(4)}$ showed some preferred orientation along the {001} family of directions.

Table 5. The refined parameters of an equimolar β-Mn type Co-Zn phase as determined by Rietveld refinement of NPD data at 293K and 500K. Numbers in parentheses are standard uncertainties in the last given digit from Rietveld fits.

293 K (*a* = 6.3343(1) Å); *Rp* = 3.83; *Rwp* = 5.17; *R*exp = 3.16; Bragg-*R* factor = 4.41; χ^2 for fit = 2.69

Atom	Wyckoff Site	Occupancy	*x*	*y*	*z*	*U* (Å)^2
Zn/Co	12*d*	0.80(2)/0.20	1/8	0.2033(1)	0.4532(1)	0.61(3)
Co2	8*c*	1	0.0648(1)	0.0648(1)	0.0648(1)	0.63(3)
Ferromagnetic moment = 0.85(3) μ_B/Co						

500 K (a = 6.3547(2) Å); Rp = 8.00; Rwp = 11.0; Rexp = 4.88; Bragg-R factor = 7.68; χ^2 for fit = 1.86

Atom	Wyckoff Site	Occupancy	x	y	z	U (Å)^2
Zn/Co	12*d*	0.80(2)/0.20	1/8	0.2028(2)	0.4533(5)	0.94(4)
Co2	8*c*	1	0.0662(5)	0.0662(5)	0.0662(5)	0.98(4)

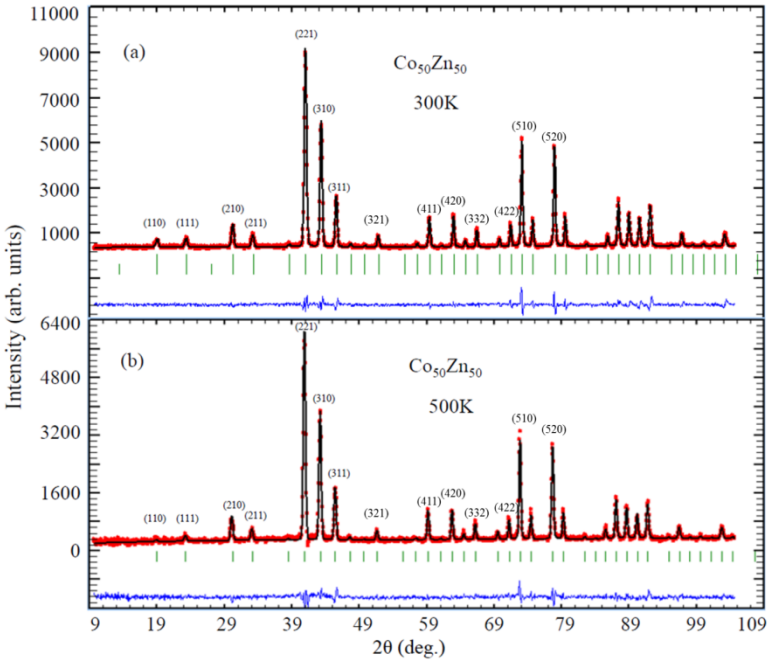

Figure 3. Neutron diffraction profile fits from Rietveld method using FULLPROF for $Co_{50}Zn_{50}$ (a) nuclear and magnetic Bragg reflections at 293 K and (b) nuclear Bragg reflections at 500 K. The observed data points are given by red circles, the calculated intensity pattern by black solid lines and corresponding residual (i.e. the difference between observed and calculated pattern) by the blue curve at the bottom of the fit. The green vertical upper tick marks reflect the Bragg positions for nuclear reflections and lower green tick give the Bragg positions for magnetic reflections.

As part of a brief discussion of the structural chemistry of α-Mn and β-Mn structures, Nesper suggested that the majority (12*d*) site in β-Mn might have slightly cationic character and the minority (8*c*) site has slightly anionic character.[42,53] Evaluation of charge densities at the 8*c* and 12*d* sites using a Bader analysis for various β-Mn model structures with late 3*d* metal atoms (Co-Zn) supports Nesper's suggestion (see Table S4 in Supporting Information) by yielding the 8*c* sites as valence electron *rich* and the 12*d* sites as valence electron *poor*. Nonetheless, a qualitative assessment of site preferences using atomic electronegativities remains unclear for the Co-Zn system. In particular, depending upon the electronegativity scale, there is no clear differentiation between Co and Zn. According to Pauling's scale, which used bond enthalpies to estimate electronegativities,[54] and Allen's configuration

energies,[55] Co (1.88; 10.85 eV) is more electronegative than Zn (1.65; 9.39 eV). On the other hand, Mulliken's scale or Pearson's absolute electronegativities,[56] which are derived from gas-phase ionization energies and electron affinities, indicate the opposite with Zn (4.45 eV) more electronegative than Co (4.27 eV). Nevertheless, in such an intermetallic compound, metallic properties would preclude any significant charge transfer between atoms, but does not discount a redistribution of orbital occupations from the ground state gaseous atoms. In fact, relative atomic sizes as reflected in 12-coordinate metallic radii may be more discriminating for observed β-Mn type examples. The 8*c* site, which is fully occupied by Co (1.25 Å) in $Co_{8+x}Zn_{12-x}$, Ru (1.34 Å) in Mg_3Ru_2, and Fe (1.26 Å) in Re_3Fe_2, attracts the smaller atom, whereas Zn (1.37 Å), Mg (1.60 Å), and Re (1.37 Å) fill the majority 12*d* sites. Only in Mg_3Ru_2 does the electronegativity argument parallel the size argument. Therefore, quantum chemical calculations are warranted to examine possible driving forces arising from the electronic structure that influence the structural stability and site preferences in β-Mn type $Co_{8+x}Zn_{12-x}$.

3.4.3 Electronic Structure and Chemical Bonding. To examine possible electronic influences for the site preferences in $Co_{8+x}Zn_{12-x}$, VASP calculations were employed to evaluate the total energies and magnetic moments of five different cases (**I**-**V**) of β-Mn type $Co_{10}Zn_{10}$ ($x = 2$) with various elemental distributions on the 8*c* and 12*d* sites. For each case, four distinct arrangements were calculated. The average relative total energies, their corresponding standard deviations, and the ranges of magnetic moments per formula unit are listed for each case in Table 6 (specific results are summarized in Table S5 in Supporting Information). Among these five cases, expressed as $(8c)_8(12d)_{12}$, **I** most closely resembles the experimental results with Co atoms filling the 8*c* sites and **III** is closest to a statistical

occupation of both crystallographic sites. According to the relative total energies in Table 6, the experimental result with Co fully occupying the 8*c* sites clearly gives the overall lowest energy. A linear regression analysis using the total energies of Models **I**-**IV** estimate a rise in total energy by ~44(2) meV/Zn atom in the 8*c* site. Fluctuations in the tabulated energies originate from the specific atomic locations within each model. Somewhat surprising, however, are the comparable total energies between Models **IV** and **V**, a result that arises from similar coordination environments in these structural models.

Table 6. Relative total energies (ΔE; meV/unit cell) with respect to the lowest energy model for various atomic distributions in β-Mn type $Co_{10}Zn_{10}$.

Model:		**I**	**II**	**III**	**IV**	**V**
Formulation:	**8*c*:**	$(Co)_8$	(Co_6Zn_2)	(Co_4Zn_4)	(Co_2Zn_6)	(Zn_8)
	12*d*:	(Co_2Zn_{10})	(Co_4Zn_8)	(Co_6Zn_6)	(Co_8Zn_4)	$(Co_{10}Zn_2)$
ΔE (meV / f.u.)		0(4)	111(4)	195(12)	264(30)	264(4)
μ (μ_B / f.u.)		12.8~13.0	11.8~12.4	12.4~13.3	13.9~14.1	~14.2

To gain further insights into the electronic influences on the site preference problem and phase width, as well as possible magnetic properties of the β-Mn type $Co_{8+x}Zn_{12-x}$, TB-LMTO-ASA calculations were carried out to evaluate and analyze the electronic DOS. With the local density approximation (LDA), the corresponding DOS curve for a hypothetical "Co_8Zn_{12}" (216 valence electrons) is illustrated in Figure 4, which emphasizes contributions from the Co valence orbitals (a more detailed orbital decomposition of the DOS curve is shown in Figure S4 of Supporting Information). Most of the DOS curve between –3 eV and +1 eV (0 eV = the Fermi level for 216 valence electrons) belongs to the Co 3*d* band; below –3 eV is a ~5 eV tail comprising a combination of Co and Zn 4*s* orbital contributions. The Zn 3*d* orbitals create a narrow band located ~7-8 eV below the Fermi level. In the LDA DOS

curve, the Co 3*d* band exhibits little fine structure except for a noticeable pseudogap at approximately –0.5 eV (204 valence electrons) and a sharp, intense peak, which is ~0.1 eV wide, just below 0 eV. According to the corresponding COHP curves, the wavefunctions contributing to this peak have strong 8*c*–8*c* (Co–Co) antibonding character. The pseudogap at –0.5 eV is associated with optimization of 8*c*–12*d* (Co–Zn) orbital interactions in this structure. On the other hand, the LDA band structure (shown in Figure S5 of Supporting Information) reveals that the peak involves Co 3*d* bands that are relatively flat (nearly dispersionless) near the Brillouin zone boundaries (near point M and along the direction M-R). These features of the LDA-DOS arise from structural influences on the orbital interactions in β-Mn type $Co_{8+x}Zn_{12-x}$. The Fermi level for $Co_{10}Zn_{10}$ (210 valence electrons) is both located on the lower energy edge of the peak just below 0.0 eV. Evaluation of the Stoner condition using the Co partial DOS gives $N(\mathrm{Co})I(\mathrm{Co}) = 1.56$; $N(\mathrm{Co}) = 3.18\ \mathrm{eV}^{-1}$, $I(\mathrm{Co}) = 0.49$ eV.[57,58] Thus, according to the LDA-DOS curves, β-Mn type $Co_{8+x}Zn_{12-x}$ ($x \sim 2$) is susceptible toward either a possible structural distortion by disrupting the antibonding Co–Co orbital interactions at the Fermi level or toward ferromagnetism by breaking the spin degeneracy.[59] To a first approximation, the Stoner condition for ferromagnetism is satisfied.

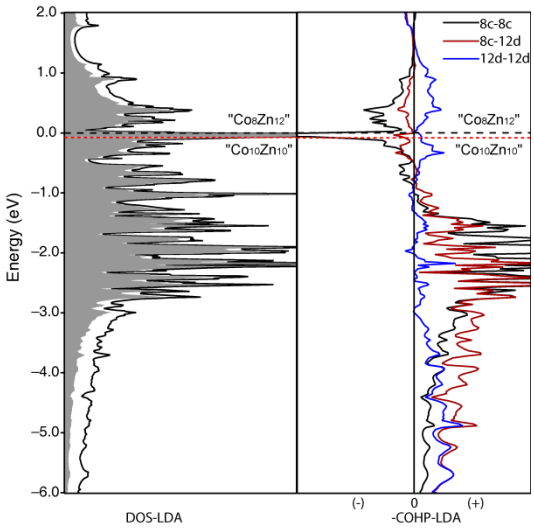

Figure 4. Partial DOS curves and –COHP curves of "Co_8Zn_{12}" obtained from non-spin-polarization (LDA). (+ is bonding/ − is anti-bonding, E_F for 216e$^-$ is set to zero.)

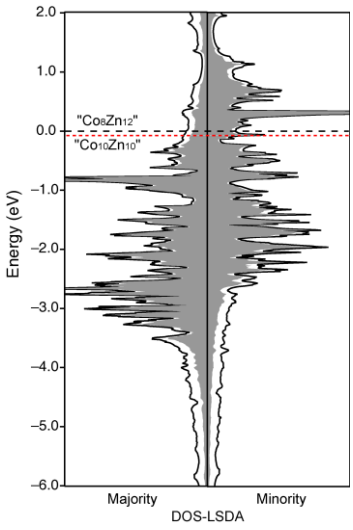

Figure 5. Partial DOS curves of "Co_8Zn_{12}" obtained from spin-polarization (LSDA). E_F for 216e$^-$ is set to zero.

Applying spin polarization via the local spin density approximation (LSDA) splits the DOS curves for the spin-up and spin-down wavefunctions, as seen in Figure 5. The corresponding Fermi levels for 210 and 216 valence electrons are shifted away from the peaks in the DOS curves, and closely approach the pseudogap in the minority spin DOS curve, at which the 8*c*–12*d* (Co–Zn) orbital interactions in this manifold of wavefunctions are optimized and occupation of 8*c*–8*c* antibonding states is avoided (see Figure S6 in Supporting Information). Therefore, the contribution from 8*c*–8*c* Co–Co orbital interactions constitute ca. 20.5% of the summed integrated COHP values over all interatomic contacts less than 4.2 Å in $Co_{10}Zn_{10}$. The 8*c*–12*d* metal-metal interactions contribute ca. 46% (see Table S6 in Supporting Information). The DOS also show peaks located at ca. –0.85 eV and +0.3 eV, respectively, in the majority and minority spin curves, features which arise from similar band dispersions seen in the LDA-DOS and LDA band structure (see also Figure S5 in Supporting Information). Integration of the spin-up and spin-down DOS curves yields a

total magnetic moment of 11.9 μ_B per formula unit for $Co_{10}Zn_{10}$. Analysis of local moments reveals essentially no net unpaired spins at each Zn atom, so the result corresponds to 1.19 μ_B per Co atom. Furthermore, the majority spin Co 3*d* band is not completely filled at the Fermi level, so the result also indicates soft ferromagnetic behavior.

Table 7. Magnetic data of $Co_{10.0(1)}Zn_{10.0}$ from magnetization measurements, NPD, and theoretical calculations.

	μ_{SAT} at 2 K (μ_B/f.u.)	μ_{SAT} at 300 K (μ_B/f.u.)	μ_{EFF} (μ_B/f.u.)	μ(Co) (μ_B)	T_{Curie} (K)
SQUID,VSM	13.0(2)	10.3(2)	8.5(2)		418(15)
NPD				0.85(3)	~420
Theory	11.9				

3.4.4 Magnetization Measurements. The isothermal magnetization curves of β-Mn type $Co_{10.0(2)}Zn_{10.0}$ (loaded as 49.85(1) atomic percent Zn) measured at 2 K and 300 K indicate the sample to be ferromagnetic. Table 7 summarizes the results of this magnetization study. The saturation is achieved at 10.0 kOe at 2 K. The saturation moments are obtained from hysteresis 13.0(2) μ_B/f.u. at 2 K and 10.3(2) μ_B/f.u. at 300 K.[60] The saturation moment observed at 2 K agrees well with the value of the total magnetic moment per unit cell (formula unit) calculated by electronic structure methods. Moreover, temperature-dependent magnetic susceptibility measurements from 300 K to 600 K confirm the ferromagnetic nature of the phase $Co_{10.0(2)}Zn_{10.0}$ with a Curie temperature of 418(15) K (see Table 7 and Figure 6 below).

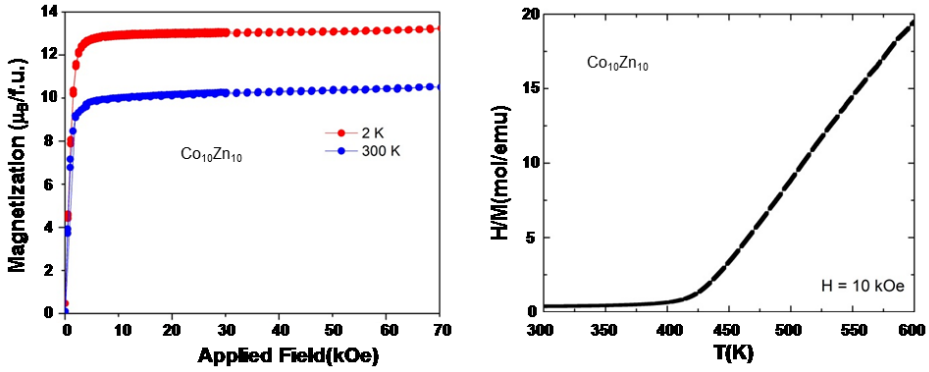

Figure 6. (Left) Hysteresis curves at 2 K and 300 K and (right) $\chi_m^{-1}(T)$ curve measured in 10 kOe field for β-Mn type $Co_{10(2)}Zn_{10}$. The corresponding magnetization vs. temperature curve in 10kOe field is shown in Figure S7 in Supporting Information.

From NPD, the magnetic structure of as-loaded $Co_{10.0(1)}Zn_{10.0}$ was refined in the space group $P\bar{1}$, with a refined composition $Co_{10.4(2)}Zn_{9.6}$. Modeling of the magnetic intensities at 293 K revealed a ferromagnetic structure giving a local Co moment of 0.85(3) μ_B with the direction at each Co atom pointing along the crystallographic ***c***-direction, and a total effective moment of 8.8(4) μ_B. This value agrees well with an effective moment of 8.5(2) μ_B obtained from a linear Curie-Weiss fit of the magnetic susceptibility data evaluated between 450 K and 600 K. In addition, from the NPD magnetization measurement, the Curie point is around 420 K, which is consistent with the magnetic measurement by VSM.

Taking the magnetization study and calculated electronic structure into account, the magnetic behavior of β-Mn type $Co_{8+x}Zn_{12-x}$ ($x \sim 2$) is best described by local moments located at the Co atoms interacting via electrons in the conduction band. The absence of temperature-independent Pauli paramagnetism above the Curie point of ~420 K, and the presence of both Curie-Weiss (linear) high temperature behavior and the split flat-band regions on the Brillouin zone boundaries in the electronic band structure point toward this local moment behavior, even though the Stoner condition is well met by the LDA-DOS curve for $Co_{8+x}Zn_{12-x}$ ($x \sim 2$). To gain a better understanding of the structural-magnetic

relationships in these Co-Zn and related β-Mn type systems, semi-empirical DFT+U[61] methods will be employed to examine how the orbital overlaps and electron-electron interactions affect the band structure and electronic distributions in these systems.

3.5 Conclusions

β-Mn type $Co_{8+x}Zn_{12-x}$ ($1.7(2) < x < 2.2(2)$) phases were synthesized and structurally characterized. They exhibit a small homogeneity width with Co atoms exclusively occupying the 8*c* sites in the noncentrosymmetric cubic structure. Moreover, the magnetic properties of a sample analyzed as $Co_{10.0(2)}Zn_{10.0}$, i.e., equiatomic in Co and Zn, show it to be a high-temperature, ferromagnetic material with a Curie point of ~420 K. First principles electronic structure calculations substantiate the ferromagnetic ground state and indicate that the saturation magnetization is derived essentially from local moments at the Co sites interacting via the conduction electrons. The binary β-Mn type structure of $Co_{8+x}Zn_{12-x}$ can be derived from the cubic Laves phase structure, $MgCu_2$-type, by creating ordered vacancies in the majority atom (Cu) positions. The arrangement of these vacancies is driven primarily by minimizing the electrostatic energy between the conduction electrons and the positive nuclei. This structural analysis demonstrates a significant relationship between β-Mn type structures and diamond-like lattices, and is providing greater insights into the complex structures of both α-Mn and β-Mn type structures.[53]

3.6 Acknowledgements

This work was carried out at the Ames Laboratory, which is operated for the U.S. Department of Energy by Iowa State University under Contract No. DE-AC02-07CH11358. This work was supported by the U.S. Department of Energy, Office of Basic Energy Sciences, Division of Materials Sciences and Engineering. The authors thank Dr. Wei Tang

in the Ames Laboratory for magnetic measurements, Dr. Warren E. Straszheim in the Ames Laboratory for SEM analysis, and three astute reviewers for their insightful comments and suggestions.

3.7 References

[1] Hume-Rothery, W. *J. Inst. Met.* **1926**, *35*, 295.

[2] Mizutani, U., *Hume-Rothery Rules for Structurally Complex Alloy Phases*, CRC Press, New York, 2011.

[3] Asahi, R.; Sato, H.; Takeuchi, T.; Mizutani, U. *Phys. Rev. B* **2005**, *B72*, 125102.

[4] Gourdon, O., Miller, G.J., *J. Solid State Chem.* **2003**, *173*, 137.

[5] Gourdon, O., Bud'ko, S.L., Williams, D., Miller, G. J., *Inorg. Chem.* **2004**, *43*, 3210.

[6] Ko, H.; Gourdon, O.; Gout, D.; Mun, E.-D.; Thimmaiah, S.; Miller, G.J. *Inorg. Chem.* **2010**, *49*, 11505.

[7] Vassilev, G.P.; Jiang, M. *J. Phase Equilib. Diffus.* **2004**, *25*, 259.

[8] Takayama, T.; Shinohara, S.; Ishida, K.; Nishizawa, T.; *J. Phase Equilib.* **1995**, *16*, 390.

[9] Okamoto, H. *J. Phase Equilib.* **2003**, *24*, 280.

[10] Buschow, K.H.J.; Van Engen, P.G.; Jongebreur, R. *J. Magn. Magn. Mater.***1983**, *38*, 1.

[11] Boström, M.; Lidin, S. *J. Solid State Chem.* **2002**, *166*, 53.

[12] Lind, H.; Boström, M.; Petricek, V.; Lidin, S. *Acta Crystallogr. B*, **2003**, *59*, 720.

[13] Skyrme, T. *Nucl. Phys.* **1962**, *31*, 556.

[14] Mühlbauer, S.; Binz, B.; Jonietz, F.; Pfleiderer, C.; Rosch, A.; Neubauer, A.; Georgii, R.; Böni, P. *Science* **2009**, *323*, 915.

[15] Yu, X.Z.; Kanazawa, N.; Onose, Y.; Kimoto, K.; Zhang, W.Z.; Ishiwata, S.; Matsui, Y.; Tokura, Y. *Nature Materials* **2011**, *10*, 106.

[16] Hama, T.; Matsumura, M.; Kato, H.; Yamagataa, H.; Kohori, Y.; Kohara, T.; Iwamoto, Y. *J. Phys. Soc. Jpn.* **2004**, *73*, 2305.

[17] Elenius, M.; Zetterling, F. H. M.; Dzugutov, M.; Fredrickson, D.C.; Lidin, S. *Phys. Rev. B*, **2009**, *79*, 144201.

[18] Lidin, S.; Fredrickson, D. *Symmetry* **2012**, *4*, 537.

[19] Wang, N.; Chen, H.; Kuo, K.H. *Phys. Rev. Lett.***1987**, *59*, 1010.

[20] Wang, N.; Fung, K.K.; Kuo, K.H. *Appl. Phys. Lett.***1988**, *52*, 2120.

[21] *PowderCell*, version 2.3, Federal Institute for Materials Research and Testing: Unter den Eichen, Berlin, Germany, 2000.

[22] Rietveld, H.M. *J. Appl. Crystallogr.* **1969**, *2*, 65.

[23] Hunter, B.A.; Howard, C.J. *LHPM-Rietica*, version 1.71: Australian Nuclear Science and Technology Organization: Menai, Australia, 2000.

[24] Sheldrick, G. M. *SADABS*, University of Gottingen: Gottingen, Germany, 2001.

[25] Sheldrick, G. M. *Acta Crystallogr. A* **2008**, *64*, 112.

[26] *SHELXTL*, version 6.10, Bruker AXS Inc.: Madison, WI, 2000.

[27] *Diamond*, version 3.2; Crystal Impact: Bonn, Germany, 2010.

[28] Rodriguez Caravajal, J. *Fullprof*, version 3.2; Laboratoire Léon Brilloui, 1997.

[29] Jepsen, O.; Andersen, O.K. *TB-LMTO*, version 47; Max-Planck-Institut für Festkörperforschung: Stuttgart, Germany, 2000.

[30] von Barth, U.; Hedin, L. *J. Phys. C: Solid State Phys.* **1972**, *5*, 1629.

[31] Lambrecht, W.R.L.; Andersen, O.K. *Phys. Rev. B* **1986**, *34*, 2439.

[32] Kresse, G.; Hafner, J. *Phys. Rev. B* **1993**, *47*, 558.

[33] Kresse, G.; Hafner, J. *Phys. Rev. B* **1994**, *49*, 14251.

[34] Kresse, G.; Furthmüller, J. *Comput. Mater. Sci.* **1996**, *6*, 15.

[35] Kresse, G.; Furthmüller, J. *Phys. Rev. B* **1996**, *54*, 11169.

[36] Tang, W.; Sanville, E.; Henkelman, G. *J. Phys.: Compute Mater.* **2009**, *21*, 084204.

[37] Sanville, E.; Kenny, S.D.; Smith, R.; Henkelman, G. *J. Comp. Chem.* **2007**, *28*, 899.

[38] Henkelman, G.; Arnaldsson, A.; Jónsson, H. *Comput. Mater. Sci.* **2006**, *36*, 254.

[39] Monkhorst, H.J.; Pack, J.D. *Phys. Rev. B* **1976**, *13*, 5188.

[40] Blöchl, P.E.; Jepsen, O.; Andersen, O.K. *Phys. Rev. B* **1994**, *49*, 16223.

[41] Massalski, T. B.; Okamoto, H. *Binary Alloy Phase Diagrams*, ASM International, 1990.

[42] Nesper, R. *Progress in Solid State Chemistry* **1990**, *20*, 1.

[43] Errandonea,D.; Ferrer-Roca,C.; Martinez-Garcia,D.; Segura,A.; Gomis,O.; Munoz,A.; Rodriguez-Hernandez,P.; Lopez-Solano, J.; Alconchel, S.; Sapina, F. *Phys. Rev. B* **2010**, *82*, 174105.

[44] Burdett, J.K.; McLarnan, T.J. *Inorg. Chem.*, **1982**, *21*, 1119.

[45] Jeitschko, W.; Nowotny, H.N.; Benesovsky, F. *Monatshefte fuer Chemie*, **1963**, *94*, 247.

[46] Wang, F.; Miller, G.J. *Inorg. Chem.* **2011**, *50*, 7625.

[47] Pauling, L. *Proc. Natl. Acad. Sci.* **1987**, *84*, 3537.

[48] Urban, K.; Feuerbacher, M. *Journal of Non-Crystalline Solids* **2004**, *334&335*,143.

[49] Ohba, T.; Kitano, Y.; Komura, Y. *Acta. Cryst.* **1984**, *40*, 1.

[50] Pottgen, R.; Hlukhyy, V.; Baranov, A.; Grin, Y. *Inorg. Chem.* **2008**, *47*, 6051.

[51] Kuz'ma, Y.B.; Kripyakevich, P.I. *Kristallografiya*, **1965**, *10*, 558.

[52] Morozkin, A.V. *Intermetallics*, **2012**, *25*, 136.

[53] Nesper, R. *Angew. Chem. Int. Ed. Engl.* **1991**, *30*, 789.

[54] Pauling, L. *J. Am. Chem. Soc.*, **1932**, *54*, 3570.

[55] Allen, L.C. J. Phys. Chem. **1993**, *97*, 5787.

[56] Mulliken, R.S. *J. Chem. Phys.* **1934**, *2*, 782.

[57] Seo, D.K.; Kim, S.H. *J. Comput. Chem.* **2008**, *29*, 2172.

[58] Janak, J.F. *Phys. Rev. B* **1977**, *16*, 225.

[59] Dronskowski, R. *Computational chemistry of solid state materials*. Wiley-VCH. 2008.

[60] Jiles, D. *Introduction to magnetism and magnetic materials*, Chapman&Hall, New York, 1998.

[61] Liechtenstein, A.I.; Anisimov, V.I.; Zaanen, J. *Phys. Rev. B* **1995**, *52*, 5467.

3.8 Supporting Information

Tables of anisotropic temperature factors and significant interatomic distances of β-Mn type $Co_{8+x}Zn_{12-x}$ single crystals, distance comparison among various β-Mn type structures, results of a Bader charge analysis, specific energies and magnetic moments from $Co_{10}Zn_{10}$ models, integrated COHP values of $Co_{10}Zn_{10}$, as well as figures of powder X-ray diffraction, electron micrographs, structures of nine defect cubic Laves phases, partial DOS curves and band structures for "Co_8Zn_{12}", and magnetization vs. temperature curve for $Co_{10.0(2)}Zn_{10.0}$ are included.

Table S1. Anisotropic displacement parameters (in $Å^2$) for four β-Mn type Co-Zn single crystals.

$Co_{10.2(2)}Zn_{9.8}$

Atom	U_{11}	U_{22}	U_{33}	U_{23}	U_{13}	U_{12}
Zn1	0.0084(3)	0.0084(3)	0.0133(4)	−0.0017(2)	0.0017(2)	−0.0004(3)
Co1	0.0084(3)	0.0084(3)	0.0133(4)	−0.0017(2)	0.0017(2)	−0.0004(3)
Co2	0.0072(3)	0.0072(3)	0.0072(3)	0.0001(2)	0.0001(2)	0.0001(2)

$Co_{10.0(2)}Zn_{10.0}$

Atom	U_{11}	U_{22}	U_{33}	U_{23}	U_{13}	U_{12}
Zn1	0.0093(3)	0.0093(3)	0.0139(4)	0.0017(2)	−0.0017(2)	−0.0005(3)
Co1	0.0093(3)	0.0093(3)	0.0139(4)	0.0017(2)	−0.0017(2)	−0.0005(3)
Co2	0.0081(3)	0.0081(3)	0.0081(3)	0.0001(2)	0.0001(2)	−0.0001(2)

$Co_{9.8(2)}Zn_{10.2}$

Atom	U_{11}	U_{22}	U_{33}	U_{23}	U_{13}	U_{12}
Zn1	0.0085(2)	0.0085(2)	0.0126(3)	−0.0012(1)	0.0012(1)	−0.0007(2)
Co1	0.0085(2)	0.0085(2)	0.0126(3)	−0.0012(1)	0.0012(1)	−0.0007(2)
Co2	0.0073(2)	0.0073(2)	0.0073(2)	0.0001(1)	0.0006(1)	0.0001(1)

$Co_{9.7(2)}Zn_{10.3}$

Atom	U_{11}	U_{22}	U_{33}	U_{23}	U_{13}	U_{12}
Zn1	0.0082(2)	0.0082(2)	0.0121(3)	−0.0010(1)	0.0010(1)	−0.0005(2)
Co1	0.0082(2)	0.0082(2)	0.0121(3)	−0.0010(1)	0.0010(1)	−0.0005(2)
Co2	0.0075(3)	0.0075(3)	0.0075(3)	0.0001(1)	0.0001(1)	0.0001(1)

Table S2. Interatomic distances for four β-Mn type Co-Zn single crystals.

Atom 1	Atom 2	C.N.	Distances (Å) $Co_{9.7}Zn_{10.3}$	Distances (Å) $Co_{9.8}Zn_{10.2}$	Distances (Å) $Co_{10.0}Zn_{10.0}$	Distances (Å) $Co_{10.2}Zn_{9.8}$	Distances (Å) Average
12d (Co1|Zn1)	12d (Co1|Zn1)	4	2.6542(4)	2.6596(7)	2.6632(4)	2.6666(6)	2.661(5)
		2	2.6617(5)	2.6684(6)	2.6731(5)	2.6801(5)	2.671(8)
		2	3.2703(6)	3.2886(7)	3.2827(6)	3.2889(7)	3.283(9)
12d (Co1|Zn1)	8c(Co2)	2	2.5852(5)	2.5914(10)	2.5948(6)	2.6001(6)	2.593(6)
		2	2.6332(6)	2.6383(11)	2.6423(6)	2.6453(7)	2.640(5)
		2	2.6858(6)	2.7004(7)	2.6953(5)	2.6994(6)	2.695(7)
8c(Co2)	8c(Co2)	3	2.3610(6)	2.3661(6)	2.3698(3)	2.3737(4)	2.368(5)
		1	4.1577(7)	4.1808(9)	4.1720(6)	4.1791(7)	4.172(9)

Table S3. Comparison of interatomic distances among different β-Mn and stuffed β-Mn type structures.

Atom 1,2	Coordination Number	Distances (Å) Mg_3Ru_2	Distances (Å) Fe_2Re_3	Distances (Å) β-Mn	Distances (Å) Mo_3Ni_2N	Distances(Å) $Co_{10(2)}Zn_{10.0}$
12d, 12d	4	2.9251(14)	2.7179(30)	2.6459(8)	2.7758(6)	2.6632(4)
	2	2.8859(13)	2.6618(29)	2.6723(10)	2.8196(3)	2.6731(5)
	2	3.5776(4)	3.3131(49)	3.2707(10)	3.4404(6)	3.2827(6)
12d, 8c	2	2.9116(9)	2.5793(33)	2.5761(7)	2.7423(8)	2.5948(6)
	2	2.8196(10)	2.7367(37)	2.6343(8)	2.7306(8)	2.6423(6)
	2	2.9635(8)	2.7349(29)	2.6795(7)	2.8177(7)	2.6953(5)
8c, 8c	3	2.5538(5)	2.4177(27)	2.3635(6)	2.4692(9)	2.3698(3)
	1	4.7755(4)	4.1430(37)	4.1260(9)	4.4135(9)	4.1720(6)

Table S4. Bader analysis of local atomic charges depending on average valence electron count for various hypothetical 3*d* metal β-Mn-type structures.

	⟨# Valence e^-⟩	12*d* sites	8*c* sites
"Co_{20}"	9.0	Co: +0.069(2)	Co: –0.104(2)
"Cu_8Co_{12}"	9.8	Co: +0.083(3)	Cu: –0.127(1)
"Ni_{20}"	10.0	Ni: +0.045(1)	Ni: –0.067(1)
"Co_8Cu_{12}"	10.2	Cu: +0.030(3)	Co: –0.042(4)
"Cu_8Ni_{12}"	10.4	Ni: +0.014(1)	Cu: –0.071(2)
"Ni_8Cu_{12}"	10.6	Cu: +0.081(2)	Ni: –0.067(2)
"Co_8Zn_{12}"	10.8	Zn: +0.124(3)	Co: –0.186(3)
"Cu_{20}"	11.0	Cu: +0.014(1)	Cu: –0.022(1)
"Ni_8Zn_{12}"	11.2	Zn: +0.164(3)	Ni: –0.246(2)

Table S5. Calculated total energies and magnetic moments for four different atomic coloring cases of the five different models of $Co_{10}Zn_{10}$: **I**, "$Co_8Co_2Zn_{10}$"; **II**, "$Co_6Zn_2Co_4Zn_8$"; **III**, "$Co_4Zn_4Co_6Zn_6$"; **IV**, "Co_2Zn_6-Co_8Zn_4"; and **V**, "$Zn_8Zn_2Co_{10}$".

E(eV)	"$Co_8Co_2Zn_{10}$"	"$Co_6Zn_2Co_4Zn_8$"	"$Co_4Zn_4Co_6Zn_6$"	"$Co_2Zn_6Co_8Zn_4$"	"$Zn_8Zn_2Co_{10}$"
Case 1	–63709.6344	–63709.5236	–63709.4516	–63709.3346	–63709.3661
Case 2	–63709.6344	–63709.5152	–63709.4387	–63709.3922	–63709.3661
Case 3	–63709.6269	–63709.5211	–63709.4384	–63709.3513	–63709.3738
Case 4	–63709.6344	–63709.5252	–63709.4219	–63709.3964	–63709.3660
Avg.	–63709.6325	–63709.5213	–63709.4377	–63709.3685	–63709.3680
ΔE (meV)	0(4)	111(4)	195(12)	264(30)	264(4)

Mag. Mom. (u_B/cell)	"$Co_8Co_2Zn_{10}$"	"$Co_6Zn_2Co_4Zn_8$"	"$Co_4Zn_4Co_6Zn_6$"	"$Co_2Zn_6Co_8Zn_4$"	"$Zn_8Zn_2Co_{10}$"
Case 1	12.83	12.13	13.30	14.08	14.25
Case 2	12.83	11.79	12.44	13.89	14.25
Case 3	13.04	11.98	13.87	13.95	14.16
Case 4	12.83	12.44	12.37	13.89	14.20
Ranges	12.83-13.04	11.79-12.44	12.37-13.87	13.89-14.08	14.16-14.25

Table S6. ICOHP values for "Co_8Zn_{12}"and "$Co_{10}Zn_{10}$" from LMTO-LDA and LMTO-LSDA calculations.

ICOHP in LDA

Atom[1,2]	Distance(Å)	Coordination Number	"Co_8Zn_{12}"	"$Co_{10}Zn_{10}$"	% in "Co_8Zn_{12}"	% in "$Co_{10}Zn_{10}$"
8c-8c	2.3676	3	22.24	16.37	22.40	16.05
	4.1724	1	0.05	0.07	0.05	0.07
8c-12d	2.5928	2	15.74	18.26	15.84	18.26
	2.6398	2	13.15	17.55	13.23	17.21
	2.6952	2	14.67	16.70	14.75	16.27
12d-12d (s,p)	2.6609	4	20.39	20.21	20.52	19.81
	2.6708	2	10.52	9.84	10.58	9.65
	3.2826	2	2.61	2.73	2.63	2.68

ICOHP in LSDA

Atom[1,2]	Distance(Å)	Coordination Number	"Co_8Zn_{12}"	"$Co_{10}Zn_{10}$"	% in "Co_8Zn_{12}"	% in "$Co_{10}Zn_{10}$"
8c-8c	2.3676	3	22.38	21.04	22.57	20.54
	4.1724	1	0.05	0.03	0.05	0.03
8c-12d	2.5928	2	15.48	17.02	15.61	16.62
	2.6398	2	13.28	14.76	13.39	14.41
	2.6952	2	14.24	15.20	14.36	14.84
12d-12d (s,p)	2.6609	4	20.47	20.82	20.64	20.33
	2.6708	2	10.66	10.74	10.75	10.49
	3.2826	2	2.61	2.81	2.63	2.74

Figure S1. Powder X-ray diffraction patterns for various Co-Zn samples examined using Co and Cu radiation.

Co radiation:

$Co_{60}Zn_{40}$

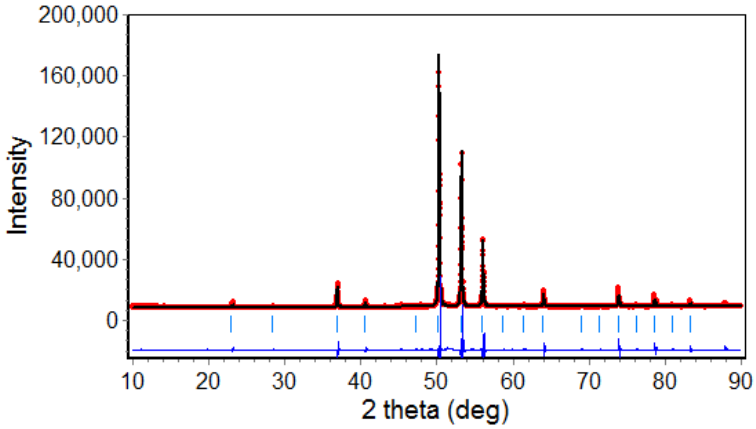

$Co_{50}Zn_{50}$

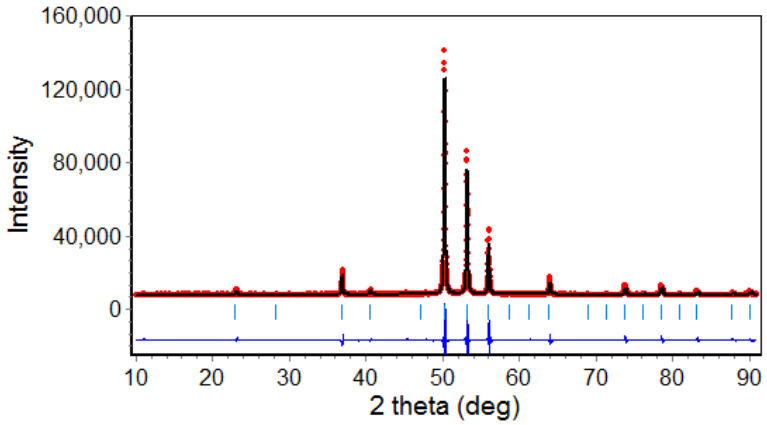

$Co_{40}Zn_{60}$

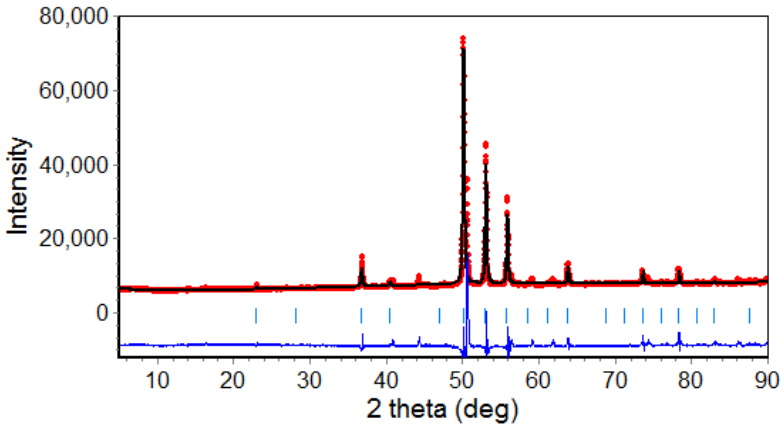

Figure S1 continued
Cu radiation:

$Co_{65}Zn_{35}$

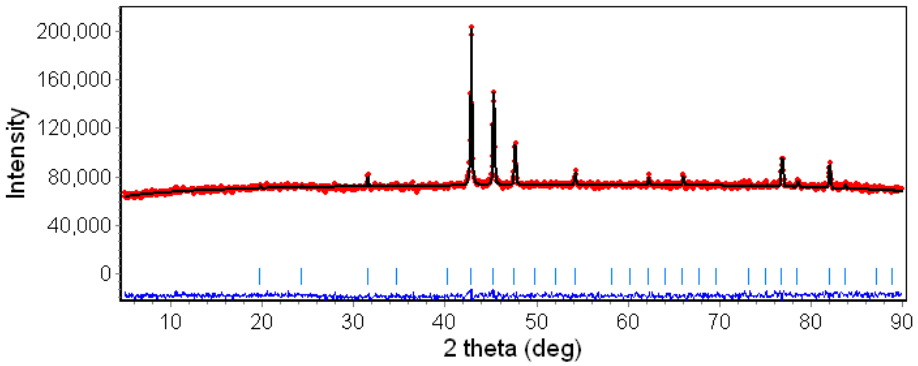

$Co_{60}Zn_{40}$

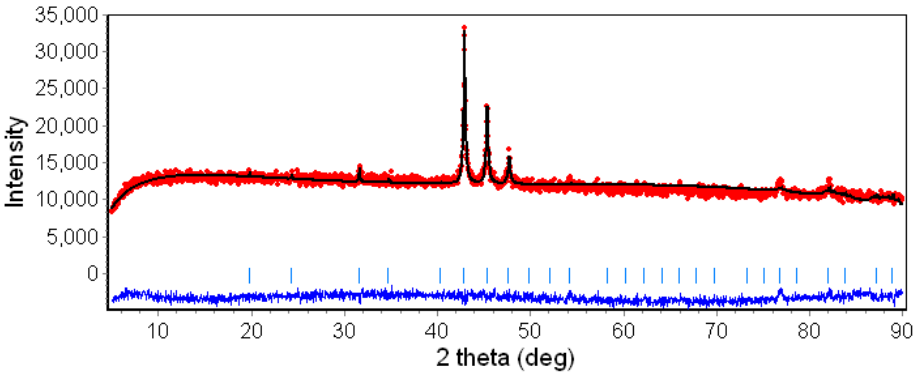

$Co_{55}Zn_{45}$

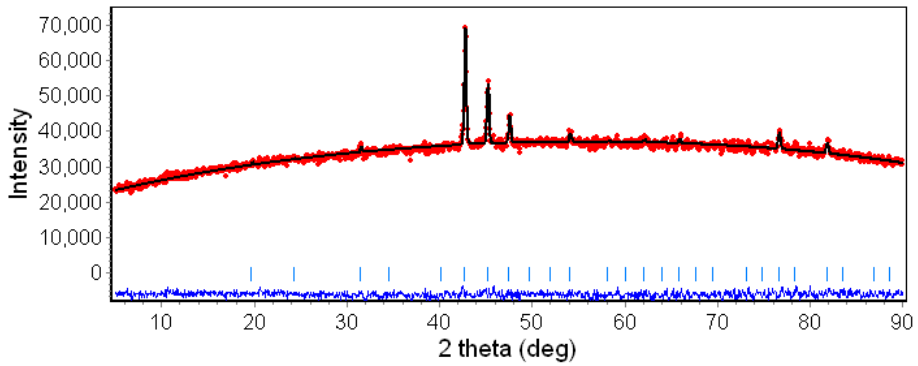

$Co_{50}Zn_{50}$

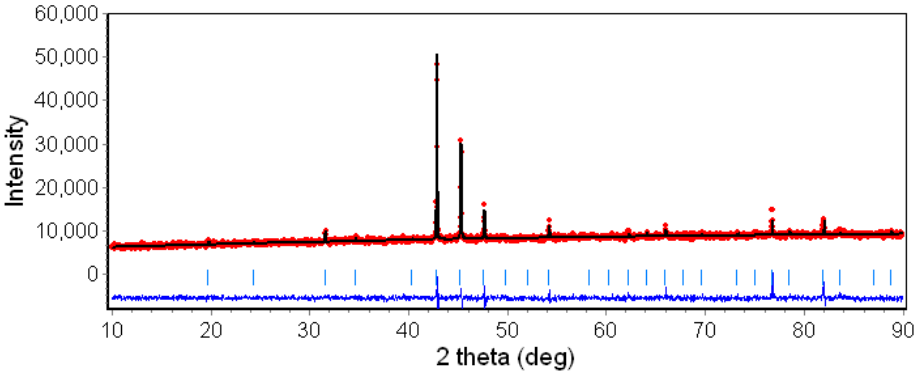

Figure S1 Continued

$Co_{45}Zn_{55}$

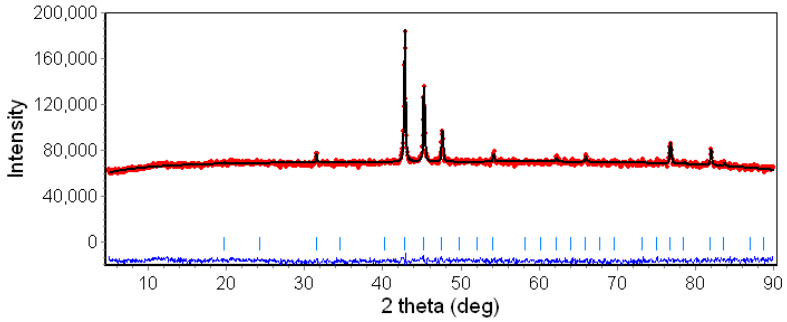

$Co_{40}Zn_{60}$

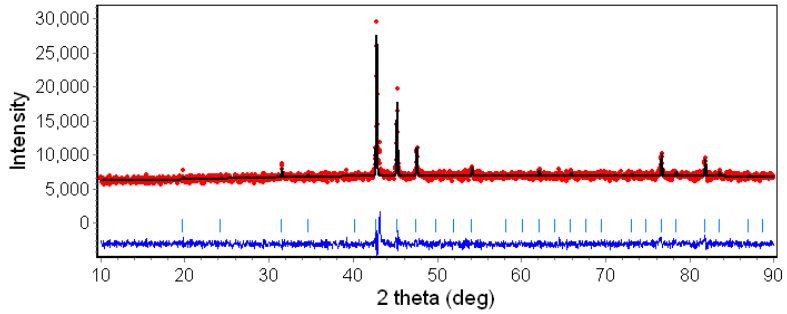

$Co_{35}Zn_{65}$

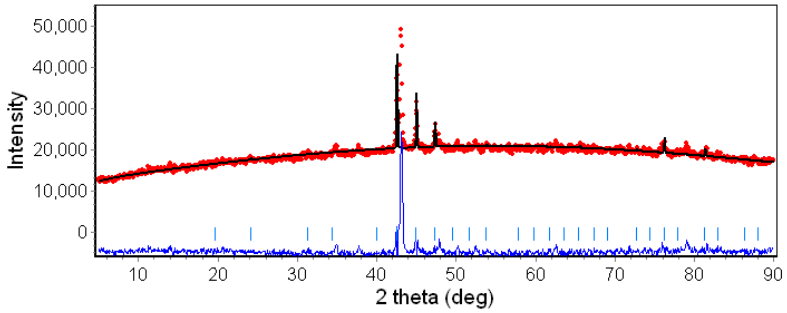

Figure S2. Scanning Electron Micrographs of three Co-Zn samples.

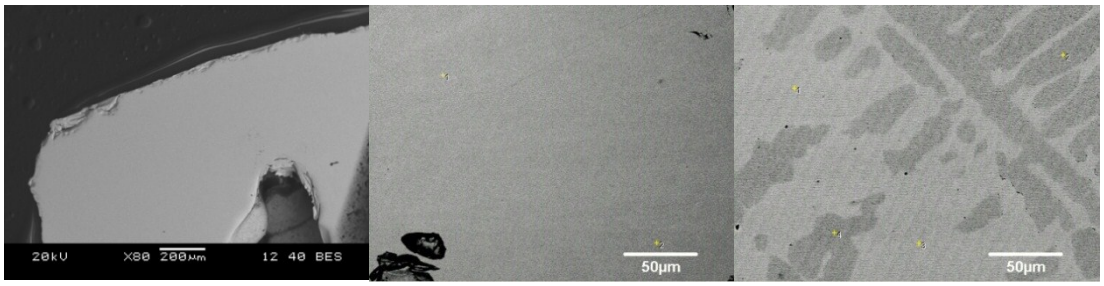

$Co_{60}Zn_{40}$ $Co_{50}Zn_{50}$ $Co_{40}Zn_{60}$

Figure S3. Nine cases of defect cubic Laves phase structures ($Co_8Zn_{12}\square_4$) before and after structural optimization using VASP.

Before VASP optimizations:

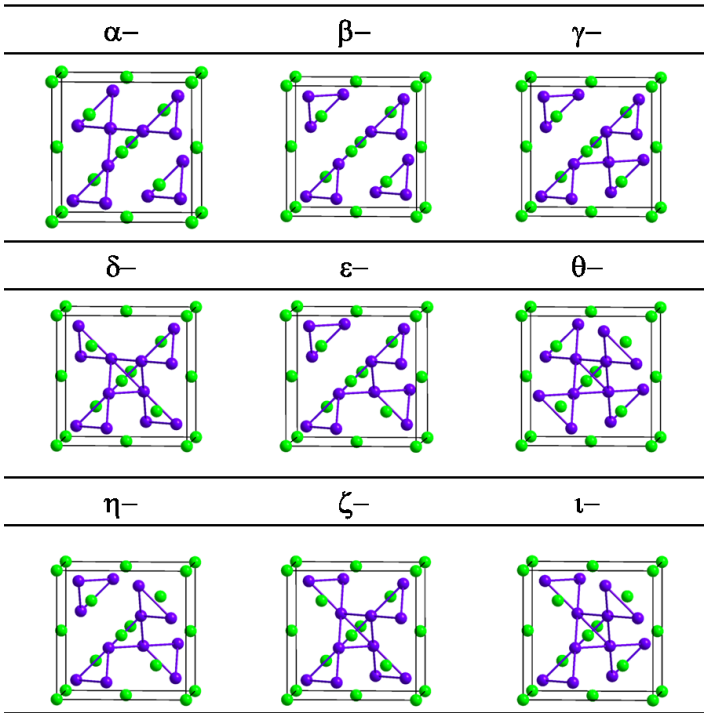

After VASP optimizations:

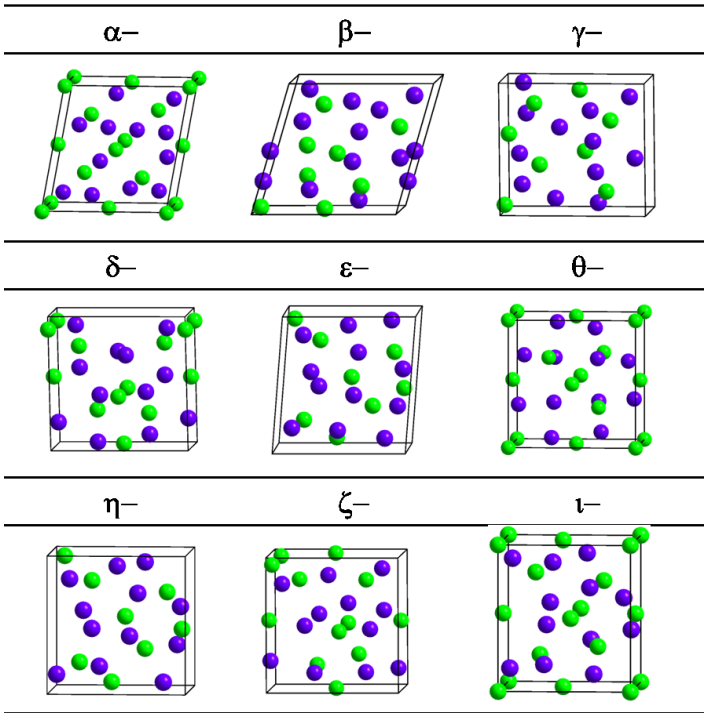

Figure S4. Partial DOS curves showing valence *s*, *p*, *d* contributions from Co and Zn atoms in β-Mn-type "Co_8Zn_{12}" obtained from LDA and LSDA methods.

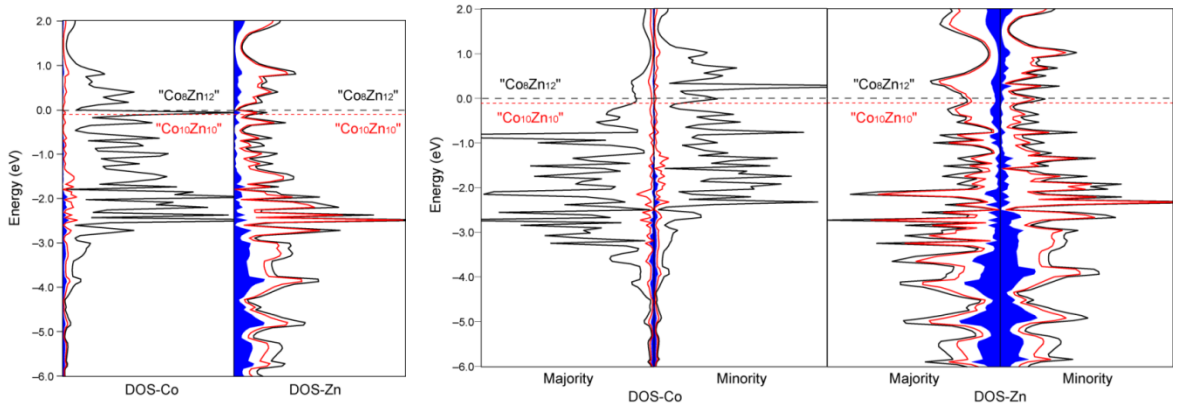

DOS-LDA **DOS-LSDA**

Figure S5. Band structures calculated for "Co_8Zn_{12}" using LDA and LSDA methods. The dispersionless bands leading to sharp peaks in the DOS curves near the Fermi level are shaded. Fermi levels for "Co_8Zn_{12}" (dashed red line) and $Co_{10}Zn_{10}$ (dashed blue line) are noted.

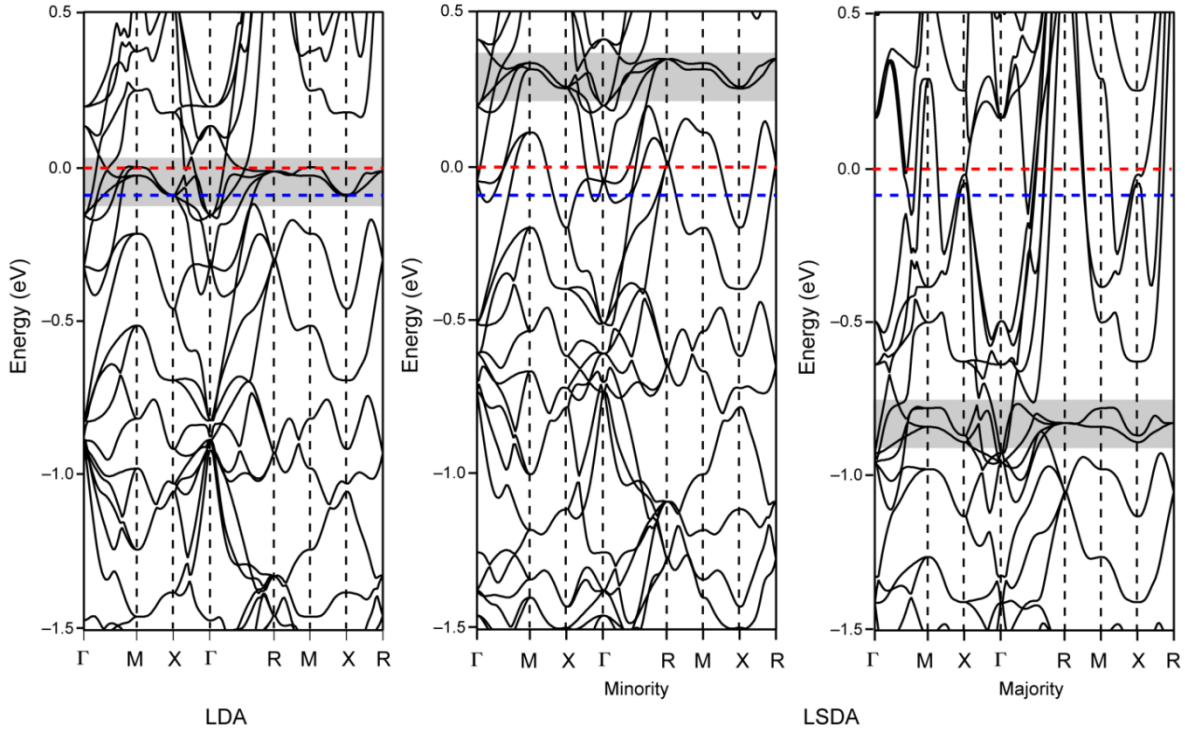

Figure S6. COHP curves for 8*c*–8*c*, 8*c*–12*d*, and 12*d*–12*d* contacts in "Co_8Zn_{12}" from LMTO-LSDA calculations.

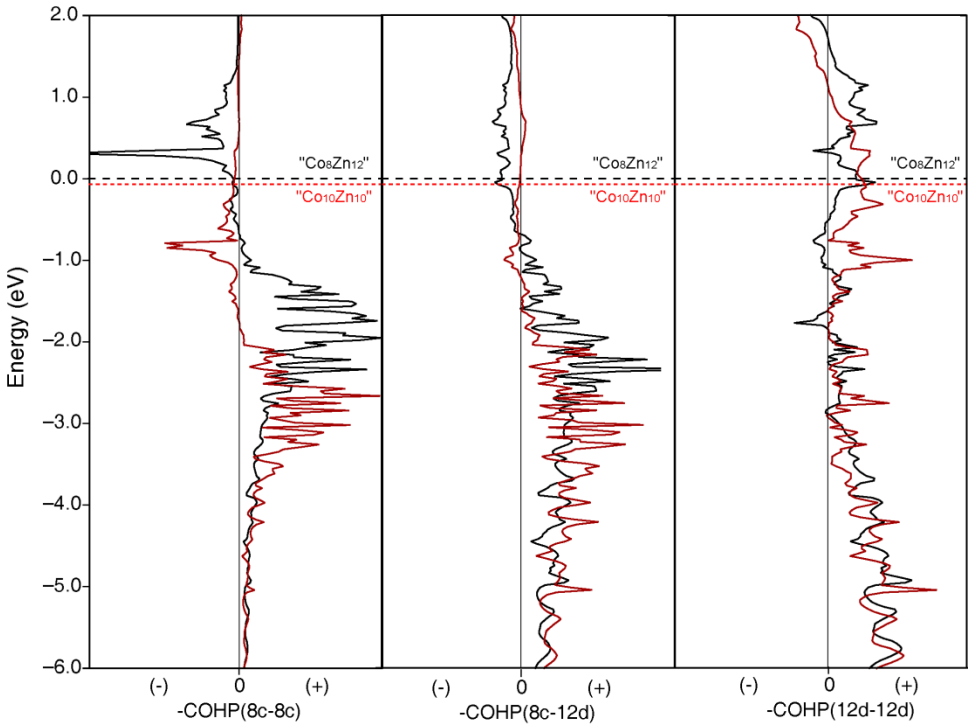

Figure S7. Magnetization vs. temperature from 2 K to 300 K at 10 kOe for β-Mn-type $Co_{10.0(2)}Zn_{10.0}$.

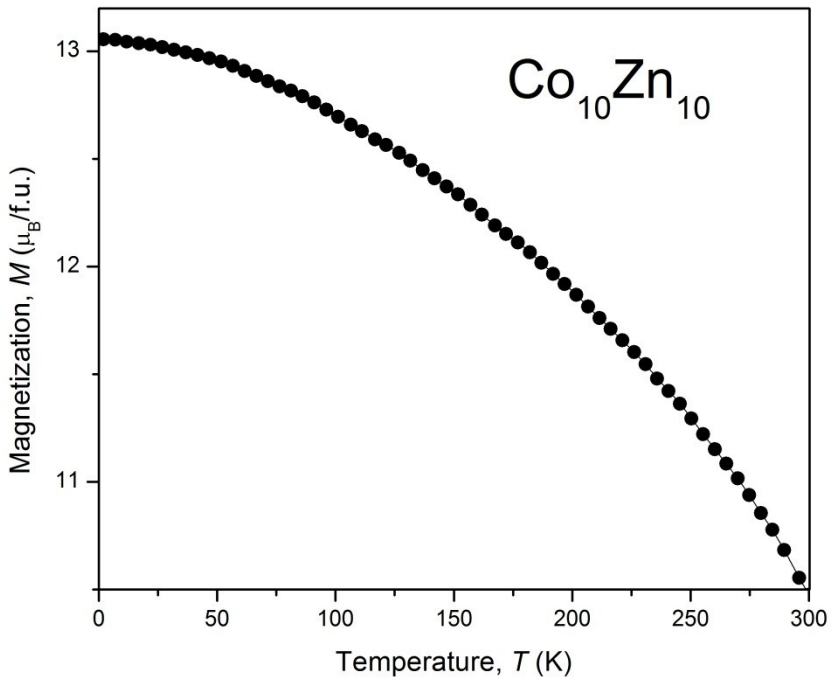

CHAPTER 4

New Co-Pd-Zn γ-Brasses with Dilute Ferrimagnetism and Co_2Zn_{11} Revisited: Establishing the Synergism between Theory and Experiment

Modified from a publication in Chemistry of Materials
(*Chem. Mater.* **2014**, *26*, 2624)

*Weiwei Xie and Gordon J. Miller**

Department of Chemistry, Iowa State University and Ames Laboratory, US-DOE
Ames, Iowa, 50011 USA

4.1 Abstract

A synergism between electronic structure theory and the targeted synthesis of new ternary γ-brass compounds is demonstrated in the Co-Zn system. Co_2Zn_{11}, which adopts a cubic γ-brass structure, is shown to be at the Zn-rich end of a homogeneity width that ranges from 15.4 to 22.1 atomic percent Co. Four samples were examined by single crystal diffraction, all of which crystallize in space group $I\bar{4}3m$ with the lattice parameter ranging from 8.9851(1)-8.8809(1) Å as Co content increases. In the 26-atom γ-brass clusters, Co atoms preferentially occupy the outer tetrahedron (OT) sites, and then replace Zn atoms at the octahedron (OH) sites at higher Co concentrations. In addition, vacancies occur on the inner tetrahedron (IT) sites. The electronic structure of Co_2Zn_{11} shows two distinct pseudogaps near the Fermi level: one at 292 valence electrons per primitive unit cell; the other centered around 304 valence electrons per primitive unit cell. Using molecular orbital arguments applied to the body-centered packing of the 26-atom Co_4Zn_{22} γ-brass cluster, these pseudogaps arise from (i) splitting among the valence *s* and *p* orbitals, which gives rise to the Hume-Rothery electron counting rule, and (ii) splitting within the manifold of Co 3*d* orbitals via Co–Zn orbital interactions. Co_2Zn_{11} is Pauli paramagnetic, although the density of states

at the Fermi level is large, whereas Curie-Weiss behavior emerges for higher Co concentrations. The electronic density of states curve of Co_2Zn_{11} suggests that the pseudogap(s) may be accessed by targeted substitution of either Co or Zn by Pd, which has similar size and electronegativity to Zn. Inspired by the electronic structure of Co_2Zn_{11}, Pd-doped γ-brass compounds are designed and two compounds were obtained: $Co_{0.92(2)}Pd_{1.08}Zn_{11}$ and $Co_{2.50(1)}Pd_{2.50}Zn_8$. The site preferences for Co and Pd can be rationalized by electronic structure calculations. The densities of states reveal that Co 3d states are the major contributors near their Fermi levels, with the Pd 4*d* band lying below by 2-3 eV. The magnetic properties of these Co-Pd-Zn γ-brasses become quite different from Co_2Zn_{11}. A giant magnetic moment on Co atom is induced by the Pd atom, and $Co_{2.50(1)}Pd_{2.50}Zn_8$ shows magnetization consistent with a dilute ferrimagnet. First-principles calculations are employed for two different models of 26-atom γ-brass clusters, the results of which indicate that intra-cluster Co–Co exchange is ferromagnetic, whereas inter-cluster Co–Co exchange is antiferromagnetic. These different magnetic exchange interactions provide rationalization for the high-temperature magnetization behavior of this phase.

4.2 Introduction

Complex metallic alloys (CMAs) generate chemical, physical, metallurgical, and engineering interest for their structural complexity, solid solution behavior, and physical features different from those of normal metallic alloys.[1] They are generally characterized by extremely large unit cells containing tens to thousands of atoms that condense into a packing of well-defined clusters. These clusters often display partial chemical disorder and/or ordered vacancies, which can also influence thermoelectric characteristics of CMAs.[2] Their electronic structures are frequently characterized by pseudogaps or, perhaps, even small gaps

at the corresponding Fermi levels, features which create unusual electronic transport mechanisms when compared to normal metals.[3] The stability ranges of particular families of CMAs are frequently identified by specific electron-to-atom (*e*/*a*) ratios, which are generally called Hume-Rothery rules and validated by the presence of pseudogaps.[3] Among the numerous complex intermetallic structures known, the γ-brasses have arisen as a superb testing ground for chemical and theoretical investigations from which to understand the unusual chemistry and physics of CMAs.[4]

The structures of γ-brasses consist of a body-centered cubic packing of 26-atom clusters built of four concentric atomic shells: (i) an inner tetrahedron (IT); (ii) an outer tetrahedron (OT); (iii) an octahedron (OH); and (iv) a distorted cuboctahedron (CO). Mizutani has identified three groups of γ-brasses according to their constituent elements: (I) a monovalent noble metal with a polyvalent metal or metalloid whose valency is well defined, e.g., Cu_5Zn_8 and Cu_9Al_4; (II) a 3*d* metal (V, Mn, Fe, Co, Ni) with either a divalent (Be, Zn, Cd) or trivalent (Al, In) metal; and (III) non-transition metals.[3] Group I γ-brasses follow the Hume-Rothery valence electron counting rule exceedingly well, existing for *e*/*a* = 21/13 if just the valence *s* and *p* electrons are considered, whereas those in Group III do not obey the "rule". However, even systems in Group I exist over a range of *e*/*a* values, such as γ-brasses in the Cu-Zn system, which has been determined by neutron diffraction to occur for 1.57(3)-1.68(3) (21/13 = 1.62). On the other hand, evaluation of *e*/*a* values for the Group II γ-brasses requires knowing the valence electrons contributed by each 3*d* metal, values which remains controversial. Thus, electronic structure calculations are valuable aids to interpreting the stability of these Hume-Rothery phases.[3,5]

Using the Group I γ-brasses, Mizutani has demonstrated how a pseudogap is generated in the electronic density of states (DOS) curves by the interaction between nearly free electron states at the Fermi surface (Fs) which have wavevectors that are nearly located on Brillouin zone (Bz) surfaces associated with the structure.[6] These interactions create stationary waves, and the corresponding wavevectors $\boldsymbol{G}$ are called critical reciprocal lattice vectors. Moreover, this phenomenon on the DOS curves is called a FsBz-induced pseudogap. To create the energetic driving force for phase stability, the pseudogap must be sufficiently deep, and its width should justify the phase widths observed in CMAs. For Group I γ-brasses in particular, Mizutani has also shown that the critical wavevectors occur for $|\boldsymbol{G}|^2 = 18$, which include the sets of {330} and {411} lattice planes, and from which the e/a value of ~1.60 emerges, in agreement with the Hume-Rothery rule. A similar analysis applied to the Group II γ-brasses Co_2Zn_{11} and Fe_2Zn_{11} indicates that the FsBz interactions involving $|\boldsymbol{G}|^2 = 18$ and 22 occur so as to avoid the 3*d* band of Co or Fe. These interactions form bonding and antibonding states near the bottom and top, respectively, of the 3*d* band, and are called *d*-state mediated FsBz interactions.[7,8] The corresponding e/a values of 1.73 for Co_2Zn_{11} and 1.80 for Fe_2Zn_{11} lead to the valences of Co and Fe to be 0.26 and 0.70, respectively. However, a clear understanding of the possible phase widths in these Group II γ-brasses remains elusive, and some features of the DOS curve of Co_2Zn_{11} suggest the possibility for magnetic properties of suitably doped phases. Thus, with these goals in mind, we have undertaken a thorough crystallographic investigation of the Co-Zn γ-brass region, and, with the aid of electronic structure calculations, have proposed a pattern of chemical substitutions that has led to the discovery of unprecedented ferrimagnetic γ-brasses.

4.3 Experiments

4.3.1 Phase Analysis: All samples were examined by powder X-ray diffraction for identification and phase purity on a STOE WinXPOW powder diffractometer employing Cu radiation ($\lambda_{K\alpha} = 1.5406$ Å). The scattered intensities were recorded as a function of Bragg angle (2θ) using a scintillation detector with a step size of 0.03° in step scan mode, ranging from 0° to 130°. The lattice parameters were refined by full-profile Rietveld refinements[9] using LHPM RIETICA[10] from reflection peaks between 5° and 90° in 2θ.

4.3.2 Structure Determination: Single crystal data were measured using a Bruker Smart Apex CCD diffractometer with Mo K_α radiation (λ = 0.71073 Å). Data were collected over a full sphere of reciprocal space with 0.5° scans in ω with an exposure time of 10s per frame. The 2θ range extended from 6° to 64°.[11] The SMART software was used for data acquisition. Intensities were extracted and corrected for Lorentz and polarization effects with the SAINT program. Empirical absorption corrections were accomplished with SADABS, which is based on modeling a transmission surface by spherical harmonics employing equivalent reflections with $I > 3\sigma(I)$.[12] With the SHELXTL package, the crystal structures were solved using direct methods and refined by full-matrix least-squares on F^2.[13,14] Since mixed site occupancies are prevalent in these phases, different permutations and combinations were tried to get the best refinement results and the refined statistical agreements were tested using the Hamilton test.[15] All crystal structure drawings were produced using the program *Diamond*.[16]

4.3.3 Scanning Electron Microscopy (SEM). Characterization was completed using a variable pressure scanning electron microscope (JEOL 5610v) and Energy-Dispersive Spectroscopy (EDS). Samples were mounted in epoxy, carefully polished, and then sputter-

coated with a thin layer of carbon prior to loading into the SEM chamber. The samples were examined at 20 kV. Spectra were collected for 60 seconds. An Oxford Instruments Tetra backscattered electron (BSE) detector was used to image the samples using the BSE signal. Multiple points were examined in each phase within multiple grains of a specimen. Compositional estimates were calculated using Oxford's SEM *Quant* software to correct intensities for matrix effects.

4.3.4 Magnetization Measurements. The magnetization measurements were performed using a superconducting quantum interference device (SQUID) magnetometer MPMS XL-7, and Vibrating Sample Magnetometer (VSM) EV11 manufactured by Quantum Design, Inc. on pieces of γ-brass type single crystals. Measurements using the SQUID were performed over a temperature range of 2-300 K and in applied fields of up to 70 kOe. The samples were placed in glass capsules for measurement. Measurements using the VSM were operated from 300K to 700K at 10kOe.

4.3.5 Electronic Structure Calculations.

Tight-Binding, Linear Muffin-Tin Orbital-Atomic Spheres Approximation (TB-LMTO-ASA): Calculations of the electronic and possible magnetic structures were performed by TB-LMTO-ASA using the Stuttgart code.[17] Exchange and correlation were treated by the local density approximation (LDA) and the local spin density approximation (LSDA).[18] In the ASA method, space is filled with overlapping Wigner-Seitz (WS) spheres. The symmetry of the potential is considered spherical inside each WS sphere and a combined correction is used to take into account the overlapping part. The WS radii were: 1.54Å (Co), 1.49Å (Zn) and 1.51Å (Pd). No empty spheres were necessary in the γ-brass structures, and the WS sphere overlaps were limited to no larger than 16%. The basis set for the calculations

included Co (4*s*, 4*p*, 3*d*), Zn (4*s*, 4*p*, 3*d*) and Pd (5*s*, 5*p*, 4*d*) wavefunctions. The convergence criterion was set to 10^{-4} eV. A mesh of 8 × 8 × 8 *k*-points in the irreducible wedge of the first Brillouin zone was used to obtain all integrated values, including the density of states (DOS) and Crystal Orbital Hamiltonian Population (COHP) curves.[19]

Vienna *ab-initio* Simulation Package (VASP): Structure optimization and charge density calculations were completed using VASP,[20] which employs projector augmented-wave (PAW)[21] pseudopotentials that were adopted with the Perdew-Burke-Ernzerhof generalized gradient approximation (PBE-GGA)[22], in which scalar relativistic effects are included. For structural optimization, the conjugate gradient algorithm was applied. The energy cutoff was 400 eV. Reciprocal space integrations were completed over a 7×7×7 Monkhorst-Pack *k*-points mesh with the linear tetrahedron method.[23] With these settings, the calculated total energies converged to less than 0.1 meV per atom.

Extended Hückel Theory: An analysis of crystal orbital symmetry and character in Co_2Zn_{11} was accomplished using semi-empirical Extended Hückel theory.[24] All orbital overlaps extended over two nearest neighbor unit cells were included. Two different minimal basis sets involving Slater-type single-zeta functions for 4*s* and 4*p* orbitals and double-zeta functions for 3*d* were applied. The parameters for Zn are 4*s*: $\zeta = 2.01$, $H_{ii} = -12.41$ eV; and 4*p*: $\zeta = 1.70$, $H_{ii} = -6.53$ eV. The parameters for Co are 4*s*: $\zeta = 2.00$, $H_{ii} = -8.21$ eV; 4*p*: $\zeta = 2.00$, $H_{ii} = -3.00$ eV, and 3*d*: $\zeta_1 = 5.55$ ($c_1 = 0.5679$), $\zeta_2 = 2.10$ ($c_2 = 0.6059$), $H_{ii} = -10.50$ eV. The Co parameters were modified to provide the best fit to the results of first-principles calculations.

4.4 Binary Co-Zn γ-Brasses

4.4.1 Synthesis and Phase Analysis: Co-Zn γ-brass type phases were obtained by fusion of mixtures of Co pieces (99.9%, Ames Laboratory) and Zn particles (99.99%, Alfa Aesar) loaded at 15.5, 18.1, 24.9, 30.0, and 32.5 atomic percent Co (see Table 1). Each reactant mixture, about 500 mg total, was sealed into an evacuated silica tube ($<10^{-5}$ Torr), heated to 800 °C for 24 hr, followed by cooling to 500 °C at a rate of 1 °C/min and annealed at this temperature for 3 days, after which the container was slowly cooled in the furnace. The products obtained from 15.5-30.0 atomic percent Co loadings yielded a single phase γ-brass. When the loading exceeded 30 atomic percent Co, a β-Mn type Co-Zn phase appears as a second phase.[25] All products summarized in Table 1 are stable toward decomposition in air and moisture, but react with dilute acid at room temperature.

Table 1. Compositions, phase analyses, lattice constants, and refined compositions for γ-brass Co-Zn phases.

Atomic % Co loaded	Phases (PXRD)	*a* (Å) (PXRD)	*a* (Å) (SCXRD)	Composition (SCXRD)	Composition (SEM-EDX)
15.54	γ-brass	8.9851(1)	8.9654(7)	Co_2Zn_{11}	$Co_{2.0(1)}Zn_{11.0(1)}$
18.10	γ-brass	8.9527(1)	8.9552(5)	$Co_{2.33(2)}Zn_{10.63}$	
24.86	γ-brass	8.9144(1)	8.911(3)	$Co_{2.66(9)}Zn_{10.29}$	$Co_{2.7(1)}Zn_{10.3(1)}$
29.95	γ-brass	8.8809(1)	8.882(4)	$Co_{2.84(9)}Zn_{10.03}$	$Co_{2.9(1)}Zn_{10.1(1)}$
32.51	γ-brass+ β-Mn	8.8814(4)			

As previously mentioned, the *e*/*a* ratios for these Group II γ-brasses require knowledge of the number of valence electrons assigned to the 3*d* metal. For the series of $Co_{2+x}Zn_{11-y}\square_{y-x}$ phases characterized by single crystal X-ray diffraction, if we use the valency of 0.26 assigned to Co from Mizutani's analysis of Co_2Zn_{11}, then the observed phases exist for *e*/*a* values ranging between 1.62 and 1.73 (or 1.60 and 1.73, if the vacancies are included),

values which are consistent with regions of other γ-brass phases. Furthermore, as the Co content increases, the *e*/*a* value and the total valence electron count decreases.

4.4.2 Atomic Ordering and Vacancies: Tables 2 and 3 summarize the crystallographic data and structural parameters refined from single crystal X-ray diffraction investigations from samples obtained from each single-phase product. Figure 1 illustrates the refined crystal structure of Co_2Zn_{11} (15.4 atomic percent Co) in which Co atoms preferentially occupy the OT sites whereas Zn atoms are exclusively on the IT, OH, and CO sites of the 26-atom γ-brass cluster located at the unit cell corners and center. With increasing Co content, the additional Co atoms occupy the OH (12*e*) sites, while vacancies become apparent on the IT sites. Instead of vacancies at the IT sites, a second model involving a mixture of Co and Zn atoms was examined, but this refinement generated large standard deviations for the occupancies. A Hamilton test[15] comparing these two models yielded the vacancy/Zn mixture to show a statistically significant improvement, at the 0.5 % significance level on the crystallographic *R*-factor, over the Co/Zn mixture at the IT sites. Table 3 also indicates that the equivalent isotropic displacement parameter of the 8*c* (OT) sites is always lowest among the four positions in the asymmetric unit, a result that is consistently observed among γ-brasses. Previous structural reports[26-29] of γ-brass phases containing Ni, Pd, or Pt with Zn or Cd describe a similar pattern of atomic ordering of the *d*-metals, i.e., Co vis-à-vis Ni, Pd, or Pt preferentially at the OT sites, and the occurrence of vacancies at the IT sites as the *d*-metal concentration increases. To confirm the occurrence of vacancies by independent means, the densities of two rod-shaped specimens (~0.2 g) extruded from samples prepared at 24.86 atomic percent Co were measured using Archimedes principle[30]. By taking into account the unit cell volume determined by X-ray powder diffraction (see Table 1), the measured density

of 7.6(1) g/cm^3 indicates a clear deficiency in the number of atoms (52) per unit cell by 1.3(6) atoms. Refinements of single crystal X-ray diffraction on 3 specimens extracted from this sample yielded ~20.5(1) atomic percent Co with ~0.3(1) vacancies per unit cell.

Table 2. Crystallographic data for γ-brass $Co_{2+x}Zn_{11-y}\square_{y-x}$ phases at 293(2) K.

Atomic % Co loaded	15.41%	18.10%	24.86%	29.95%
Refined Formula	Co_2Zn_{11}	$Co_{2.34(2)}Zn_{10.63(3)}$	$Co_{2.66(2)}Zn_{10.29(3)}$	$Co_{2.84(2)}Zn_{10.03(3)}$
F.W. (g/mol);	836.93	832.78	829.13	824.76
Space group; Z	$I\bar{4}3m$ (No.217); 4	$I\bar{4}3m$ (No.217); 4	$I\bar{4}3m$ (No.217); 4	$I\bar{4}3m$ (No.217); 4
a (Å)	8.9654(2)	8.9552(5)	8.911(3)	8.882(4)
V (Å^3)	720.62(3)	718.17(7)	707.7(5)	700.8(6)
Absorption Correction	Multi-Scan	Multi-Scan	Multi-Scan	Multi-Scan
Extinction Coefficient	0.0016(1)	0.0105(4)	0.0035(2)	0.0009(1)
μ(mm^{-1})	40.232	40.117	40.102	40.058
θ range (deg)	3.21-28.19	3.22-28.22	3.23-27.71	3.24-28.25
hkl ranges	$-11 \le h,k,l \le 11$	$-11 \le h,k,l \le 11$	$-11 \le h,k,l \le 11$	$-11 \le h,k,l \le 11$
No. reflections; R_{int}	1388; 0.0381	1632; 0.0379	1174; 0.0400	2087; 0.0472
No. independent reflections	187	188	182	186
No. parameters	19	21	22	22
R_1; wR_2 (all I)	0.0166; 0.0365	0.0154; 0.0342	0.0153; 0.0297	0.0165; 0.0381
Goodness of fit	1.221	1.226	1.093	1.079
Diffraction peak and hole (e$^-$/Å^3)	0.481; –0.497	0.807; –0.548	0.321; –0.788	0.505; –0.484

Table 3. Atomic coordinates, site occupancies, and equivalent isotropic displacement parameters for γ-brass $Co_{2+x}Zn_{11-y}\square_{y-x}$ phases. U_{eq} is defined as one-third of the trace of the orthogonalized U^{ij} tensor (Å^2).

Co_2Zn_{11} (15.4 atomic percent Co)

Atom	Wyckoff.	Occupancy.	x	y	z	U_{eq}
Zn1	8c(IT)	1	0.1041(1)	0.1041(1)	0.1041(1)	0.0090(3)
Co2	8c(OT)	1	0.3281(1)	0.3281(1)	0.3281(1)	0.0056(3)

Table 3. continued

Zn3	12*e*(OH)	1	0.3542(1)	0	0	0.0087(2)
Zn4	24*g*(CO)	1	0.3057(1)	0.3057(1)	0.0464(1)	0.0104(2)

$Co_{2.34(2)}Zn_{10.63(3)}$ (18.0 atomic percent Co)

Atom	Wyckoff.	Occupancy.	*x*	*y*	*z*	U_{eq}
Zn1	8*c*(IT)	0.986(5)	0.1044(1)	0.1044(1)	0.1044(1)	0.0073(3)
Co2	8*c*(OT)	1	0.3284(1)	0.3284(1)	0.3284(1)	0.0047(3)
Co/Zn3	12*e*(OH)	0.19(3)/0.81	0.3543(1)	0	0	0.0072(4)
Zn4	24*g*(CO)	1	0.3060(1)	0.3060(1)	0.0457(1)	0.0098(3)

$Co_{2.66(2)}Zn_{10.29(3)}$ (20.5 atomic percent Co)

Atom	Wyckoff.	Occupancy.	*x*	*y*	*z*	U_{eq}
Zn1	8*c*(IT)	0.973(6)	0.1046(1)	0.1046(1)	0.1046(1)	0.0100(4)
Co2	8*c*(OT)	1	0.3304(1)	0.3304(1)	0.3304(1)	0.0049(3)
Co/Zn3	12*e*(OH)	0.22(3)/0.78	0.3547(1)	0	0	0.0082(4)
Zn4	24*g*(CO)	1	0.3066(1)	0.3066(1)	0.0445(1)	0.0133(3)

$Co_{2.84(2)}Zn_{10.03(3)}$ (22.1 atomic percent Co)

Atom	Wyckoff.	Occupancy.	*x*	*y*	*z*	U_{eq}
Zn1	8*c*(IT)	0.937(4)	0.1016(1)	0.1016(1)	0.1016(1)	0.0129(3)
Co2	8*c*(OT)	1	0.3322(1)	0.3322(1)	0.3322(1)	0.0069(3)
Co/Zn3	12*e*(OH)	0.28(3)/0.72	0.3544(1)	0	0	0.0105(3)
Zn4	24*g*(CO)	1	0.3038(1)	0.3038(1)	0.0477(1)	0.0166(3)

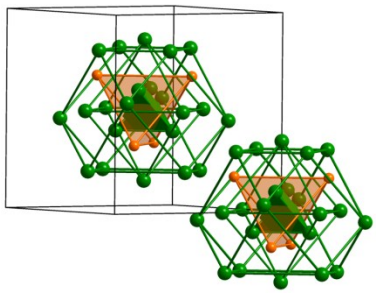

Figure 1. Crystal structure of Co_2Zn_{11} at 293(2) K emphasizing the 26-atom γ-brass clusters located at the unit cell corner(s) and center. Orange circles are Co; green circles are Zn.

To examine the site preference of Co atoms for the IT sites in Co_2Zn_{11} by quantum chemical means, two models of Co_2Zn_{11} were constructed, one in which Co atoms are located at the IT sites and the other at the OT sites. These two models were compared by total energy-vs-volume curves between 10 and 19 $Å^3$/atom using VASP (see Figure S1 in

Supporting Information). To avoid any influence on the total energies by distance variations, the coordinates obtained from single crystal data (see Table 3) of Co_2Zn_{11} were used for both models. As seen in Figure S1, the minimum total energy of Co_2Zn_{11} with Co on the OT site is 65.8 meV/atom lower than the minimum energy of the alternative model, in agreement with the experimental results, and there is no crossing between the two $E(V)$ curves within the entire volume range. In addition, the calculated optimum volume of Co_2Zn_{11} (13.91 $Å^3$/atom) is in excellent agreement with experiment (13.95 $Å^3$/atom) and is *slightly* smaller than the optimum volume of "Co_2Zn_{11}" with Co atoms in the IT sites (14.14 $Å^3$/atom). This site preference or "coloring" problem for two elements on different crystallographic sites is driven by optimizing the "site energy" and the "bond energy".[31] To examine the "site energy", we analyzed the Mulliken populations for the four different crystallographic positions in the γ-brass structure using the Extended Hückel theory with Ni, Cu, and Zn parameters at every site. The minimal basis sets for Ni and Cu included 3*d*, 4*s*, and 4*p* atomic orbitals; that for Zn used just 4*s* and 4*p* orbitals. Over the range of valence electron concentrations (*e*/*a* values) observed for the Co-Zn γ-brasses, the Ni and Cu basis sets gave preferences to the IT and OT sites for the Co atoms, which have lower valence electron counts than Zn. The Zn basis set essentially gives the OT site as the preferred site for Co atoms (see Figure S2 in Supporting Information). The "bond energy" term is evaluated by comparing the crystal orbital Hamilton populations (COHP) curves for the two structural models for Co_2Zn_{11}. These curves, illustrated in Figure S3 of Supporting Information, show that there is a strong Co–Co antibonding interactions at the Fermi level for Co atoms at the IT sites; this antibonding interaction is significantly alleviated when Co atoms are located at

the OT sites. Therefore, placing Co atoms at the OT sites in Co_2Zn_{11} is driven by both "site energy" and "bond energy" terms in the total electronic energy.

For binary Co-Zn γ-brasses formulated as $Co_{2+x}Zn_{11-y}\square_{y-x}$, refinements indicated that x Co atoms replace x Zn atoms at the OH sites while $y–x$ vacancies occur at the IT sites. Preliminary studies using VASP to explore these two outcomes were examined: (i) "Co_9Zn_{43}" (= $[Co_4Zn_{22}][Co_5Zn_{21}]$) with all OT sites plus either one OH or one IT site occupied by Co atoms; and (ii) "Co_8Zn_{43}" (= $[Co_4Zn_{22}][Co_4Zn_{21}\square]$) with all OT sites occupied by Co atoms and one vacant position located at either the OH or IT sites. For both cases, energy-vs-volume curves were evaluated between 10 and 19 $Å^3$/atom. In agreement with our experimental refinements, we find that the OH site is preferred for Co-atom substitution, whereas the IT site is preferred for vacancy formation. At this point, however, further theoretical investigations are required to fully understand the correlated occurrence of Co-substitution and vacancy formation as the e/a ratio decreases.

4.4.3 Electronic Structures: Figure 2 illustrates the total electronic DOS curve calculated using the TB-LMTO-ASA method and LDA for Co_2Zn_{11}, in which the OT sites were completely occupied by Co atoms and all other sites by Zn atoms. The qualitative features obtained by this calculation closely resemble the DOS curve obtained using the FLAPW method.[3,32] States that are 2-6 eV below the Fermi level (E_F) arise primarily from valence 4s and 4p orbitals from Zn, whereas the Zn 3d band is narrow and located ~7-8 eV below E_F. The contribution of Co valence orbitals to the DOS curve, as shaded in Figure 2, shows significant Co content to states between –2 eV and +1 eV relative to E_F. Furthermore, states between –1.7 eV and +0.3 eV are largely Co 3d orbitals. The Fermi level for Co_2Zn_{11} falls just above the topmost peak of the largely Co 3d bands. Therefore, we employed LSDA to

see if a magnetic moment would spontaneously develop, but the converged result yielded zero magnetic moment. This result agrees with the weak Pauli paramagnetism observed for the product of the sample loaded at 15.41 atomic percent Co, i.e., Co_2Zn_{11}.

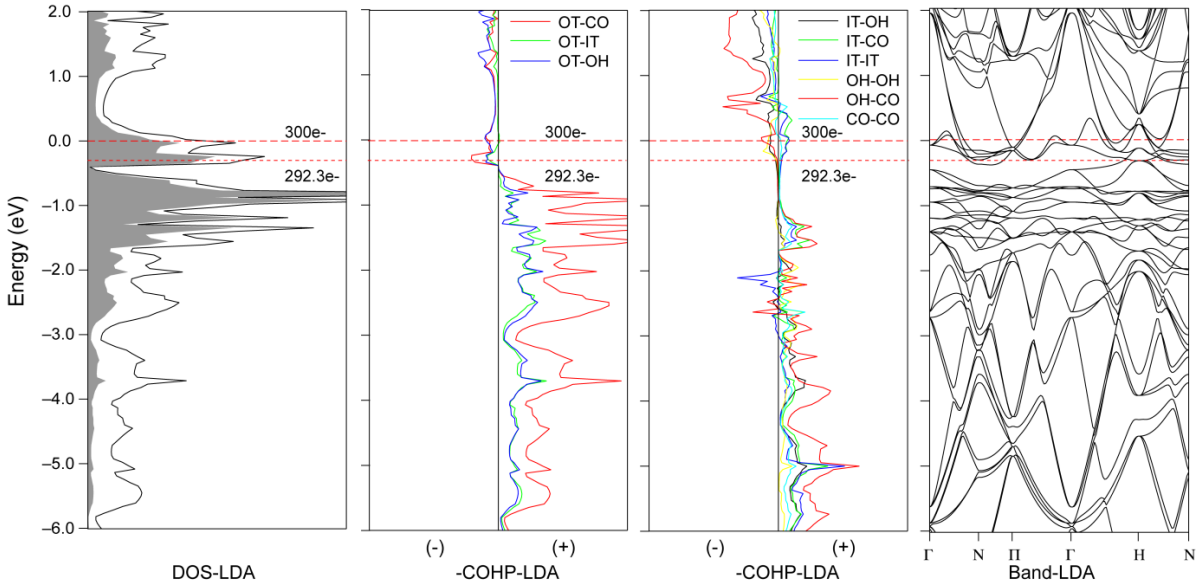

Figure 2. Results of TB-LMTO-ASA (LDA) electronic structure calculations on Co_2Zn_{11}. (Left) Total DOS curve with contributions from Co states shaded. (Middle) COHP curves among all near-neighbor interatomic contacts (+ is bonding/− is antibonding). (Right) Energy band structure between special points of the first Brillouin zone. Energy values are with respect to 300 e^- ($Co_2Zn_{11} \times 2$); the dashed red lines indicate the upper (300 e^-) and lower (292.3 e^-) bounds of valence electron counts observed for Co-Zn γ-brasses.

In the DOS curve of Co_2Zn_{11} (space group $I\bar{4}3m$; $Z = 2$ in the primitive cell), there is a broad pseudogap located around +0.5 eV (~304 e^-/primitive cell) and a much sharper pseudogap near –0.4 eV (292 e^-/primitive cell), a result that implies there are six electronic states associated with the region of the DOS corresponding to the Fermi level of Co_2Zn_{11} (300 e^-/primitive cell). From the various COHP curves for all near-neighbor metal-metal orbital interactions, the broad pseudogap around +0.5 eV generally corresponds to the separation between bonding (below) and antibonding (above) states involving the IT sites. On the other hand, the deep pseudogap at –0.4 eV (292 e^-/primitive cell) differentiates bonding and antibonding states involving the OT sites, i.e., where Co atoms are located.

States near E_F for the entire range of Co-Zn γ-brasses show weakly antibonding or nearly nonbonding orbital interactions for all metal-metal contacts.

To analyze the crystal orbitals of the Co_2Zn_{11} γ-brass from a "molecular" perspective, Extended Hückel theory[24] was applied using two different atomic orbital basis sets: (i) only 4*s* and 4*p* orbitals on all atoms; and (ii) 4*s*, 4*p*, and 3*d* orbitals on Co, and only 4*s* and 4*p* orbitals on Zn atoms. The primitive unit cell contains one 26-atom γ-brass cluster Co_4Zn_{22}. Figure 3 illustrates the crystal orbital energy diagrams for the two cases evaluated at the Γ-point (point symmetry $\bar{4}3m$) with orbital energies given relative to the corresponding Fermi levels. As seen in Figure 2, dispersion will create the quasi-continuous DOS curves. These crystal orbital energy diagrams, however, provide a rationale for the Hume-Rothery valence electron counting rule for these γ-brasses, as well an interpretation of the features of the DOS of Co_2Zn_{11} of Figure 2. The broad pseudogap, which is indicated by the shaded energy range for both models in Figure 3, corresponds to ~20-22 filled cluster valence *s* and *p* orbitals, a result which leads to e/a = 1.54-1.69 (= 40-44 e^- / 26 atoms) and is consistent with the FsBz-induced pseudogap for Group I γ-brasses like Cu_5Zn_8.[3,6] With valence 3*d* orbitals included at Co atoms, the additional pseudogap emerges by splitting of these 20 3*d*-centered crystal orbitals into 15 to lower energies and 5 ($e + t_2$) to higher energy. The peak in the DOS curve near E_F for Co_2Zn_{11} corresponds to these 5 ($e + t_2$) states, which are Co-Zn antibonding between all Co-Zn near neighbor contacts. Thus, the electronic structures of Groups I and II γ-brasses can also be interpreted using a "molecular orbital" perspective, and not just via the nearly free electron model.[5]

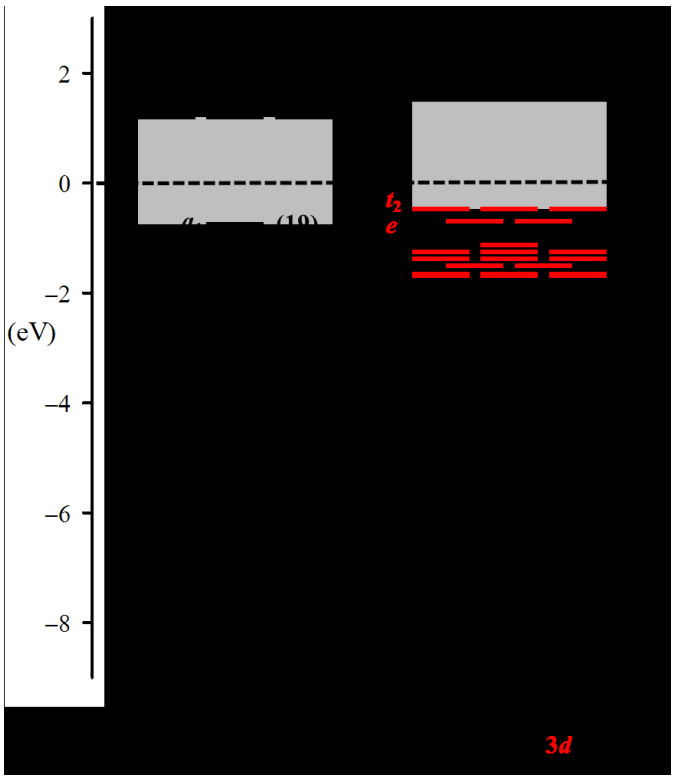

Figure 3. Crystal orbital energy diagrams at the Γ point for Co_4Zn_{22} calculated with and without 3*d* orbitals at the Co atoms using Extended Hückel theory. Those orbitals that have majority contributions from 3*d* orbitals are shown in red. The numbers in ( )'s are the numbers of orbitals at or below the designated level. The labels of the irreducible representations are given for orbitals near the corresponding Fermi levels (EF). The shaded region corresponds to the broad pseudogap region seen in the DOS curve of Figure 2.

4.5 Pd-doping in γ-brass Co_2Zn_{11}

Analysis of the electronic structure of the Group II γ-brass compound Co_2Zn_{11} inspired us to investigate their electronic versatility by targeting new ternary derivatives. To accomplish this chemistry, we selected Pd as the ternary component because its absolute electronegativity [33] and size match those of Zn (4.45 eV; 1.37 Å), whereas its chemical hardness (3.89 eV) resembles that of Co (3.60 eV). Our goal to adjust both the total valence electron and the *d*-electron counts in these γ-brasses would be accomplished by considering Pd substitutions for both Co and Zn positions because Pd has one more *d*-electron than Co, but two less valence electrons than Zn. In addition, since bulk Pd with filled 4*d* orbitals is Pauli paramagnetic but can become ferromagnetic if expanded,[34, 35] some interesting magnetic responses are anticipated.

Table 4. Compositions, phase analyses, lattice constants (Å), and refined compositions for γ-brass Co-Pd-Zn phases. Refined compositions are expressed with respect to γ-brass formalism. VE = total valence electron count per unit cell; PXRD = powder X-ray diffraction; SCXRD = single crystal X-ray diffraction; SEM-EDX = electron microscopy. + and ++ signify additional phases seen by PXRD.

Co/Pd Loaded (At %)	Target (VE)	Phases (PXRD)	*a* (Å) (PXRD)	*a* (Å) (SCXRD)	Composition (SCXRD)	Composition (SEM-EDX)
7.58 / 7.74	$CoPdZn_{11}$ (302 e^-)	γ_1	9.053(2)	9.0510(7)	$Co_{0.92(2)}Pd_{1.08}Zn_{11}$	$Co_{1.0(1)}Pd_{1.0(1)}Zn_{11.0(2)}$
7.97 / 15.29	$CoPd_2Zn_{10}$ (298 e^-)	γ_1 +	9.046(3)			$Co_{1.0(1)}Pd_{1.0(1)}Zn_{11.0(2)}$ $Co_{0.2(1)}Pd_{3.5(2)}Zn_{6.3(1)}$
11.72 / 11.52	$Co_{1.5}Pd_{1.5}Zn_{10}$ (297 e^-)	γ_1 + ++	9.051(4)			$Co_{0.8(1)}Pd_{1.1(1)}Zn_{11.1(2)}$ $Co_{0.3(1)}Pd_{3.4(2)}Zn_{6.3(2)}$ $Co_{7.2(2)}Zn_{2.8(2)}$
15.24 / 7.94	Co_2PdZn_{10} (296 e^-)	γ_1 +	9.056(3)			$Co_{1.0(1)}Pd_{1.1(1)}Zn_{11.0(2)}$ $Co_{7.4(2)}Zn_{2.6(2)}$
15.61 / 15.34	$Co_2Pd_2Zn_9$ (292 e^-)	γ_2	9.076(1)	9.098(1)	$Co_{2.50(1)}Pd_{2.50}Zn_8$	$Co_{2.6(3)}Pd_{2.4(3)}Zn_{8.0(3)}$
19.35 / 19.24	$Co_{2.5}Pd_{2.5}Zn_8$ (287 e^-)	γ_2 + ++	9.076(1)			$Co_{2.5(2)}Pd_{2.5(2)}Zn_{8.0(3)}$ $Co_{0.1(1)}Pd_{3.8(2)}Zn_{6.1(2)}$ $Co_{9.1(2)}Zn_{0.9(1)}$

4.5.1 Synthesis and Phase Analysis: Five different Co-Pd-Zn samples targeting γ-brass phases with 292-302 valence electrons per cubic unit cell were loaded to synthesize our target compounds (see Table 4). After the results of loading "$Co_2Pd_2Zn_9$" (292 e^-), a sixth sample which mimicked the refined composition was prepared. Each reactant mixture, about 500 mg total, was sealed into an evacuated silica tube (< 10^{-5} Torr), heated to 1000°C for 24 hr, followed by cooling to 600°C at a rate of 1°C/min and annealed at this temperature for 3 days, after which the container was slowly cooled in the furnace. In general, synthetic attempts to prepare γ-brass type Co-Pd-Zn phases yielded a series of mixed phases. Only those reactant mixtures that were loaded for "$CoPdZn_{11}$" and "$Co_2Pd_2Zn_9$" yielded single phase, crystalline products according the results of powder X-ray diffraction and scanning electron microscopy. The intermediate loadings, "$CoPd_2Zn_{10}$" and "Co_2PdZn_{10}", gave a γ-

brass phase $(Co_{1-x}Pd_x)_2Zn_{11}$ and, respectively, ~$PdZn_2$ and Co particles. The "$Co_{1.5}Pd_{1.5}Zn_{10}$" loading yielded γ-brass $Co_{1-x}Pd_xZn_{11}$, ~$PdZn_2$ and Co particles. On the other hand, the $Co_{2.5}Pd_{2.5}Zn_8$ γ-brass produced $(Co_{1-x}Pd_x)_5Zn_8$, ~$PdZn_2$, and Co particles. Crystalline specimens suitable for single crystal X-ray diffraction analysis were extracted from the two single phase products. For the loaded composition "$CoPdZn_{11}$", the refined crystal structure agreed closely with the loading, i.e., $Co_{0.92(2)}Pd_{1.08}Zn_{11}$, with Co and Pd atoms sharing the OT (8*c*) sites and Zn atoms fully occupying all other (IT, OH, and CO) sites. The corresponding number of valence electrons for this compound is 302.2(4) electrons per unit cell, which corresponds closely to the position of the pseudogap around +0.5eV in total DOS of Co_2Zn_{11}. For the loaded composition "$Co_2Pd_2Zn_9$", however, the refined crystal structure is $Co_{2.50(1)}Pd_{2.50}Zn_8$, with Co and Pd atoms mixing on the OT (8*c*) and OH (12*e*) sites and the other two (IT, CO) sites occupied exclusively by Zn atom, as shown in Figure 4. The results of these crystal structure refinements are summarized in Tables 5 and 6.

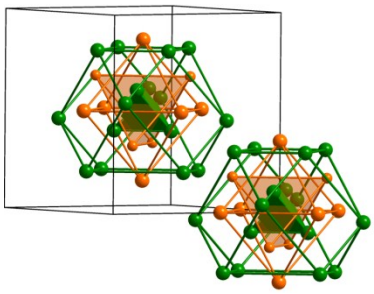

Figure 4. The crystal structure of $Co_{2.5(1)}Pd_{2.5}Zn_8$ at 293(2) K emphasizing the 26-atom γ-brass clusters located at the unit cell corner(s) and center. Orange circles are Co/Pd mixed sites; green circles are Zn.

Table 5. Crystallographic data for "$CoPdZn_{11}$" and $Co_{2.5(1)}Pd_{2.5}Zn_8$ at 293(2) K.

Loading Composition	$CoPd_1Zn_{11}$	$Co_2Pd_2Zn_9$
Refined Formula	$Co_{0.92(2)}Pd_{1.08}Zn_{11}$	$Co_{2.50(1)}Pd_{2.50}Zn_8$
F.W. (g/mol);	887.84	934.78
Space group; *Z*	$I\bar{4}3m$ (No.217); 4	$I\bar{4}3m$ (No.217); 4
a (Å)	9.0510(7)	9.098(1)

Table 5. continued

V (Å^3)	741.46(10)	753.07(16)
Absorption Correction	Multi-Scan	Multi-Scan
Extinction Coefficient	0.0005(1)	None
μ(mm^{-1})	39.304	36.091
θ range (deg)	3.18-28.11	3.17-28.23
hkl ranges	$-11 \le h,k,l \le 11$	$-11 \le h,k,l \le 11$
No. reflections; R_{int}	1516; 0.0573	2356; 0.0305
No. independent reflections	193	198
No. parameters	20	20
R_1; wR_2 (all I)	0.0226; 0.0457	0.0152; 0.0405
Goodness of fit	1.061	1.108
Diffraction peak and hole (e$^-$/Å^3)	0.836; –0.851	0.426; –0.584

Table 6. Atomic coordinates, site occupancies, and equivalent isotropic displacement parameters for $CoPdZn_{11}$ and $Co_{2.5(1)}Pd_{2.5}Zn_8$. U_{eq} is defined as one-third of the trace of the orthogonalized U^{ij} tensor (Å^2).

"$CoPdZn_{11}$": $Co_{0.92(2)}Pd_{1.08}Zn_{11}$ (302.2 e^-)

Atom	Wyckoff.	Occupancy.	x	y	z	U_{eq}
Zn1	8*d*(IT)	1	0.1061(1)	0.1061(1)	0.1061(1)	0.014(1)
Co/Pd	8*c*(OT)	0.46(1)/0.54	0.3266(1)	0.3266(1)	0.3266(1)	0.008(1)
Zn2	12*e*(OH)	1	0.3555(1)	0	0	0.012(1)
Zn3	24*g*(CO)	1	0.3086(1)	0.3086(1)	0.0426(1)	0.015(1)

"$Co_2Pd_2Zn_9$": $Co_{2.50(1)}Pd_{2.50}Zn_8$ (287.0 e^-)

Atom	Wyckoff.	Occupancy.	x	y	z	U_{eq}
Zn1	8*d*(IT)	1	0.1037(2)	0.1037(2)	0.1037(2)	0.015(1)
Co/Pd	8*c*(OT)	0.25(1)/0.75	0.3281(2)	0.3281(2)	0.3281(2)	0.009(1)
Co/Pd	12*e*(OH)	0.67(1)/0.33	0.3539(3)	0	0	0.011(1)
Zn2	24*g*(CO)	1	0.3052(1)	0.3052(1)	0.0472(2)	0.016(1)

The outcome of phase analysis of Co-Pd-Zn γ-brasses and refinements from single crystal X-ray diffraction indicate that Co and Pd mix on the OT sites at low concentrations, but then combine at both the OT and OH sites at high concentrations. The Mulliken population analysis described above for site preferences in the Co-Zn γ-brasses may also be applied here

to evaluate the "site energy" term of the total electronic energy. Again, the OT site is clearly favored for the element(s) with lower valence electron count, i.e., Co and Pd. Moreover, the next favored site for substitution by Co and/or Pd atoms is the IT site according to this model, but these sites are occupied solely by Zn atoms. Thus, it is the "bond energy" term to the total electronic energy that influences preferred occupation for Co and Pd atoms at the OH rather than the IT sites at higher Co/Pd concentrations.

4.5.2 Electronic Structures of "$Co_{2.5}Pd_{2.5}Zn_8$": TB-LMTO and VASP calculations using both LDA and LSDA were applied to two hypothetical ordered models of "$Co_{2.5}Pd_{2.5}Zn_8$" (see Figure 5) both of which took into account the observed site preferences from single crystal X-ray diffraction. Although diffraction results indicated an *I*-centered cubic unit cell, these two models utilized primitive lattices by decorating the OT and OH sites of the two 26-atom γ-brass clusters in different ways (in all clusters, Zn atoms fully occupied the IT and CO sites as seen experimentally). For model (*a*), the two clusters are formulated as $[Zn_4Co_4Pd_6Zn_{12}]$ and $[Zn_4Pd_4Co_6Zn_{12}]$ with the occupations of OT and OH sites by Co and Pd atoms switched between the two distinct clusters. For model (*b*), the two clusters involve binary Co-Zn and Pd-Zn arrangements, i.e., formulated as $[Zn_4Co_4Co_6Zn_{12}]$ and $[Zn_4Pd_4Pd_6Zn_{12}]$. According to the results of VASP calculations including LSDA, the total energies of models (*a*) and (*b*) differ by ~5 meV/atom near their energy minima with a slight preference for model (*b*).

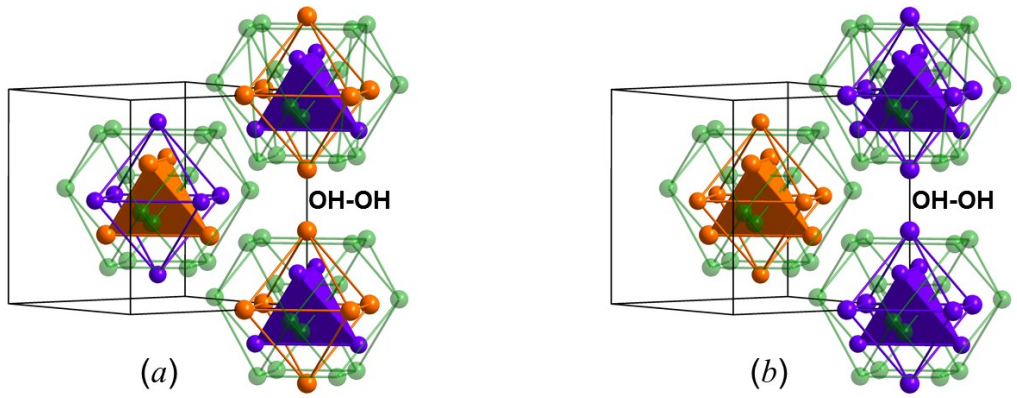

Figure 5. Hypothetical models (*a*) and (*b*) for $Co_{2.5}Pd_{2.5}Zn_8$ emphasizing the 26-atom γ-brass clusters in the unit cells (purple: Co atoms; orange: Pd atoms; green: Zn atoms). See text for detailed descriptions.

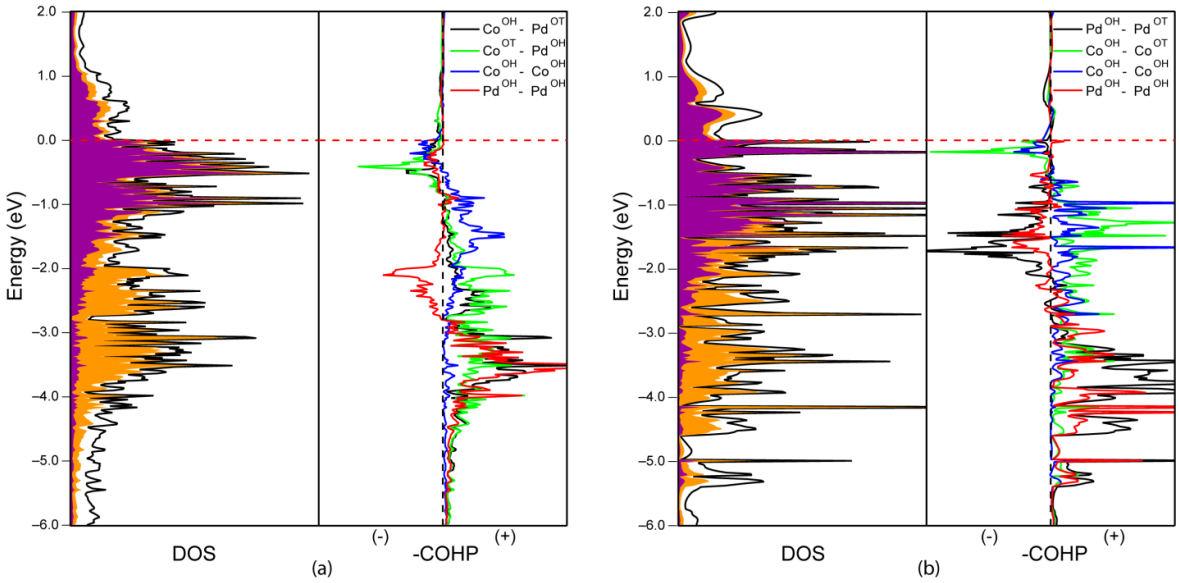

Figure 6. Non-spin polarized total and partial DOS curves with OT–OH and OT–OH COHP curves for models (*a*) and (*b*) of "$Co_{2.5}Pd_{2.5}Zn_8$" (+ is bonding / − is antibonding; E_F indicated by the red dashed line for 287 e^-). In the DOS curves, purple shading indicates Co contributions, orange shading indicates Pd contributions.

In Figure 6, the LDA-based DOS curves and the corresponding OT–OH and OH–OH COHP curves for both models are illustrated for an energy range between –6 and +2 eV relative to their Fermi levels. When compared to the DOS curves of other γ-brasses,[3,36] they also show the broad pseudogap in the DOS between +1 and +2 eV corresponding to *e*/*a* values ranging from 1.55-1.73. The presence of both Co and Pd atoms, however, with valence *d* orbitals creates a rather broad (~4 eV) *d* band that decomposes into mostly Pd 4*d*

wavefunctions toward the bottom of the band and mostly Co 3*d* orbitals toward the top of the band. The Fermi levels fall within and near the top of this broad *d* band, in the midst of the Co-rich region with rather large values of 44.6 eV^{-1} for (*a*) and 116.0 eV^{-1} for (*b*). The LDA-based COHP curves indicate that all *d*-*d* bonding and most *d*-*d* antibonding orbitals are filled, with the most significant antibonding contributions at the E_F values arising from interactions with Co atoms.

On applying the LSDA, the electronic structures of both models converged to new and different magnetically ordered ground states. In both cases, the total magnetic moments arise primarily from net unpaired spins at the Co atoms with small moments arising at Pd and Zn sites (see next section on magnetic properties). The DOS curves for the majority-spin and minority-spin wavefunctions, shown in Figure 7, clearly illustrate this outcome because the Co projected DOS curves are quite unsymmetrical, but also show that the corresponding Fermi levels fall just below sharp peaks in the minority-spin states. According to the accompanying COHP curves, these peaks involve Co–Co antibonding interactions in each model. In fact, the EF values for each model correspond to the crossover point between Co–Co bonding and antibonding states in the DOS. Thus, unlike Co_2Zn_{11}, which showed no net magnetization using LSDA, $Co_{2.5}Pd_{2.5}Zn_8$ should spontaneously give net magnetization, results that were confirmed by subsequent measurements.

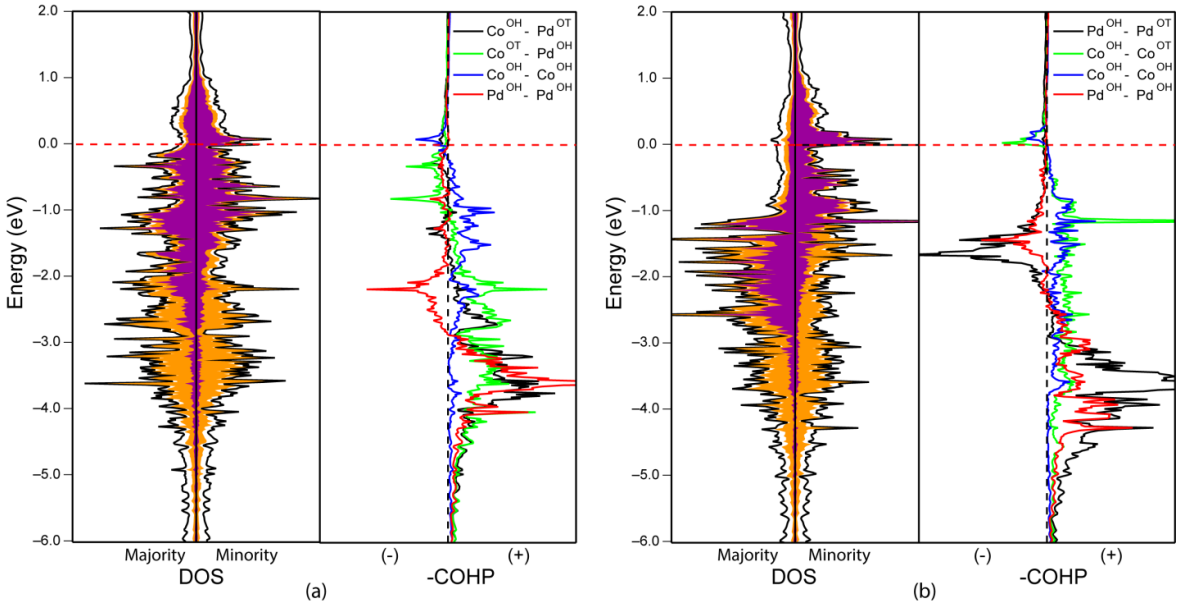

Figure 7. Spin polarized total and partial DOS curves with OT–OH and OT–OH COHP curves for models (*a*) and (*b*) of "$Co_{2.5}Pd_{2.5}Zn_8$" (+ is bonding / − is antibonding; E_F indicated by the red dashed line for 287 e^-). In the DOS curves, purple shading indicates Co contributions, orange shading indicates Pd contributions.

4.6 Magnetic Properties of Co-Zn and Co-Pd-Zn γ-brasses

The magnetic susceptibility curves of Co_2Zn_{11} and $Co_{2.66(2)}Zn_{10.29(3)}$ (loaded as 24.86 at% Co), shown in Figure 8, indicate paramagnetic properties for both samples. In particular, Co_2Zn_{11} is Pauli paramagnetic with a very small magnetic susceptibility of ~5 × 10^{-4} emu/mol·Oe. This low susceptibility leads to a magnetic moment $\mu \approx 0.06(1)\ \mu_B$ and a low-temperature magnetization that should vary linearly with magnetic field, which is verified in Figure 8. For the Co-richer sample, $Co_{2.66(2)}Zn_{10.29(3)}$, the magnetic susceptibility follows Curie-Weiss behavior with an effective moment per Co atom of 0.6(1) μ_B and a small, negative Weiss temperature of –6(1)K. The nonlinear relationship between magnetization and applied field is verified in Figure 8 (see Supporting Information for further data analysis).

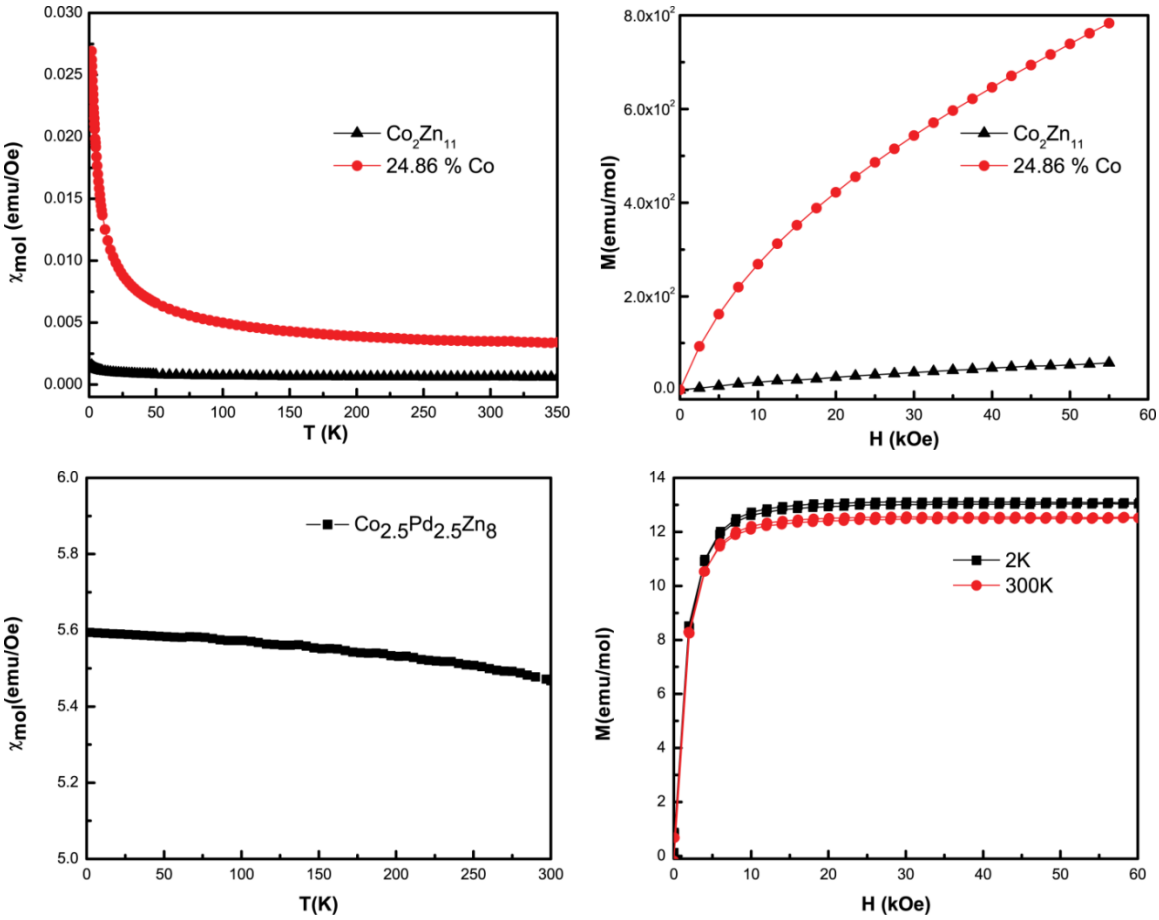

Figure 8. (Left) Temperature-dependent molar susceptibility measured from 2 K to 300 K at 10 kOe for (top) Co_2Zn_{11} and $Co_{2.66(2)}Zn_{10.29(3)}$ and (bottom) $Co_{2.5(1)}Pd_{2.5}Zn_8$. (Right) Magnetization vs. applied field (top) measured at 1.8 K for Co_2Zn_{11} and $Co_{2.66(2)}Zn_{10.29(3)}$ and (bottom) measured at 2 K and 300 K for $Co_{2.5(1)}Pd_{2.5}Zn_8$.

The isothermal magnetization curves of the $Co_{2.50(1)}Pd_{2.50}Zn_8$ sample measured at 2 K and 300 K indicate the sample to be ferromagnetic. Saturation is achieved at ~7.0 kOe. The saturation moments are 0.88(5) μ_B/f.u. at 2 K and 0.80(5) μ_B/f.u. at 300 K. Moreover, temperature-dependent magnetic susceptibility measurements from 300 K to 700 K (see Figure S9 in Supporting Information) can be divided into two parts: (i) from 300 K to 450 K during which the magnetic moment decreases from ~2.3 to ~1.8 μ_B/f.u; and (ii) from 500 K to 700 K during the magnetic moment decreases slightly from ~1.8 to ~1.7 μ_B/f.u. The larger magnetic susceptibility of the $Co_{2.50(1)}Pd_{2.50}Zn_8$ sample as compared to the binary Co-Zn γ

brasses is presumably caused by enhanced Stoner ferromagnetism upon doping Pd in the system.[37-39] According to the LDA-based DOS curves for Co_2Zn_{11} (Figure 2) and the two models of $Co_{2.5}Pd_{2.5}Zn_8$ (Figure 6), the density of states at the Fermi level $N(E_F)$ per atom increases from 0.623 eV^{-1} in the binary to 2.25 eV^{-1} (averaged) in the ternary case. Moreover, the two stages of magnetic response above room temperature may arise because different magnetically-active sites will have their own different Curie temperatures.[40] The current data are not enough to make a clear judgment on the magnetic properties of $Co_{2.5}Pd_{2.5}Zn_8$ at high temperature.

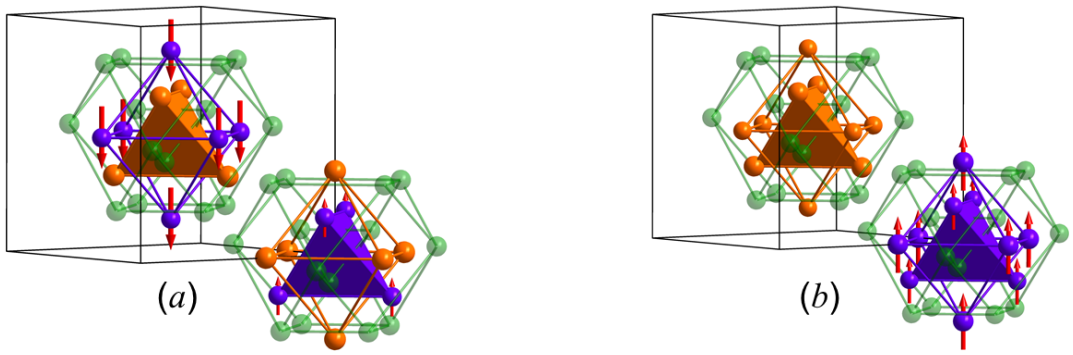

Figure 9. Converged magnetic structures of models (*a*) and (*b*) for $Co_{2.5}Pd_{2.5}Zn_8$ (see Figure 4). Relative moments at the Co atoms, which have the largest contributions, and indicated by arrow lengths and directions.

As mentioned above, LSDA calculations of two different models (*a*) and (*b*) of $Co_{2.5}Pd_{2.5}Zn_8$ yielded spontaneous magnetization arising primarily from net unpaired spins at the Co atoms and with different magnetically ordered ground states, which are illustrated in Figure 9. Using the Co partial DOS curves for both models at the intra-atomic exchange parameter for Co of 0.49 eV[41,42], the Stoner condition for ferromagnetism is satisfied to a first approximation since $N_{(a)}(Co) = 2.21\ eV^{-1}$ and $N_{(b)}(Co) = 3.20\ eV^{-1}$ at E_F. In model (*a*), which has Co and Pd atoms on both 26-atom γ-brass clusters in the cubic unit cell, the local moments on the two different sets of Co atoms are antiferromagnetically aligned: 1.39 μ_B at OH sites for the cluster at (½, ½, ½); –0.78 μ_B at the OT sites for the cluster at (0, 0, 0) and a

total magnetic moment of 2.76 μ_B/f.u., which corresponds to 0.55 μ_B/Co atom. In model (*b*), with Co and Pd segregated onto different clusters, the Co moments are ferromagnetically aligned: 1.50 μ_B at OH sites and 1.31 μ_B at the OT sites for the cluster at (0,0,0) and a total magnetic moment of 6.63 μ_B/f.u., which corresponds to 1.36 μ_B/Co atom. To evaluate the total moments, the Pd and Zn atoms are slightly polarized (see Table S4 for a complete listing of these calculated moments). Since the results of single crystal X-ray diffraction on $Co_{2.5}Pd_{2.5}Zn_8$ gave no clear evidence of any long-range ordering of Co and Pd atoms among the OT and OH sites of the 26-atom γ-brass clusters, then the observed saturation moments of 0.80(5)-0.88(5) μ_B/f.u. from 300 K to 2 K are consistent with the results of these LSDA calculations. In particular, theory suggests ferromagnetically coupled Co-atom moments within a cluster, and antiferromagnetically coupled Co-atom moments between neighboring clusters. The occurrence of ferromagnetic (or ferrimagnetic) behavior in $Co_{2.5}Pd_{2.5}Zn_8$ seems to arise from both the change in valence electron count as well as the presence of valence orbitals introduced by Pd atoms. Additional experiments and theoretical calculations are warranted, however, to assess fully the nature of both these through-space and through-bond interactions.

4.7 Summary

The Group II γ-brasses in the Co-Zn system were shown to exist over a homogeneity range $Co_{2+x}Zn_{11-y}\square_{y-x}$ that included a small concentration of vacancies as the Co content increased as well as clear site preference of Co atoms for the OT and OH sites. Stoichiometric Co_2Zn_{11} is Pauli paramagnetic whereas they become Curie-Weiss paramagnetic with increasing Co content. As an alternative interpretation to the FsBz-interaction to stabilize the γ-brass structure for Co_2Zn_{11}, a molecular orbital based model shows that the bcc packing of 26-atom

Co_4Zn_{22} γ-brass clusters also accounts for its stability. Inspired by the electronic structure calculated for Co_2Zn_{11}, substituting Pd atoms for Zn or Co atoms in the Co-Zn system led to the discovery of a ferromagnetic (ferrimagnetic) $Co_{2.5}Pd_{2.5}Zn_8$ γ-brass compound with Co and Pd atoms occupying the OT and OH sites. States at the Fermi level of this ternary compound arise mostly from Co 3*d* orbitals, and form spontaneous magnetic moments in two distinct structural models. Magnetization measurements indicate ferromagnetic or ferrimagnetic behavior, while theory predicts ferromagnetic Co–Co intra-cluster interactions but antiferromagnetic Co–Co inter-cluster interactions.

4.8 Acknowledgements

Ms. Jing Liu and Dr. Wei Tang of Ames Laboratory are indebted for the collection of magnetization data. Also, the authors gratefully acknowledge Mr. Tai Kong, Dr. Sergey L. Bud'ko, and Prof. Robert J. McQueeney in the Department of Physics & Astronomy at Iowa State University for useful discussions on the magnetic properties. This research was supported by the Office of the Basic Energy Sciences, Materials Sciences Division, U.S. Department of Energy (DOE). Ames Laboratory is operated for DOE by Iowa State University under contract No. DE-AC02-07CH11358

4.9 References

[1] Dubois, J. M.; Belin-Ferré, E.; Feuerbacher, M., *Complex Metallic Alloys: Fundamentals and Applications*, Wiley, New York, 2010.

[2] Snyder, G. J.; Toberer, E. S., *Nat. Mater.* **2008,** *72*, 105.

[3] Mizutani, U., *Hume-Rothery Rules for Structurally Complex Alloy Phases*, CRC Press, New York, *2010*.

[4] Mizutani, U.; Takeuchi, T.; Sato, H., *Prog. Mater Sci.* **2004,** *49*, 227.

[5] Berger, R.F.; Lee, S.; Johnson, J.; Nebgen, B.; So, A.C.Y. *Chem. Eur. J.* **2008,** *14*, 6627.

[6] Mizutani, U.; Inukai, M.; Sato, H., *Philos. Mag.* **2011,** *91*, 2536.

[7] Sato, H.; Takeuchi, T.; Mizutani, U., *Phys. Rev. B* **2001,** *64*, 094207.

[8] Degtyareva, V. F.; Smirnova, I. S., *Z. Kristallogr.* **2007,** *222*, 718.

[9] Rietveld, H. *J. Appl. Crystallogr.* **1969,** *2*, 65.

[10] Hunter, B., LHPM-Rietica, 1.7. 7. **1998**.

[11] SMART, version 5, *Bruker AXS*, Madison, WI*,* **2003**.

[12] Blessing, R. *Acta Crystallogr. A* **1995,** *51*, 33.

[13] Sheldrick, G. *SHELX*, version 5.1. *Bruker AXS,* Madison, WI, **2002**.

[14] Larson, A. *Acta Crystallogr.* **1967,** *23*, 664.

[15] Hamilton, W. C. *Acta Crystallogr.* **1965,** *18*, 502.

[16] Brandenburg, K., *Diamond*, version 3.2, *Crystal Impact GbR,* Bonn, Germany, **2011**.

[17] Jepsen, O.; Burkhardt, A.; Andersen, O., The Program TB-LMTO-ASA, 47, Stuttgart, Germany, **2000.**

[18] Kotani, T. *Phys. Rev. Lett.* **1995,** *74*, 2989.

[19] Dronskowski, R.; Bloechl, P. E., *J. Phys. Chem.* **1993,** *97*, 8617.

[20] Hafner, J. R. *J Comput. Chem.* **2008,** *29*, 2044.

[21] Blöchl, P.E. *Phys. Rev. B* **1994,** *50*, 17953.

[22] Perdew, J. P.; Burke, K.; Wang, Y., *Phys. Rev. B* **1996,** *54*, 16533.

[23] Monkhorst, H. J.; Pack, J. D., *Phys. Rev. B* **1976,** *13*, 5188.

[24] Hoffmann, R., *J. Chem. Phys.* **1963**, *39*, 1397.

[25] Xie, W.; Thimmaiah, S.; Lamsal, J.; Liu, J.; Heitmann, T. W.; Quirinale, D.; Goldman, A. I.; Pecharsky, V.; Miller, G. J., Inorg. Chem. **2013,** *52,* 9399.

[26] Pearson, W. B. *Z. Kristallogr.* **1981,** *156*, 281.

[27] Gourdon, O.; Izaola, Z.; Elcoro, L.; Petricék, V.; Miller, G. J., *Inorg. Chem.* **2009,** *48*, 9715.

[28] Johansson, A.; Ljung, H.; Westman, S., *Acta Chem. Scand.* **1968,** *22*, 2743.

[29] Harbrecht, B.; Thimmaiah, S.; Armbrüster, M.; Lee, S.; Pietzonka, C. *Z. Anorg. Allg. Chem.* **2002,** *628*, 2744.

[30] Black, G. R.; Hartge, K. H., *Methods of Soil Analysis*, *Part 1: Physical and Mineralogical Methods*, American Society of Agronomy, Inc., United States, **1986**.

[31] Miller, G.J., *Eur. J. Inorg. Chem.* **1998**, 523.

[32] Wimmer, E.; Krakauer, H.; Weinert, M.; Freeman, A. J., *Phys. Rev. B*, **1981,** *24*, 864.

[33] Pearson, R.G., *Inorg. Chem.* **1988**, *27*, 734.

[34] Teng, X.; Han, W. Q.; Ku, W.; Hücker, M., *Angew. Chem.* **2008,** *120*, 2085.

[35] Kudasov, Y. B.; Korshunov, A. S., *Phys. Lett. A* **2007,** *364*, 348.

[36] Gourdon, O.; Gout, D.; Williams, D.J.; Proffen, T.; Hobbs, S.; Miller, G.J., *Inorg. Chem.* **2007,** *46*, 251-260.

[37] Jarlborg, T.; Freeman, A. J., *Phys. Rev. B* **1981,** *23,* 3577.

[38] Takahashi, S.; Takahashi, A. Y.; Chiba, A. *J. Phys.: Condens. Matter*, **1994,** *6*, 6011.

[39] De Boer, F. R.; Schinkel, C. J.; Biesterbos, J.; Proost, S. *J. Appl. Phys.*, **1969,** *40*, 1049.

[40] Kondo, J. *Progr. Theor. Phys.* **1964,** *32*, 37.

[41] Seo, D.K.; Kim, S.H., *J. Comput. Chem.* **2008**, *29*, 2172.

[42] Janak, J.F. *Phys. Rev. B* **1977**, *16*, 255.

4.10 Supporting Information

Table S1. Anisotropic displacements parameters for Co-Zn and Co-Pd-Zn γ-brass crystal structures.

Co_2Zn_{11}

Atom	U_{11}	U_{22}	U_{33}	U_{23}	U_{13}	U_{12}
Zn1	0.0090(3)	0.0090(3)	0.0090(3)	0.0020(3)	0.0020(3)	0.0020(3)
Co2	0.0056(3)	0.0056(3)	0.0056(3)	0.0012(3)	0.0012(3)	0.0012(3)
Zn3	0.0099(4)	0.0099(3)	0.0064(3)	0	0	0.0022(4)
Zn4	0.0113(3)	0.0113(3)	0.0087(3)	–0.0027(2)	–0.0027(2)	–0.0015(3)

$Co_{2.34(2)}Zn_{10.63(3)}$

Atom	U_{11}	U_{22}	U_{33}	U_{23}	U_{13}	U_{12}
Zn1	0.0073(3)	0.0073(3)	0.0073(3)	0.0021(3)	0.0021(3)	0.0021(3)
Co2	0.0047(3)	0.0047(3)	0.0047(3)	0.0015(3)	0.0015(3)	0.0015(3)
Co/Zn3	0.0080(4)	0.0080(4)	0.0056(5)	0	0	0.0027(4)
Zn4	0.0109(3)	0.0109(3)	0.0075(3)	–0.0029(2)	–0.0029(2)	–0.0015(3)

$Co_{2.66(2)}Zn_{10.29(3)}$

Atom	U_{11}	U_{22}	U_{33}	U_{23}	U_{13}	U_{12}
Zn1	0.0100(4)	0.0100(4)	0.0100(4)	0.0035(3)	0.0035(3)	0.0035(3)
Co2	0.0049(3)	0.0049(3)	0.0049(3)	0.0008(3)	0.0008(3)	0.0008(3)
Co/Zn3	0.0086(4)	0.0086(4)	0.0073(5)	0	0	0.0021(4)
Zn4	0.0153(3)	0.0153(3)	0.0092(3)	–0.0047(2)	–0.0047(2)	–0.0014(3)

$Co_{2.84(2)}Zn_{10.05(3)}$

Atom	U_{11}	U_{22}	U_{33}	U_{23}	U_{13}	U_{12}
Zn1	0.0129(3)	0.0129(3)	0.0129(3)	0.0042(3)	0.0042(3)	0.0042(3)
Co2	0.0070(3)	0.0070(3)	0.0070(3)	0.0036(3)	0.0036(3)	0.0036(3)
Co/Zn3	0.0110(4)	0.0110(4)	0.0094(5)	0	0	0.0021(4)
Zn4	0.0185(3)	0.0185(3)	0.0128(3)	–0.0052(2)	–0.0052(2)	–0.0007(3)

$Co_{0.92(2)}Pd_{1.08}Zn_{11}$

Atom	U_{11}	U_{22}	U_{33}	U_{23}	U_{13}	U_{12}
Zn1	0.0142(4)	0.0142(4)	0.0142(4)	0.0034(3)	0.0034(3)	0.0034(3)
Co/Pd2	0.0078(4)	0.0078(4)	0.0078(4)	0.0102(3)	0.0102(3)	0.0102(3)
Zn3	0.0140(4)	0.0140(4)	0.0097(5)	0	0	–0.0025(5)
Zn4	0.0166(4)	0.0166(4)	0.0145(4)	–0.0044(3)	–0.0044(3)	–0.0002(4)

$Co_{2.50(1)}Pd_{2.50}Zn_8$

Atom	U_{11}	U_{22}	U_{33}	U_{23}	U_{13}	U_{12}
Zn1	0.0152(3)	0.0152(3)	0.0152(3)	0.0047(3)	0.0047(3)	0.0047(3)
Co/Pd2	0.0095(3)	0.0095(3)	0.0095(3)	0.0009(2)	0.0009(2)	0.0009(2)
Co/Pd3	0.0123(4)	0.0123(4)	0.0096(5)	0	0	–0.0031(4)
Zn4	0.0178(3)	0.0178(3)	0.0141(4)	–0.0046(2)	–0.0046(2)	–0.0011(3)

Table S2. Significant interatomic distances (Å) in Co-Zn and Co-Pd-Zn γ-brass structures.

Pairs	C.N.	Co_2Zn_{11}	$Co_{2.34(2)}Zn_{10.63(3)}$	$Co_{2.66(2)}Zn_{10.29(3)}$	$Co_{2.84(2)}Zn_{10.03(3)}$
IT–IT	3	2.639(2)	2.643(1)	2.637(1)	2.552(2)
IT–OT	3	2.619(2)	2.614(1)	2.577(1)	2.534(2)
IT–OH	3	2.602(1)	2.599(1)	2.590(1)	2.583(1)
IT–CO	3	2.609(1)	2.607(1)	2.601(1)	2.585(1)
OT–OH	3	2.724(1)	2.720(1)	2.700(1)	2.681(1)
OT–CO	3	2.542(1)	2.546(1)	2.565(1)	2.552(1)
	3	2.590(1)	2.587(1)	2.573(1)	2.566(1)
OH–OH	1	2.614(2)	2.610(2)	2.589(2)	2.587(2)
OH–CO	2	2.620(1)	2.615(1)	2.598(1)	2.613(1)
	4	2.806(1)	2.805(1)	2.794(1)	2.768(1)
	2	3.006(1)	2.997(1)	2.966(1)	3.003(1)
CO–CO	4	2.722(1)	2.717(1)	2.697(1)	2.710(1)

Pairs	C.N.	$Co_{0.92(2)}Pd_{1.08}Zn_{11}$	$Co_{2.50(1)}Pd_{2.50}Zn_8$
IT–IT	3	2.716(1)	2.760(1)
IT–OT	3	2.672(1)	2.688(1)
IT–OH	3	2.634(1)	2.655(1)
IT–CO	3	2.655(1)	2.668(1)
OT–OH	3	2.764(1)	2.783(1)
OT–CO	3	2.582(1)	2.610(1)
	3	2.611(1)	2.611(1)
OH–OH	1	2.617(1)	2.591(1)
OH–CO	2	2.619(1)	2.614(1)
	4	2.851(1)	2.868(1)
	2	2.979(1)	2.952(1)
CO–CO	4	2.725(1)	2.721(1)

Table S3. Unit cell parameters and valence electron concentrations in Group II γ-brass structures.

System	Composition	e^-/unit cell	a (Å)	V (Å^3)	e^-/V (Å^{-3})	e/a
Fe-Zn	$Fe_{13}Zn_{39}$[1]	572	8.994	727.54	0.786	11.00
	Fe_3Zn_{10}[2]	576	9.018	733.38	0.785	11.08
Co-Zn	Co_2Zn_{11}	600	8.9654	720.62	0.833	11.54
	$Co_{2.34}Zn_{10.63}$	594.48	8.9552	718.17	0.828	11.46

Table S3. continued

	$Co_{2.66}Zn_{10.29}$	589.68	8.911	707.59	0.833	11.38
	$Co_{2.84}Zn_{10.03}$	583.68	8.882	700.70	0.833	11.34
Ni-Zn[3]	$Ni_{8.8}Zn_{42.5}$	598	8.9231	710.47	0.842	11.66
	$Ni_8Zn_{42.5}$	590	8.9206	709.88	0.831	11.68
Cu-Zn[4]	$Cu_{4.21}Zn_{8.79}$	607.16	8.8829	700.91	0.866	11.68
	$Cu_{4.56}Zn_{8.44}$	605.76	8.8744	698.90	0.867	11.65
	Cu_5Zn_8	604	8.8664	697.01	0.867	11.62
	$Cu_{5.31}Zn_{7.69}$	602.76	8.8601	695.53	0.867	11.59
	$Cu_{5.59}Zn_{7.41}$	601.64	8.8565	694.98	0.866	11.57

[1] Belin, C. H. E., Belin, R. C. H. *J. Solid State Chem.* **2000**, *151*, 85.

[2] Brandon, J. K.; Brizard, R. Y.; Chieh, P. C.; McMillan, R. K.; Pearson, W. B. *Acta Crystallogr. B* **1974**, *30*, 1412.

[3] Pearson, W. B. *Zeitschrift für Kristallographie*, **1981**, *156*, 281.

[4] Gourdon, O.; Gout, D.; Williams, D. J.; Proffen, T.; Hobbs, S.; Miller, G. J. *Inorg. Chem.* **2007**, *46(1)*, 251.

Table S4. Magnetic moments (μ_B) calculated for models (a) and (b) for "$Co_{2.5}Pd_{2.5}Zn_8$" using TB-LMTO-ASA with LSDA.

Position / Cluster	Model (a)		Model (b)	
	Atom	Moment (μ_B)	Atom	Moment (μ_B)
IT / (0, 0, 0)	Zn	0.024	Zn	–0.044
OT / (0, 0, 0)	Co	–0.777	Co	1.310
OH / (0, 0, 0)	Pd	0.009	Co	1.503
CO / (0, 0, 0)	Zn	–0.001	Zn	–0.017
IT / (½ , ½, ½)	Zn	–0.012	Zn	–0.004
OT / (½ , ½, ½)	Pd	0.041	Pd	0.001
OH / (½ , ½, ½)	Co	1.393	Pd	–0.007
CO / (½ , ½, ½)	Zn	0.002	Zn	–0.022

Figure S1. Total energy vs.volume curves for Co_2Zn_{11} in two structural models: (i) Co atoms in IT sites; and (ii) Co atoms in OT sites. Also shown are the results of fitting each curve with the Birch-Murnaghan equation of state.

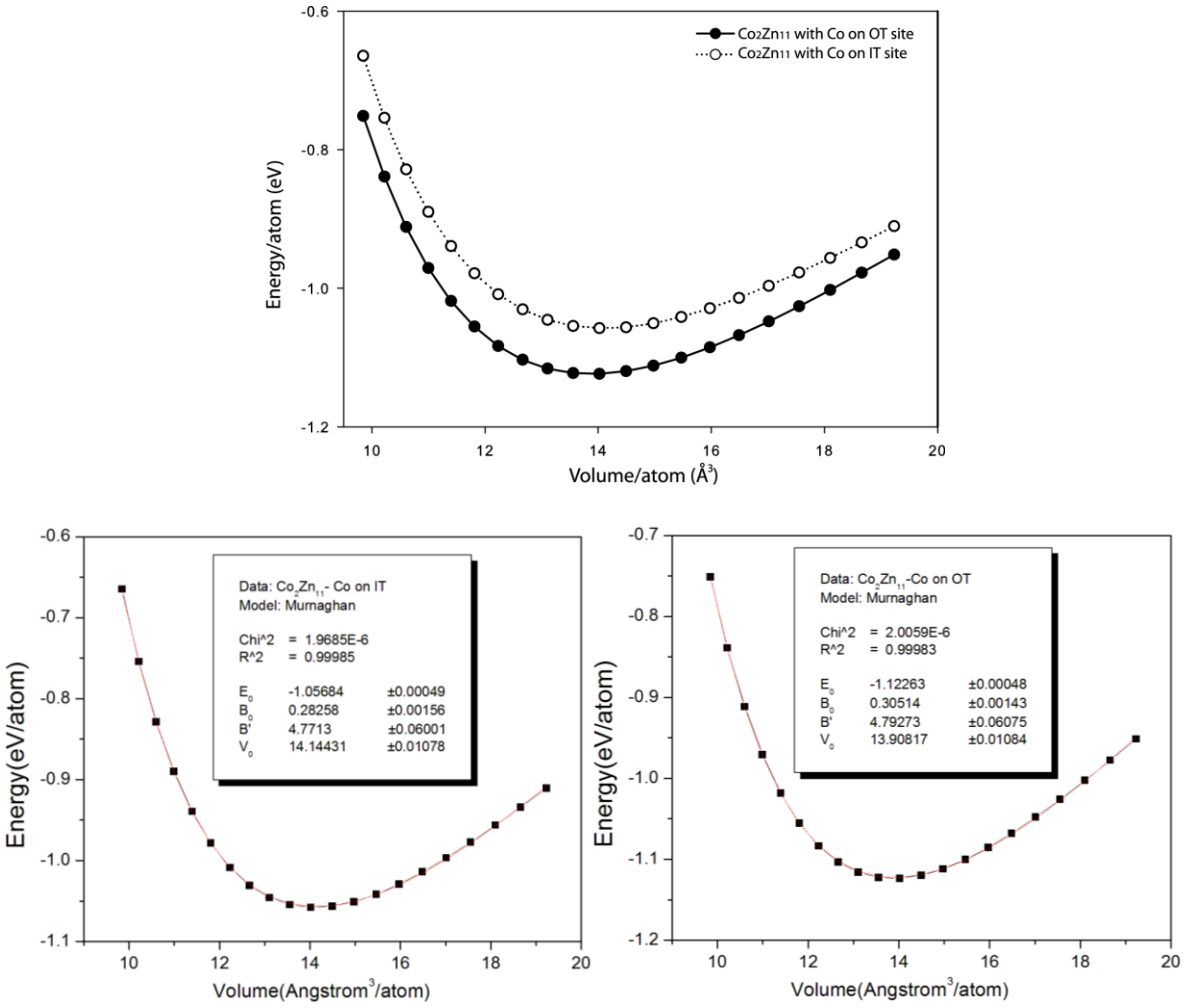

Birch–Murnaghan equation:

$$E(V) = E_0 + \frac{9V_0B_0}{16}\left\{\left[\left(\frac{V_0}{V}\right)^{\frac{2}{3}} - 1\right]^3 B_0' + \left[\left(\frac{V_0}{V}\right)^{\frac{2}{3}} - 1\right]^2 \left[6 - 4\left(\frac{V_0}{V}\right)^{\frac{2}{3}}\right]\right\}$$

Figure S2. Relative Mulliken populations ($Q_{site} - \langle Q \rangle$) as determined by Extended Hückel calculations for the four crystallographic sites in the γ-brass-type structure. Graphs are plotted for (upper left) Ni parameters (4*s*: $\zeta = 1.93$, $H_{ii} = -8.86$; 4*p*: $\zeta = 1.93$, $H_{ii} = -4.90$; 3*d*: $\zeta_1 = 5.75$ ($c_1 = 0.5817$), $\zeta_2 = 2.20$ ($c_2 = 0.5800$), $H_{ii} = -12.99$); (upper right) Cu parameters (4*s*: $\zeta = 2.20$, $H_{ii} = -11.40$; 4*p*: $\zeta = 2.20$, $H_{ii} = -6.06$; 3*d*: $\zeta_1 = 5.95$ ($c_1 = 0.5933$), $\zeta_2 = 2.30$ ($c_2 = 0.5744$), $H_{ii} = -14.00$); (lower right) Zn parameters (4*s*: $\zeta = 2.01$, $H_{ii} = -12.41$; 4*p*: $\zeta = 1.70$, $H_{ii} = -6.53$); and (lower left) Ni parameters on OT sites and Cu parameters on IT, OH, and CO sites.

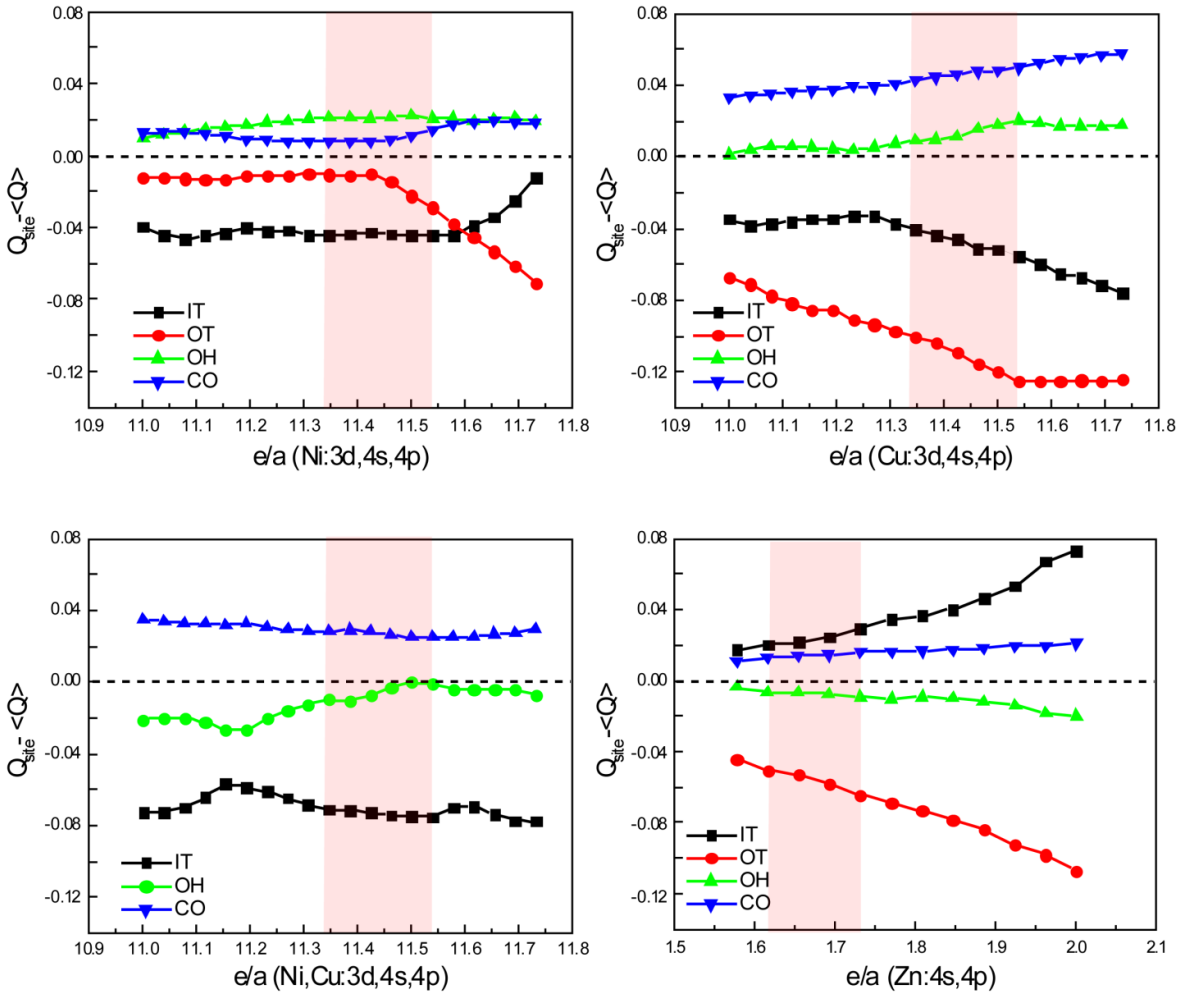

Figure S3. Electronic DOS and COHP curves, as well as band structure of "Co_2Zn_{11}" with Co atoms on the IT sites.

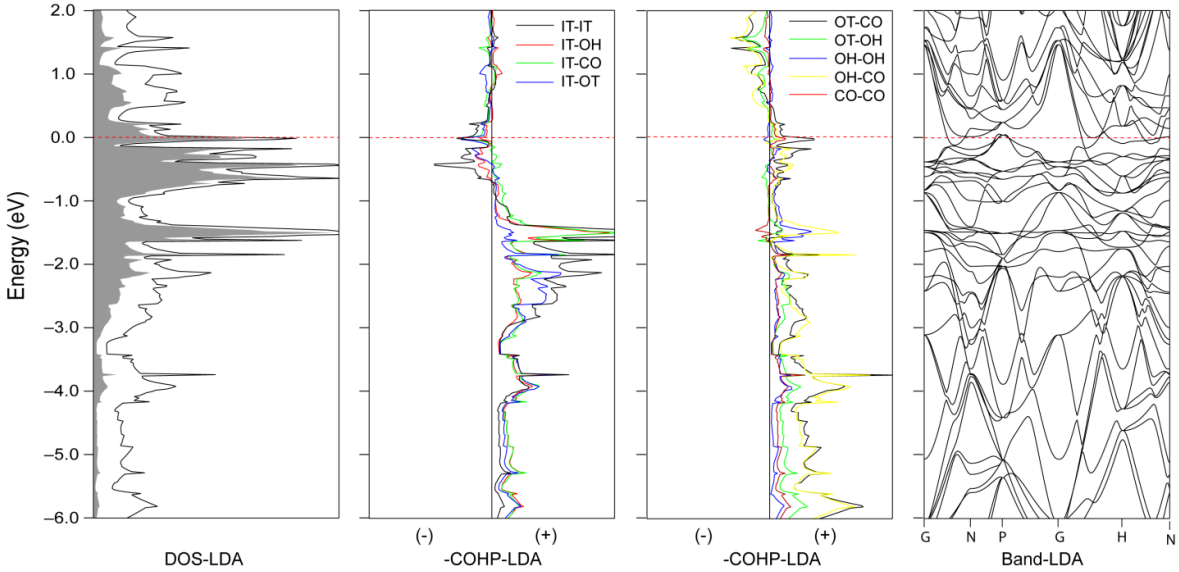

Figure S4. Vegard's law analysis for Co-Zn γ-brass structures.

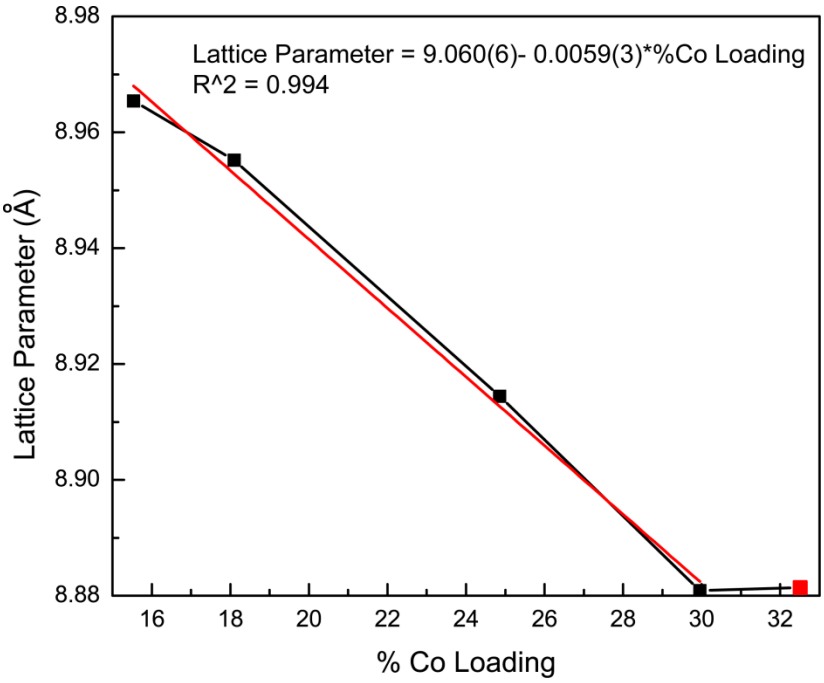

Figure S5. SEM-BES images for Co-Zn and Co-Pd-Zn samples.

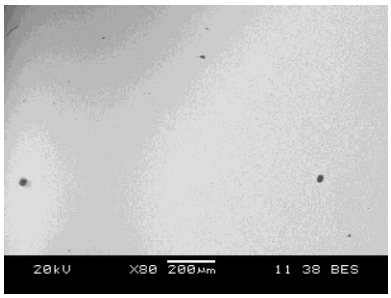

(a) $Co_{2.0(1)}Zn_{11.0(1)}$

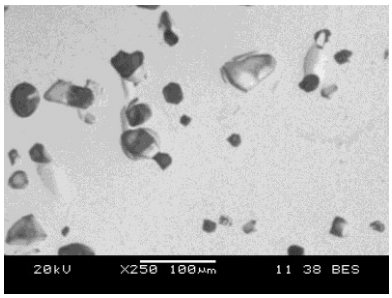

(b) $Co_{2.7(1)}Zn_{10.3(1)}$

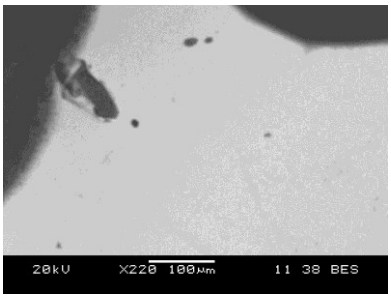

(c) $Co_{2.9(1)}Zn_{10.1(1)}$

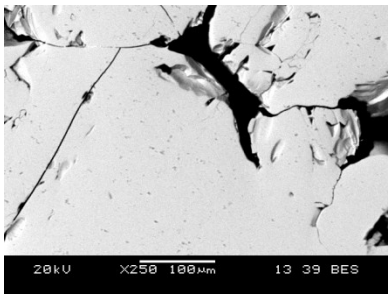

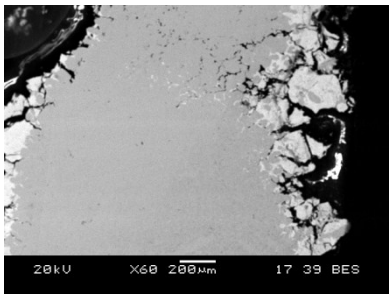

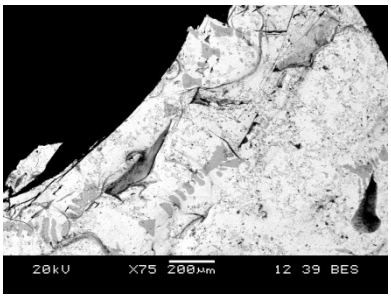

(d) $Co_{1.0(1)}Pd_{1.0(1)}Zn_{11.0(2)}$
(e) $Co_{1.0(1)}Pd_{1.0(1)}Zn_{11.0(2)}$& $Co_{0.2(1)}Pd_{3.5(2)}Zn_{6.3(1)}$
(f) $Co_{0.8(1)}Pd_{1.1(1)}Zn_{11.1(2)}$& $Co_{0.3(1)}Pd_{3.4(2)}Zn_{6.3(2)}$& $Co_{7.2(2)}Zn_{2.8(2)}$

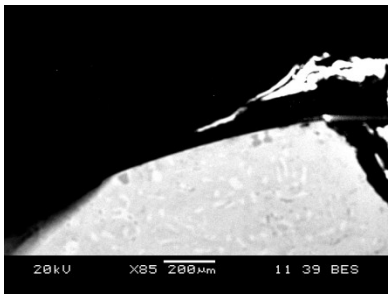

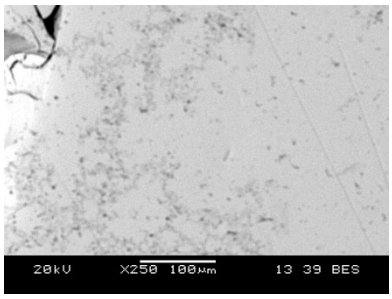

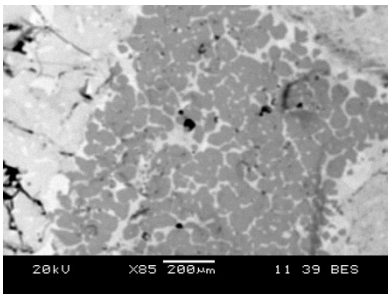

(g) $Co_{1.0(1)}Pd_{1.1(1)}Zn_{11.0(2)}$& $Co_{7.4(2)}Zn_{2.6(2)}$
(h) $Co_{2.6(3)}Pd_{2.4(3)}Zn_{8.0(3)}$
(i) $Co_{2.5(2)}Pd_{2.5(2)}Zn_{8.0(3)}$ &$Co_{0.1(1)}Pd_{3.8(2)}Zn_{6.1(2)}$ &$Co_{9.1(2)}Zn_{0.9(1)}$

Figure S6. Total energies vs. volume of models (a) and (b) for $Co_{2.5}Pd_{2.5}Zn_8$ using VASP with LSDA.

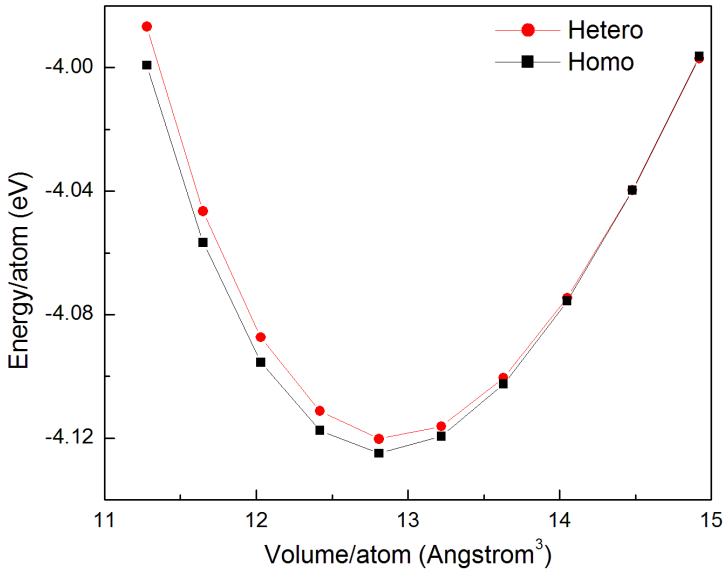

Figure S7. Magnetization hysteresis of $Co_{2.50(1)}Pd_{2.50}Zn_8$ at 2 K and 300 K measured between –70 kOe and 70kOe.

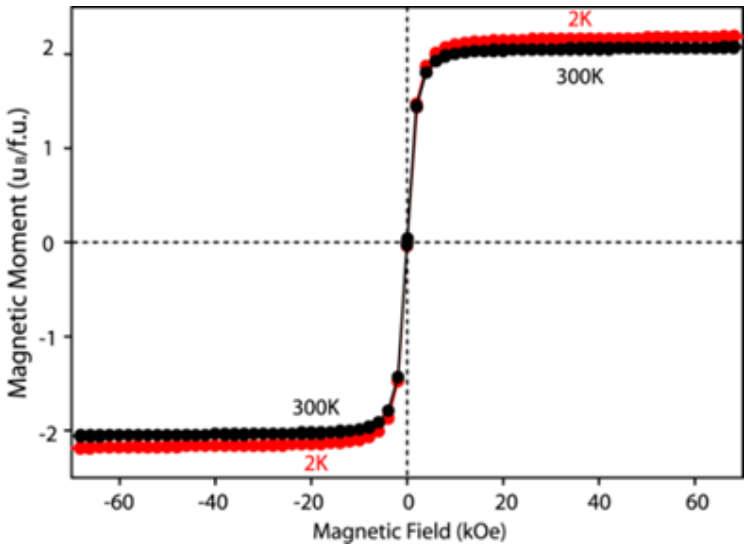

Figure S8. Temperature-dependent χ_{mol} and $1/\chi_{mol}$ for Co_2Zn_{11} and $Co_{2.66(2)}Zn_{10.29(3)}$ (loaded as 24.86 at% Co).

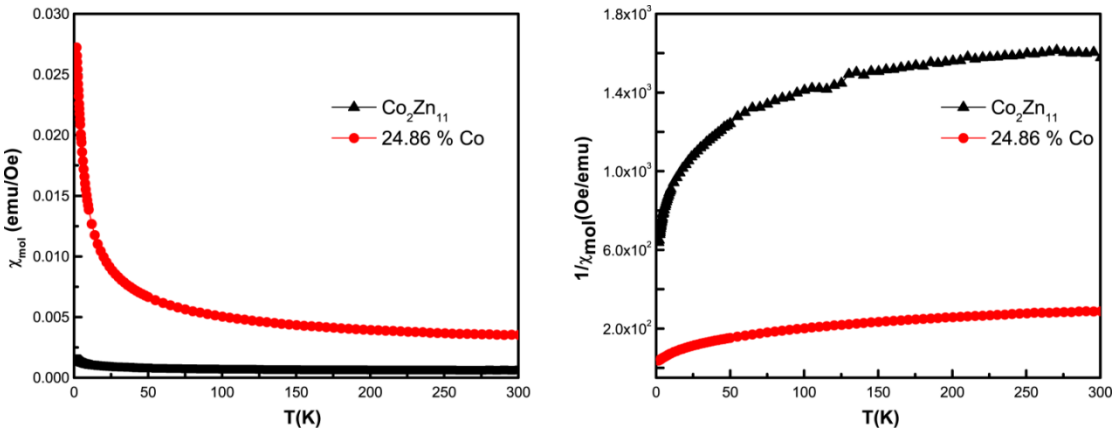

Figure S9. Temperature-dependent χ_{mol} and $1/\chi_{mol}$ for $Co_{2.50(1)}Pd_{2.50}Zn_8$ measured up to 700K.

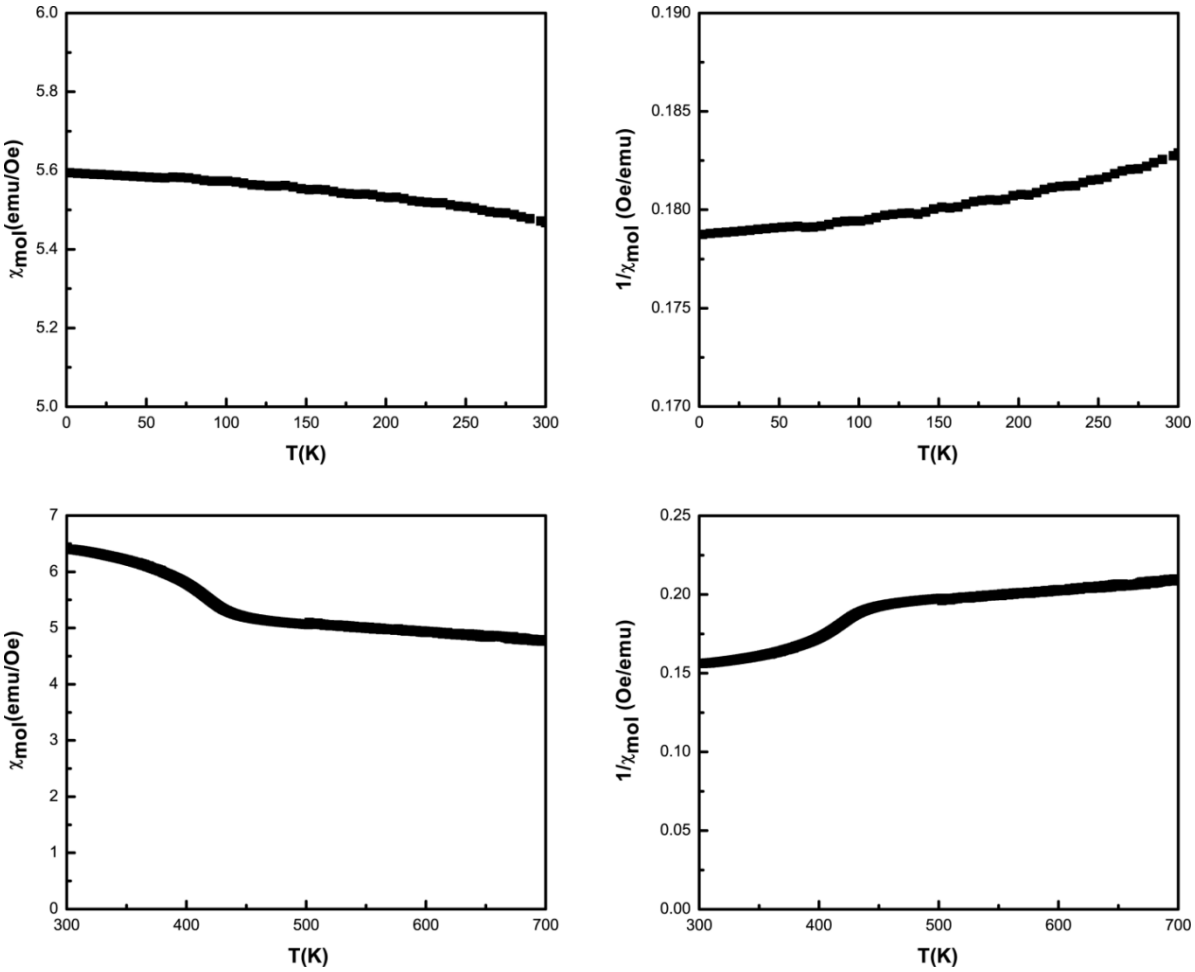

CHAPTER 5

Investigation in crystal structures and magnetic properties in γ-brass Fe-Pd-Zn system

*Weiwei Xie[1], Liu Jing[2], Vitalij Pecharsky[2], Gordon J. Miller[1]**

[1]Department of Chemistry, Iowa State University and Ames Laboratory, US-DOE, Ames, Iowa, 50011 USA
[2]Department of Material Science and Engineering, Iowa State University and Ames Laboratory, US-DOE, Ames, Iowa, 50011 USA

5.1 Abstract

A new series of γ-brass compounds in the Zn-rich Fe-Pd-Zn system are synthesized and characterized both of their structures and magnetic properties. $(Fe_{0.72(1)}Pd_{0.28})_3(Zn_{0.18(1)}Pd_{y0.82})_2Zn_8$ and $(Fe_{0.62(1)}Pd_{0.38})_3(Zn_{0.04(1)}Pd_{0.96})_2Zn_8$ are crystallized with cubic symmetry, space group $I\bar{4}3m$, with the lattice parameters 9.0775(9)Å ~ 9.0803(2)Å and 9.0973(8)Å ~ 9.1028(4)Å, respectively. $(Fe_{0.72(1)}Pd_{0.28})_3(Zn_{0.18(1)}Pd_{y0.82})_2Zn_8$ shows Fe/Pd mixing on the sites forming octahedron (Wyckoff sites 12*e*), Zn/Pd mixing on the sites forming outer tetrahedral (8*c*), and Zn atoms occupy the sites forming inner tetrahedral (8*c*) and cub-octahedron (24*g*). Upon increasing the amount of Pd, in $(Fe_{0.62(1)}Pd_{0.38})_3(Zn_{0.04(1)}Pd_{0.96})_2Zn_8$, outer tetrahedral (8*c*) is near-fully occupied by Pd atoms. The electronic structures are calculated by Tight-Binding Linear Muffin-Tin Orbital (TB-LMTO) and Extended Hückel Theory (EHT), which indicate Fe prefer 12*e* rather than other sites as valence electrons/ atom (e/a) increases. Moreover, magnetic measurements demonstrate the diluted ferromagnetic properties of $(Fe_{0.72(1)}Pd_{0.28})_3(Zn_{0.18(1)}Pd_{y0.82})_2Zn_8$ and $(Fe_{0.62(1)}Pd_{0.38})_3(Zn_{0.04(1)}Pd_{0.96})_2Zn_8$, which are in agreement with theoretical calculations very well.

5.2 Introduction

The structures of γ-brasses consist of a body-centered cubic packing of 26-atom clusters built of four concentric atomic shells: (i) an inner tetrahedron (IT); (ii) an outer tetrahedron (OT); (iii) an octahedron (OH); and (iv)a distorted cuboctahedron (CO). The site preferences in binary γ-brass compounds containing a *d* metal (V, Mn, Fe, Co, Ni, Pd) with either a divalent (Be, Zn, Cd) or trivalent (Al, In) metal can vary significantly from each other depending on composition and valence electron count.[1] For example, in $Co_{2+x}Zn_{11-x}$ and $Pd_{2.35}Zn_{10.65}$, the transition metals Co and Pd prefer to locate on the OT and OH sites. [2,3] However, in $Fe_{3.25}Zn_{9.75}$, Fe atoms occupy the IT and OT sites.[4] How changes in valence electron counts affect metal-atom site preferences in γ-brass is the main problem to be studied in this paper. Also, according to our previous work on γ-brasses in the Co-Zn system, we established a synergism between the results of electronic structure theory and targeted synthesis of new magnetic materials. The electronic structure of γ-brass Co_2Zn_{11} shows two distinct pseudogaps near the Fermi level: one at $292e^-$ and the other around $302\text{-}304e^-$ per primitive unit cell. Co_2Zn_{11} has $300e^-$ per primitive cell. Therefore, since Pd has a similar size and electronegativity to Zn but different number of valence electrons than either Co or Zn, and inspired by the pseudogaps in the electronic density of states curve of Co_2Zn_{11}, Pd-doped γ-brass compounds were designed and synthesized. [5] In these ternary Co-Pd-Zn γ-brasses, the transition metals Co and Pd atoms prefer mixing on the OT and OH sites. To investigate the generality of this site substitution pattern, the synthesis of Fe-Pd-Zn γ-brasses has been designed.

Moreover, in the new γ-brass $Co_{2.50(1)}Pd_{2.50}Zn_8$ phase, a giant magnetic moment on Co atom was induced by the Pd atoms, and the compound shows magnetization consistent with a dilute ferrimagnet. Replacing Co with Fe in the ternary γ-brass phase also suggests the possibility for interesting magnetic properties. Combining the magnetic properties and probably different site preferences in γ-brass Fe-Pd-Zn from Co-Pd-Zn system, the different site occupancy of atoms may be related with different magnetic properties. Thus, with these goals in mind, we have examined two specific targeted loadings in the Fe-Pd-Zn systemsfor their crystallographic and magnetic properties.

5.3 Experimental Section

5.3.1 Phase Analyses. The samples were examined by powder X-ray diffraction for identification and phase purity on a STOE WinXPOW powder diffractometer employing Cu radiation ($\lambda_{K\alpha}$= 1.5406 Å) for all the samples. The scattered intensity was recorded as a function of Bragg angle (2θ) using a scintillation detector with a step of 0.03° 2θ in step scan mode, ranging from 0° to 130°. Phase identifications and lattice parameters were refined by full-profile Rietveld refinement [6] using LHPM RIETICA [7] from reflection peaks between 5° and 90° in 2θ with γ-brass type compounds with random grinded samples.

5.3.2 Structure Determination. Single crystals from the samples were mounted on the tips of glass fibers. Room temperature intensity data were collected on a Bruker Smart Apex CCD diffractometer with Mo radiation ($\lambda_{K\alpha}$=0.71073 Å). Data were collected over a full sphere of reciprocal space with 0.5° scans in ω with an exposure time of 10s per frame. The 2θ range extended from 4° to 60°. [8] The SMART software was used for data acquisition. Intensities were extracted and corrected for Lorentz and polarization effects with the SAINT

program. Empirical absorption corrections were accomplished with SADABS which is based on modeling a transmission surface by spherical harmonics employing equivalent reflections with $I > 3\sigma(I)$. [9] With the SHELXTL package, the crystal structures were solved using direct methods and refined by full-matrix least-squares on F^2.[10-11] All crystal structure drawings were produced using the program *Diamond*. [12]

5.3.3 Scanning Electron Microscopy(SEM). Characterization was accomplished using a variable pressure scanning electron microscope (Hitachi S-2460N) and Energy-Dispersive Spectroscopy (EDS) (Oxford Instruments Isis X-ray analyzer). Samples were mounted in epoxy, carefully polished, and then sputter-coated with a thin layer of carbon prior to loading into the SEM chamber. The samples were examined at 20 kV. Spectra were collected for 100 seconds. An Oxford Instruments Tetra backscattered electron (BSE) detector was used to image the samples using the BSE signal. Multiple points were examined in each phase within multiple grains of a specimen. Compositional estimates were calculated using Oxford's SEM Quant software to correct intensities for matrix effects.

5.3.4 Magnetization Measurements. The magnetization measurements were performed using a superconducting quantum interference device (SQUID) magnetometer MPMS XL-7, and Vibrating Sample Magnetometer (VSM) EV11 manufactured by Quantum Design, Inc. SQUID operates over a temperature range of 5-300 K and in applied fields of up to 70 kOe. The samples were placed in glass capsules for measurement. The pieces of single-crystal from γ-brass type $Fe_2Pd_2Zn_9$ sample were manually selected and measured.

5.3.5 Electronic Structure Calculations

Tight-Binding, Linear Muffin-Tin Orbital -Atomic Spheres Approximation (TB-LMTO-ASA): Calculations of the electronic and possible magnetic structures were

performed by TB-LMTO-ASA using the Stuttgart code. [13] Exchange and correlation were treated by the local density approximation (LDA) and the local spin density approximation (LSDA). [14] In the ASA method, space is filled with overlapping Wigner-Seitz (WS) spheres. The symmetry of the potential is considered spherical inside each WS sphere and a combined correction is used to take into account of the overlapping part. The WS radii are: 1.55Å (Fe), 1.49 Å (Zn), 1.50 Å (Pd). No empty sphere is necessary in both models, and the WS sphere overlaps are limited to no larger than 16%. The basis set for the calculations included Fe (4*s*, 4*p*, 3*d*), Zn (4*s*, 4*p*, 3*d*) and Pd (5*s*, 5*p*, 4*d*) wavefunctions. The convergence criteria was set to 1×10^{-4} eV. A mesh of 54 k points in the irreducible wedge of the first Brillouin zone was used to obtain all integrated values, including the density of states (DOS) and Crystal Orbital Hamiltonian Population (COHP) curves. [15] Additionally, with LSDA, the magnetic moments of each atom can be examined by TB-LMTO.

Mulliken Populations Analysis. Calculating the relative atomic Mulliken populations with semiempirical, extended Hückel theory (EHT) is well-suited to address the site energy contribution. [16] All orbital overlaps extended over two nearest neighbor unit cells were included. Two different minimal basis sets involving Slater-type single-zeta functions for *s* and *p* orbitals and double-zeta functions for *d* were applied. The parameters for Pd are 5*s*: ζ = 2.19, H_{ii} = –8.64 eV; 5*p*: ζ = 2.15, H_{ii} = –2.68 eV, and 4*d*: ζ_1 = 5.98 (c_1 = 0.5535), ζ_2 = 2.61 (c_2 = 0.6701), H_{ii} = –12.65 eV. The parameters for Cu are 4*s*: ζ = 2.20, H_{ii} = –11.40 eV; 4*p*: ζ = 2.20, H_{ii} = –6.06 eV, and 3*d*: ζ_1 = 5.95 (c_1 = 0.5933), ζ_2 = 2.30 (c_2 = 0.5744), H_{ii} = –14.00 eV. Relative atomic Mulliken populations for each crystallographic site in a structure (‹Q› - Q_{site}) are evaluated by setting the atomic orbital parameters to be the same for every site in the crystal structure and calculating the difference between the calculated site population at

each site (Q_{site}) and the average value all of sites (‹Q›) for a range of valence electron counts. In this way, when the relative atomic Mulliken population at a site is negative, the site is attractive for electron-rich atoms; when it is positive, the site is attractive for electron-deficient atoms.

5.4 Results

5.4.1 Synthesis. Two samples loaded as "$Fe_{1.5}Pd_{1.5}Zn_{10}$" (294 e^-) and "$Fe_2Pd_2Zn_9$" (288 e^-) around the boundary of the sharp pseudogap at 292e^- in the DOS curve for Co_2Zn_{11} were reacted to synthesize our target compounds (see Table 1). Each reactant mixture, about 500 mg total, was sealed into an evacuated silica tube (< 10^{-5} Torr), heated to 1000°C for 24 hr, followed by cooling to 600°C at a rate of 1°C/min and annealed at this temperature for 3 days, after which the container was slowly cooled in the furnace. Through the microscope, γ-brass $Fe_{1.5}Pd_{1.5}Zn_{10}$ and $Fe_2Pd_2Zn_9$ crystals are rectangular with silvery luster. The samples are stable in air and moisture, but react with dilute acid at room temperature.

All high-temperature synthetic attempts to prepare $Fe_{1.5}Pd_{1.5}Zn_{10}$ and $Fe_2Pd_2Zn_9$ yielded major phases of $(Fe_{0.72(1)}Pd_{0.28})_3(Zn_{0.18(1)}Pd_{y0.82})_2Zn_8$ and $(Fe_{0.62(1)}Pd_{0.38})_3(Zn_{0.04(1)}Pd_{0.96})_2Zn_8$, respectively. Partial Zn vapored and condensed on the surface of the silica tube. Extra Fe forms alloys with Zn as minor phase according to the SEM analysis. The highest quality products, as determined by a combination of EDS, powder and single crystal X-ray diffraction, were those samples richest in $Fe_{1.5}Pd_{1.5}Zn_{10}$ and $Fe_2Pd_2Zn_9$.

Table 1. Compositions, phase analyses, lattice constants, and refined compositions for γ-brass Fe-Pd-Zn phases.

Fe/Pd Loaded (at%)	Phases (PXRD)	*a* (Å) (PXRD)	*a* (Å) (SCXRD)[a]	Composition (SCXRD)[a]	Composition (SEM-EDX)
11.62/11.59	γ-brass	9.0908(1)	9.079(1)	$Fe_{2.14(2)}Pd_{2.48(4)}Zn_{8.38(2)}$	$Fe_{1.6(1)}Pd_{1.7(1)}Zn_{9.7(4)}$
15.27/15.42	γ-brass, +	9.0940(1)	9.100(2)	$Fe_{1.84(2)}Pd_{3.08(4)}Zn_{8.08(2)}$	$Fe_{1.9(1)}Pd_{2.7(2)}Zn_{8.4(4)}$ $Fe_{7.9(3)}Zn_{2.1(2)}$

[a] 293 K; Numbers in ( )'s are standard uncertainties using at least two different measurements of similar loadings.

Refinements of site occupancies based on single crystal X-ray diffraction data, discussed in more detail in the next section, always led to a mixture of Fe/Pd and Zn/Pd on two single crystallographic sites (Wyckoff 12*e* and 8*c* sites) to eliminate non-positive definite displacement parameters at this position.

5.4.2 Structure Determination. The observed powder X-ray diffraction patterns of $(Fe_{0.72(1)}Pd_{0.28})_3(Zn_{0.18(1)}Pd_{y0.82})_2Zn_8$ and $(Fe_{0.62(1)}Pd_{0.38})_3(Zn_{0.04(1)}Pd_{0.96})_2Zn_8$ samples yielded, the refined lattice parameters of a = 9.0908(1) Å and 9.0940(1) Å, respectively, with the space group $I\bar{4}3m$. The results of single crystal diffraction on specimens extracted from the samples are listed in Tables 2 and 3. The $(Fe_{0.72(1)}Pd_{0.28})_3(Zn_{0.18(1)}Pd_{y0.82})_2Zn_8$ and $(Fe_{0.62(1)}Pd_{0.38})_3(Zn_{0.04(1)}Pd_{0.96})_2Zn_8$ structures are shown in Figure 1.

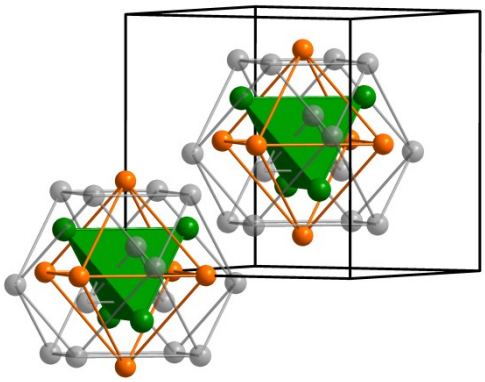

Figure 1. The structure of $(Fe_{0.72(1)}Pd_{0.28})_3(Zn_{0.18(1)}Pd_{y0.82})_2Zn_8$ and $(Fe_{0.62(1)}Pd_{0.38})_3(Zn_{0.04(1)}Pd_{0.96})_2Zn_8$ at 293K emphasizing the 26-atom γ-brass clusters located at the unit cell corner(s) and center (I.T.(Grey), O.T.(Green), O.H.(Orange) and C.O.(Grey) and (Fe/Pd-O.H., Zn/Pd-O.T., Zn-I.T. and Zn-C.O.)

Table 2. Crystallographic data for samples $Fe_{1.5}Pd_{1.5}Zn_{10}$ and $Fe_2Pd_2Zn_9$ at 293(2) K

Specimen	$Fe_{1.5}Pd_{1.5}Zn_{10}$	$Fe_2Pd_2Zn_9$
Refined Formula	$Fe_{2.13(2)}Pd_{2.51(4)}Zn_{8.36(2)}$	$Fe_{1.85(2)}Pd_{3.09(4)}Zn_{8.06(2)}$
F.W. (g/mol);	932.09	958.90
Space group; Z	$I\bar{4}3m$ (No.217); 4	$I\bar{4}3m$ (No.217); 4
	Table 2. continued	
Lattice Parameters	a= 9.0775(9) Å	a= 9.0973(8) Å

Volume (Å^3)	747.99(13)	752.90(11)
Absorption Correction	Multi-Scan	Multi-Scan
Extinction Coefficient	36.015	35.686
μ(mm^{-1})	0.0010(1)	0.0010(1)
Θ range (deg)	3.17 to 27.37	3.17 to 28.16
Completeness to Θ=max	100%	100%
hkl ranges	-12<=*h,k,l*<=12	-12<=*h,k,l*<=12
No. reflections; R_{int}	1200; 0.0370	5480; 0.0455
No. independent reflections	202	202
No. parameters	21	21
R_1; wR_2 (all *I*)	0.0183;0.0391	0.0128; 0.0317
Goodness of fit	1.119	1.104
Diffraction peak and hole (e$^-$/Å^3)	0.519; -0.433	0.355;-0.541

Table 3. Atomic coordinates and equivalent isotropic displacement parameters of $Fe_{2.13(2)}Pd_{2.51(4)}Zn_{8.36(2)}$ and $Fe_{1.85(2)}Pd_{3.09(4)}Zn_{8.06(2)}$ (U_{eq} is defined as one-third of the trace of the orthogonalized U^{ij} tensor (Å^2)).

$Fe_{2.13(2)}Pd_{2.51(4)}Zn_{8.36(2)}$

Atom	Wyck.	Occ.	*x*	*y*	*z*	U_{eq}
Zn1	8*c*(I.T.)	1	0.1080(1)	0.1080(1)	0.1080(1)	0.0131(4)
Zn/Pd2	8*c*(O.T.)	0.18(1)/0.82	0.3271(1)	0.3271(1)	0.3271(1)	0.0079(3)
Fe/Pd3	12*e*(O.H.)	0.71(1)/0.29	0.3567(1)	0	0	0.0094(4)
Zn4	24*g*(C.O.)	1	0.3104(1)	0.3104(1)	0.0398(1)	0.0139(3)

$Fe_{1.85(2)}Pd_{3.09(4)}Zn_{8.06(2)}$

Atom	Wyck.	Occ.	*x*	*y*	*z*	U_{eq}
Zn1	8*c*(I.T.)	1	0.1087(1)	0.1087(1)	0.1087(1)	0.0130(3)
Zn/Pd2	8*c*(O.T.)	0.03(1)/0.97	0.3268(1)	0.3268(1)	0.3268(1)	0.0083(2)
Fe/Pd3	12*e*(O.H.)	0.61(1)/0.39	0.3580(1)	0	0	0.0095(3)
Zn4	24*g*(C.O.)	1	0.3110(1)	0.3110(1)	0.3110(1)	0.0139(2)

5.4.3 Site Preference. The outcome of phase analysis of Fe-Pd-Zn γ-brasses and refinements from single crystal X-ray diffraction indicate that Fe and Pd mix on the OH sites, but Pd near fully occupies the OT sites at higher Pd concentrations. This site preference or "coloring" problem for two elements on different crystallographic sites is driven by optimizing the "site energy".[17] To examine this, we analyzed the Mulliken populations for the IT, OH and CO positions while fixing the OT sites with Pd atoms in the γ-brass structure using Extended Hückel theory with Cu parameters at the other three sites. The minimal basis sets for Cu included 3*d*, 4*s*, and 4*p* atomic orbitals; that for Pd used 4*d*, 5*s*, and 5*p* orbitals. The Mulliken population gave preferences to the OH sites for the Fe atoms, which have lower valence electron counts than Zn in the range of the *e*/*a* values for the Fe-Pd-Zn γ-brasses and shaded in pink in Figure 2.

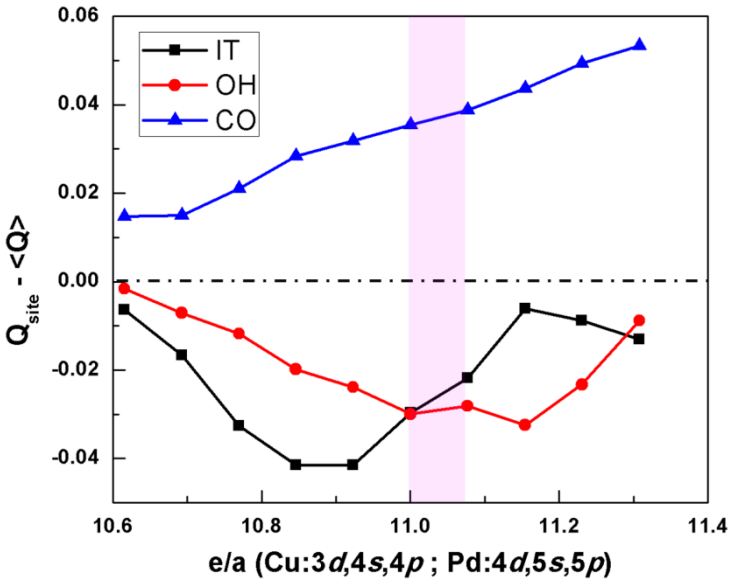

Figure 2. Relative Mulliken populations (<Q> - Qsite) for the three crystallographic sites in the γ-brass-type structure Cu as a function of valence electrons.

5.4.4 Electronic Structures of "$Fe_{1.5}Pd_{3.5}Zn_8$": TB-LMTO calculations using both LDA and LSDA were applied to the hypothetical ordered model of "$Fe_{1.5}Pd_{3.5}Zn_8$" (see Figure 3)

which took into account the observed site preferences from single crystal X-ray diffraction. Although diffraction results indicated an *I*-centered cubic unit cell, these two models utilized primitive lattices by decorating the OT and OH sites of the two 26-atom γ-brass clusters in different ways (in all clusters, Zn atoms fully occupied the IT and CO sites as seen experimentally). In the model, the two clusters are formulated as $[Zn_4Pd_4Pd_6Zn_{12}]$ and $[Zn_4Pd_4Fe_6Zn_{12}]$.

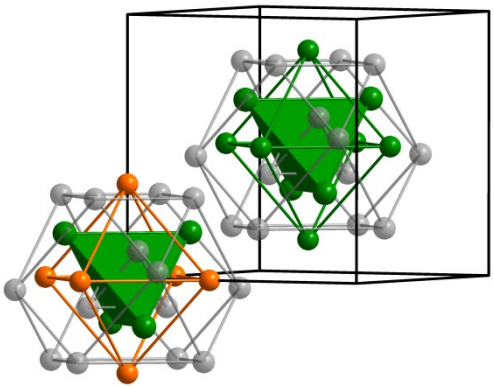

Figure 3. Hypothetical model for $Fe_{1.5}Pd_{3.5}Zn_8$ emphasizing the 26-atom γ-brass clusters in the unit cells (green: Pd atoms; orange: Fe atoms; grey: Zn atoms). See text for detailed descriptions.

The electronic structure of the hypothetical model "$Fe_{1.5}Pd_{3.5}Zn_8$" was studied computationally to understand thoroughly the electronic structure. The zinc 3*d* orbital makes a great contribution less than -6 eV and the peaks of DOS are very high and narrow. However, there is still a little contribution from palladium atoms. From -1.5eV~+1.0eV, iron orbital donates more than zinc and palladium orbital, and the peaks of DOS are broader and shorter. The sharp and high peak at Fermi level indicates the instability of electronic structure in "$Fe_{1.5}Pd_{3.5}Zn_8$". Moreover, the Fermi level lies in the -COHP curve and thereby falls in the Fe-Fe, Fe-Pd and Fe-Zn anti-bonding regions. As a result, there exists a drive towards ferromagnetism, which confirms the DOS analysis in LDA well. Thus, according to the LDA-DOS curves, "$Fe_{1.5}Pd_{3.5}Zn_8$" is susceptible toward either a possible structural distortion

by disrupting the antibonding Fe–Fe orbital interactions at the Fermi level or toward ferromagnetism by breaking the spin degeneracy. Applying spin polarization via the local spin density approximation (LSDA) splits the DOS curves for the spin-up and spin-down wavefunctions, as seen in Figure 5. The Fermi levels are shifted away from the peaks in the DOS curves, and closely approach the pseudogap in the minority spin DOS curve. The DOS also show peaks located at ca. –1.5 eV and -0.5 eV, respectively, in the majority and minority spin curves. Integration of the spin-up and spin-down DOS curves yields a total magnetic moment of 4.09 μ_B per formula unit for "$Fe_{1.5}Pd_{3.5}Zn_8$". Analysis of local moments reveals essentially no net unpaired at each Pd or Zn atom, so the result corresponds to 2.73 μ_B per Fe atom.

Table 4. Magnetic moments (μ_B) calculated for hypothetical model "$Fe_{1.5}Pd_{3.5}Zn_8$" using TB-LMTO-ASA with LSDA.

Position / Cluster	Model "$Fe_{1.5}Pd_{3.5}Zn_8$"	
	Atom	Moment (μ_B)
IT / (0, 0, 0)	Zn	–0.02
OT / (0, 0, 0)	Pd	0.11
OH / (0, 0, 0)	Fe	2.57
CO / (0, 0, 0)	Zn	0.03
Cluster:		16.14
IT / (½ , ½, ½)	Zn	–0.02
OT / (½ , ½, ½)	Pd	–0.002
OH / (½ , ½, ½)	Pd	–0.01
CO / (½ , ½, ½)	Zn	0.03
Cluster:		0.212

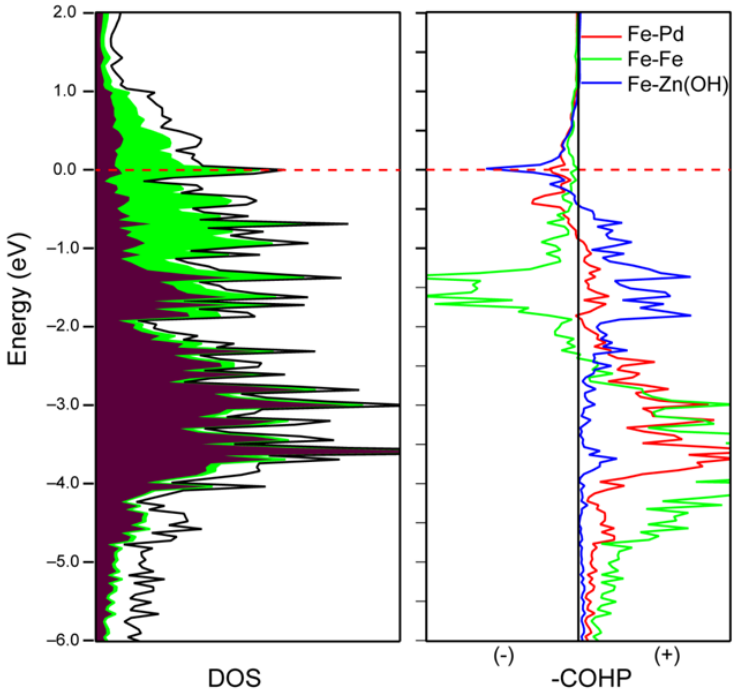

Figure 4. Partial DOS curves and –COHP curves of "$Fe_{1.5}Pd_{3.5}Zn_8$" obtained from local density approximation (LDA) without spin-polarization calculation. (+ is bonding/ − is anti-bonding, E_F indicated by the red dashed line for 286 e^-). In the DOS curves, purple shading indicates Pd contributions, green shading indicates Fe contributions.

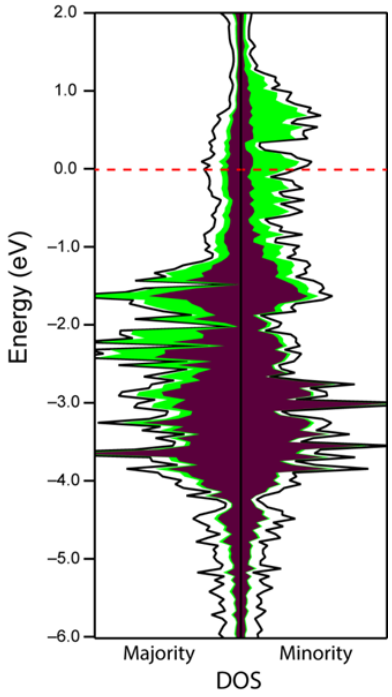

Figure 5. Spin polarized total and partial DOS curves for models of "$Fe_{1.5}Pd_{3.5}Zn_8$" (majority: spin down; minority: spin up; E_F indicated by the red dashed line for 286 e^-). (Purple shading indicates Pd contributions, green shading indicates Fe contributions.)

5.4.5 Magnetic Properties. The isothermal magnetization curves of the $Fe_{1.85(2)}Pd_{3.09(4)}Zn_{8.06(2)}$ sample measured at 5 K and 300 K indicate the sample to be ferromagnetic. Saturation is achieved at ~8.0 kOe. The saturation moments are 0.45(2) μ_B/f.u. at 5 K and 0.40(2) μ_B/f.u. at 300 K. Ferromagnetic behavior of this sample is also confirmed by temperature-dependent magnetization measured at 500 Oe (see Figure 6(Right)). According to the LDA-based DOS curves for $Fe_{1.5}Pd_{3.5}Zn_8$, evaluation of the Stoner condition using the Fe partial DOS gives $N(Fe)I(Fe) = 1.56$; $N(Fe) = 3.18$ eV^{-1}, $I(Fe) = 0.46$ eV.[18-19] Theoretically, the Stoner condition for ferromagnetism is satisfied, which is in great agreement with experimental measurements.

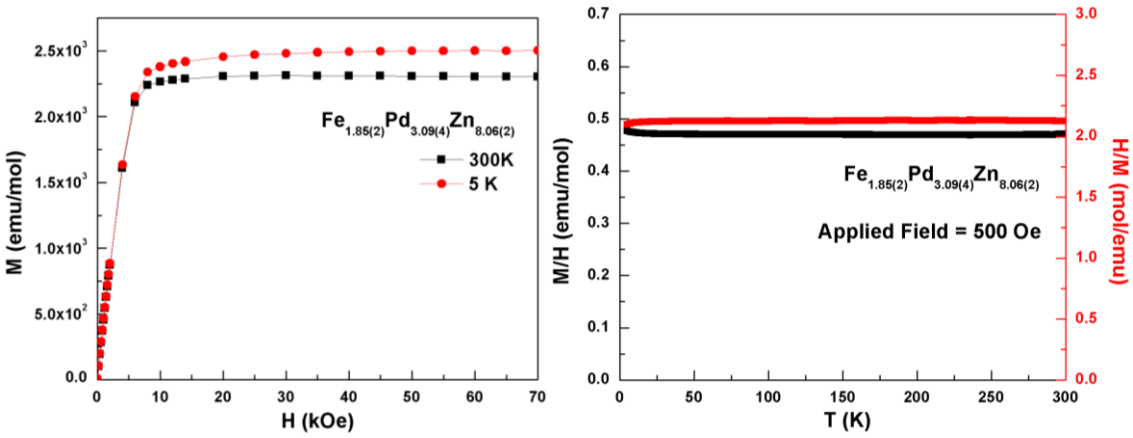

Figure 6. (Left) Magnetization vs. applied field measured at 5 K and 300 K for $Fe_{1.85(2)}Pd_{3.09(4)}Zn_{8.06(2)}$. (Right) Temperature-dependent *M*/*H* and *H*/*M* values measured from 2 K to 300 K at 500 Oe for $Fe_{1.85(2)}Pd_{3.09(4)}Zn_{8.06(2)}$.

5.5 Conclusions. A γ-brass type Fe-Pd-Zn system well crystallized and structurally analyzed was shown a clear site preference of Fe atoms for OH sites. Mulliken population analysis illustrated the "coloring" problem driven by "site energy". Furthermore, states at the Fermi level of hypothetical model "$Fe_{1.5}Pd_{3.5}Zn_8$" in DOS-LDA arise mostly from Fe 3*d* orbitals, and form spontaneous magnetic moments in the model. Magnetization measurements indicate ferromagnetic behavior, which match with theoretical prediction well.

5.6 Acknowledgement

This work was carried out at the Ames Laboratory, which is operated for the U.S. Department of Energy by Iowa State University under Contract No. DE-AC02-07CH11358. This work was supported by the U.S. Department of Energy, Office of Basic Energy Sciences, Division of Materials Sciences and Engineering. Thanks Wei Tang for magnetic measurements.

5.7 Reference

[1] Mizutani, U., *Hume-Rothery Rules for Structurally Complex Alloy Phases*, CRC Press, New York, *2010*.

[2] Xie, W.; Miller, G. J. *Chem. Mater.* **2014**, *26*, 2624.

[3] Gourdon, O.; Izaola, Z.; Elcoro, L.; Petricék, V.; Miller, G. J., *Inorg. Chem.* **2009,** *48*, 9715.

[4] Belin, C. H.; Belin, R. C. *J. Solid State Chem.* **2000**, *151*, 85.

[5] Pearson, R.G., *Inorg. Chem.* **1988**, *27*, 734.

[6] Rietveld, H. *J. Appl. Crystallogr.* **1969,** *2*, 65.

[7] Hunter, B., LHPM-Rietica, 1.7. 7. **1998**.

[8] SMART, version 5, *Bruker AXS*, Madison, WI*,* **2003**.

[9] Blessing, R. *Acta Crystallogr. A* **1995,** *51*, 33.

[10] Sheldrick, G. *SHELX*, version 5.1. *Bruker AXS,* Madison, WI, **2002**.

[11] Larson, A. *Acta Crystallogr.* **1967,** *23*, 664.

[12] Brandenburg, K., *Diamond*, version 3.2, *Crystal Impact GbR,* Bonn, Germany, **2011**.

[13] Jepsen, O.; Burkhardt, A.; Andersen, O., The Program TB-LMTO-ASA, 47, Stuttgart, Germany, **2000.**

[14] Kotani, T. *Phys. Rev. Lett.* **1995,** *74*, 2989.

[15] Dronskowski, R.; Bloechl, P. E., *J. Phys. Chem.* **1993,** *97*, 8617.

[16] Hoffmann, R., *J. Chem. Phys.* **1963**, *39*, 1397.

[17] Miller, G.J., *Eur. J. Inorg. Chem.* **1998**, 523.

[18] Seo, D.K.; Kim, S.H., *J. Comput. Chem.* **2008**, *29*, 2172.

[19] Janak, J.F. *Phys. Rev. B* **1977**, *16*, 255.

5.8 Supporting Information

Table S1. Anisotropic displacements parameters for Fe-Pd-Zn γ-brass crystal structures.

$Fe_{2.13(2)}Pd_{2.51(4)}Zn_{8.36(2)}$

Atom	U_{11}	U_{22}	U_{33}	U_{23}	U_{13}	U_{12}
Zn1	0.0131(4)	0.0131(4)	0.0131(4)	0.0029(4)	0.0029(4)	0.0029(4)
Zn/Pd2	0.0079(3)	0.0079(3)	0.0079(3)	0.0006(2)	0.0006(2)	0.0006(2)
Fe/Pd3	0.0082(6)	0.0101(4)	0.0101(4)	0.0029(5)	0	0
Zn4	0.0154(4)	0.0154(4)	0.0108(4)	–0.0034(2)	–0.0034(2)	–0.0014(4)

$Fe_{1.85(2)}Pd_{3.09(4)}Zn_{8.06(2)}$

Atom	U_{11}	U_{22}	U_{33}	U_{23}	U_{13}	U_{12}
Zn1	0.0130(3)	0.0130(3)	0.0130(3)	0.0030(3)	0.0030(3)	0.0030(3)
Zn/Pd2	0.0083(2)	0.0083(2)	0.0083(2)	0.0005(2)	0.0005(2)	0.0005(2)
Fe/Pd3	0.0081(4)	0.0102(3)	0.0102(3)	0.0032(3)	0	0
Zn4	0.0158(3)	0.0158(3)	0.0101(3)	–0.0031(2)	–0.0031(2)	–0.0026(3)

CHAPTER 6

Nanoscale Cubic Periodicity of Ordered and Disordered *d*-Metal Intermetallic Compounds Grown from a Zn-Sn Reactive Flux

*Weiwei Xie and Gordon J. Miller**

Department of Chemistry, Iowa State University and Ames Laboratory, Ames, IA, 50011, US

6.1 Abstract

Two new complex isotypic intermetallic compounds with giant cubic unit cells that were grown in high yield from a Zn-Sn flux are reported. $Cr_{22}Sn_{24}Zn_{72}$ and $V_{23.3(1)}Sn_{26.3(1)}Zn_{68.4(1)}$ crystallize in space group $Fm\bar{3}c$, Z = 8, Pearson symbol *cF*944, with unit cell parameters, respectively, a = 25.184(4) Å and 25.080(3) Å. Their structures can be described as a cubic $NaZn_{13}$-type packing of two distinct, yet condensed intermetallic clusters: (i) $Cr@(Cr_8Zn_6)(Sn)_{24}(Zn)_{60}$ or $Zn@\{(V/Sn)_8(Zn/Sn)_6\}(V/Sn)_{24}(Sn_{24}Zn_{36})$ centered at the 8*a* (¼, ¼, ¼) sites with octahedral point symmetry *O* (432), composed of a central atom encapsulated by three successive shells of, respectively, a distorted rhombic dodecahedron, snub-cube, and a rhombi-icosidodecahedron; and (ii) a Mackay cluster $Cr@(Zn)_{12}(Zn)_{30}(Zn)_{12}$ or $(V/Sn)@(Zn)_{12}(Zn)_{30}(Zn)_{12}$, centered at the 8*b* (0,0,0) sites with tetrahedral point symmetry T_h ($m\bar{3}$), composed of a central Cr or V/Sn site surrounded by three successive shells of an icosahedron, an icosidodecahedron, and a larger icosahedron. The radius ratio between the two types of clusters around the 8*a* and 8*b* sites is 0.74. An alternative description, which is similar but eliminates condensation between the two structural moieties, involves a simple cubic packing of I13 clusters condensed via extreme Zn sites with rhombic dodecahedra Cr@Cr8Zn6 or $Zn@\{(V/Sn)_8(Zn/Sn)_6\}$ in the voids. These results indicate that complex intermetallic compounds with nanometer-sized periodicities can

be synthesized by flux growth to yield homogeneous, ordered nanocrystals (NCs) or partially disordered NCs.

6.2 Introduction

Intermetallic crystals with nanoscale periodicities are of interest because quantum size effects and the large number of surface atoms can influence their chemical, electronic, magnetic, and optical behavior.[1-2] But the growth and identification of such crystals are infrequently reported because the characterization of such intermetallic compounds is tremendously challenging and, often insufficient data are collected to account for all positions in the asymmetric unit of the crystallographic cell. According to the literature, Zn-, Al-, Cd- and Mg-rich intermetallic compounds are the most common systems that form giant unit cells encompassing hundreds to thousands of atoms, like Mg_2Al_3, which has a lattice parameter of 2.824 nm with 1832 possible atomic positions per unit cell.[3] According to advances in the last 20-25 years, such compounds belong to a broader class of periodic and quasiperiodic complex metallic alloys (CMAs).

CMAs encompass different kinds of structurally complex materials sharing a basic property, which is that these alloys exhibit a well-defined, long-range order of atoms. Over shorter length scales, it is possible to identify aggregates of atoms, “clusters”, which can be condensed or overlapping.[4] Moreover, CMAs exhibit several attractive properties for engineering applications, such as high strength-to-weight ratio, good oxidation resistance, high-temperature strength and thermoelectric properties because of the disordered crystal structures.[5-6] For instance, $Ru_{13}Sb_{6.29}Zn_{91.56}$, which has been reported with a cubic lattice parameter exceeding 2 nm and partially disordered crystallographic sites, is a potentially good thermoelectric material.[7] As the number of identified and characterized CMAs grows,

chemists and materials scientists can begin to assess structural chemical principles that can lead to new systems with useful properties. In the electronic structures of small-scale models of CMAs, a signature of stability for a given chemical composition is the occurrence of a pseudogap in the density of states (DOS) curves at the Fermi level. Analysis of inter-orbital bonding typically shows that this pseudogap separates metal-metal bonding states below from metal-metal antibonding states above the Fermi level, but there can be other reasons, such as relative electronegativities of the atomic constituents or, from the perspective of the nearly free-electron gas, Fermi surface–Brillouin zone (FsBz) interactions are important mechanisms to form pseudogaps in the DOS curves. [8-9]

One useful synthetic tool is the use of a eutectic mixture of elements as a flux medium for growing crystals of intermetallic compounds. In particular, a mixture of Zn and Sn has been reported to facilitate the synthesis of two giant-unit-cell ternary compounds, $Mo_7Sn_{12}Zn_{40}$[10] and $Ru_4Sn_{2.88}Zn_{11.73}$[11]. In the report, we extend this mixture's effectiveness to produce new CMAs by the discovery and characterization of two new cubic phases with nanoscale periodicities, $Cr_{22}Sn_{24}Zn_{72}$ and $V_{23.3(1)}Sn_{26.3(1)}Zn_{68.4(1)}$.

6.3 Synthesis and Structural Characterization

6.3.1 Synthesis. Crystalline specimens of the title compounds are best obtained from mixtures, ~3g total, of Cr or V (99.9%, Ames Lab), Sn pieces (99.99%, Ames Lab), and Zn particles (99.99%, Ames Lab) with a molar ratio of Cr/V:Sn:Zn = 1:3:3 in atomic weight and loaded into alumina crucibles that was, in turn, sealed in evacuated (pressure < 10^{-5} torr) silica jackets to avoid air oxidation. The samples were heated to 800°C for 24 hrs, followed by cooling to 600°C at a rate of 1.0°C/min, and finally spun at 600°C at a speed of 3000 rps

for 15 sec. The mass of crystalline products ranged from 0.1-0.2g and the products are identified as cubic crystals under an optical microscope.

The first products were obtained by seeking to replicate "$Mo_7Sn_{12}Zn_{40}$" [10] using Cr rather than Mo. So, a mixture, 0.5g total, of Cr, Sn, and Zn in the molar ratio 1:2:6 was sealed in an evacuated silica jacket, heated to 850°C for 24 hrs, followed by slow cooling to 200°C at a rate of 0.02°C/min. Although cubic crystals with a total mass of 0.02-0.05g could be obtained using optical microscopy, much of the product was too ductile for powder X-ray diffraction analysis. Other attempts that involved different annealing temperatures, cooling rates, and Cr:Sn:Zn molar ratios ultimately led to the prescription described above. These alternative synthetic attempts are summarized in Supporting Information. Furthermore, once this optimal procedure was identified for the Cr-Sn-Zn system, it was applied to the V-Sn-Zn system as well without further synthetic explorations.

6.3.2 Phase Analyses. The samples were examined by powder X-ray diffraction for identification and phase purity on a STOE WinXPOW powder diffractometer employing Cu Kα radiation ($\lambda = 1.5406$ Å) for all samples. The scattered intensities were recorded as a function of Bragg angle (2θ) using a scintillation detector with 0.03° steps in 2θ using the step scan mode from 0° to 130°. Phase identifications were accomplished with the aid of calculations from PowderCell using samples obtained by grinding several cubic crystals, and lattice parameters were refined by full-profile Rietveld refinement[12] using LHPM RIETICA[13] from reflection peaks between 10° and 90° in 2θ.

6.3.3 High-Resolution Transmission Electron Microscopy (HRTEM). HRTEM images were collected and energy dispersive X-ray spectroscopy (EDS) analyses were conducted using a JEOL JEM 2100F FEGTEM (200 keV) with a Gatan UltraScan 1000 (2048×2048)

CCD camera. Samples for TEM analysis were prepared by dropping an ethanol solution containing the samples onto the surface of a carbon-coated copper grid.

6.3.4 Structure Determination. Single crystals from the samples were mounted on the tips of glass fibers. Room temperature intensity data were collected on a Bruker Smart Apex CCD diffractometer with Mo Kα radiation (λ = 0.71073 Å). Data were collected over a full sphere of reciprocal space by taking three sets of 606 frames with 0.3° scans in ω with an exposure time of 20s per frame. The 2θ range extended from 3° to 60°. The SMART software was used for data acquisition. Intensities were extracted and corrected for Lorentz and polarization effects with the SAINT program.[14] Empirical absorption corrections were accomplished with SADABS, which is based on modeling a transmission surface by spherical harmonics employing equivalent reflections with $I > 3\sigma(I)$.[15] With the SHELXTL package, the crystal structures were solved using direct methods and refined by full-matrix least-squares on F^2.[16] All crystal structure drawings were produced using the program *Diamond*.[17]

6.4 Results and Discussion

Our synthetic exploration of Cr or V dissolved in Zn-Sn fluxes yielded two new phases which crystallized in large cubic unit cells with compositions refined from single crystal X-ray diffraction to be $Cr_{22}Sn_{24}Zn_{72}$ and $V_{21.7(1)}Sn_{26.9(1)}Zn_{69.4(1)}$. Their crystal structures, which are discussed in a subsequent subsection, are closely related to $Mo_7Sn_{12}Zn_{40}$[10] and Ru-Zn-Sb phases[11]. These products formed brittle, cubic-shaped crystals that are stable upon exposure to air and moisture, but react with dilute aqueous acid at room temperature. Although crystals could be obtained by nearly stoichiometric mixtures of the corresponding

elements, there was always some additional ductile alloy which could not be easily ground for X-ray powder diffraction analysis.

To date, the Zn-Sn phase diagram has not been fully characterized, but a calculated diagram, which covers temperatures up to 1500°C is available.[18] In this diagram, there are no binary compounds, but a eutectic point occurs at 198.5°C at 14.9 atomic percent Zn.[19] According to our synthetic attempts, Sn-rich flux mixtures yielded only ductile products, with no evidence for the cubic crystals. These structures emerged when the Zn:*T* molar ratio (*T* = V or Cr) exceeded 2:1 and for at least a equimolar mixture of *T* and Sn.

6.4.1 Phase Analyses. Once cubic crystals were extracted from the reaction mixtures, phase analysis was conducted by X-ray powder diffraction and electron microscopy. Results are summarized in Table 1. According to X-ray powder diffraction, these crystalline samples were single phase and their patterns could be successfully indexed and refined using the atomic positions obtained from single crystal diffraction experiments. For the X-ray powder diffraction patterns, the scale factors, lattice parameters, atomic positions, and site occupancies were refined, whereas the displacement parameters of all atoms were assumed to be isotropic (see Tables S2 and S3 in Supporting Information). The resulting profile residuals *Rp* varied between ~4.59 and ~7.18 with weighted profile residuals *Rwp* between ~5.08 and ~7.43. The cubic lattice parameter for the Cr-Sn-Zn compound is systematically larger, regardless of measurement, than the corresponding parameter for the V-Sn-Zn compound, and these values are somewhat smaller than 25.447(1) Å for $Mo_7Sn_{12}Zn_{40}$[10] (single crystal X-ray diffraction) but are slightly larger than those reported for Ru-Zn-Sb phases[11] (24.340(6)-25.133(9); powder X-ray diffraction).

Table 1. Loaded compositions, yields, lattice constants, and refined compositions obtained from cubic crystals obtained from Cr-Sn-Zn and V-Sn-Zn flux syntheses. PXRD = powder X-ray diffraction; SCXRD = single crystal X-ray diffraction; HRTEM = high resolution transmission electron microscopy; EDX = energy dispersive X-ray spectroscopy.

Loaded Composition	"$CrSn_3Zn_3$"	"VSn_3Zn_3"
Yield	Cubic crystals: 0.1-0.2g Flux: 2.8-2.9g	Cubic crystals: 0.1-0.2g Flux: 2.8-2.9g
a (Å) (PXRD)	25.256(3)	25.032(3)
a (Å) (SCXRD)	25.184(4)	25.080(3)
a (Å) (HRTEM)	24.90(1)	23.92(1)
Composition (PXRD)	$Cr_{22}Sn_{24}Zn_{72.0(1)}$	$V_{23.3(1)}Sn_{26.1(1)}Zn_{68.6(1)}$
Composition (SCXRD)	$Cr_{22}Sn_{24}Zn_{72}$	$V_{23.3(1)}Sn_{26.3(1)}Zn_{68.4(1)}$
Composition (EDX)	$Cr_{20.8(4)}Sn_{28.7(4)}Zn_{68.7(6)}$	$V_{19(1)}Sn_{23(1)}Zn_{76(2)}$

Samples for TEM investigations were dispersed in ethanol. After complete evaporation of the ethanol, TEM tilting experiments were also employed to examine [001] projections of $Cr_{22}Sn_{24}Zn_{72}$ and $V_{23.3(1)}Sn_{26.3(1)}Zn_{68.4(1)}$ (see Figures 1*a*, 1*b*) to study the purity of these crystalline specimens. The TEM dark-field (DF) images of the crystalline [001] axes (see Figure SX in Supporting Information) of each specimen determined the *d*-spacings d_{002} for $Cr_{22}Sn_{24}Zn_{72}$ (12.46 Å) and $V_{23.3(1)}Sn_{26.3(1)}Zn_{68.4(1)}$ (11.96 Å), and, thus, the corresponding lattice parameters, 24.92 Å and 23.92 Å. In the Fast Fourier Transform (FFT) filtered images (see Figures 1*c*, 1*d*), the square grid identifies a simple cubic-like arrangement of clusters with diameters of approximately the d_{002} spacing in each sample, i.e., ~12.5 Å for $Cr_{22}Sn_{24}Zn_{72}$ and 12.0 Å for $V_{23.3(1)}Sn_{26.3(1)}Zn_{68.4(1)}$. In these images, the light regions would correspond to Sn-rich areas, whereas dark regions would correspond to Cr/Zn-rich areas at the surfaces. At least in the surface regions where TEM investigations were surveyed, there exists some variation in local compositions, although the pattern of Sn-rich and Cr/Zn-rich areas remains essentially periodic.

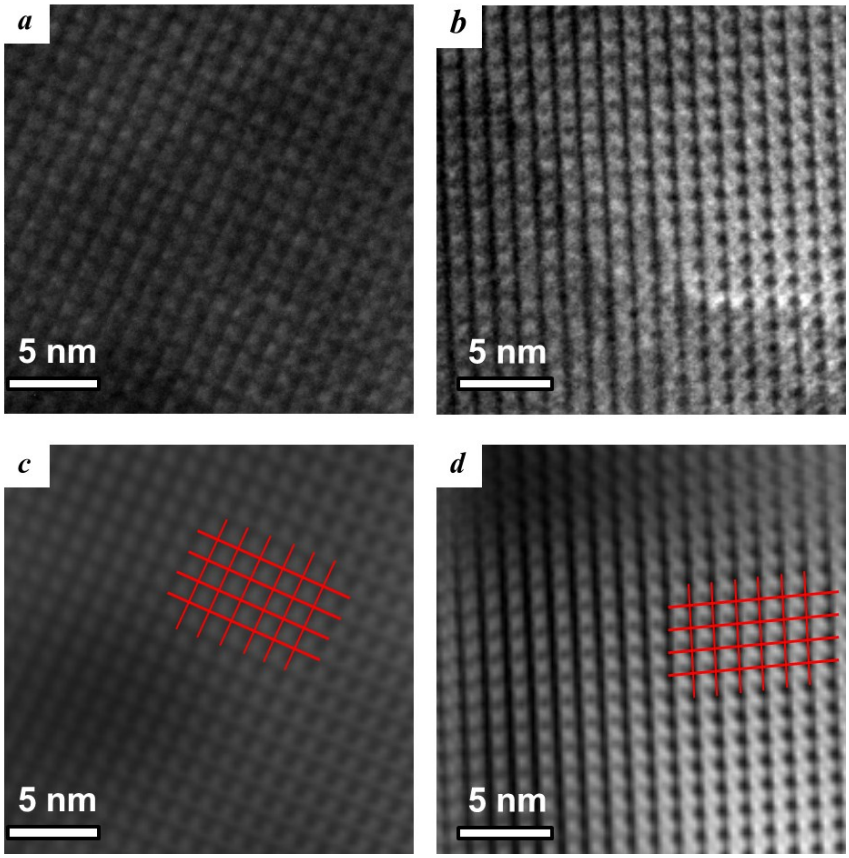

Figure 1. [001] Projections of (*a*) $Cr_{22}Sn_{24}Zn_{72}$ and (*b*) $V_{23.3(1)}Sn_{26.3(1)}Zn_{68.4(1)}$ obtained by HRTEM tilting experiments. Fast Fourier Transform (FFT) filtered images of (*c*) $Cr_{22}Sn_{24}Zn_{72}$ and (*d*) $V_{23.3(1)}Sn_{26.3(1)}Zn_{68.4(1)}$. The square grids outlined in red emphasize the regular array of clusters, which are further examined by SCXRD.

6.4.2 Crystal Structures. To obtain further insights into the structural features of these complex intermetallic compounds, single crystals were extracted from each sample and studied by X-ray diffraction. The results of these single crystal X-ray diffraction investigations are summarized in Table 2 with the atomic positions, site occupancies, and isotropic thermal displacements listed in Table 3. The corresponding anisotropic displacement parameters and significant interatomic distances are available via their CIF-files, which are part of the Supporting Information. In both cases, although the molar ratios of loadings were (V or Cr):Sn:Zn = 1: 3: 3, the refined compositions were closer to 1: 1: 3, i.e., $Cr_{22}Sn_{24}Zn_{72}$ (1: 1.09: 3.27) and $V_{23.3(1)}Sn_{26.3(1)}Zn_{68.4(1)}$ (1: 1.12(1): 2.92(1)).

Furthermore, the atomic positions and corresponding site occupancies indicated that the distributions of elements in the two structures have some subtle differences.

Table 2. Selected crystallographic data for Cr-Sn-Zn and V-Sn-Zn cubic phases at 293(2) K.

Specimen (Loaded)	"$Cr_1Sn_3Zn_3$"	"$V_1Sn_3Zn_3$"
Refined Formula	$Cr_{22}Sn_{24}Zn_{72}$	$V_{23.3(1)}Sn_{26.3(1)}Zn_{68.4(1)}$
F.W. (g/mol); *F*(000)	8699.20; 31104	8776.94; 31214
Space group; *Z*	*Fm*–3*c* (No. 226); 8	F m -3 c(No. 226); 8
Lattice Parameter (Å)	*a* = 25.184(4)	a= 25.080(3)
Volume ($Å^3$)	15972(4)	15775(3)
d_{calc} (Mg/m^3)	7.235	7.391
Absorption Correction	Multi-scan	Multi-scan
μ(mm^{-1})	31.320	31.065
θ range (°)	1.62-28.33	1.62 to 27.58
hkl ranges	–33 ≤ *h*, *k*, *l* ≤ 33	-32<=h,k,l<=32
No. independent reflections; R_{int}	896; 0.0817	831; 0.0772
No. parameters	60	60
R_1; wR_2 (all *I*)	0.0406; 0.0699	0.0365;0.0690
Goodness of fit	1.094	1.316
Diffraction peak and hole ($e^-/Å^3$)	2.938;–2.464	1.183;-1.019

Table 3. Atomic coordinates, site occupancies, and equivalent isotropic displacement parameters of Cr-Sn-Zn and V-Sn-Zn phases examined at 293(2) K. U_{eq} is defined as one-third of the trace of the orthogonalized U_{ij} tensor ($Å^2$).

$Cr_{22}Sn_{24}Zn_{72}$

	Atom	Wyckoff Site	Occupancy	*x*	*y*	*z*	U_{eq}
*"I*13*"*-Cluster	Cr1	8*b*	1	0	0	0	0.005(1)
	Cr2	96*i*	1	0	0.1103(1)	0.1756(1)	0.007(1)
	Zn3	48*e*	1	0.1778(1)	0	0	0.009(1)
	Zn4	96*i*	1	0	0.0547(1)	0.0869(1)	0.007(1)
	Zn5	96*i*	1	0	0.2189(1)	0.1483(1)	0.012(1)
	Zn6	96*h*	1	¼	0.0563(1)	0.0563(1)	0.009(1)
	Zn7	192*j*	1	0.0571(1)	0.1463(1)	0.0901(1)	0.010(1)
	Sn8	192*j*	1	0.0960(1)	0.1630(1)	0.2054(1)	0.017(1)

Table 3. continued

"bcc"-Cluster	Cr9	8*a*	1	¼	¼	¼	0.005(1)
	Cr10	64*g*	1	0.1904(1)	0.1904(1)	0.1904(1)	0.047(1)
	Zn11	192*j*	¼	0.1538(2)	0.2677(3)	0.2677(3)	0.068(5)

$V_{23.3(1)}Sn_{26.3(1)}Zn_{68.4(1)}$

	Atom	Wyckoff Site	Occupancy	*x*	*y*	*z*	U_{eq}
*"I*13*"*-Cluster	V1	8*b*	1	0	0	0	0.001(1)
	V/Sn2	96*i*	0.72(1)/0.28	0	0.1150(1)	0.1783(1)	0.001(1)
	Zn3	48*e*	1	0.1815(1)	0	0	0.008(1)
	Zn4	96*i*	1	0	0.0557(1)	0.0879(1)	0.004(1)
	Sn5	96*i*	1	0	0.2222(1)	0.1577(1)	0.009(1)
	V/Sn6	96*h*	0.66(1)/0.34	¼	0.0607(1)	0.0607(1)	0.009(1)
	Zn7	192*j*	1	0.0586(1)	0.1466(1)	0.0891(1)	0.007(1)
	Zn8	192*j*	1	0.0953(1)	0.1561(1)	0.1954(1)	0.020(1)
"bcc"-Cluster	V/Sn9	8*a*	0.75(3)/0.25	¼	¼	¼	0.006(2)
	V/Sn10	64*g*	0.62(1)/0.38	0.1910(1)	0.1910(1)	0.1910(1)	0.025(1)
	Zn/Sn11	48*f*	0.40(1)/0.60	0.1165(1)	¼	¼	0.014(1)

Both structures crystallize in the face-centered cubic space group $Fm\bar{3}c$ (No. 226) with 944 atoms per unit cell distributed among 11 crystallographic sites in the asymmetric unit. In $Cr_{22}Sn_{24}Zn_{72}$, there are no mixed occupancies, but the site labeled Zn11 (192*j*) could be maximally occupied by 25% from distance restrictions. In fact, allowing the occupancy to refine yielded 27.1(4)% occupancy by Zn, so the occupancy was set to 25% for further refinement steps (see the electron density distribution in a Fourier map in Figure S2). In $V_{23.3(1)}Sn_{26.3(1)}Zn_{68.4(1)}$, however, five crystallographic sites refined with mixed occupancies, four of which involved V and Sn mixing, while one site, Zn/Sn11 (48*f*) refined using Zn and Sn atoms. Furthermore, this site corresponds to the four-fold split Zn11 (192*j*) site that is 25% occupied by Zn atoms in $Cr_{22}Sn_{24}Zn_{72}$.

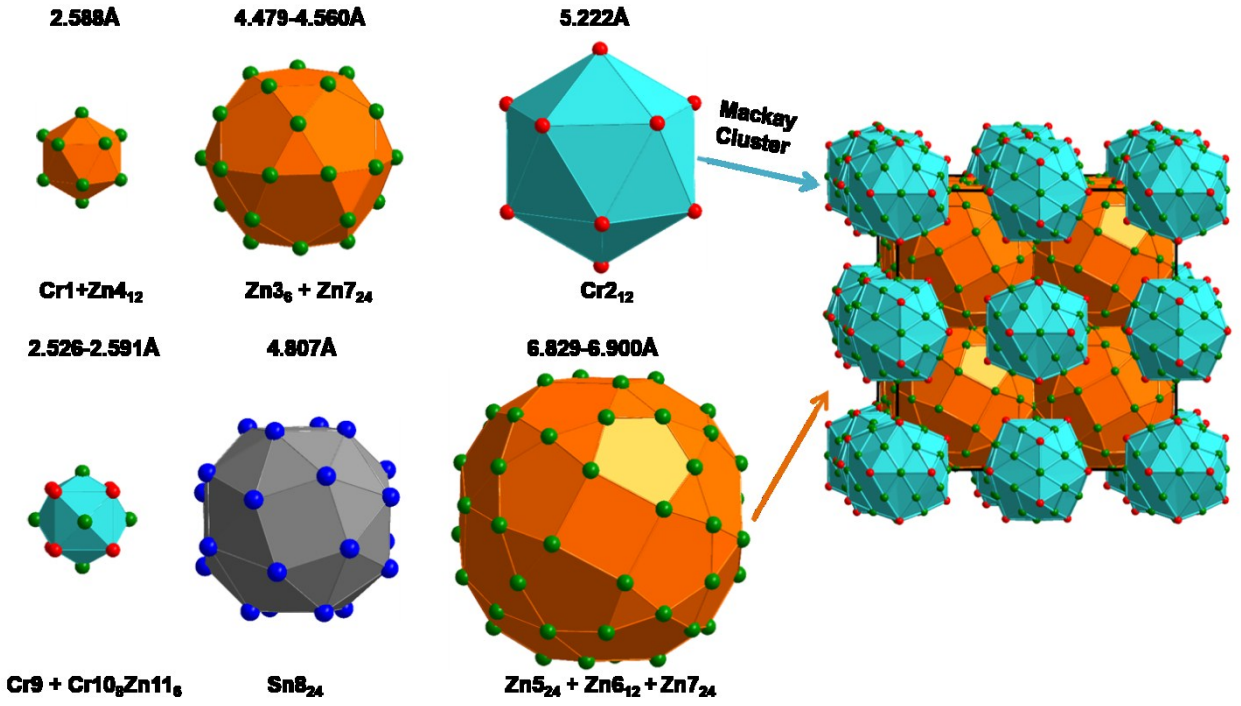
2.588Å
4.479-4.560Å
5.222Å
Mackay Cluster
Cr1+Zn4$_{12}$
Zn3$_6$ + Zn7$_{24}$
Cr2$_{12}$
2.526-2.591Å
4.807Å
6.829-6.900Å
Cr9 + Cr10$_9$Zn11$_6$
Sn8$_{24}$
Zn5$_{24}$ + Zn6$_{12}$ + Zn7$_{24}$

(*a*)

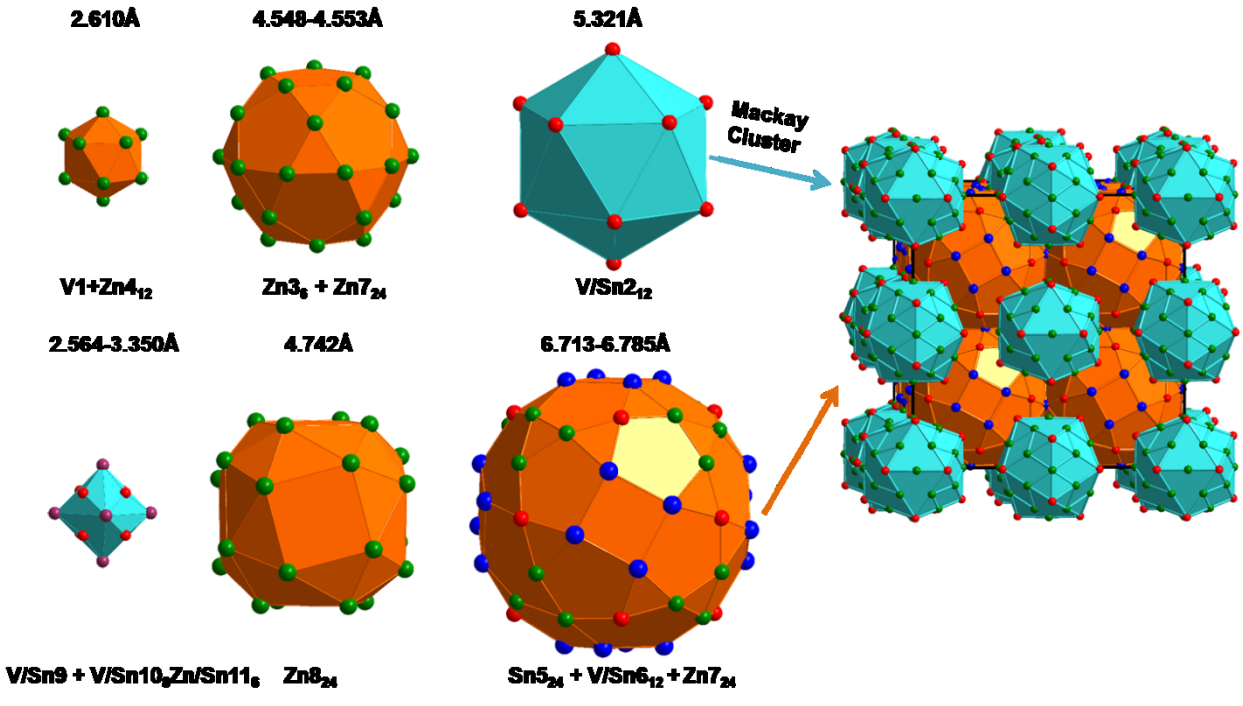
2.610Å
4.548-4.553Å
5.321Å
Mackay Cluster
V1+Zn4$_{12}$
Zn3$_6$ + Zn7$_{24}$
V/Sn2$_{12}$
2.564-3.350Å
4.742Å
6.713-6.785Å
V/Sn9 + V/Sn10$_9$Zn/Sn11$_6$
Zn8$_{24}$
Sn5$_{24}$ + V/Sn6$_{12}$ + Zn7$_{24}$

(*b*)

Figure 2. Crystal structures constructed by a body-centered cubic type packing of large atomic clusters in (*a*) $Cr_{22}Sn_{24}Zn_{72}$ (red: Cr; green: Zn; blue: Sn) and (*b*) $V_{23.3(1)}Sn_{26.3(1)}Zn_{68.4(1)}$ (red: V; pink V/Sn; green: Zn; blue: Sn; purple: Zn/Sn).

The structures of these two compounds can be described by two complementary yet related perspectives that each provides some important insights about this small class of complex intermetallic compounds. The first perspective is illustrated in Figure 2, which emphasizes their relationship with $NaZn_{13}$-type structures by identifying a body-centered cubic packing of two distinct intermetallic clusters which are condensed along {111} directions. These two clusters are (1) an icosahedral-like 55-atom Mackay cluster centered at the 8*b* (0, 0, 0) sites, point symmetry T_h ($m\ \bar{3}$), $Cr@(Zn)_{12}(Zn)_{30}(Cr)_{12}$ and $V@(Zn)_{12}(Zn)_{30}(V_{0.72(1)}Sn_{0.28})_{12}$; and (2) an octahedrally symmetric 99-atom cluster centered at the 8*a* (¼, ¼, ¼) sites, point symmetry *O* (432), $Cr@(Cr)_8(Zn)_6(Sn)_{24}(Zn)_{60}$ and $(V_{0.75(3)}Sn_{0.25})@(V_{0.62(1)}Sn_{0.38})_8(Zn_{0.40(1)}Sn_{0.60})_6(Zn)_{24}$-$(V_{0.13(1)}Sn_{0.47}Zn_{0.40})_{60}$. The 55-atom Mackay clusters consist of a single atom surrounded by three successive shells of an icosahedron, an icosidodecahedron, and a second icosahedron that caps every pentagonal face of the icosidodecahedron. The other 99-atom octahedrally symmetric cluster contains a rhombic dodecahedron, which is distorted in $Cr_{22}Sn_{24}Zn_{72}$, that successively encapsulated by a snub cube and a rhombi-icosidodecahedron. In $NaZn_{13}$, $Zn@(Zn)_{12}$ icosahedra are centered at the 8*b* (0, 0, 0) sites, and Na atoms are located at the 8*a* (¼, ¼, ¼) sites, surrounded by a snub cube of 24 Zn atoms. The radius ratios of the two different clusters in the two compounds are approximately 0.76, which is in line with expectations of filling voids of a simple cubic packing of spheres. In this case, there is a simple cubic packing of 99-atom octahedrally symmetric rhombi-icosidodecahedra with the voids filled by icosahedrally symmetric Mackay clusters.

The second perspective again divides these structures into two fragments, shown in Figure 3, but now emphasizes their construction by condensing icosahedrally symmetric *I*13-type clusters along {100} directions, and placing rhombic dodecahedra, which are small fragments of body-centered cubic packing, into the large octahedrally symmetric voids. The *I*13 cluster, which contains 127 atoms consists of 12 metal-centered icosahedra vertex-connected to a central icosahedron that is also metal-centered. In $Cr_{22}Sn_{24}Zn_{72}$, the *I*13 cluster is formulated as $[Cr@(Zn_{12/2})][Cr@(Zn_{6/2}Zn_4Sn_2]_{12}$, but these are condensed via 48 terminal Zn atoms, 8 each along the six {100} directions to give the final structural formula as $[Cr@(Zn_{12/2})][Cr@(Zn_{6/2}\ Zn_{4/2}Sn_2]_{12}$. As revealed by the structural formula and Figure 3, the sites occupied by Sn atoms belong to a single *I*13 cluster. Moreover, these Sn atoms form a 24-atom snub cube that encapsulates the rhombic dodecahedra, which are formulated as $Cr@(Cr_8)(Zn_6)$.

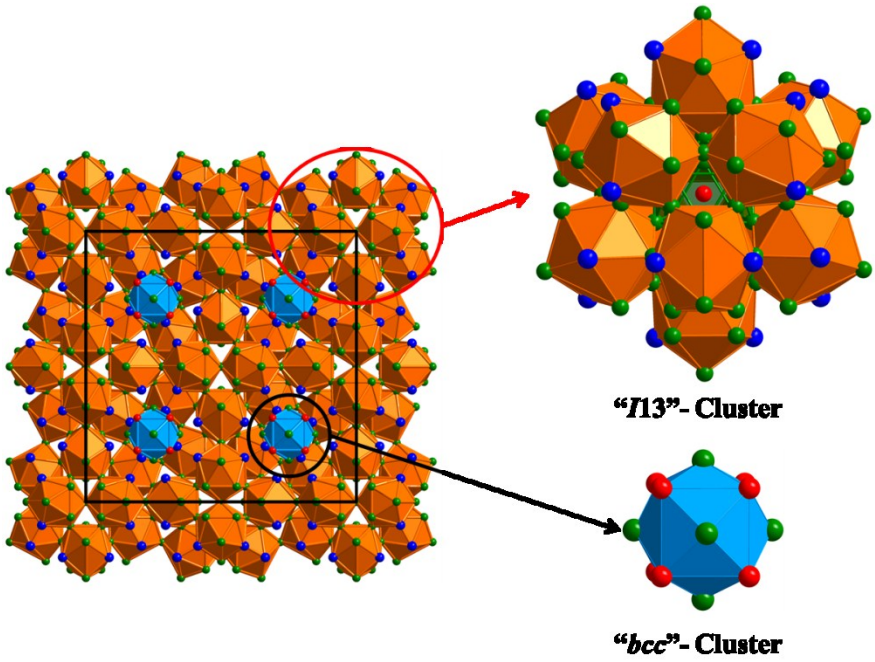

(*a*)

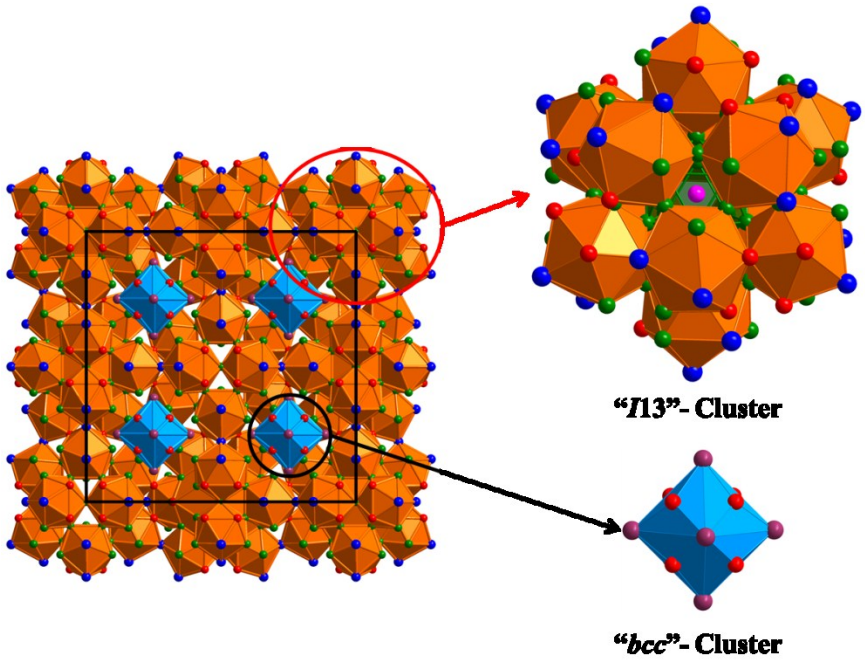

(*b*)

Figure 3. Crystal structures emphasizing the *I*13- and bcc-clusters in (*a*) $Cr_{22}Sn_{24}Zn_{72}$ (red: Cr; green: Zn; blue: Sn) and (*b*) $V_{23.3(1)}Sn_{26.3(1)}Zn_{68.4(1)}$ (red: V; pink V/Sn; green: Zn; blue: Sn; purple: Zn/Sn).

6.4.3 Electronic Structure. The chemical compositions and structures of many CMAs have been rationalized using a Hume-Rothery valence electron counting mechanism. In this model, which relies on the nearly-free-electron model for electronic states, the spherical Fermi surface lies close to a large number of Brillouin zone faces set up by the periodic potential of atomic sites. Since the radius of the Fermi sphere is the Fermi wavevector k_F and Brillouin zone faces bisect reciprocal lattice vectors $\boldsymbol{K}_{hkl}$, for a cubic system with lattice constant a this criterion is

$$k_F \approx |\boldsymbol{K}_{hkl}|/2 = (\pi/a)[h^2 + k^2 + l^2]^{1/2}. \quad (1)$$

When this condition is met, the ensuing Fermi surface-Brillouin zone (Fs-Bz) interaction creates gaps at the Fermi level in the electronic energy band structure near certain zone boundaries of the Brillouin zone and, consequently, expresses a pseudogap in the electronic

density of states (DOS) curve. Since the Fermi surface is set by the number of valence electrons N or occupied states (N/2) within the Fermi sphere, the criterion of strong Fs-Bz interactions, equation (1), sets the number of valence electrons per unit cell N_{cell} to be

$$N_{cell} = (k_F^3 V_{cell})/3\pi^2 = (\pi/3)[h^2 + k^2 + l^2]^{1/2}, \quad (2)$$

and, therefore, a corresponding valence electron concentration expressed as an electron-to-atom (e/a) ratio as

$$e/a = N_{cell}/A_{cell} = (\pi/3A_{cell})[h^2 + k^2 + l^2]^{1/2}, \quad (3)$$

in which A_{cell} is the number of atoms per unit cell. This model has been successfully applied to CMAs ranging from γ-brasses like Cu_5Zn_8 (*cI*52) and Cu_9Al_4 (*cP*52), which show optimal e/a ratios of ~1.615,[9] as well as a series of Mackay-type icosahedral quasicrystals in the Al–Cu–T (T = Fe, Ru, Os) and Al–Pd–T (T = Mn, Re) systems for e/a = 1.75.[20-21] In these CMAs, the appropriate Brillouin zone faces for optimal Fs-Bz interactions occurs for the most intense (*hkl*) peaks observed in the X-ray diffraction pattern.

Therefore, for $Cr_{22}Sn_{24}Zn_{72}$ and $V_{23.3(1)}Sn_{26.3(1)}Zn_{68.4(1)}$, the most four intense peaks occur in the range of scattering angle 2θ of 36°-44°. Listed in Table 4 are the requisite pieces of information that, when used in equations (1)-(3), derive e/a values of 1.657 for $Cr_{22}Sn_{24}Zn_{72}$ and 1.627 for $V_{23.3(1)}Sn_{26.3(1)}Zn_{68.4(1)}$. These values lie between 1.615 (γ-brass) and 1.75 (Mackay-type icosahedral QCs), to suggest that these CMAs, $Cr_{22}Sn_{24}Zn_{72}$ and $V_{23.3(1)}Sn_{26.3(1)}Zn_{68.4(1)}$, identify a transition from cubic periodic structures to QCs.

Table 4. (h, k, l), d-spacing, K_{hkl} and k_F for most four intensity peaks in the powder X-ray diffraction patterns of Cr-Sn-Zn and V-Sn-Zn cubic phases.

Most Intense Peaks	Cr-Sn-Zn	V-Sn-Zn-
(h, k, l)	(0,6,10)*24, (6,6,8)*24 (3,5,9)*48 (2,8,8)*24, (4,4,10)*24	(0,6,10)*24, (6,6,8)*24 (3,5,9)*48 (2,8,8)*24, (4,4,10)*24

Table 4. continued

	(3,7,9)*48	(1,3,11)*48, (1,7,9)*48
d-spacing(1/Å)	2.1598	2.1598
	2.3487	2.3487
	2.1922	2.1922
	2.1363	2.2006
½ $*K_{hkl}$	1.455	1.455
	1.338	1.338
	1.433	1.433
	1.471	1.428
k_F	1.455	1.455
	1.338	1.338
	1.433	1.433
	1.471	1.428
e/a	1.759	1.759
	1.368	1.368
	1.682	1.682
	1.818	1.663
⟨*e/a*⟩	1.657	1.627

Tight-binding electronic structure calculations using the LMTO code reveals that the Fermi level for $Cr_{22}Sn_{24}Zn_{72}$ falls within a pseudogap in the electronic density of states (see Figure 4). Further computational analysis is required to understand features of the chemical bonding in these CMAs.

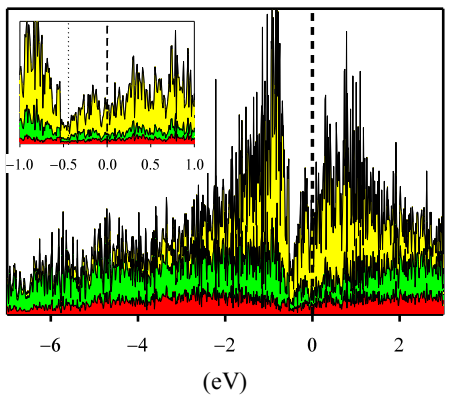

Figure 4. Electronic density of states curve for $Cr_{22}Sn_{24}Zn_{72}$. Cr states shaded in yellow; zinc states shaded in green; tin states shaded in red. The Fermi level is the energy reference.

6.5 Conclusion: The synthesis and structural characteristics of two new complex metallic compounds $Cr_{22}Sn_{24}Zn_{72}$ and $V_{23.3(1)}Sn_{26.3(1)}Zn_{68.4(1)}$ are presented, both of which show nanoscale lattice parameters. There are two types of clusters in the compounds, *I*13-type and bcc-type, which are packed in a body-centered cubic packing. The *e*/*a* ratios evaluated for these two CMAs place them between cubic γ-brasses and icosahedral quasicrystals, and their electronic DOS curve show a pseudogap near the Fermi level, results which suggest that these CMAs satisfy some type of Hume-Rothery valence electron counting rule.

6.6 Acknowledgements

The authors thank Dr. Kewei Sun in the Ames Laboratory for HR-TEM analysis. This work was carried out at the Ames Laboratory, which is operated for the U.S. Department of Energy by Iowa State University under Contract No. DE-AC02-07CH11358. This work was supported by the U.S. Department of Energy, Office of Basic Energy Sciences, Division of Materials Sciences and Engineering.

6.7 Reference

[1] Wang, Y.; Herron, N. *J. Phys. Chem.* **1991**, *95*, 525.

[2] Leutwyler, W. K.; Bürgi, S. L.; Burgl, H. B. *Science* **1996**, *271*, 933.

[3] Mizutani, U.; Kondo, Y.; Nishino, Y.; Inukai, M.; Feuerbacher, M.; Sato, H. *J. Phys.: Condens. Matter*, **2010**, *22*, 485501.

[4] Dubois, J. M. *Nat. Mater.* **2010**, *9*, 287.

[5] Urban, K.; Dubois, J. M.; Belin-Ferré, E. *Complex Metallic Alloys: Fundamentals and Applications*. Wiley-VCH, Verlag, 2011.

[6] Snyder, G. J.; Toberer, E. S. Nat. Mater. **2008**, *7*, 105.

[7] Xiong, D. B.; Okamoto, N. L.; Inui, H. *Inorg. Chem.* **2011**, *50*, 827.

[8] Degtyareva, V. F.; Smirnova, I. S. *Z. Kristallogr.***2007**, *222*, 718.

[9] Mizutani, U. *Hume-Rothery Rules for Structurally Complex Alloy Phases*. Taylor & Francis, US, 2010.

[10] Hillebrecht, H.; Kuntze, V.; Gebhardt, K.; *Z. Kristallogr.* **1997**, *212*, 840.

[11] Xiong, D. B., Yang, K., Zhao, Y.; Ma, J. *Dalton Trans.*, **2010**, *39*, 8331.

[12] Rietveld, H.M. *J. Appl. Crystallogr.* **1969**, *2*, 65.

[13] Hunter, B.A.; Howard, C.J. *LHPM-Rietica*, version 1.71: Australian Nuclear Science and Technology Organization: Menai, Australia, 2000.

[14] Sheldrick, G. M. *SADABS*, University of Gottingen: Gottingen, Germany, 2001.

[15] Sheldrick, G. M. *Acta Crystallogr. A* **2008**, *64*, 112.

[16] *SHELXTL*, version 6.10, Bruker AXS Inc.: Madison, WI, 2000.

[17] *Diamond*, version 3.2; Crystal Impact: Bonn, Germany, 2010.

[18] Doi, K.; Ono, S.; Ohtanl, H.; Hasebe, M. *J. Phase Equil. Diffus.* **2006**, *27*, 63.

[19] Okamoto, H. *Desk handbook: phase diagrams for binary alloys*. ASM international, 2000.

[20] Tsai, A. P.; Guo, J. Q.; Abe, E.; Takakura, H.; Sato, T. J. *Nature*, **2000**, *408*, 537.

[21] Tsai, A. P.; Inoue, A.; Yokoyama, Y.; Masumoto, T. *Mater. Trans. JIM*, **1990**, *31*, 98.

[22] Tsai, A. P.; Inoue, A.; Masumoto, T. *Jpn. J. Appl. Phys.* **1987**, *26*, L1505-L1507.

6.8 Supporting Information

Table S1. The refined parameters of TM-Sn-Zn as determined by Rietveld refinement of PXRD data at 293K.

$Cr_{22}Sn_{24}Zn_{72}$ Crystallographic unit cell: cubic (space group: *Fm-3c*), *a* = *b* = *c*= 25.2562(1) Å, Rp = 4.588, Rwp = 5.084.						
Atom	*Wyckoff*	*Occupancy*	*x*	*y*	*z*	*U*(*eq*) (Å)
Cr1	8*a*	1	¼	¼	¼	0.042
Cr2	8*b*	1	0	0	0	0.045
Cr3	64*g*	1	0.19441	0.19441	0.19441	0.054
Cr4	96*i*	1	0	0.10998	0.16782	0.045

Table S1. continued

Zn5	192*j*	¼	0.13832	0.27097	0.26737	0.051
Zn6	48*e*	1	0.18984	0	0	0.054
Zn7	96*i*	1	0	0.05511	0.08944	0.046
Zn8	96*i*	1	0	0.21475	0.14173	0.045
Zn9	96*h*	1	¼	0.05701	0.05701	0.045
Zn10	192*j*	1	0.05372	0.14996	0.09111	0.048
Sn11	192*j*	1	0.08802	0.16267	0.20472	0.050

$V_{23.3}Sn_{26.1}Zn_{68.6}$
Crystallographic unit cell: cubic (space group: *Fm-3c*), *a* = *b* = *c*= 25.0322(1) Å, Rp = 6.898, Rwp = 7.139.

Atom	*Wyckoff*	*Occupancy*	*x*	*y*	*z*	*U*(*eq*) (Å)
V/Sn1	8*a*	0.70(1)/0.30	¼	¼	¼	0.080
V2	8*b*	1	0	0	0	0.083
Zn/Sn3	48*f*	0.44(1)/0.56	0.12070	¼	¼	0.094
V/Sn4	64*g*	0.60(1)/0.40	0.18874	0.18874	0.18874	0.093
Zn5	96*i*	1	0	0.11065	0.18013	0.091
Zn6	48*e*	1	0.18179	0	0	0.082
V/Sn7	96*i*	0.74(1)/0.26	0	0.05493	0.09141	0.089
Sn8	96*i*	1	0	0.22054	0.16256	0.097
V/Sn9	96*h*	0.66(1)/0.34	¼	0.06009	0.06009	0.090
Zn10	192*j*	1	0.05860	0.14790	0.08644	0.085
Zn11	192*j*	1	0.09400	0.15630	0.19623	0.090

Table S2. Anisotropic displacements parameters of Cr-Sn-Zn and V-Sn-Zn phases examined at 293(2) K.

$Cr_{22}Sn_{24}Zn_{72}$

	Atom	U_{11}	U_{22}	U_{33}	U_{23}	U_{13}	U_{12}
*"I*13*"*-Cluster	Cr1	0.005(1)	0.005(1)	0.005(1)	0	0	0
	Cr2	0.007(1)	0.008(1)	0.006(1)	-0.000(1)	0	0
	Zn3	0.011(1)	0.015(1)	0.009(1)	0	0	0
	Zn4	0.010(1)	0.010(1)	0.008(1)	-0.001(1)	0	0
	Zn5	0.017(1)	0.013(1)	0.019(1)	0.001(1)	0	0
	Zn6	0.009(1)	0.014(1)	0.014(1)	0.002(1)	0.001(1)	-0.001(1)
	Zn7	0.015(1)	0.011(1)	0.010(1)	0.002(1)	0.002(1)	0.001(1)
	Sn8	0.015(1)	0.020(1)	0.018(1)	0.001(1)	-0.004(1)	-0.006(1)
"bcc"-Cluster	Cr9	0.005(1)	0.005(1)	0.005(1)	0	0	0
	Cr10	0.047(1)	0.047(1)	0.047(1)	-0.018(1)	-0.018(1)	-0.018(1)
	Zn11	0.047(3)	0.077(7)	0.012(7)	0.076(6)	0.095(7)	0.050(4)

$V_{23.3(1)}Sn_{26.3(1)}Zn_{68.4(1)}$

	Atom	U_{11}	U_{22}	U_{33}	U_{23}	U_{13}	U_{12}
*"I*13*"*-Cluster	V1	0.001(1)	0.001(1)	0.001(1)	0	0	0
	V/Sn2	0.002(1)	0.001(1)	-0.001(1)	0.001(1)	0	0
	Zn3	0.008(1)	0.009(1)	0.006(1)	0	0	0
	Zn4	0.005(1)	0.005(1)	0.003(1)	-0.002(1)	0	0
	Sn5	0.015(1)	0.003(1)	0.008(1)	0.002(1)	0	0

Table S2. continued

	V/Sn6	0.006(1)	0.011(1)	0.011(1)	0.002(1)	0.001(1)	-0.001(1)
	Zn7	0.010(1)	0.005(1)	0.006(1)	0.001(1)	0.002(1)	0.001(1)
	Zn8	0.015(1)	0.019(1)	0.025(1)	0.001(1)	-0.005(1)	-0.011(1)
"bcc"-Cluster	V/Sn9	0.006(2)	0.006(2)	0.006(2)	0	0	0
	V/Sn10	0.025(1)	0.025(1)	0.025(1)	-0.006(1)	-0.006(1)	-0.006(1)
	Zn/Sn11	0.024(1)	0.009(1)	0.009(1)	0	0	0

Figure S1. The refined powder X-ray patterns of TM-Sn-Zn as determined by Rietveld refinement at 293K.

$Cr_{22}Sn_{24}Zn_{72}$

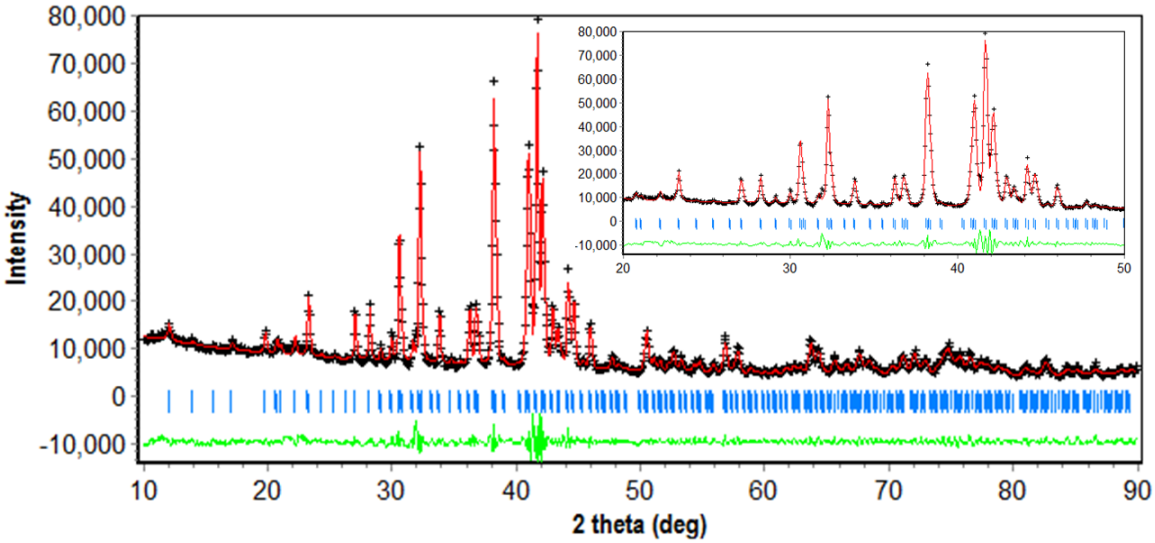

$V_{23.3}Sn_{26.1}Zn_{68.6}$

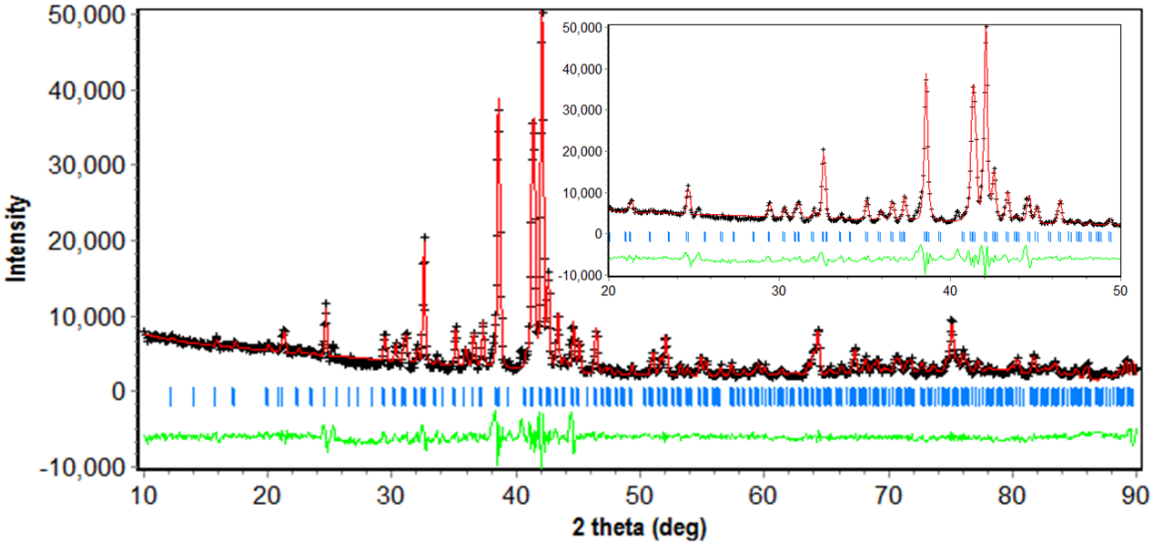

Figure S2. Electronic density distribution in Cr-Sn-Zn without Zn11 (192*j*) site along *x* axis.

***x*=0.158**

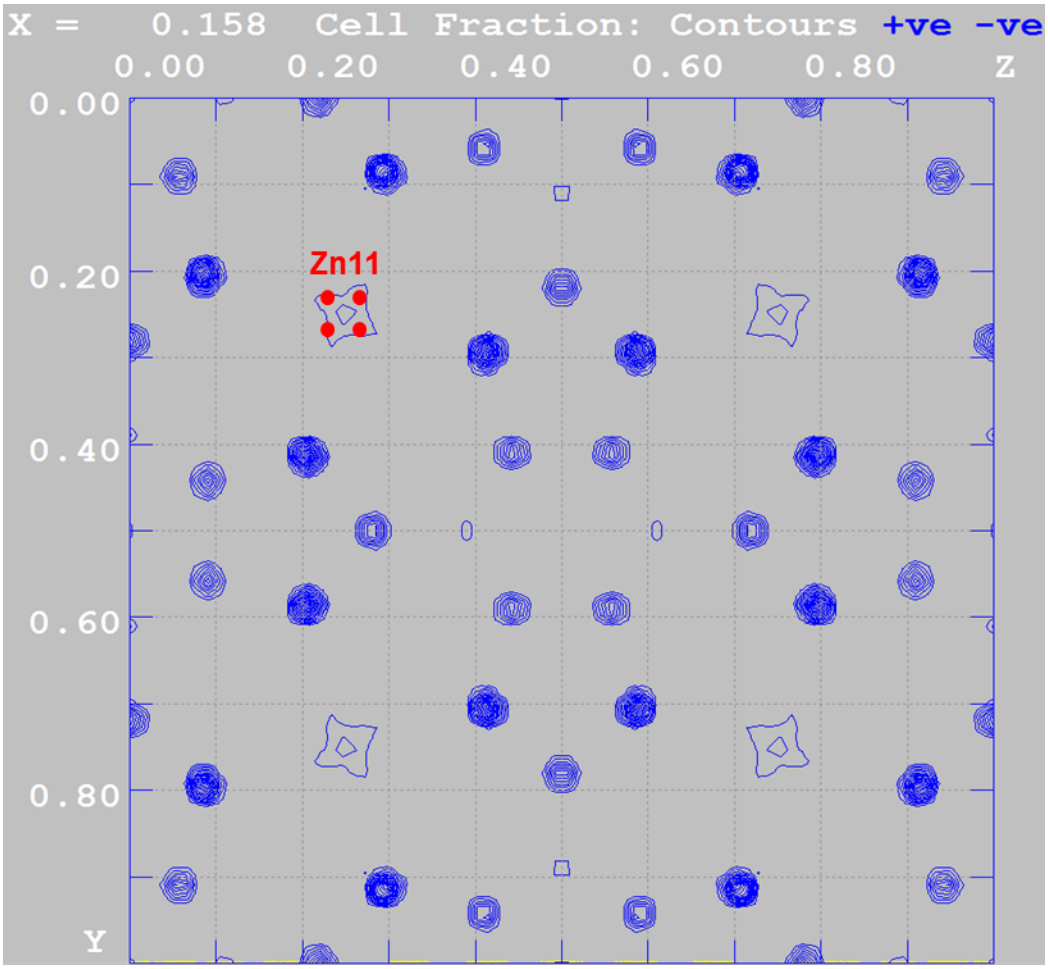

To investigate the relationship between Cr/V-Sn-Zn and QCs, the views on each layer of Cr/V-Sn-Zn are shown in Figure S3. Because of the space group symmetry, only one-quarter of cubic unit cell marked by red along {001} directions are listed. The first, second, and fourth layers are built up by irregular pentagons, and the third layer is made by irregular decagons. The pentagons and decagons are connected to form decagons again. Moreover, the polyhedra circled by light green contain pentagonal prisms surrounding by five distorted icosahedra. The distorted icosahedra form C_4 operation which breaks the C_5 operation. The polyhedra circled in pink contain icosahedra and distorted cubes, which form irregular decagons.

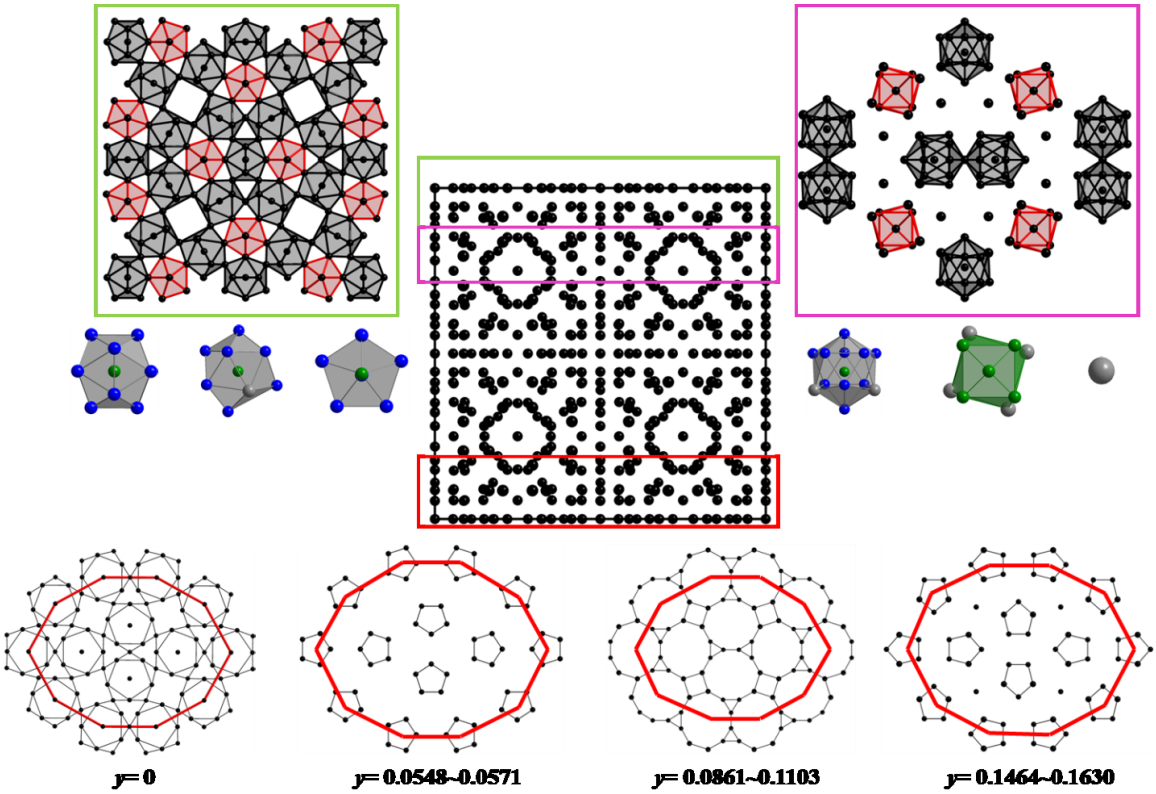

Figure S3. Red: The four layers along {010} direction in the Cr/V-Sn-Zn. (from (0, 0, 0) plane to (0, ¼, 0) plane); Light Green: Polyhedrons corresponding to the layers in the crystal; Pink: Polyhedrons corresponding to the layers in the crystal.

Figure S4. Dark field images of (*a*) $Cr_{22}Sn_{24}Zn_{72}$ and (*b*) $V_{21.7(1)}Sn_{26.9(1)}Zn_{69.4(1)}$ obtained by HRTEM tilting experiments.

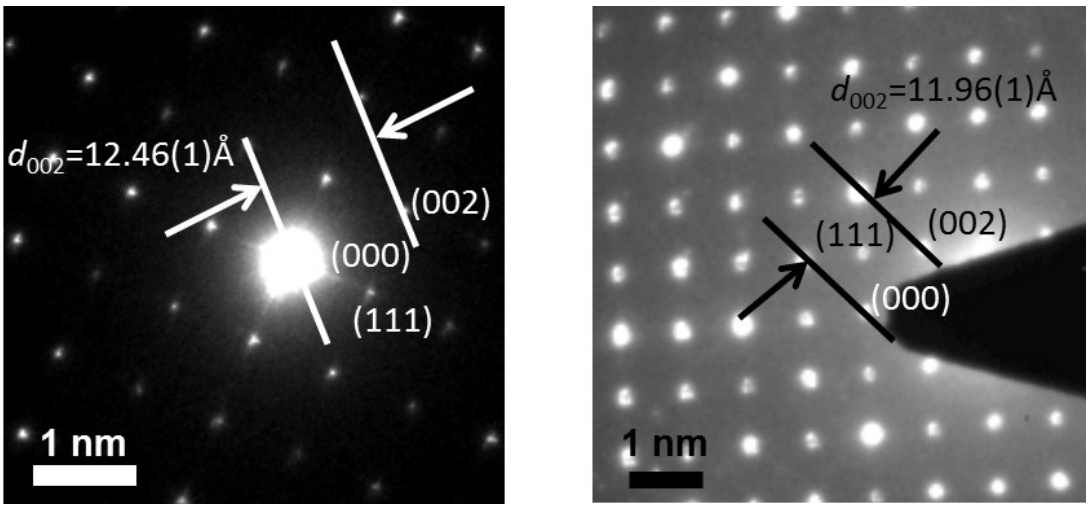

(*a*) (*b*)

CHAPTER 7

Crystal Structure, Physical Properties and Electronic Investigation on New $CeCu_6$-type Intermetallic Compounds $Ce(Sn_{1-x}Zn_x)_6$

*Weiwei Xie[1], Jing Liu[2], Tai Kong[3], Vitalij K. Pecharsky[2], Paul Canfield[3] and Gordon J. Miller[1]**

[1] Department of Chemistry, Iowa State University and Ames Laboratory, US-DOE, Ames, Iowa, 50011 USA
[2] Department of Material Science and Engineering, Iowa State University and Ames Laboratory, US-DOE, Ames, Iowa, 50011 USA
[3] Department of Physics and Astronomy, Iowa State University and Ames Laboratory, US-DOE, Ames, Iowa, 50011 USA

7.1 Abstract

The crystal structure, physical properties and computational investigation of new cerium based compounds, $Ce(Sn_{1-x}Zn_x)_6$, are presented. The orthorhombic $CeCu_6$-type phase crystallizes in the space group *P*nma (Pearson symbol *oP*28; a = 8.797(1)-8.823(2) Å, b = 5.394(1)-5.402(2) Å and c = 11.140(2)-11.167(1) Å) at room temperature and the stoichiometry may be expressed as $Ce(Sn_{1-x}Zn_x)_6$, ($0.45(1) < x < 0.49(1)$). Crystal structure can be treated as distorted octahedral, which are connected by vertex-sharing, edge-sharing and face-sharing. With decreasing the temperature, single crystal and magnetic measurements indicate that the crystal structure would transit from orthorhombic to monoclinic by slightly changing β from 90° to 90.38(3)° and flattening distorted octahedral. Temperature-dependent magnetic measurements and AC susceptibility confirm the paramagnetic properties of $Ce(Sn_{1-x}Zn_x)_6$ above 20 K. Above about 20 K, $\chi^{-1}(T)$ follows the Curie-Weiss law with the effective magnetic moment μ= 2.81(3) μ_B/f.u. and the paramagnetic Curie temperature θ_p= 8.5(7) K, which means the Ce ions in the compound are

trivalent with carrying a Ce^{3+} magnetic moment. More, the specific heat capacity of $Ce(Sn_{1-x}Zn_x)_6$ shows the unusual peak below 2K possibly caused by low temperature magnetic transition. Theoretical calculation conducted by density functional theory[1] plus U (GGA+U) [2] applied for predict the magnetic properties below 2K shows hypothetical model "$CeSn_{3.5}Zn_{2.5}$" preferring the ferromagnetic properties at 0K with magnetic moment $0.99\mu_B$/Ce.

7.2 Introduction

Cerium based intermetallic compounds have been widely studied for decades because of their unusual physical properties.[3] One major physical behavior is the heavy-fermion (HF) property[4], observed for the first time in $CeAl_3$.[5] Heavy fermion materials have a greater effective mass than the value expected from the free-electron theory. Recently, $CeCu_6$-type compounds like $CeCu_{6-x}Au_x$ are new heavy-fermion superconductor systems attracting research.[7] In a conventional superconductor, the binding of electrons into the paired states that collectively carry the supercurrent is mediated by phonons—vibrations of the crystal lattice. However, in the case of the heavy fermion superconductors like $CePd_2Si_2$ [8], $CeIn_3$ [9] and $CeCu_{6-x}Au_x$ [7], the charge carriers are bound together in pairs by magnetic spin–spin interactions called magnetically mediated superconductivity.[10] On the other hand, as sub-family of cerium-transition-metal stannides, CeTSn has been interesting for the magnetic properties. For example, CeTSn(T=Ni [11], Rh[12], Ir[13]) are intermediate valence systems, CeTSn(T=Pd[14], Pt[15]) are antiferromagnetic Kondo lattices, and $CeRh_3B_2$[16] is so far the highest Curie-temperature ferromagnetic material in the system. Thus, new cerium-transition-metal stannide, $Ce(Sn_{1-x}Zn_x)_6$, adopting to $CeCu_6$-type structure may have both intriguing magnetic and heavy-fermion superconductor properties.

In the aspect of structure, $LnCu_6$ (Ln=La, Ce, Pr) compounds revealed the same type of the structural phase transition from orthorhombic to monoclinic.[17] Neutron scattering experiments show that the major contribution to this phase transition attributed not to rare earth atoms but to Cu atoms.[18] Also, in $CeCu_6$, Ce has a state with $4f^1$ configuration and a magnetic state j=5/2 with an effective moment of $2.54\mu_B$.[19] $Ce(Sn_{1-x}Zn_x)_6$ with localized 3*d* and 4*d* electrons in Zn and Sn still has structural transition from orthorhombic to monoclinic according to our magnetic and structural measurements. Moreover, the Sn and Zn have similar localized *d*-electron with Cu, the magnetic properties of $CeCu_6$-type $Ce(Sn_{1-x}Zn_x)_6$ is also as straightforward as $CeCu_6$, resulting from $Ce(4f^1)$.

With these magnetic and structural features in mind, we report herein a thorough structural characterization and investigation of the magnetic properties and theoretical electronic structures of $Ce(Sn_{1-x}Zn_x)_6$, with an emphasis on relationship between physical properties and crystal structure.

7.3 Experimental Section

7.3.1 Synthesis. Different Ce/Sn/Zn binary and ternary phases were obtained by fusion of mixtures of Ce pieces (99.99%, Ames Laboratory), Sn pieces (99.99%, Ames Laboratory) and Zn particles (99.99%, Alfa Aesar), combinations as different atomic ratio of Ce:Sn:Zn with their products shown in Table 1. Each reactant mixture, about 400 mg total, was sealed into precleaned Ta tube in an Ar-filled glove box. After being transferred into an arc welder, the crimped Ta tubes were weld-sealed under argon and then enclosed in evacuated SiO_2 jackets ($<10^{-5}$ Torr) to protect them from air during heating. The samples were heated to 800 °C for 24 hr, followed by cooling to 500 °C at a rate of 1 °C/hr and annealed at this temperature for 6 days, after which the containers were slowly cooled in the furnace. Only

atomic ratio of Ce:Sn:Zn=1:1:1 can produce $CeCu_6$-type $Ce(Sn_{1-x}Zn_x)_6$ as major phase, and all products are silvery shining, but change to golden shining after several days.

7.3.2 Phase Analysis. All samples were finely ground and examined by powder X-ray diffraction for identification and phase purity on a STOE WinXPOW powder diffractometer employing Cu radiation ($\lambda_{K\alpha}$= 1.5406 Å) for all the samples. The scattered intensity was recorded as a function of Bragg angle (2θ) [20] using a scintillation detector with a step of 0.03° 2θ in step scan mode, ranging from 0° to 130°. Phase identification and the lattice parameters were refined by full-profile Rietveld [21] refinements using LHPM RIETICA [22] from reflection peaks between 5° and 90° in 2θ.

7.3.3 Structure Determination. Crystals from each reaction sample were mounted on the tips of glass fibers. Temperatures at 143K and 293K intensity data were collected on a Bruker Smart Apex CCD diffractometer using Mo Kα radiation (λ = 0.71073 Å). Data were collected over a full sphere of reciprocal space with 0.5° scans in ω with an exposure time of 10s per frame. The 2θ range extended from 3° to 60°. The *SMART* software was used for data acquisition. Intensities were extracted and corrected for Lorentz and polarization effects using the *SAINT* program. Empirical absorption corrections were accomplished with *SADABS*, which is based on modeling transmission by spherical harmonics employing equivalent reflections with $I > 3\sigma(I)$.[23-24] With the *SHELXTL* package,[25] the crystal structures were solved using direct methods and refined by full-matrix least-squares on F^2. All crystal structure drawings were produced using the program *Diamond*.[26]

7.3.4 Magnetic Measurement. The magnetization measurements were performed using a superconducting quantum interference device (SQUID) magnetometer MPMS XL-7 manufactured by Quantum Design, Inc. on pieces of single crystals that were manually

selected from the product. The SQUID operates over a temperature range of 2-300 K and in applied fields of up to 70 kOe under DC measurement. Moreover, the AC susceptibility was measured at 1Hz and 100Hz. The samples were placed in glass capsules for measurement.

7.3.5 Specific Heat Capacity Measurement. The heat capacity is measured by Physical Property Measurement System (PPMS) manufactured by Quantum Design, Inc. The temperature ranges from 2K to 100K with non-applied field and pressure at 9.40×10^{-6} Torr.

7.3.6 Vienna ab-initio Simulation Package[27-30] (VASP). Energy and magnetic properties calculations[31-33] were completed using VASP, which employs projector augmented-wave (PAW) pseudopotentials that were adopted with the Perdew-Burke-Ernzerhof generalized gradient approximation (PBE-GGA), in which scalar relativistic effects are included. For structural optimization, the conjugate gradient algorithm was applied. The energy cutoff was 400.0 eV. Reciprocal space integrations were completed over a 5×3×6 Monkhorst-Pack *k*-points mesh[34] with the linear tetrahedron method.[35] With these settings, the calculated total energy converged to less than 0.1 meV per atom.

7.4 Results

According to the Sn-Zn phase diagram, Sn and Zn do not form any binary compounds, but a eutectic point occurs at 198.5°C at 14.9 atomic percent Zn.[36] Since previous experiments involving Cr and V yielded new ternary compounds, we explored Ce as a possible rare-earth metal that could lead to novel intermetallic phases. Five different loadings (see Table 1) led primarily to Ce_2Zn_{17}-type phases except for the molar ratio Ce:Sn:Zn = 1:1:1, for which a new $CeCu_6$-type phase, $Ce(Sn_{1-x}Zn_x)_6$, emerged as the major product. $CeZn_2$ also crystallized, according to the results of X-ray diffraction. Because the $CeZn_2$ are

needle-shaped, whereas that for $Ce(Sn_{1-x}Zn_x)_6$ is block-shaped, they can be easily manually separated for measuring physical properties.

Table 1. Compositions, phase analyses, and refined compositions for different loading Ce-Sn-Zn systems.

Loaded Composition	$Ce_{33.13}Sn_{33.39}Zn_{33.48}$ (CeSnZn)	$Ce_{25.16}Sn_{37.45}Zn_{37.39}$ ($CeSn_{1.5}Zn_{1.5}$)	$Ce_{14.23}Sn_{49.94}Zn_{35.84}$ ($Ce_1Sn_{3.5}Zn_{2.5}$)	$Ce_{14.29}Sn_{43.00}Zn_{42.71}$ ($Ce_1Sn_3Zn_3$)	$Ce_{14.30}Sn_{35.87}Zn_{49.82}$ ($Ce_1Sn_{2.5}Zn_{3.5}$)
Phases (PXRD)	$CeCu_6$-type(major) +$CeZn_2$ (minor)	Ce_2Zn_{17}(major)	Ce_2Zn_{17}(major)	Ce_2Zn_{17}(major)	Ce_2Zn_{17}(major)

7.4.1 Phase Analysis. For the X-ray powder diffraction patterns, all scale factors and lattice parameters were refined, whereas the displacement parameters of all atoms were assumed to be isotropic at $B = 0.01$ according to single crystal XRD measurement and were not refined. The diffraction peaks in powder XRD are broad, which is probably caused by a homogenous phase of $Ce(Sn_{1-x}Zn_x)_6$ in the product. Two same $Ce(Sn_{1-x}Zn_x)_6$ phases with different lattice parameters are set to refine the powder pattern. The resulting profile residuals R_p was 5.082 with weighted profile residuals R_{wp} 6.197. The refined lattice parameters for major phase of $Ce(Sn_{1-x}Zn_x)_6$ is a= 8.698-8.794(1) Å, b= 5.393-5.397(1) Å and c= 11.140-11.247(1) Å.

7.4.2 Room Temperature Crystal Structure. Single crystals were investigated to obtain further insights into the structural features of cerium based compounds. The results of single crystal diffraction extracted from the specimen at 143K and 293K are summarized in Tables 2 and 3. Corresponding anisotropic displacement parameters are summarized in Tables S1 in Supporting Information. All structures at room temperature crystallize in the orthorhombic space group *P*nma (No. 62) with Ce atoms located at the 4*c* site and Sn and Zn atoms mixed on another four 4*c* and one 8*d* sites (marked from Sn/Zn1 to Sn/Zn5). Ce, Sn/Zn1, Sn/Zn2, Sn/Zn3 and Sn/Zn4 all situate on the mirror planes whereas the Sn/Zn5 exists on a general position. The crystal structure can be constructed as distorted octahedral with Ce atoms as

vertex. Along *b*-axis, there are two types of distorted octahedra, one consists of Sn/Zn1 and Sn/Zn2 with Ce atoms as vertex, and the other one is made of Sn/Zn3 and Sn/Zn5 also with Ce atoms as vertex. The two types of distorted octahedra are connected by Ce vertex. The Sn/Zn4 atoms marked in green in Figure 1 are located between the layers along *b*-axis. From the Table 2, the Sn/Zn1, Sn/Zn2 and Sn/Sn3 are mostly occupied by Sn atoms, whereas Sn/Zn5 is mostly occupied by Zn atoms, but only Sn/Zn4 sites are closely half-and-half occupied Sn and Zn atoms. If viewed along c-axis, the distorted octahedra made by Sn/Zn1, Sn/Sn2 and Ce are face-sharing and forming layer A in Figure 1(*b*), while the distorted octahedra containing Sn/Zn3, Sn/Zn5 and Ce are edge-sharing by Ce-Sn/Zn3 only in layer B.

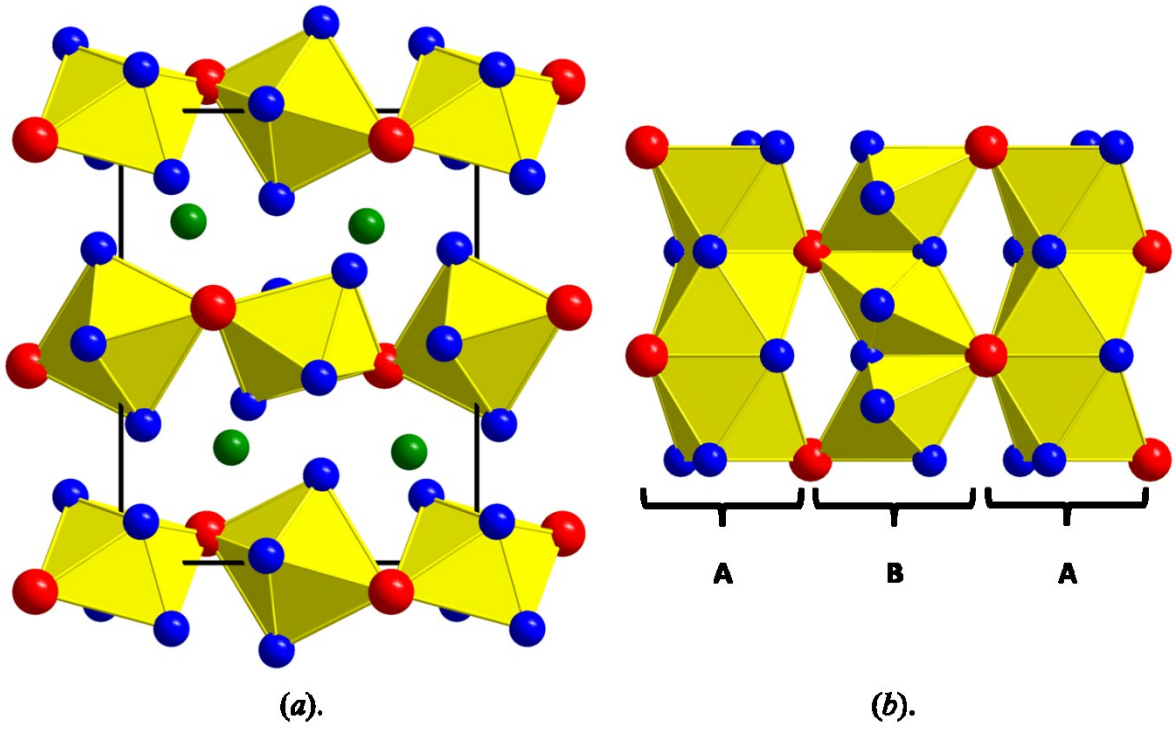

Figure 1. Crystal structure of $Ce(Sn_{1-x}Zn_x)_6$ at room temperature constructed as distorted octahedral with Red as Ce atoms; Blue as Sn/Zn1, Sn/Zn2, Sn/Zn3, Sn/Zn5 and Green as Sn/Zn4 (*a*) Projection view from (010). (*b*) Projection view from (001), A and B mark the layering sequence along *c*-axis.

Table 1. Single crystal data for $Ce(Sn_{1-x}Zn_x)_6$ at 293(2)K, 223(2)K, 173(2)K and 143(2)K.

Measuring Temperature	293K	223K	173K	143K

Table 1. continued

Refined Formula	$CeSn_{3.33}Zn_{2.67}$	$CeSn_{3.33}Zn_{2.67}$	$CeSn_{3.33}Zn_{2.67}$	$CeSn_{3.33(4)}Zn_{2.67}$
F.W. (g/mol)	709.90	709.90	709.90	709.90
F(000)	1218	1218	1218	1218
Space Group; Z	Pnma(No. 62); 4	Pnma(No. 62); 4	Pnma(No. 62); 4	$P2_1$/c(No. 14); 4
a (Å)	5.402(2)	5.397(1)	5.393(1)	5.3880(2)
b (Å)	8.809(3)	8.804(2)	8.795(2)	8.7853(3)
c (Å)	11.162(3)	11.154(2)	11.144(2)	11.1313(3)
β (°)	90	90	90	90.38(3)
V (Å^3)	531.1(3)	529.9(2)	528.6(2)	526.90(3)
d_{calc} (Mg/m^3)	8.878	8.898	8.920	8.941
Abs. Corr.	Multi-scan	Multi-scan	Multi-scan	Multi-scan
Ext. Coeff.	0.0014(2)	0.0024(4)	0.0013(2)	0.0013(1)
μ (mm^{-1})	35.468	35.546	35.636	35.729
θ range (deg)	4.79–28.37	3.65–28.29	3.66–28.31	2.95–28.32
hkl ranges	-11<=h<=11 -5<=k<=7 -14<=l<=14	-11<=h<=11 -7<=k<=7 -12<=l<=14	-11<=h<=11 -7<=k<=7 -12<=l<=14	-7<=h<=7 -11<=k<=11 -14<=l<=13
No. Refl. (R_{int})	2988 (0.0621)	4084 (0.1337)	4087 (0.0527)	3650 (0.0546)
No. Indep. Refl.	724	726	726	1287
No. Par.	41	41	41	71
R_1; wR_2 (I>2sigma(I))	0.0320; 0.0696	0.0614; 0.1419	0.0272; 0.0617	0.0340; 0.0698
R_1; wR_2 (all I)	0.0496; 0.0769	0.0738; 0.1514	0.0375; 0.0658	0.0473; 0.0752
Goodness of fit	1.033	1.019	1.039	1.002
Peak; Hole (e$^-$/Å^3)	1.862; -2.164	4.230; -4.987	1.704; -1.836	2.255; -2.236

Table 2. Atomic coordinates, site occupancies, and equivalent isotropic displacement parameters of $Ce(Sn_{1-x}Zn_x)_6$ at 293(2)K, 223(2)K, 173(2)K and 143(2)K. U_{eq} is defined as one-third of the trace of the orthogonalized U_{ij} tensor (Å^2).

293(2) K

Atom	Wyckoff Site	Occupancy	x	y	z	U_{eq}
Ce	4*c*	1	0.2594(1)	¼	0.5641(1)	0.0126(2)
Sn/Zn1	4*c*	0.76/0.24	0.0561(1)	¼	0.0907(1)	0.0166(3)
Sn/Zn2	4*c*	0.81/0.19	0.4087(1)	¼	0.0150(1)	0.0141(3)
Sn/Zn3	4*c*	0.79/0.21	0.1418(1)	¼	0.8539(1)	0.0152(3)
Sn/Zn4	4*c*	0.57/0.43	0.3100(1)	¼	0.2551(1)	0.0122(3)
Sn/Zn5	8*d*	0.20/0.80	0.0623(1)	0.5076(2)	0.3070(1)	0.0114(3)

223(2) K

Atom	Wyckoff Site	Occupancy	*x*	*y*	*z*	U_{eq}
Ce	4*c*	1	0.2593(2)	¼	0.5642(2)	0.0111(4)
Sn/Zn1	4*c*	0.76/0.24	0.0564(2)	¼	0.0905(2)	0.0144(5)
Sn/Zn2	4*c*	0.81/0.19	0.4085(2)	¼	0.0151(2)	0.0117(4)
Sn/Zn3	4*c*	0.79/0.21	0.1417(2)	¼	0.8536(2)	0.0135(5)
Sn/Zn4	4*c*	0.57/0.43	0.3100(2)	¼	0.2549(2)	0.0104(5)
Sn/Zn5	8*d*	0.20/0.80	0.0625(2)	0.5072(2)	0.3068(2)	0.0094(4)

173(2) K

Atom	Wyckoff Site	Occupancy	*x*	*y*	*z*	U_{eq}
Ce	4*c*	1	0.2593(1)	¼	0.5643(1)	0.0088(2)
Sn/Zn1	4*c*	0.76/0.24	0.0564(1)	¼	0.0906(1)	0.0113(2)
Sn/Zn2	4*c*	0.81/0.19	0.4083(1)	¼	0.0150(1)	0.0091(2)
Sn/Zn3	4*c*	0.79/0.21	0.1420(1)	¼	0.8537(1)	0.0102(2)
Sn/Zn4	4*c*	0.57/0.43	0.3100(1)	¼	0.2550(1)	0.0082(2)
Sn/Zn5	8*d*	0.20/0.80	0.0622(1)	0.5076(1)	0.3070(1)	0.0077(2)

143(2) K

Atom	Wyckoff Site	Occupancy	*x*	*y*	*z*	U_{eq}
Ce	4*e*	1	0.2594(1)	0.2497(1)	0.5642(1)	0.0085(2)
Sn/Zn1	4*e*	0.76(1)/0.24	0.0565(1)	0.2504(2)	0.0907(1)	0.0110(3)
Sn/Zn2	4*e*	0.81(1)/0.19	0.4083(1)	0.2502(2)	0.0151(1)	0.0097(3)
Sn/Zn3	4*e*	0.79(1)/0.21	0.1421(1)	0.2496(2)	0.8537(1)	0.0104(3)
Sn/Zn4	4*e*	0.57(1)/0.43	0.3099(1)	0.2501(2)	0.2552(1)	0.0080(3)
Sn/Zn5	4*e*	0.20(1)/0.80	0.0622(1)	0.0073(2)	0.3070(1)	0.0082(4)
Sn/Zn6	4*e*	0.20(1)/0.80	0.0625(1)	0.5077(2)	0.3071(1)	0.0079(4)

7.4.3 Low Temperature Crystal Structure. For $LnCu_6$ (Ln=La, Ce, Pr) compounds, as temperature decreases, the orthorhombic system would transit to monoclinic structure. [17] The temperature-dependent magnetism measurements in Figure 2(*b*) at applied filed of 1kOe indicates the structure transition beginning at 150K. Thus, the low temperature crystal data at 143K were collected to identify the existence of structure transition from orthorhombic to

monoclinic. The crystal data in Table 2 and 3 shows the structure transition from orthorhombic (*P*nma) to monoclinic ($P2_1/c$) with β changing from 90° to 90.38(3) °. The sites of Ce, Sn/Zn1, Sn/Zn2, Sn/Zn3 and Sn/Zn4 locate on general sites in monoclinic rather than mirror plane in orthorhombic structure. The octahedron built up by Sn/Zn1 and Sn/Zn2 with Ce atoms as vertex becomes flattening while the other octahedron built up by Sn/Zn3 and Sn/Zn5 with Ce atoms in orthorhombic structure becomes expanded in monoclinic phase. Furthermore, the angle between the distorted octahedral is slightly smaller in monoclinic (110.38°) than orthorhombic (110.46°) phase.

7.4.4 Magnetic Properties of $Ce(Sn_{1-x}Zn_x)_6$. The hysteresis curve of $Ce(Sn_{1-x}Zn_x)_6$ at 2K in Fig 2(*a*) indicates the non-linear relationship between magnetization and magnetic field.[37] Moreover, the magnetic susceptibility curves of $Ce(Sn_{1-x}Zn_x)_6$ (Fig. 2(b) and Fig. S1) measured by SQUID indicate Pauli paramagnetic properties.[38] The magnetic susceptibility in Figure S1 at 10kOe of $Ce(Sn_{1-x}Zn_x)_6$ can be fitted by the Curie-Weiss law with the effective magnetic moment $\mu = 2.81(3)\ \mu_B$/f.u. and the paramagnetic Curie temperature $\theta_p = 8.5(7)$ K. The magnetic results illustrate the Ce ions in the compound are trivalent with carrying a stable Ce^{3+} magnetic moment. What's more, the temperature-dependent magnetic susceptibility measured at a lower applied field (1 kOe) intimates the structural or magnetic transition below 150K in Figure 2(*b*). The AC susceptibility of $Ce(Sn_{1-x}Zn_x)_6$ was measured at 1Hz and 100Hz from 2K to 65K to confirm the magnetic properties in Fig S2. χ' is small and negative, also χ'' is small and χ' follows the Curie law $\chi' \propto T^{-1}$, as expected for paramagnetic behavior. [39]

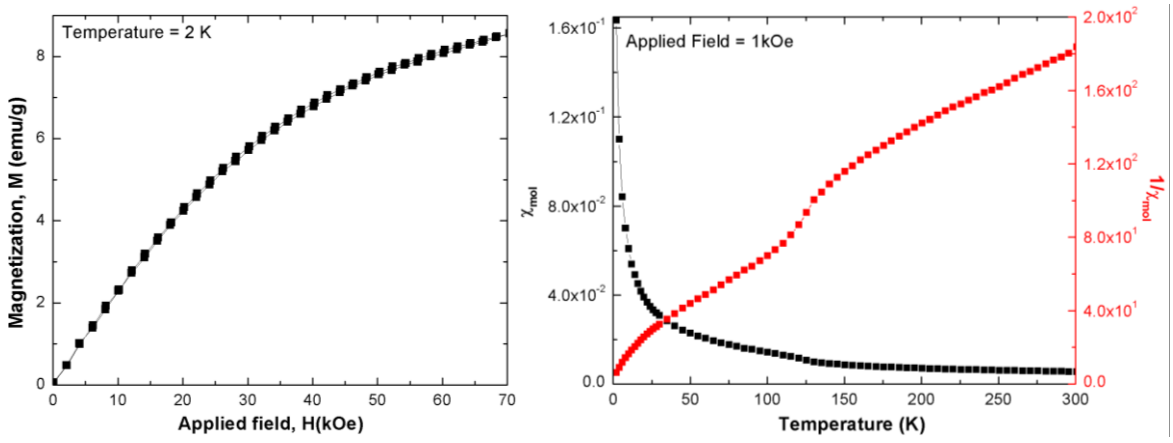

(*a*) (*b*)

Figure 2. (*a*) Magnetization changes with applied field curve at 2 K and (*b*) magnetic susceptibility curves (χ(T) and 1/χ(T)) measured in 1 kOe field for $Ce(Sn_{1-x}Zn_x)_6$.

7.4.5 Heat capacity of $Ce(Sn_{1-x}Zn_x)_6$. The total specific heat consists of electronic, phonon and magnetic contributions. The electronic coefficient provides information concerning the conduction band density of states at the Fermi level. [40] Figure 3 shows the overall heat capacity of $Ce(Sn_{1-x}Zn_x)_6$ plotted as C*p*~T between 2K and 165K. The decreasing peak around 150K is due to the phase transition from orthorhombic to monoclinic structures, confirmed by magnetic and crystal structure measurements. The inserted figure in Fig. 3 is fitted with the formula: $Cp= \gamma T+\beta T^3$ from 5K to 20K, without consideration of magnetic contribution since in the range of temperature, there is no structural or magnetic transitions. The first and second terms correspond to electronic and phonon contributions. The obtained values of the parameters are: the electronic specific heat coefficient γ=115(9) mJ/(mol K2) and phonon specific heat coefficient β=2.28(7) mJ/(mol K^4). The obtained large γ value less than 400 mJ/(mol K^2) is not a sign of a heavy-fermion type behavior. From both magnetic and heat capacity measurements, there is no magnetic ordering observed above 2K in $Ce(Sn_{1-x}Zn_x)_6$.

To estimate the physical properties at low temperature (<2 K), the Density Functional Theory (DFT) using Vienna Ab-initio Simulation Package (VASP) is applied for the theoretical calculations. VASP calculations were employed to evaluate the total energies and magnetic moments of hypothetical model of "$CeSn_{3.5}Zn_{2.5}$" ($x \sim 0.42$) with Sn/Zn1, Sn/Zn2 and Sn/Zn3 occupied by Sn atoms, Sn/Zn5 occupied by Zn atoms, and Sn/Zn4 located by two Zn atoms and two Sn atoms. To avoid any distance influence on magnetic properties, the calculations used the same set of crystal data. The LDA and LSDA (FM/AFM) models [41] were assigned the parallel/antiparallel spin alignment between Ce atoms along *b*-axis. The relative total energies and atom projected magnetic moments (μ_B/Ce) are listed for each case in Table 4. Among these three models, ferromagnetic model gives the overall lowest energy, with magnetic moment around 0.99 μ_B/Ce. Thus, the sharp peak in specific heat capacity beginning from 10K and continuing below 2K in a zero magnetic field is high possibly ascribed to the transition into a magnetically ordered phase.

Table 4. The total energies, relative total energy and atom projected magnetic moments (μ_B/Ce) of cerium atoms of $CeSn_{3.5}Zn_{2.5}$ by three different sets of DFT+U calculation. (U_1=6.89eV, J_1=0.89eV; U_2=6.39eV, J_2=0.89eV; U_3=5.39eV, J_3=0.89eV)

$CeSn_{3.5}Zn_{2.5}$	LDA	LSDA	
		FM	AFM
ΔE(meV/f.u.)	1327	0	243
μ(Ce)	0	0.97(2) 0.96(2)	±0.96(2) ±0.96(2)

Among these three models, ferromagnetic model gives the overall lowest energy, with magnetic moment around 0.99 μ_B/Ce. Experimental magnetic measurements indicate about 1.05μ_B/Ce at 2K. The experimental and theoretical results intimate the ferromagnetic properties below 2K, which also hints the unusual peak in heat capacity coming from the magnetic transition.

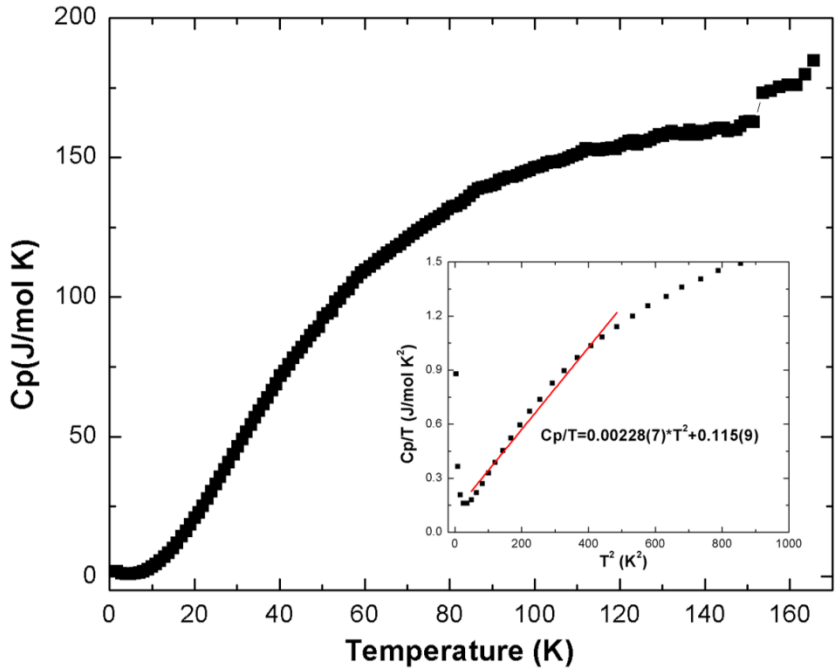

Figure 3. Temperature dependence of specific heat capacity (C*p*) curve of $Ce(Sn_{1-x}Zn_x)_6$ from 2K to 165K at 9.40×10^{-5} Torr and non-applied magnetic field. Insert: the low temperature range 5-20K is fitted with the formula: $Cp= \gamma T+\beta T^3$.

7.5 Summary. The new cerium based ternary intermetallic compounds, $Ce(Sn_{1-x}Zn_x)_6$ ($0.45(1) < x < 0.49(1)$), were synthesized and structurally characterized. They exhibit totally mixed compositions between Sn and Zn with Sn/Zn on Cu sites in $CeCu_6$ structure. Moreover, the magnetic properties of a sample analyzed as $CeSn_{3.33(6)}Zn_{2.67}$ shows it to be paramagnetic material above 2K. The heat capacity curves of $CeSn_{3.33(6)}Zn_{2.67}$ dependent on temperature demonstrate the possible phase transition behavior of the new compound with unusual peak below 2K. Ab-initio calculations substantiate the ferromagnetic ground state and indicate that the unusual peak in heat capacity below 2K is derived likely from magnetic transition at the Ce sites. The $CeCu_6$-type structure can be treated as continuous distorted octahedral by vertex-, edge- and face-sharing. The temperature-dependent magnetism measurements intimate the structural transition of the compound, which was also proved by single crystal measurement at low temperature.

7.6 Acknowledgements

This work was carried out at the Ames Laboratory, which is operated for the U.S. Department of Energy by Iowa State University under Contract No. DE-AC02-07CH11358. This work was supported by the U.S. Department of Energy, Office of Basic Energy Sciences, Division of Materials Sciences and Engineering.

7.7 References

[1] Parr, R. G.; Yang, W.; *Density-functional theory of atoms and molecules*. Oxford university press, 1989.

[2] Cococcioni, M.; de Gironcoli, S. *Phys. Rev. B* **2005**, *71*, 035105.

[3] Matar, S. F. *Review on Cerium Intermetallic Compounds: a bird's eye outlook through DFT.* Progress in Solid State Chemistry, 2013.

[4] Stewart, G. R. *Rev. Mod. Phys.* **1984**, *56*, 755.

[5] Garnier, M.; Breuer, K.; Purdie, D.; Hengsberger, M.; Baer, Y.; Delley, B. (1997). *Phys. Rev. Lett.* **1997**, *78*, 4127.

[6] Schröder, A.; Aeppli, G.; Coldea, R.; Adams, M.; Stockert, O.; v Löhneysen, H.; Bucher, E.; Ramazashvili, R.; Coleman, P. *Nature*, **2000**, *407*, 351.

[7] Germann, A.; v Löhneysen, H. *EPL*, **1989**, *9*, 367.

[8] Movshovich, R.; Graf, T.; Mandrus, D.; Thompson, J.D.; Smith, J.L.; Fisk, Z. *Phys. Rev. B*, **1996**, *53*, 8241.

[9] Shishido, H.; Shibauchi, T.; Yasu, K.; Kato, T.; Kontani, H.; Terashima, T.; Matsuda, Y. *Science*, **2010**, *327*, 980.

[10] Mathur, N. D.; Grosche, F. M.; Julian, S. R.; Walker, I. R.; Freye, D. M.; Haselwimmer, R. K. W.; Lonzarich; G. G. *Nature*, **1998**, *394*, 39.

[11] Takabatake, T., Teshima, F.; Fujii, H.; Nishigori, S.; Suzuki, T.; Fujita, T.; Yamaguchi, Y.; Sakurai, J.; Jaccard, D. *Phys. Rev. B* **1990**,*41*, 9607.

[12] Chevalier, B.; Sebastian, C. P.; Pöttgen, R. *Solid State Science* **2006**, *8*, 1000.

[13] Bando, Y.; Suemitsu, T.; Takagi, K.; Tokushima, H.; Echizen, Y.; Katoh, K.; Umeo, K.; Maeda, Y.; Takabatake, T. *J. Alloys Compd.* **2000**, *313*, 1.

[14] Adroja, D. T.; Malik, S. K.; Padalia, B. D.; Vijayaraghavan, R. *Solid State Commun.* **1988**, *66*, 1201.

[15] Takabatake, T.; Iwasaki, H.; Nakamoto, G.; Fujii, H.; Nakotte, H.; de Boer, F. R.; Sechovský, V. *Physica B: Condensed Matter*, **1993**, *183*, 108.

[16] Lenkewitz, M.; Corsépius, S.; Stewart, G. R. (1996). *J. Alloys Compd.***1996**, *241*, 121.

[17] Vrtis, M. L.; Jorgensen, J. D.; Hinks, D. G. *J. Solid State Chem.* **1990**, *84*, 93.

[18] Yamada, K.; Hirosawa, I.; Noda, Y.; Endoh, Y.; Onuki, Y.; Komatsubara, T. *J. Phys. Soc. Jpn.* **1987**, *56*, 3553.

[19] Õnuki, Y.; Shimizu, Y.; Komatsubara, T. *J. Phys. Soc. Jpn.* **1984**, *53*, 1210.

[20] Pecharsky, V. K.; Zavalij, P.Y. *Fundamentals of powder diffraction and structural characterization of materials*. Springer, 2004.

[21] Rietveld, H.M. *J. Appl. Crystallogr.* **1969**, *2*, 65.

[22] Hunter, B.A.; Howard, C.J. *LHPM-Rietica*, version 1.71: Australian Nuclear Science and Technology Organization: Menai, Australia, 2000.

[23] Sheldrick, G. M. *SADABS*, University of Gottingen: Gottingen, Germany, 2001.

[24] Sheldrick, G. M. *Acta Crystallogr. A* **2008**, *64*, 112.

[25] *SHELXTL*, version 6.10, Bruker AXS Inc.: Madison, WI, 2000.

[26] *Diamond*, version 3.2; Crystal Impact: Bonn, Germany, 2010.

[27] Kresse, G.; Hafner, J. *Phys. Rev. B* **1993**, *47*, 558.

[28] Kresse, G.; Hafner, J. *Phys. Rev. B* **1994**, *49*, 14251.

[29] Kresse, G.; Furthmüller, J. *Comput. Mater. Sci.* **1996**, *6*, 15.

[30] Kresse, G.; Furthmüller, J. *Phys. Rev. B* **1996**, *54*, 11169.

[31] Tang, W.; Sanville, E.; Henkelman, G. *J. Phys.: Compute Mater.* **2009**, *21*, 084204.

[32] Sanville, E.; Kenny, S.D.; Smith, R.; Henkelman, G. *J. Comp. Chem.* **2007**, *28*, 899.

[33] Henkelman, G.; Arnaldsson, A.; Jónsson, H. *Comput. Mater. Sci.* **2006**, *36*, 254.

[34] Monkhorst, H.J.; Pack, J.D. *Phys. Rev. B* **1976**, *13*, 5188.

[35] Blöchl, P.E.; Jepsen, O.; Andersen, O.K. *Phys. Rev. B* **1994**, *49*, 16223.

[36] Okamoto H., *Phase Diagrams for Binary Alloys*, Desk Handbook, Vol. 1, 2000.

[37] Morrish, A. H. *The Physical Principles of Magnetism,* Wiley-VCH, 2001.

[38] Jiles, D.C.; Atherton, D. L. *J. Magn. Magn. Mater.* **1986**, *61*, 48.

[39] Nogués, J.; Schuller, I. K. *J. Magn. Magn. Mater.* **1999**, *192*, 203.

[40] Ashcroft, N. W.; Mermin, N. D. *Solid State Physics*, Rinehart and Winston: New York, 1976.

[41] Casida, M. E.; Jamorski, C.; Casida, K. C.; Salahub, D. R. *J. Chem. Phys*. **1998**, *108*, 4439.

7.8 Supporting Information

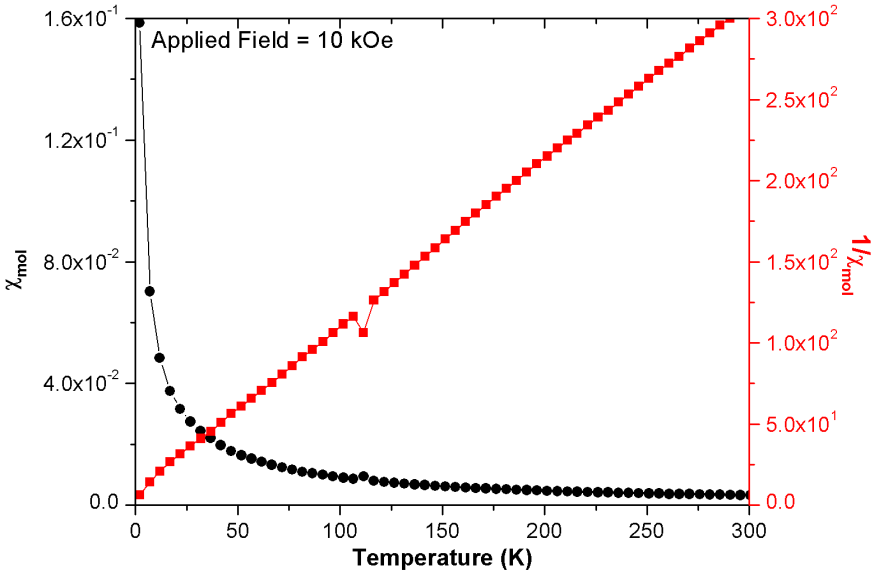

Figure S1. magnetic susceptibility curves (χ(T) and 1/χ(T)) measured in 10 kOe field for $Ce(Sn_{1-x}Zn_x)_6$.

CHAPTER 8

Summary

The work in this dissertation investigated the synthesis, crystal and electronic structures, and physical properties of Zn-based, complex intermetallic compounds. The results deepen our understanding of the relationship among chemical composition, atomic structure, physical properties and chemical bonding in Zn-containing complex intermetallic phases. Moreover, these findings also point to more questions that require further investigations.

The fully-filled 3*d*-subshell, atomic size and electronegativity of zinc act as crucial roles in determining the stable structures and site preferences in complex intermetallic compounds. Modifying the valence electron count (*vec*) is one of the skillful methods employed for seeking stable phases in solid state chemistry. When counting the valence electrons of zinc in complex intermetallic compounds, the number of valence electrons can be treated as 2 like alkali earth element, Mg, because of localized 3*d*-electron. For instance, Zn is always considered having 2 valence electrons in γ-brasses containing transition metals, like γ-brass Co-Zn, to simplify problems of controlling the compositions by adjusting *vec*.

Fully-filled 3*d*-subshell Zn has similar atomic size with partially-filled 4*d*-subshell transition metals, Ru, Rh, and Pd. When doping Ru, Rh, or Pd in Zn-based compounds, these 4*d* transition metals have great preference to replace Zn or mix with Zn. For example, Pd atoms replaced Zn in γ-brass Co-Pd-Zn system.

Moreover, when Zn reacts with *p*-block elements, like Ga, In, Ge and Sn, they could not form any compound. However, Zn becomes more activate with the elements involving *d*-electron. To synthesize Zn-based ternary compounds, choosing *p*-block elements as one of minority components is a useful way to reduce the binary impurities in final products. In

ternary compounds T-Zn-M (T: early transition metals or rare earth elements; M: main group elements), Zn has the closer electronegativity with main group elements, thus Zn and main group elements have great possibility to mix together in complex intermetallic compounds.

The influence of zinc was well understood in our research systems by predicting the physical properties like magnetism by electronic structure calculation. Combination between Stoner criterion and density of states is used to illustrate the ferromagnetism of the compounds, like β-Mn Co-Zn, γ-brasses Co-Zn and Fe-Zn, and Pd-doped Co-Zn and Fe-Zn systems. Based on our results, diamagnetic zinc does not only play as a simple role of "solvent" to dilute the magnetic moments in the compounds, but also controls the nature of magnetism by changing compositions. For example, γ-brasses Co-Zn change from weak paramagnetic to strong paramagnetic with less zinc loaded in the compounds. Furthermore, Zn decreases the Curie temperature from 1115°C for cobalt to 175°C for β-Mn CoZn, instead of diluting the magnetic moments. Future work will involve more investigation on the role of fully-filled 3*d*-subshell in controlling physical properties in Zn-containing intermetallic compounds.

CHAPTER 9

Appendix

Appendix I. High Temperature Thermoelectric Properties of the Solid Solution Zintl Phase $Eu_{11}Cd_6Sb_{12-x}As_x$ ($x < 3$)

Modified from a paper in Chemistry of Materials
(*Chem. Mater.* **2014**, 26, 1393)

Nasrin Kazem[1], Weiwei Xie[2], Saneyuki Ohno[3], Alexandra Zevalkink[3], Gordon J. Miller[2], G. Jeffrey Snyder [3], Susan M. Kauzlarich[1,4]

1 — Department of Chemistry, University of California, One Shields Ave., Davis, CA 95616, USA
2 — Department of Chemistry, Ames Laboratory, Iowa State University, US-DOE, Ames, IA 50011, USA
3 — Materials Science, California Institute of Technology, 1200 E. California Boulevard, Pasadena, CA 91125, USA

9.1.1 Abstract

Zintl phases are compounds that have shown promise for thermoelectric applications. The title solid-solution Zintl compounds were prepared from the elements as single crystals using a tin flux for compositions x = 0, 1, 2 and 3. $Eu_{11}Cd_6Sb_{12-x}As_x$ ($x < 3$) crystallize isostructurally in the centrosymmetric monoclinic space group $C2/m$ (no. 12, Z = 2) as the $Sr_{11}Cd_6Sb_{12}$ structure type (Pearson symbol $mC58$). Efforts to make the As compositions for x exceeding ~3 resulted in structures other than the $Sr_{11}Cd_6Sb_{12}$ structure type. Single crystal X-ray diffraction indicates that As does not randomly substitute for Sb in the structure, but is site specific for each composition. The amount of As determined by structural refinement was verified by electron microprobe analysis. Electronic structures and energies calculated for various model structures of $Eu_{11}Cd_6Sb_{10}As_2$ (x = 2) indicated that the preferred As

substitution pattern involves a mixture of three of the six pnicogen sites in the asymmetric unit. In addition, As substitution at the Pn4 site opens an energy gap at the Fermi level, whereas substitution at the other five pnicogen sites remain semimetallic with a pseudo gap. The thermoelectric properties of these compounds were measured on hot pressed, fully densified pellets. The samples show exceptionally low lattice thermal conductivities from room temperature to 775 K: 0.78-0.49 W/mK for $x = 0$; 0.72-0.53 W/mK for $x = 1$; and 0.70-0.56 W/mK for $x = 2$. $Eu_{11}Cd_6Sb_{12}$ shows a high p-type Seebeck coefficient (+118 to 153 μV/K), but also high electrical resistivity (6.8 to 12.8 mΩ·cm). The value of zT reaches 0.23 at 774 K. The properties of $Eu_{11}Cd_6Sb_{12-x}As_x$ are interpreted in discussion with the As site substitution.

9.1.2 Introduction

Thermoelectric materials enable the generation of electricity from a heat gradient and vice versa with no harmful emissions. However, this energy conversion is a low efficiency process which has prevented broader usage of thermoelectric devices. The operation of thermoelectric materials is described by a figure of merit, $zT = \alpha^2 T/\kappa\rho$, in which α is the Seebeck coefficient, ρ is the electrical resistivity, and κ is the thermal conductivity. The figure of merit characterizes how efficiently a material converts a heat gradient into electricity - the higher zT, the greater the efficiency.

An ideal compound for thermoelectric applications can be imagined as a material that possesses different pathways to transport electrons and phonons. In this way, thermal conductivity can be tuned while the electronic properties remain unaffected, and vice versa, leading to the idea of the "phonon glass-electron crystal" (PGEC) approach introduced by Slack.[1] In principle, electronic and thermal properties of materials can be independently

optimized while minimizing effects on the other quantities to achieve maximum *zT* values. Among the best candidates that can satisfy this idea of different charge carrier and heat carrier routes in one material are Zintl phases.[2]

Zintl phases are made of elements with different electronegativities in which the most electropositive element formally donates its valence electrons to the more electronegative elements, which form (poly)anionic networks that satisfy the octet rule. The electropositive element, serving now as a cations, can be considered as guest atoms within the cavities formed by the (poly)anionic network.[2] These cations, therefore, have important roles for thermoelectric properties both to tune the carrier concentrations and to contribute to phonon scattering mechanisms. On the other hand, the covalent bonds in the (poly)anionic network are responsible for the electron-crystal region.[2] One of the interesting characteristics of Zintl phases is that they are favorable for isovalent substitutions as seen, for example, in $Yb_{1-x}Ca_xCd_2Sb_2$,[3] $Eu_{1-x}Yb_xCd_2Sb_2$,[4] and $Yb_{13}CaMnSb_{11}$.[5] Because the exact electron donating abilities of various cations are slightly different due to their different electronegativities, the charge carrier concentration can be finely tuned by such mixed occupancies at the cation sites to maximize *zT* without strongly perturbing the anionic network.[6] Many high *zT* Zintl compounds, such as $Yb_{14}MnSb_{11}$,[7] $Yb_{1-x}Ca_xZn_2Sb_2$,[3] and $Ba_{0.08}La_{0.05}Yb_{0.04}Co_4Sb_{12}$ skutterudites,[8] have been synthesized for thermoelectric applications.

Although Zintl phases form a large family of inorganic compounds with many different crystal structures,[9] only a small fraction of them have been studied for their thermoelectric properties. $Eu_{11}Cd_6Sb_{12}$ was selected in this study for its potential thermoelectric applications because it shows low electrical resistivity, contains heavy atoms, and adopts a complex

structure (Figure 1), similar to other compounds which have good thermoelectric properties.[3-5] $Eu_{11}Cd_6Sb_{12}$ adopts the $Sr_{11}Cd_6Sb_{12}$[10] structure type, which can be described as infinite, one-dimensional tubes of two edge-fused pentagons. The overall structure of $Sr_{11}Cd_6Sb_{12}$,[10] projected along the *b*-axis, is shown in Fig. 1. Infinite $[Cd_6Sb_{12}]^{22-}$ chains running along the *b*-axis involve a covalent network of vertex-sharing $CdSb_4$ tetrahedra that are separated by Sr^{2+} cations. In this paper, we explore the chemical and physical flexibility of this structure type by using the pnicogen sites for alloying, leading to lower lattice thermal conductivities, and investigate this alloying effect on the subsequent thermoelectric properties of $Eu_{11}Cd_6Sb_{12-x}As_x$ phases. Theoretical calculations were carried out to understand the As site preferences and to assess their effects on electronic energy bands, which in turn influences thermoelectric performance of $Eu_{11}Cd_6Sb_{12-x}As_x$. We present herein details of the synthesis, structural characterization, and transport properties of the solid solution $Eu_{11}Cd_6Sb_{12-x}As_x$ (x = 0, 1 and 2), along with discussing the observed As site specificity behavior which is noticed in other phases such as $Ba_2Cd_2(Sb_{1-x}As_x)_3$.[11]

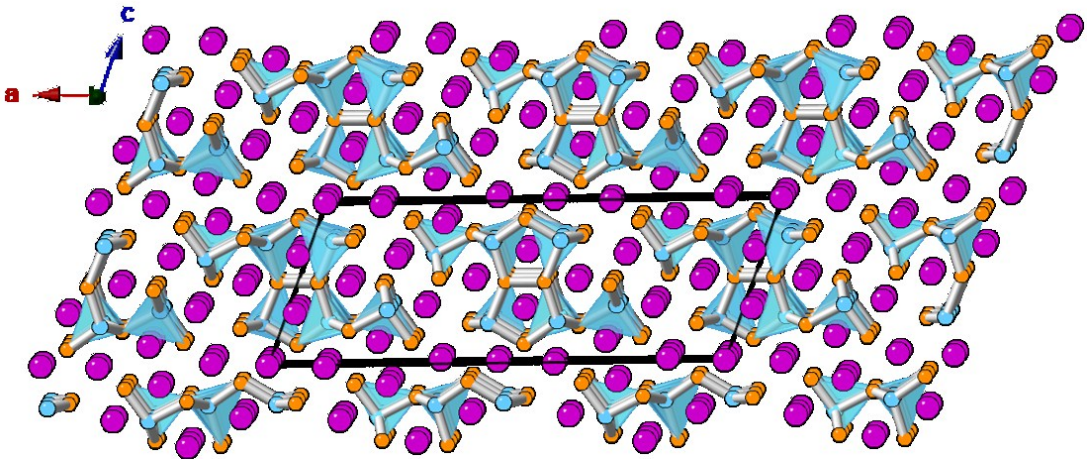

Figure 1. A perspective view of the crystal structure of $Sr_{11}Cd_6Sb_{12}$ down the *b*-axis. The network of Cd–Sb covalent bonds and [$CdSb_4$] tetrahedra are emphasized. One unit cell outline is included.

9.1.3 Experiments

9.1.3.1 Synthesis. $Eu_{11}Cd_6Sb_{12-x}As_x$ compounds were prepared similarly to the literature procedure,[12] but using a 30-fold excess tin flux instead of a 50-fold excess lead; details of flux-growth synthetic procedures can be found elsewhere. All manipulations were carried out in argon or nitrogen-filled glove boxes or under vacuum.[13] All starting elements were loaded in 5 cm^3 alumina crucibles in the respective Eu:Cd:Sb:As:Sn molar ratios of 11:6:12–x_{syn}:x_{syn}:30 (x_{syn} is an integer from 0 to 12) to a total weight of ~10 g; (Sources: Eu, Ames Lab, 99.999%; Cd pieces, Alfa, 99.98%; Sb shot, Alpha Aesar 99.9 %; and Sn shot, Alpha Aesar 99.99 %). The crucibles were placed into fused silica tubes with a second crucible filled with SiO_2 wool placed on top, and the fused silica tubes were sealed under less than 200 mtorr of vacuum. The sealed silica tubes were placed upright in a box furnace and heated at 10 ˚C/h to 500 ˚C, allowed to dwell 6 h, and then heated at 10 ˚C/h to 950 ˚C for 96 h. Subsequently, the reaction vessels were slowly cooled at 5 ˚C/h to 600 ˚C, at which point molten tin was removed by inverting and placing the reaction vessels into a centrifuge, and spinning for 2-3 min at 6500 rpm. Finally, the reaction vessels were opened in a N_2-filled glove box equipped with an optical microscope and at moisture levels below 1 ppm. Silver–colored, reflective crystals of $Eu_{11}Cd_6Sb_{12-x}As_x$ were observed as the product.

9.1.3.2 Single-Crystal X-ray Diffraction. Structure determination for the products of each reaction was performed on more than two crystals and unit cell determination was accomplished for at least ten crystals of a variety of shapes from each reaction to determine the phase width and purity of each reaction product. Single crystals of $Eu_{11}Cd_6Sb_{12-x}As_x$ (x_{syn} > 0) were selected in Paratone N oil to minimize the oxidation of the sample under a microscope and then, if necessary, cut in to the desired dimensions for data collection. Selected crystals were positioned on the tops of glass fibers or MiTeGen micro loops and

quickly transferred to the nitrogen stream and mounted on the goniometer. Diffraction data for $Eu_{11}Cd_6Sb_{12-x}As_x$ were collected at 90 K on a Bruker Apex II diffractometer with graphite-monochromated Mo-Kα radiation (λ = 0.71073 Å) and CCD area detector. Several sets of ω-scans (0.3°/frames) at different Φ settings were collected while in a nitrogen stream. Determinations of unit cell parameters, refinements, and raw frame data integrations were completed using the APEX II v2011.4-1 software. The space group was determined on the basis of systematic absences using XPREP, followed by a semi-empirical absorption correction based on symmetrically equivalent reflections with the program SADABS and the structure was solved using direct methods from the SHELXTL Version 6.14 package. After successful assignments of the high electron density peaks as Eu, Cd, and Sb, the occupancy on each atomic site was examined. For all compounds, the refined occupancies of only some of the six pnicogen sites (i.e. Pn1, Pn2 and Pn5 sites in $x_{syn} = 1$) which were initially assigned to Sb atoms, were significantly low indicating that lighter As atoms were involved into those sites. Occupancies of the shared Sb/As sites were fixed to fully fill each crystallographic sites and they were assigned the same coordinates and atomic displacement parameters. An unrestrained refinement of site occupancies, coordinates and thermal parameters lead to an unstable refinement. The final optimized R-factors, U-values, and peak/hole values was obtained by applying the restriction on aforementioned parameters. Similar refinements for each structure lead to the structural models described herein. The CIFs are provided in the Supporting Information.

9.1.3.3 Electron Microprobe Analysis. Single crystalline and pelleted samples were enclosed in epoxy and polished to provide flat surfaces for analysis. The polished samples were mounted on 25 mm metal rounds using adhesive carbon tape and were carbon coated to

make them conducting. Microprobe analysis was performed by using a Camera SX-100 Electron Probe Microanalyzer with wavelength-dispersive spectrometers. Back scattered electrons were used for imaging the surfaces of the samples, characteristic X-rays generated by samples were analyzed by wavelength-dispersive spectroscopy to determine the compositions of samples, and element mapping was accomplished to assess the spatial distribution of elements in the samples. X-ray intensities of Eu, Cd, Sb, As and Sn were compared with the calibrated standards $EuPO_3$, Cd (metal), Sb (metal), GaAs and Sn (metal) for quantitative analysis. At least 15 different points with a spot size of 1 μm were analyzed for each sample.

9.1.3.4 Electronic Structure Calculations. Electronic structures and total energies of various model structures of $Eu_{11}Cd_6Sb_{10}As_2$ (x = 2) were calculated by the tight-binding, linear muffin-tin orbital method in the atomic sphere approximation (TB-LMTO-ASA) using the Stuttgart code.[14] Exchange and correlation were treated by the local density approximation (LDA).[15] In the ASA method, space is filled with overlapping Wigner-Seitz (WS) spheres. The symmetry of the potential is considered spherical inside each WS sphere and a combined correction is used to take into account the overlapping part.[16] The ranges of WS radii are: 3.79-4.01 Å for Eu sites; 2.80-2.97 Å for Cd sites; and 3.06-3.49 Å for Sb/As sites. Empty spheres were necessary to achieve the LMTO volume criterion, and the overlap of WS spheres was limited to no larger than 16%. The basis set for the calculations included Eu 6*s*, 6*p*, 5*d*; Cd 5*s*, 5*p*, 4*d*; Sb 5*s*, 5*p*, 5*d*; and As 4*s*, 4*p*, 3*d* wavefunctions. The convergence criterion was set to 0.5 meV. A mesh of 14-20 *k* points in the irreducible wedge of the first Brillouin zone was used to obtain all integrated values, including the density of states (DOS) and crystal orbital Hamiltonian population (COHP) curves.

9.1.3.5 Synchrotron Powder X-ray diffraction. High resolution synchrotron powder diffraction data for $Eu_{11}Cd_6Sb_{12-x}As_x$ were collected at room temperature (295.0 K) using beamline 11-BM at the Advanced Photon Source (APS),[17] Argonne National Laboratory, using an average wavelength of 0.41396 Å produced by a bending magnet (BM) with 30 keV energy. Si(111) double crystals were used as the monochromator and a sagittally bent Si(111) crystal focused the beam to the dimensions of 1.5 mm (horizontal) × 0.5 mm (vertical) on the sample. Twelve discrete detectors covering an angular range from –6º to 16º 2θ are scanned over a 34º 2θ range, with data points collected every 0.001º at a scan speed of 0.01º/s.[18] All samples were diluted by mixing with pulverized fused silica with the mass ratio 1:1 amorphous SiO_2:sample. The amorphous SiO_2 dilutant was necessary to overcome the strong absorption issues due to the presence of high-*Z* elements in these solid solutions. The diluted samples were sealed in quartz capillaries of 0.3 mm in diameter to minimize oxidation. A small broad peak at a low 2θ angle, especially for x = 2, comes from the amorphous SiO_2. The program FullProf was used to perform profile matching with constant scale factor by employing pseudo-Voigt axial divergence asymmetry peak shape for the calculated patterns.

9.1.3.6 Sample Preparation for Transport Properties. High temperature thermoelectric property measurements were performed on $Eu_{11}Cd_6Sb_{12-x}As_x$ ($x < 3$) hot pressed pellets. To get dense samples, polycrystalline powder samples were first cold-pressed at 415 MPa in hardened steel die sets, then the pressure was released to 206 MPa and immediately hot-pressed at this pressure for 30 min under an argon atmosphere at 500 ^{0}C to make 10-mm diameter pellets with approximately 1.5-mm thickness. Densities of the pellets found to be about 95% of the calculated densities. Samples were polished to obtain smooth and parallel faces appropriate for electrical and thermal transport properties measurements.

9.1.3.7 Transport Properties Measurements. High temperature resistivity (ρ) data were measured to 773 K by using the van der Pauw technique and pressed niobium contacts. The Hall effect was measured simultaneously in a 2 T magnetic field.[19] Seebeck data were obtained using Chromel–Nb thermocouples. The Seebeck coefficient at each temperature obtained by oscillating ΔT by ±10 K about a fixed average temperature. The resulting linear voltage response yields the Seebeck coefficient ($\Delta V = \alpha \Delta T$).[20] Thermal diffusivity data were collected using a Netzsch LFA 457. The temperature of measurements was limited to 773 K because of the thermal instability of $Eu_{11}Cd_6Sb_{12-x}As_x$ (x = 0, 1, 2) observed above this temperature; TG-DSC data are provided in the Supporting Information, mass loss was observed at around 887 K can be caused by As sublimation. The final product after TG-DSC was not investigated further. Thermal conductivities were calculated from the equation, $\kappa_{total} = C_p dD$, in which C_p is the Dulong–Petit heat capacity ($C_p = 3RM/N$; R is the gas constant, M is the molar mass, and N is number of atoms per formula unit), d is the geometric density, and D is measured thermal diffusivity from flash diffusivity measurements given in the Supporting Information.

9.1.4 Results and discussion

9.1.4.1 Structures and Compositions. Single crystal and powder X-ray diffraction (PXRD) and electron microprobe analysis (EMPA) were used to investigate the products of each reaction to prepare the solid solutions $Eu_{11}Cd_6Sb_{12-x}As_x$ (x_{syn} = 0 to 12). Single crystal X-ray diffraction studies show that there is a small range of compositions of $Eu_{11}Cd_6Sb_{12-x}As_x$ that crystallize in the $Sr_{11}Cd_6Sb_{12}$ structure type. The compound with the highest As content characterized by single crystal X-ray diffraction was $Eu_{11}Cd_6Sb_{7.76}As_{4.24(6)}$ from the reaction of x_{syn} = 3. However, this phase appeared as a minor product together with a new structure,

which was the major phase and will be reported in another publication. Herein, samples of $Eu_{11}Cd_6Sb_{12-x}As_x$ with the $Sr_{11}Cd_6Sb_{12}$ structure type as the major phases of each product will be discussed, so $x_{syn} < 3$. These structures are solved with acceptable R_1 and wR_2 values ($R_1 < 2.3\%$ and $wR_2 < 5\%$); the details can be found in the Supporting Information. There was no evidence for Sn substitution from the structure refinements, in good agreement with EMPA on single crystals. Figure 2a shows that the lattice parameters decrease with increasing As content *x* (determined from single crystal X-ray diffraction), a result which is in agreement with the covalent radii of Sb (1.39 Å) and As (1.19 Å).[21] The *b*-axis decreases slightly compared with the decreases in *a*- and *c*-axes with increasing As content. Moreover, the linear variation in lattice constants with As content indicate its solid solution behavior, in accordance with Vegard's law.[22, 23]

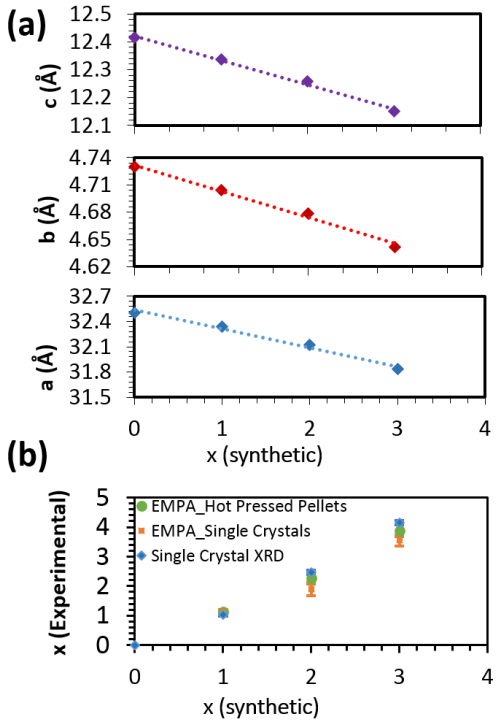

Figure 2. **a)** Lattice parameters for $Eu_{11}Cd_6Sb_{12-x}As_x$ obtained from single-crystal X-ray diffraction plotted as a function of synthetic values x, *x*(Synthetic). *a*-axis (squares), *b*-axis (circles), and *c*-axis (triangles) are presented in the bottom, middle, and top plot, respectively, lattice parameters for x = 0 are obtained from the

literature.[12] **b)** Experimentally determined composition, x(Experimental), for $Eu_{11}Cd_6Sb_{12-x}As_x$ from single crystal X-ray diffraction (triangles) and EMPA of the single crystals (squares) and hot pressed pellets (circles) vs synthetic values, x(Synthetic).

Figure 2b shows the x values in $Eu_{11}Cd_6Sb_{12-x}As_x$ determined independently from single crystal data refinements and EMPA on single crystal samples and the hot pressed pellets vs their loaded (synthetic) values, x_{syn}. The microprobe results from the single crystal samples and the hot pressed pellets give similar values for the amount of As present in the compounds especially for the low x_{syn} amounts. The backscattered electron microscopy (BSE) and elemental mapping images of hot pressed slices with total area sizes more than 4 mm^2 shown in Figure 3 indicate that As is homogenously distributed. EMPA on single crystals did not show the presence of other phases. However, the electron microprobe studies on the pressed pellets indicate that there is a minor phase with the possible composition of $Eu_{10}CdSb_{10-x-y}Sn_xAs_y$, an unknown phase., the bright gray areas in the backscattered images in Fig. 3 were identified as this composition and indicated by arrows. Our attempts to find single crystals of this phase as a possible minority phase in the single crystal product were unsuccessful suggesting that this minor phase arises via the hot press procedure through the reaction between the residual tin and the main phase of each compound at high temperature and pressure. The pellets also showed a very minor presence of Eu_2O_3 impurities.

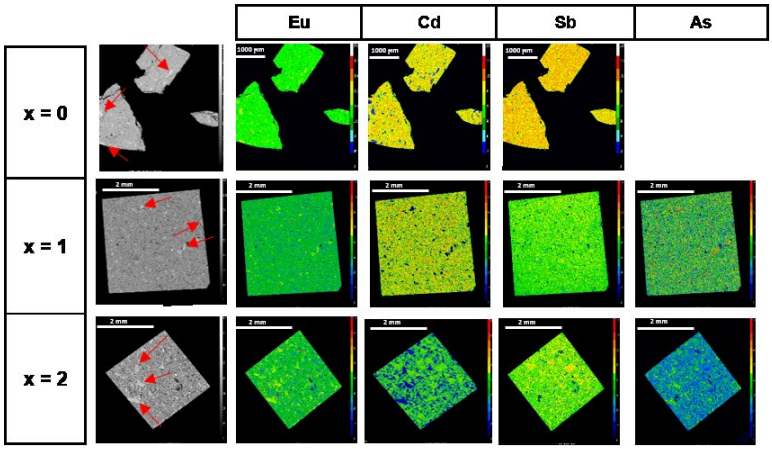

Figure 3. BSE images and X-ray maps of hot pressed slices for $Eu_{11}Cd_6Sb_{12-x}As_x$ solid solutions (x = 0, 1, 2), the areas of bright contrast identified with the $Eu_{10}Cd_1Sb_{10-x-y}Sn_xAs_y$ composition are indicated by arrows.

The average compositions with standard deviations in parentheses from EMPA on single crystals and pressed pellets are provided in Table 1 along with the compositions from single crystal X-ray diffraction. There is good agreement between the compositions obtained from single crystal X-ray diffraction and from EMPA (see also Figure 2b). The presence of the minor phase $Eu_{10}Cd_1Sb_{10-x-y}Sn_xAs_y$ (generalized stoichiometry: $Eu_{10}MPn_{10}$) and Eu_2O_3 observed by EMPA in the pressed pellets is not apparent in the powder patterns obtained from a conventional powder X-ray diffractometer of samples obtained before or after hot pressing. Therefore, to investigate the quality of each sample, synchrotron powder XRD (SPXRD) was utilized. Representative patterns of the x = 0, 1, and 2 samples of $Eu_{11}Cd_6Sb_{12-x}As_x$ are shown in Figure 4. The best profile matching was achieved by using the crystal structures solved for crystals of each reaction. The corresponding calculated patterns are shown as orange dashed lines overlaid on each observed pattern, shown in black, and the difference profile is also shown below each pattern in black. The difference profiles indicate some unassigned peaks are present in the 2θ range of 7˚-10˚. Assigning these peaks and utilizing software such as Dicvol and Treor to determine a solution for their unit cells were not successful. However, these unassigned diffraction peaks might be attributed to the minor

phase identified by EMPA as $Eu_{10}MPn_{10}$. Further analysis by the Rietveld method was not reliable as a result of the presence of unassigned peaks belonging to an unknown phase (or phases) because the contribution of each phase to each peak cannot be properly evaluate. However, most of the peaks are fully matched with the parent structure $Eu_{11}Cd_6Sb_{12}$ as shown in Figure 4.

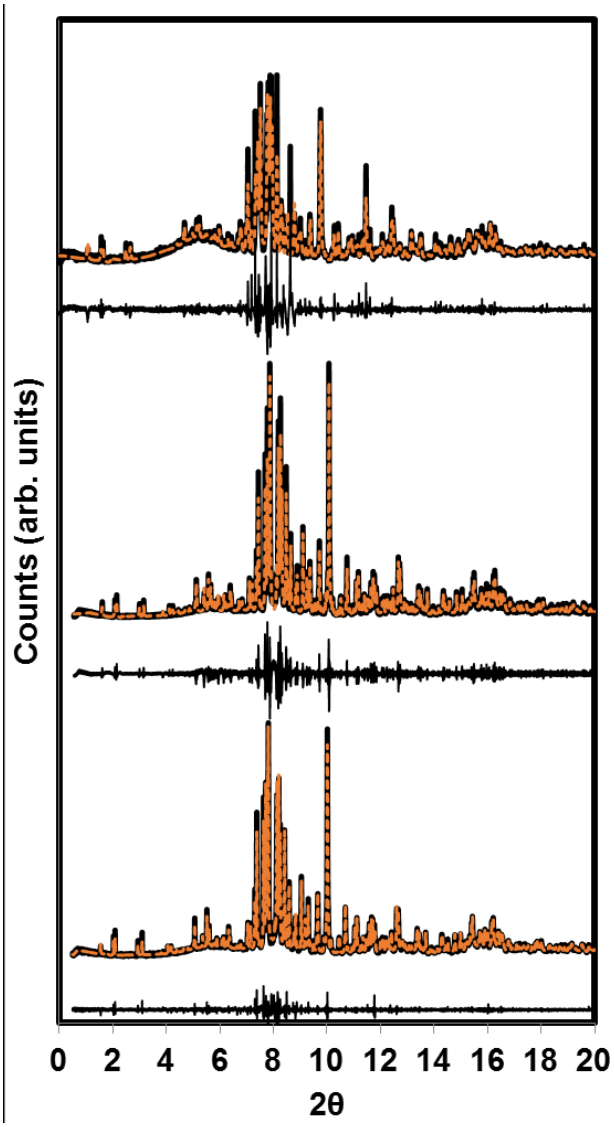

Figure 4. High resolution synchrotron powder X-ray diffraction patterns for $Eu_{11}Cd_6Sb_{12-x}As_x$ solid solutions, x = 0 (lower pattern), x = 1 (middle pattern) and x = 2 (top pattern) and their overlaid calculated patterns (in orange dashed lines) and difference profiles (in black) below each set.

Table 1. Comparisons of Elemental Analysis from Single-Crystal X-ray Diffraction, and EMPA from Single Crystals and Hot-Pressed Pellets of $Eu_{11}Cd_6Sb_{12-x}As_x$

			Composition from EMPA on Pellets	
X_{Syn}	Composition from Single Crystal XRD	Composition from EMPA on Single Crystals	Major phase 11_6_12	Minor phase 10_1_10
0.0	$Eu_{11}Cd_6Sb_{12}$	$Eu_{10.95(7)}Cd_{6.03(5)}Sb_{12.01(2)}$	$Eu_{10.95(7)}Cd_{6.03(5)}Sb_{12.01(2)}$	$Eu_{10.07(9)}Cd_{0.96(18)}Sb_{9.02(4)}Sn_{0.95(9)}$
1.0	$Eu_{11}Cd_6Sb_{10.97}As_{1.03(3)}$	$Eu_{10.95(5)}Cd_{6.06(5)}Sb_{10.88(4)}As_{1.11(3)}$	$Eu_{10.95(3)}Cd_{6.05(1)}Sb_{10.90(7)}As_{1.12(5)}$	$Eu_{10.0(1)}Cd_{1.05(1)}Sb_{7.53(4)}As_{1.43(7)}Sn_{1.0(1)}$
2.0	$Eu_{11}Cd_6Sb_{9.64}As_{2.46(5)}$	$Eu_{11.01(5)}Cd_{6.05(3)}Sb_{9.7(2)}As_{2.2(2)}$	$Eu_{11.04(3)}Cd_{5.99(3)}Sb_{10.1(2)}As_{1.8(2)}$	$Eu_{10.07(9)}Cd_{1.02(4)}Sb_{6.61(12)}As_{2.32(11)}Sn_{0.98(9)}$

9.1.4.2 Arsenic Site Preferences. Refined site occupancies obtained from single crystal diffraction data show that As substitution on the pnicogen sites is not statistically random, but that some pnicogen positions are more susceptible to substitution than others, a result which is called the "coloring problem".[24] In the crystal structure of the parent compound, $Eu_{11}Cd_6Sb_{12}$, which has been studied in detail by Saparov et al.,[12] there are six different crystallographic sites for Sb (shown in Figure 5) that can be substituted by As atoms. Table 2 summarizes our experimental results, which shows, for example in $Eu_{11}Cd_6Sb_{10.97}As_{1.03}$, preferential substitution occurs at the Pn2, Pn1, and Pn5 sites, respectively.

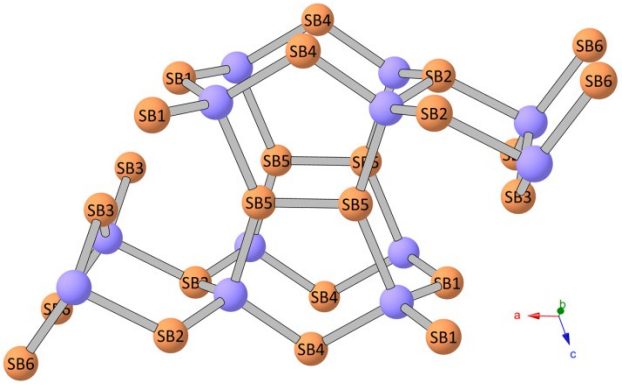

Figure 5. Double pentagonal tubes repeated along the crystallographic *b*-axis made by the connecting $CdSb_4$ tetrahedral units (sky blue spheres = Cd; orange spheres = Sb). The six distinct crystallographic pnicogen sites are labeled; Eu atoms are removed for clarity.

This preferential substitution cannot be explained by simple chemical reasoning such as electronegativities of As and Sb and the respective formal charges for each pnicogen (Pn) site (i.e. one-bonded Pn = –2, two-bonded Pn = –1, three-bonded Pn = 0), which are listed in Table 1 using the Zintl-Klemm formalism.[9] According to this simple idea, the more electronegative As atoms should substitute for Sb at those sites with the more negative formal charges, but the most preferred site is, in fact, Pn2, which has the most positive formal charge of zero. Since this simplistic idea does not readily interpret the refined As substitution patterns, quantum chemical calculations were carried out on six model structures of "$Eu_{11}Cd_6Sb_{10}As_2$" in which As completely replaces Sb at each of the six independent pnicogens sites.

Table 2. Percent occupation As (and the standard deviations) in the six crystallographic positions of pnicogen atoms in $Eu_{11}Cd_6Sb_{12-x}As_x$ and relative total energies (ΔE) in meV/f.u. and K/f.u. with respect to the lowest energy model for As substitution in the six sites for "$Eu_{11}Cd_6Sb_{10}As_2$."

Site	Pn1	Pn2	Pn3	Pn4	Pn5	Pn6
Formal Charge	–1	0	–1	–1	0	–2
$Eu_{11}Cd_6Sb_{10.97}As_{1.03}$	10.6(5)%	34.5(5)%	No As	No As	6.5(5)%	No As
$Eu_{11}Cd_6Sb_{9.64}As_{2.46}$	28.9(7)%	60.4(6)%	No As	11.8(6)%	19.0(7)%	No As
$Eu_{11}Cd_6Sb_{7.85}As_{4.15}$	53.87(6)%	79.6(6)%	9.9(6)%	27.9(6)%	37.9(6)%	2.8(6)%
ΔE (meV/f.u.)	63.9	21.6	235.1	133.7	0	165.5
ΔE (K/f.u.)	741	251	2727	1551	0	1920

The total energies of the six different substitution patterns of $Eu_{11}Cd_6Sb_{10}As_2$ are also listed in Table 2 relative to the lowest energy case Pn5. According to these relative total energies, the pattern of As substitution for Sb atoms in ternary "$Eu_{11}Cd_6Sb_{12}$" follows the qualitative order (Pn5-Pn2-Pn1)—(Pn4-Pn6)—(Pn3). We can use these relative total

energies to estimate the distribution of As atoms among the six different pnicogen sites as a function of temperature by using a Boltzmann distribution for these six models. At 300 K, the calculated As site occupancies are 66% (Pn5), 28% (Pn2), and 6% (Pn1); at 800 K, the As site occupancies become 42% (Pn5), 31% (Pn2), 17% (Pn1), 6% (Pn4), and 4% (Pn6). Clearly, the calculations reproduce gross trends in the As substitution pattern, by identifying the three sites at which As is found to replace Sb for the lowest As content $x = 1.03$. On the other hand, the calculations do not correctly follow the quantitative results that site Pn2 is most favorable for As substitution.

To understand the relative energies of the six different As substitution patterns, analysis of the electronic structures of $Eu_{11}Cd_6Sb_{12}$ and "$Eu_{11}Cd_6Sb_{10}As_2$" is warranted. In the valence orbital region of the electronic DOS curve for $Eu_{11}Cd_6Sb_{12}$,[12] shown in Figure 6, there are three distinct regions: (i) 8-12 eV below the Fermi level E_F show mostly Sb 5*s* bands mixed with Cd 5*s* and 4*d* and small amounts of Eu valence orbitals; (ii) 0-6 eV below E_F arises mostly from Sb 5*p* bands mixed with Cd 5*p* and Eu 6*s*/5*d* states; and (iii) above E_F, which contains mostly Eu 6*s* and 5*d* character. There is a clear pseudogap at E_F, which would suggest $Eu_{11}Cd_6Sb_{12}$ to be, at best, semimetallic. In line with the Zintl-Klemm formalism, the Cd–Sb and Sb5–Sb5 COHP curves indicate maximum orbital interactions, i.e., "covalency", in $Eu_{11}Cd_6Sb_{12}$, which can be formulated as $(Eu^{2+})_{11}(Cd^{2+})_6(Sb^{3-})_{10}(Sb_2^{4-})$.

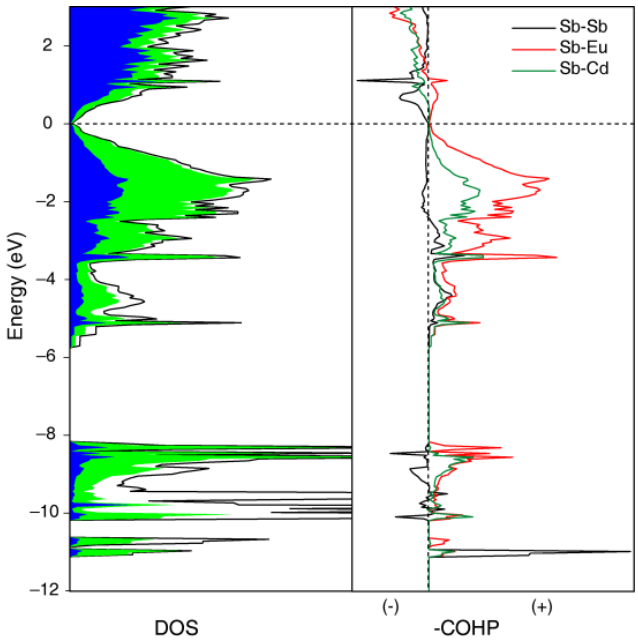

Figure 6. DOS curve decomposed into its atomic components (Eu: blue; Sb: green; Cd: white) and significant COHP curves for $Eu_{11}Cd_6Sb_{12}$ (+ is bonding; − is antibonding). E_F for 154 e^- is set to 0 eV.

For comparison, the DOS curves for the six different As-substitution models $Eu_{11}Cd_6Sb_{10}As_2$ are presented in Figure 7. These curves provide some insights about the preferred pattern of As substitution by focusing on the As partial DOS contributions. For the cases As2 and As5, which are the two lowest energy substitution patterns, the As partial DOS extends throughout all of region (ii), that is, throughout the entire valence band. Thus, these states show enhanced electronic occupation as compared to the other pnictide states and will be favored for substitution by the electronegative As atoms. This outcome can be more clearly visualized by taking ratios of each As partial DOS curve with respect to the partial DOS curve for the As4 site (see Supporting Information): from 2-6 eV below E_F, contributions from As2 and As5 clearly dominate the total DOS, whereas contributions from the remaining pnictide sites show a more uniform, yet oscillating, distribution throughout the entire valence band. The broad partial DOS arising from the As2 and As5 contributions is a signature of greater orbital overlap with their neighboring sites as compared to the other

pnictide positions. These two sites have the largest connectivity within the formal Zintl polyanion, $[Cd_6Sb_{12-x}As_x]^{22-}$: Pn5 is three-bonded to 2 Cd atoms and 1 site Pn5 atom (Sb or As); Pn2 is also three-bonded, but to 3 Cd atoms. Sites Pn1, Pn3, and Pn4 are two-bonded to Cd sites, whereas site Pn6 is one-bonded to a Cd site.

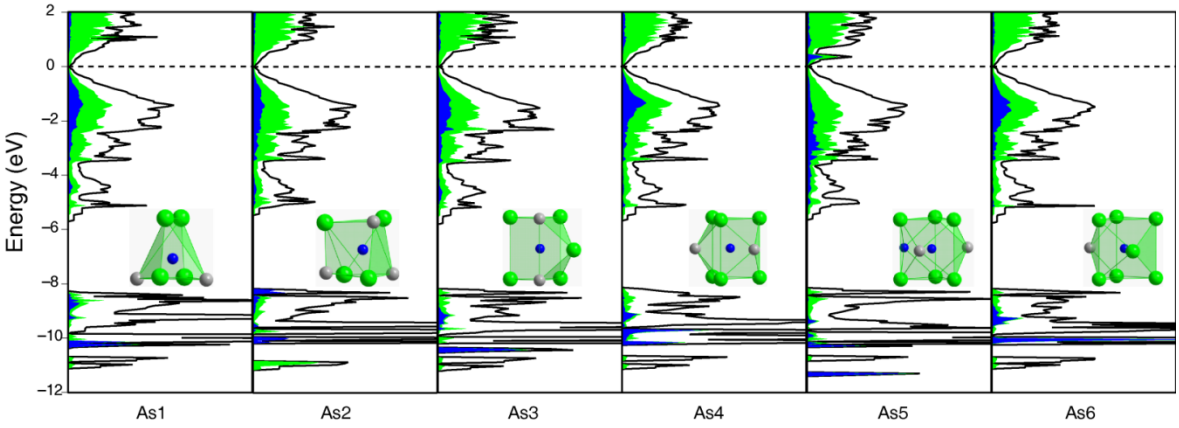

Figure 7. DOS curves emphasizing the pnicogens contributions (As: blue; Eu: green; Cd+Sb: white) for six different models of $Eu_{11}Cd_6Sb_{10}As_2$. E_F for 154 e^- is set to 0 eV. The coordination polyhedron for each site (for distances less than 4.0 Å) are included (Eu: green; Cd: gray; Sb/As: blue).

In model As5 above, all dimers were treated as formally $(As–As)^{4-}$. To examine the realistic possibility that mixed site substitution patterns may be energetically favorable, three additional sets of structural models of $Eu_{11}Cd_6Sb_{10}As_2$ were constructed, in which the dimers are heteroatomic $(Sb–As)^{4-}$, listed as cases (a)-(c) in Figure 8. Since the unit cell contains two formula units, the dimer positions Pn5 are assigned 2 As and 2 Sb atoms for which there are three possible distinct patterns per unit cell, and various arrangements with the remaining two As atoms occupying two of sites Pn1, Pn2, Pn3, Pn4, or Pn6 were examined. For completion, Figure 8 includes the two homoatomic cases $(As–As)^{4-}$ (d) and $(Sb–Sb)^{4-}$ (e). Table 3 summarizes the relative average total energies for each case relative to case (d), which is model As5 described above. The average total energy for case (e) corresponds to the average value of models (Pn1-Pn4 + Pn6) listed in Table 2.

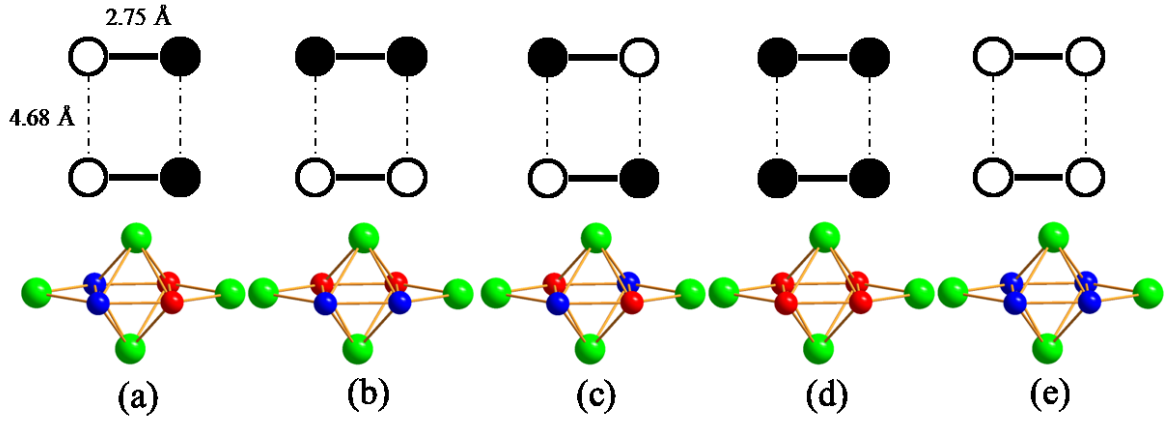

Figure 8. Five different As/Sb distributions among site Pn5, including three heteroatomic (a-c) and two homoatomic (d-e) cases. (Eu: green; As: red/black; Sb: blue/white)

According to the results in Table 3, there is a clear energetic preference for mixed site substitution by As atoms throughout the structure of $Eu_{11}Cd_6Sb_{12-x}As_x$. On average, there is a slight preference toward heteroatomic $(Sb–As)^{4–}$ units, model (a), with additional As atoms substituting across the remaining pnictide sites. On the other hand, the overall lowest energy configurations specifically for $Eu_{11}Cd_6Sb_{10}As_2$ yield homoatomic $(As–As)^{4–}$and $(Sb–Sb)^{4–}$ units with additional As substitution occurring at sites Pn1 and Pn2. Thus, there is a synergistic energetic influence on the substitution pattern of As atoms among the various pnictide sites in $Eu_{11}Cd_6Sb_{12-x}As_x$.

Table 3. Relative average total energies (ΔE; meV/f.u.) with respect to Case (d) for $Eu_{11}Cd_6Sb_{10}As_2$ (Z = 2). Values in "( )" are standard deviations from 5 different structural models in each case.

Case:	***A***	***b***	***c***	***d***	***e***	**Average**
Pn1	–169.8	–199.2	–60.6	---	63.9	–99.4
Pn2	–163.8	–192.9	–39.7	---	21.6	–96.4
Pn3	–176.2	–133.0	–40.9	---	235.1	–58.1
Pn4	–165.5	–94.5	–45.1	---	133.7	–59.6
Pn6	–185.8	–111.5	–99.5	---	165.5	–78.5
ΔE (meV/f.u.)	–172(9)	–146(47)	–47(12)	0	+124(84)	----

In summary, the results of electronic structure theory agree reasonably well with the experimental refinements of As-substituted $Eu_{11}Cd_6Sb_{12-x}As_x$. The results indicate that As substitution at a mixture of the sites Pn1, Pn2, and Pn5 is strongly preferred over any other specific site substitution. This distribution pattern arises because the sites Pn1, Pn2, and Pn5 engage in the most significant polar-covalent Cd–Pn orbital interactions (see DOS curves in Figure 7) and the covalent Pn5–Pn5 orbital interactions are enhanced by mixed occupation by As and Sb. Moreover, the energy differences between heteroatomic $(Sb–As)^{4–}$ and a mixture of homoatomic $(As–As)^{4–}$and $(Sb–Sb)^{4–}$ units are relatively small (~300 K/f.u., on average; compare columns *a* and *b* in Table 3) and there is no preferential ordering at the Pn5 sites throughout the crystal.

9.1.4.3 Arsenic substitution effects on transport properties. The substitution pattern of As for Sb in $Eu_{11}Cd_6Sb_{12}$ is expected to have a significant impact on the electrical transport properties of this system. As seen in Figure 9, magnification of the theoretical DOS curves near the Fermi level for each substitutional model reveals that As substitution at the Pn4 site creates a definite band gap of ~17 meV, whereas As substitution at the other five pnictide sites leaves a pseudogap. The band structures indicate that there are energy gaps at every wavevector for 154 valence electrons (77 valence bands), but the reason for pseudogaps arises because band overlaps occur from different regions of wavevector space. Only for substitution at the Pn4 sites is this energy band overlap eliminated. An evaluation of integrated COHP values for the various Eu–Sb contacts indicate that the largest Eu–Sb polar-covalent interactions occur with the Pn4 sites. Such interactions are related to $S_{ij}^2/\Delta E^{(0)}$ in which S_{ij} is the overlap integral between atomic orbitals *i* and *j* and $\Delta E^{(0)}$ is their energy difference. Substitution by As, which is more electronegative and smaller than Sb, will

decrease this covalency because S_{ij} decreases and $\Delta E^{(0)}$ increases. We see the greatest changes in integrated COHP values occurring for As substitution at the Pn4 positions.

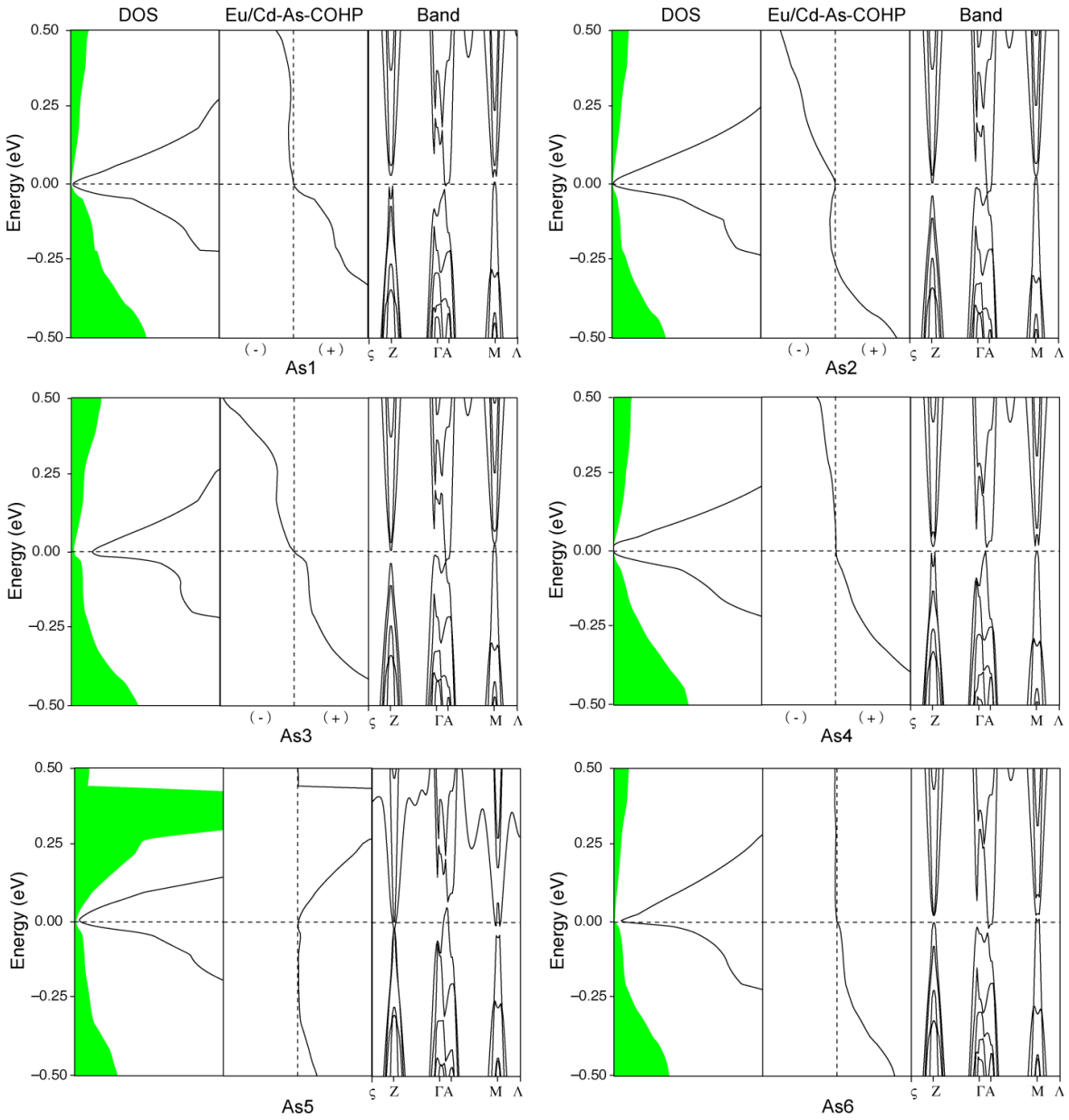

Figure 9. DOS curves (As partial DOS: Green; Eu+Cd+Sb: white), (Eu+Cd)–As COHP curves, and energy band structures for six different substitution models of "$Eu_{11}Cd_6Sb_{10}As_2$." Only As4 substitution opens a band gap in the DOS curve at the Fermi level.

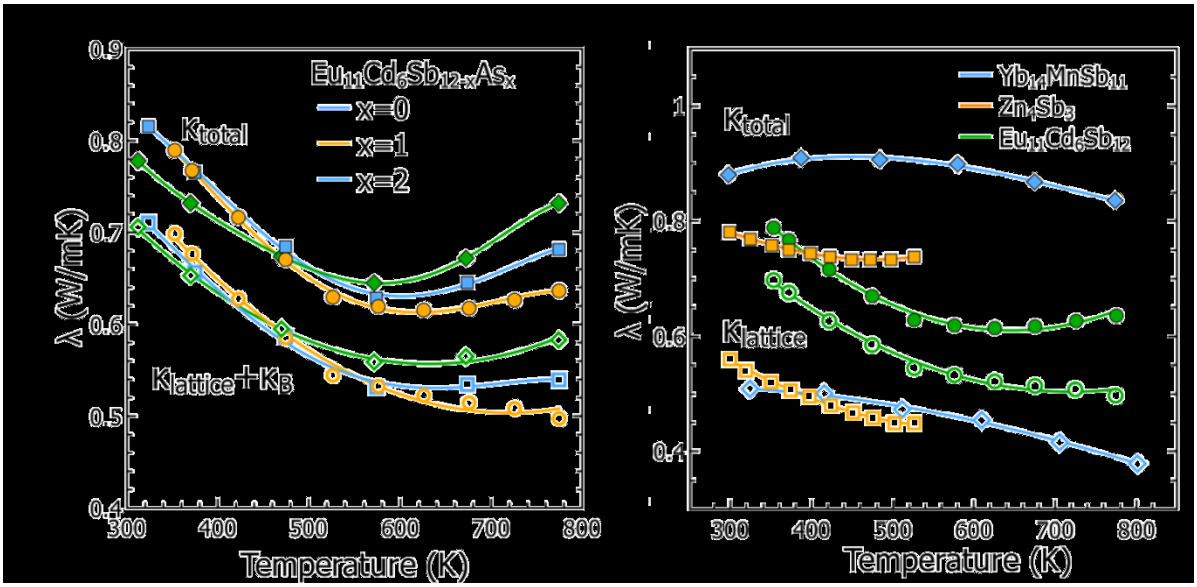

Figure 10. (a) The total thermal conductivity, κ_{total}, (color coded solid markers) and $\kappa_{lattice} + \kappa_B$ (color coded hollow markers) in samples of $Eu_{11}Cd_6Sb_{12-x}As_x$ are shown; the bipolar contribution is apparent at temperatures higher than 500K. **(b)** Total thermal conductivity (green solid circles) and lattice thermal conductivity (green hollow circles) of $Eu_{11}Cd_6Sb_{12}$ as a function of temperature are compared to the corresponding properties in $Yb_{14}MnSb_{11}$ (blue diamonds) and Zn_4Sb_3 (orange squares) from the literature.

9.1.4.4 Electronic transport properties. The total thermal conductivities for $Eu_{11}Cd_6Sb_{12-x}As_x$ samples are shown in the Figure 10a, indicating that they tend to decrease with increasing As concentration, a result which is in good agreement with the trend of higher electronic resistivity observed in more As-containing solid solutions discussed later. The electronic contribution to κ_{total} can be estimated from $\kappa_e = LT/\rho$, where T is temperature, ρ is electrical resistivity and L is the Lorenz number calculated using the single parabolic band (SPB) model. In Figure 10a, the $\kappa_{total} - \kappa_e$ values for each sample represent the cumulative effect of the lattice ($\kappa_{lattice}$) and bipolar (κ_B) contributions to the thermal conductivities, since $\kappa_{total} = \kappa_e + \kappa_B + \kappa_{lattice}$. In the absence of a bipolar contribution, $\kappa_{total} - \kappa_e$ is expected to decrease with increasing temperature. However, the $\kappa_{total} - \kappa_e$ values for samples of $Eu_{11}Cd_6Sb_{12-x}As_x$ decrease to around 550 K and then it starts to

increase, indicating a significant bipolar contribution at higher temperatures, in agreement with the temperature dependence of the Hall charge carrier concentrations discussed later. At room temperature, the bipolar term is insignificant, and it can thus be assumed that the $\kappa_{total} - \kappa_e$ values approach the intrinsic lattice thermal conductivities. All samples of $Eu_{11}Cd_6Sb_{12-x}As_x$ show very similar low lattice thermal conductivities but a rough comparison of $\kappa_{lattice}$ values near room temperature follows the expected trend based on the introducing point defects through the synthesis of isostructural solid solutions. The samples with mixed occupancies of As and Sb show lower lattice thermal conductivities since solid solutions provide an environment of atomic mass fluctuation throughout the crystal lattice (i.e. disorder) providing phonon scattering which generally results in low thermal conductivity.[25]

The measured thermal conductivities of $Eu_{11}Cd_6Sb_{12}$ are as low as 0.6 W/mK, comparable to state of the art thermoelectric materials such as $Yb_{14}MnSb_{11}$ and Zn_4Sb_3 which are about 0.9 W/mK and 0.75 W/mK, respectively, as shown in Figure 10b. However, the lattice thermal conductivity values of both $Yb_{14}MnSb_{11}$[7] and Zn_4Sb_3[26] materials are lower than $Eu_{11}Cd_6Sb_{12}$ because the electronic thermal conductivity has a significant contribution for κ_{total} in these two compounds; κ_e is minor in $Eu_{11}Cd_6Sb_{12}$ due to high electronic resistivity.

Figure 11a shows the temperature-dependent electrical resistivity (ρ) of $Eu_{11}Cd_6Sb_{12-x}As_x$ samples from room temperature to 773 K. Resistivity for all samples increases approximately linearly with increasing temperature up to 500 K consistent with degenerate semiconducting electrical conductivity properties (metallic behavior with transport dominated by extrinsic carriers). The electrical resistivity shows a sharp rise at

approximately 500 K, which can be attributed to melting of residual tin (T_M(Sn) ≈ 500 K) from the flux synthesis in the samples. Above 550 K, the resistivity decreases with increasing temperature for all samples, as minority carrier activation leads to a transition from extrinsic semiconducting behavior to intrinsic, two-carrier type behavior.

Hall effect measurements were carried out for better understanding of electronic properties of these compounds. The positive Hall coefficients of all the samples reveal that holes are the dominant carriers at room temperature ($n_H = {}^{1}/_{eR_H}$). Hall carrier concentration data shown in Figure 11b reveal that all samples have an extrinsic p-type carrier concentration of 2.5–4 × 10^{19} holes/cm^3 at room temperature, which may be attributed to the inherent defects in the crystal structure. The carrier concentration of all samples is constant to ~550 K, indicative of extrinsic carriers. At high temperatures, a sharp rise in carrier concentration is observed due to the thermally excited carriers across the band gap, defining the bipolar regime. At very high temperature, the hole carrier concentration will be overestimated since a single carrier type description is no longer valid equation in the bipolar regime. Samples with higher arsenic content have higher carrier concentrations, which may be due to a higher concentration of intrinsic crystallographic defects in these samples.

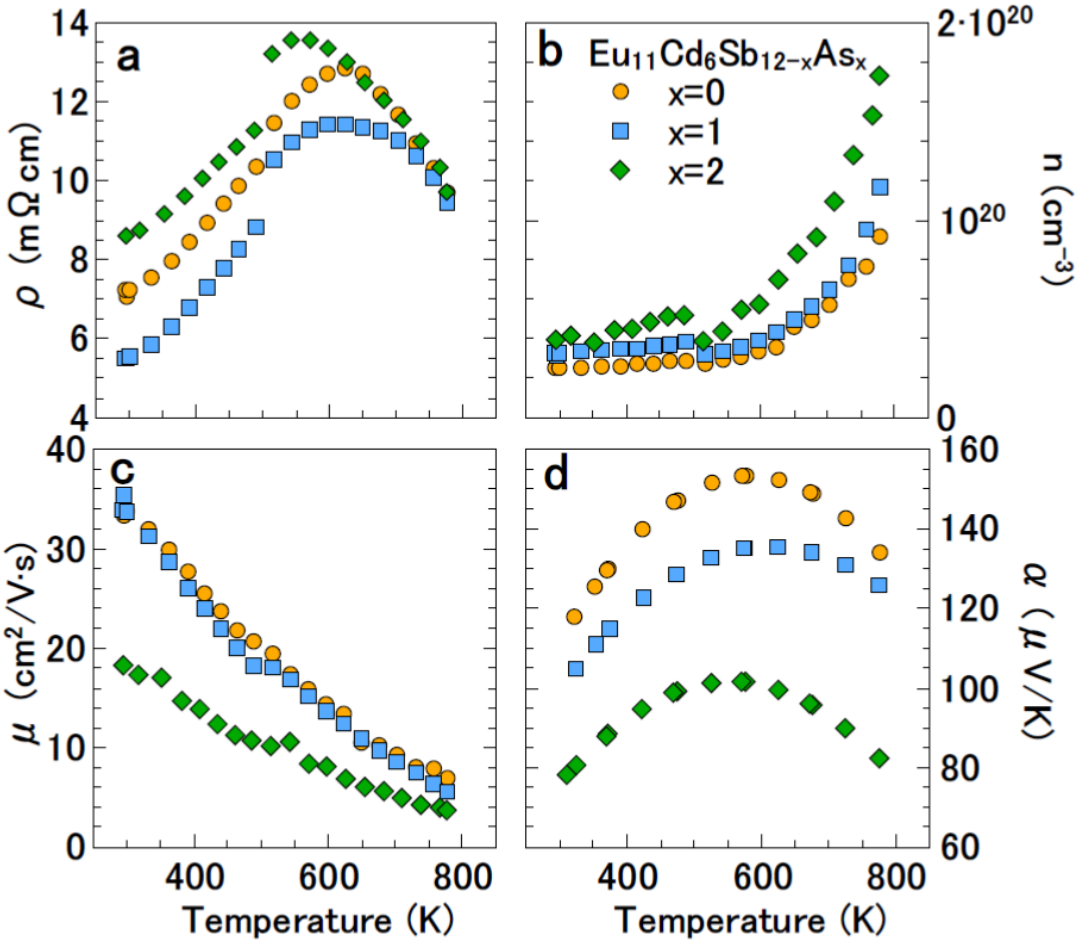

Figure 11. (a) The temperature dependence of the electrical resistivity for $Eu_{11}Cd_6Sb_{12-x}As_x$. (b) The Hall carrier concentration for $Eu_{11}Cd_6Sb_{12-x}As_x$ illustrates the transition from extrinsic regime to intrinsic regime around 550 K. (c) The Hall mobility is indicative of acoustic phonon scattering. (d) Temperature dependence of Seebeck coefficient for $Eu_{11}Cd_6Sb_{12-x}As_x$ compounds.

Hall mobility values shown in the Figure 11c were calculated from the Hall coefficient measurements ($\rho = {}^{1}/_{n_H e \mu_H}$). The mobility of the doped samples, in general, decreases with increasing x. However, while samples x = 0 and 1 have comparable mobilities, the mobility is decreased by half in sample of x = 2 (35 and 17 cm^2/v.s for x = 1 and x = 2, respectively). The sudden decrease in mobility of $Eu_{11}Cd_6Sb_{12-x}As_x$ (x ~ 2) sample can be explained by the As site specificity substitution. As discussed above in modeling calculation, it is expected that Eu1−Sb4 interaction has an important role in electronic properties in

$Eu_{11}Cd_6Sb_{12}$ which is in good agreement with the modeling calculations done on $Sr_{11}Cd_6Sb_{12}$ and $Ba_{11}Cd_6Sb_{12}$ by Xia et al.[27] Their calculation shows that the bottom of the conduction bands and the top of the valence bands originate predominantly from dz^2-orbitals of Sr1/Ba1 and p_y orbitals of Sb4. It is expected that substitution of As (with smaller 4p orbitals) in Sb sites (with larger 5p orbitals) lead to less Eu1−Pn4 orbital overlap as discussed before and, as a result, causes lower mobility. According to Table 1, As begins to preferentially substitute Sb4 sites at higher concentration $x \sim 2$ in $Eu_{11}Cd_6Sb_{12-x}As_x$ resulting in a strong effect on the electronic properties as predicted by the modeling calculation. The mobility in all samples decreases with increasing temperature. The temperature dependence of μ_H is indicative of acoustic phonon scattering ($\mu_H = T^{-v}$, where v ranges from 1 to 1.5 for degenerate and non-degenerate semiconductors, respectively). For all samples in this study, v ranges from 1.4 to 1.7.[28]

The Hall measurements indicate that despite the fact that charge carrier concentration increases by substituting As in Sb sites, the mobility is strongly affected by the As site substitution. As a result, for x = 1, where the As is not substituting the important Sb4 site, slightly increased charge carrier concentration leads to lower resistivity compared to x = 0. However, for x = 2, the increased charge carrier concentration introduced by As substitution is counteracted by lower mobility attributed to substitution on the Sb4 site, resulting in the highest resistivity among all the three samples.

Figure 11d shows the Seebeck coefficient of $Eu_{11}Cd_6Sb_{12-x}As_x$ as a function of temperature over the range 300 to 750 K. The Seebeck coefficients of all samples are positive in the measured temperature range, which agrees with the results of Hall measurement indicating that the dominant carrier concentrations are holes. The value of the Seebeck

coefficients decrease with increasing As, consistent with the increasing charge carrier concentrations. The Seebeck coefficients of all samples increase with increasing temperature and reach their maximum value at about 550 K (consistent with the temperature dependency of carrier concentration) and then decrease with further increase in temperature showing the transformation from the extrinsic to intrinsic regime. From this peak, a band gap (E_g) of between 0.1 and 0.2 eV can be estimated for $Eu_{11}Cd_6Sb_{12-x}As_x$ samples from the relation $E_g = 2\alpha_{max}T_{max}$.

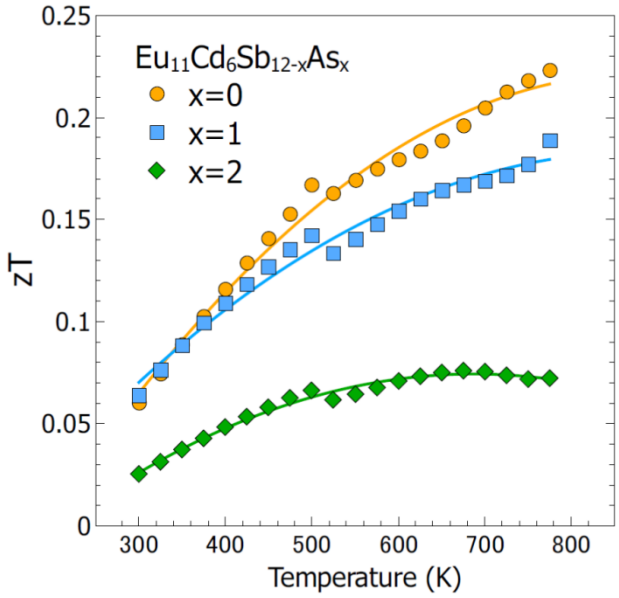

Figure 12. Color coded curves of Figure of Merit for $Eu_{11}Cd_6Sb_{12-x}As_x$ (x = 0, 1, 2) solid solutions.

The zT values of $Eu_{11}Cd_6Sb_{12-x}As_x$ (x = 0, 1, 2) as a function of temperature are shown in Figure 12. It is not surprising that $Eu_{11}Cd_6Sb_{12-x}As_x$ do not show exceptional thermoelectric performance because of the poor electrical conductivity in these samples; the calculated zT values are less than 0.25 in the measured temperature range, as indicated in Figure 12. However, the fairly high Seebeck coefficient and low thermal conductivity at room temperature results in $zT \sim 0.07$ at room temperature which is high for a Zintl phase.[29] It

suggests that $Eu_{11}Cd_6Sb_{12}$ will be a fruitful area for discovery of new materials for thermoelectric refrigeration provided that the electrical conductivity can be further tuned to achieve higher *zT* values. Optimization of *zT* can be investigated through a doping strategy such as introducing more holes by aliovalent substitutions instead of isovalent substitutions. The As solid solution samples in this study have lower *zT* values than the undoped sample due to lower Seebeck coefficients (caused by higher charge carrier concentrations through substituting As) and lower charge carrier mobilities attributed to point defect scattering.

9.1.5 Conclusions

In this work, the role of the pnicogen sites in the thermal and electronic properties of $Eu_{11}Cd_6Sb_{12}$-type Zintl compounds is studied by examining the trends in chemical and transport properties of the $Eu_{11}Cd_6Sb_{12-x}As_x$ system. It is shown that a limited amount of As can replace Sb in the $Eu_{11}Cd_6Sb_{12}$ structure through Sn-flux synthesis. Electronic structure calculations predict that As substitution on the pnicogen sites in $Eu_{11}Cd_6Sb_{12}$ prefers As/Sb mixing in the Pn5–Pn5 dimers with additional substitution at Pn1 and Pn2 sites, an outcome that is consistent with single crystal structure refinements. This substitution pattern is the result of both size and electronic factors. Refinement of the synchrotron powder X-ray diffraction patterns shows the major phase for all the samples is monoclinic $Eu_{11}Cd_6Sb_{12-x}As_x$ solid solutions. All the synthesized solid solutions show surprisingly low thermal conductivities ranging $0.60 - 0.65\ \frac{w}{mK}$ at 571 K and positive Seebeck coefficient of 120, 105 and 75 μV/K at room temperature for $x = 0$, $x = 1$ and $x = 2$ samples reaching to the maximum of 156, 140 and 120 at ~570 K. Although the charge carriers increase by substituting As in Sb sites, the mobilities decrease. As a result, in $x = 1$, which the increased carrier concentration is not completely counteracted by decreased mobility, the lowest

electrical resistivity is observed and, in $x = 2$, where the mobility is much lower than the increased carrier concentration, the highest resistivity is observed. The figures of merit of $Eu_{11}Cd_6Sb_{12-x}As_x$ are low, approximately 0.21, 0.18 and 0.07 at ~ 755, 700 and 715 K for $x = 0$, $x = 1$ and $x = 2$, respectively. The combination of theoretical and experimental results provides insight into this system and shows the potential for optimization through extrinsic doping.

9.1.6 Acknowledgements

We thank Prof. Marilyn Olmstead for assistance with crystallography, Dr. Sarah Roeske for assistance with microprobe analysis, Dr. Catherine Uvarov at Romny Scientific Inc. for assistance with the hot press and Dr. Oliver Janka for many helpful discussions. This research was funded by GAANN fellowship and NSF DMR-1100313. Use of the Advanced Photon Source was supported by the U. S. Department of Energy, Office of Science, Office of Basic Energy Sciences, under Contract No. DE-AC02-06CH11357. The research carried out at the Ames Laboratory was supported by the U. S. Department of Energy, Office of Basic Energy Science, Division of Materials Sciences and Engineering. The Ames Laboratory is operated for the U.S. Department of Energy by Iowa State University under Contract No. DE-AC02-07CH11358.

9.1.7 References

[1] Slack G. A., Rowe D., CRC, Boca Raton, FL 1995, 407.

[2] Kauzlarich S. M., Brown S. R., Snyder G. J., *Dalton Trans*. **2007**, 2099.

[3] Cao Q.-G., Zhang H., Tang M.-B., Chen H.-H., Yang X.-X., Grin Y., Zhao J.-T., *J. Appl. Phys.* **2010**, *107*, 053714.

[4] Zhang H., Fang L., Tang M. B., Man Z. Y., Chen H. H., Yang X. X., Baitinger M., Grin Y., Zhao J. T., *J. Chem. Phys.* **2010**, *133*, 194701.

[5] Cox C. A., Brown S. R., Snyder G. J., Kauzlarich S. M., *J. Electron. Mater.* **2010**, *39*, 1373.

[6] Toberer E. S., May A. F., Snyder G. J., *Chem. Mater.* **2009**, *22*, 624.

[7] Brown S. R., Kauzlarich S. M., Gascoin F., Snyder G. J., *Chem. Mater.* **2006**, *18*, 1873.

[8] Shi X., Yang J., Salvador J. R., Chi M., Cho J. Y., Wang H., Bai S., Yang J., Zhang W., Chen L., *J. Am. Chem. Soc.* **2011**, *133*, 7837.

[9] Kauzlarich S. M., Chemistry, structure, and bonding of Zintl phases and ions, VCH New York, 1996.

[10] Park S.-M., Kim S.-J., *J. Solid State Chem.* **2004**, *177*, 3418.

[11] Saparov B., He H., Zhang X., Greene R., Bobev S., *Dalton Trans.* **2010**, *39*, 1063.

[12] Saparov B., Bobev S., Ozbay A., Nowak E. R., *J. Solid State Chem.* **2008**, *181*, 2690.

[13] Canfield, P., Fisk Z., *Philos. Mag. B* **1992**, *65*, 1117.

[14] Ove Jepsen, Ole K. Andersen, TB-LMTO, 47; Max-Planck-Institut fur Festkorperforschung, 2000.

[15] Wang J., Liu X.-C., Xia S.-Q., Tao X.-T., *J. Am. Chem. Soc.* **2013**, *135*, 11840.

[16] Lambrecht W. R., Andersen O. K., *Phys. Rev. B* **1986**, *34*, 2439.

[17] Wang J., Toby B. H., Lee P. L., Ribaud L., Antao S. M., Kurtz C., Ramanathan M., Von Dreele R. B., Beno M. A., *Rev. Sci. Instrum.* **2008**, *79*, 085105.

[18] Lee P. L., Shu D., Ramanathan M., Preissner C., Wang J., Beno M. A., Von Dreele R. B., Ribaud L., Kurtz C., Antao S. M., *J. Synchrotron Rad.* **2008**, *15*, 427.

[19] Borup K. A., Toberer E. S., Zoltan L. D., Nakatsukasa G., Errico M., Fleurial J.-P., Iversen B. B., Snyder G. J., *Rev. Sci. Instrum.* **2012**, *83*, 123902.

[20] Iwanaga S., Toberer E. S., LaLonde A., Snyder G. J., *Rev. Sci. Instrum.* **2011**, *82*, 063905.

[21] Cordero B., Gómez V., Platero-Prats A. E., Revés M., Echeverría J., Cremades E., Barragán F., Alvarez S., *Dalton Trans.* **2008**, 2832.

[22] Denton A. R., Ashcroft N. W., *Phys. Rev. A* **1991**, *43*, 3161.

[23] Von L. Vegard, *Zeitschrift für Physik*, **1921**, 5.

[24] Miller G. J., *Eur. J. Inorg. Chem.* **1998**, 523.

[25] Sootsman J. R., Chung D. Y., Kanatzidis M. G., *Angew. Chem., Int. Ed.* **2009**, *48*, 8616.

[26] Toberer E. S., Rauwel P., Gariel S., Taftø J., Snyder G. J., *J. Mater. Chem.* **2010**, *20*, 9877.

[27] Xia S. Q., Bobev S., *J. Comput. Chem.* **2008**, *29*, 2125.

[28] I͡Uriĭ I. Ravich, Bella A. Efimova, Igor′ A. Smirnov, *Semiconducting lead chalcogenides*, Plenum Press, New York, 1970.

[29] Gaultois M. W., Sparks T. D., Borg C. K., Seshadri R., Bonificio W. D., Clarke D. R., *Chem. Mater.* **2013**, *25*, 2911.

Appendix II. Spin-glass behavior in giant unit cell compound $Tb_{117}Fe_{54.7}Ge_{112}$

Modified from a paper submitted to *J Appl. Phys.*

J. Liu[1,2], W. Xie[1,3], K. A. Gschneidner, Jr.[1,2], G. J. Miller[1,3], and V. K. Pecharsky[1,2]

[1]The Ames Laboratory, U.S. Department of Energy, Iowa State University, Ames, IA, 50011-3020, US
[2]Department of Material Science and Engineering, Iowa State University, Ames, IA, 50011-2300, US
[3]Department of Chemistry, Iowa State University, Ames, IA 50011-3111, US

9.2.1 Abstract

In this letter, we show the presence of a cluster spin glass in $Tb_{117}Fe_{54.7}Ge_{112}$ (a unique compound with a giant cubic unit cell) via ac and dc susceptibility, magnetization, magnetic relaxation and heat capacity measurements. The results clearly show that $Tb_{117}Fe_{54.7}Ge_{112}$ undergoes a spin glass phase transition at the freezing temperature, ~38 K. The good fit of the frequency dependence of the freezing temperature to the critical slowing down model and Vogel-Fulcher law strongly suggest the existence of cluster glass behavior in the $Tb_{117}Fe_{54.7}Ge_{112}$ system. The heat capacity data exhibit no evidence for long-range magnetic order, and yields a large value of Sommerfeld coefficient. The spin glass behavior of $Tb_{117}Fe_{54.7}Ge_{112}$ may be understood in terms of the outcome of the competing interactions of the multiple non-equivalent Tb sites arising from the highly complex unit cell.

9.2.2 Introduction

Spin glasses (SG) with an unconventional phase transition have been extensively studied, both experimentally and theoretically, for the last several decades. SG can exist in amorphous, diluted metallic alloys, nanostructured systems, and single crystal and polycrystalline materials. More recently, our work on the $R_{117}M_{52+x}X_{112+y}$ (R= rare earth metals, M = Fe, Co and Cr, X = Ge, Sn) giant crystallize compounds led to the discovery of spin glass clusters with short range antiferromagnetic ordering coexist in $Pr_{117}Co_{54.5}Sn_{115.2}$. [1] The $R_{117}M_{52+x}X_{112+y}$-based ternary intermetallic compounds have a unique structure with a large cubic cell with unit cell volume larger than 20,000 $Å^3$. These compounds crystallize in two closely related structures, either cubic $Tb_{117}Fe_{52}Ge_{112}$ –type [2] or $Dy_{117}Co_{57}Sn_{112}$ –type [3].

The spin glass behavior of $Pr_{117}Co_{54.5}Sn_{115.2}$, which crystallizes in $Dy_{117}Co_{57}Sn_{112}$ –type structure, is attributed to the crystallographic disorder in atomic clusters. Such origin of the SG behavior is similar to those in uranium-based nonmagnetic atom disorder (NMAD) compounds U_2XSi_3 (X = transition metal) and is due to the inherent nature of the crystal structure but is different from that in amorphous or diluted metallic spin glasses. [4] Different from the $Dy_{117}Co_{57}Sn_{112}$ –type, no atomic disorder has been reported in $Tb_{117}Fe_{52}Ge_{112}$ –type. However, considering this extremely complex system, atomic disorder may also exist in $Tb_{117}Fe_{52}Ge_{112}$ –type. Ever since the $Tb_{117}Fe_{52}Ge_{112}$ –type crystal structure was first discovered in 1987, a single crystal analysis of this type structure has not been reported. Therefore, it is interesting to reinvestigate the $Tb_{117}Fe_{52}Ge_{112}$ –type crystal structure using single crystal diffraction. In addition, until now, no studies of the physical properties of $Tb_{117}Fe_{52}Ge_{112}$, the first compound discovered with this extremely structurally complex system, have been reported. Thus, the main objective of this Letter is to report on the atomic

disorder and spin glass behavior in $Tb_{117}Fe_{52}Ge_{112}$. In this work, we have investigated the magnetic behavior of $Tb_{117}Fe_{52}Ge_{112}$ using dc and ac magnetic susceptibility measurements.

9.2.3 Experimental Procedure

The polycrystalline sample of the nominal composition $Tb_{117}Fe_{52}Ge_{112}$ was prepared by arc melting pure constituents Tb (99.9 wt.%), Fe (99.9838 wt.%) and Ge (> 99.99 wt.%) in an arc furnace under argon atmosphere. The alloys were flipped and re-melted four times to achieve the homogenous composition. Then the sample is sealed in a helium-filled quartz glass tube and annealed at 1050 °C for 102 days. The phase analysis and room temperature crystal structure determination were based on the refinement of the measured X-ray powder diffraction (XRD) patterns collected on a Philips X'Pert diffractometer (Cu $K\alpha_1$ radiation) using the Rietveld method. A single crystal measuring around $60\times80\times80\mu m^3$ which was picked out of the heat treated sample was mounted on the tip a of glass fiber. An x-ray single crystal investigation was also performed by using Bruker APEX CCD single crystal diffractometer equipped with graphite-monochromatized Mo Kα (λ = 0.71069 Å) radiation. The ac and dc magnetic measurements were performed by using a superconducting quantum interference device (SQUID) magnetometer MPMS XL-7. The heat capacity data were collected on a physical property measurement system (PPMS).

9.2.4 Results and Discussions

An analysis of the powder x-ray diffraction pattern of the $Tb_{117}Fe_{52}Ge_{112}$ revealed that it is almost pure single phase with only 0.2 wt.% $TbFe_2Ge_2$ minor phase. The single crystal analysis of $Tb_{117}Fe_{52}Ge_{112}$ shows that it crystallizes in $Tb_{117}Fe_{52}Ge_{112}$-type with a lattice parameter a = 28.553(1) Å, which is comparable to the earlier reported value. However, an extra position 24e (0, 0, 0.0664) is occupied by Fe5 with an occupancy of 45%. This

indicates that some atomic disorder also exists in $Tb_{117}Fe_{52}Ge_{112}$-type crystal structure, and that the actual chemical formula of this compound is $Tb_{117}Fe_{54.7}Ge_{112}$.

Magnetization data of $Tb_{117}Fe_{54.7}Ge_{112}$ as a function of temperature collected in magnetic fields from 100 Oe to 10 kOe under both zero field cooling warming (ZFC) and field cooled cooling (FCC) protocols are show in Fig.1. For H = 100 Oe, the $M(T)$ curve displays one sharp peak at 38 K (T_f) and below which magnetic irreversibility is manifest as a bifurcation between the ZFC and FCC curves. Below T_f, ZFC branch decreases rapidly while FC decrease slowly to a plateau. With increasing field, the sharp peak observed in low magnetic field becomes broader with smaller amplitude and shifts toward lower temperature. The variation of temperature T_f with magnetic field follows the de Almedia-Thouless Law [5] ($T_f \propto H^{2/3}$), as shown in the inset of Fig.1. A peak in the ZFC plot and the distinctive bifurcation between the ZFC and FCC curves below T_f are typical features of spin glasses.

Figure 2(a) shows the ac susceptibility of $Tb_{117}Fe_{54.7}Ge_{112}$ as a function of temperature at frequencies from 1 to 1000 Hz. The measurements were performed at an ac field of 5 Oe after ZFC. $\chi'(w, T)$ and $\chi''(w, T)$ display a peak at ~40 K and ~38 K, respectively. The peak temperature shifts upwards with increasing frequency in both χ' and χ'' plots. However, as frequency increases, the magnitudes of the peak decrease in $\chi'(w, T)$ but increase in $\chi''(w, T)$. Except for the peak, another anomaly appears at ~ 12 K in $\chi'(w, T)$ and a small peak at ~ 9K and a slope change at ~ 23 K are seen in $\chi''(w, T)$. The small peak at around 9 K in χ'' plot also shifts up to higher temperature with the increase of the frequency. The initial frequency shift $\delta T_f = \Delta T_f / (T_f \Delta \log w)$ has often been used as a criterion to compare different spin glass systems. The measurements show that T_f varies from ~39.5 K (1 Hz) to ~43 K (1000 Hz) in χ' data while it varies from ~37.5 K (1 Hz) to ~40.5 K (100 0Hz) in χ'' data. Therefore, the

calculated peak shift δT_f is 0.0295 and 0.0267 for χ' and χ", respectively. The sensitivity of the frequency strongly depends on the interaction between the magnetic entities. The values obtained for $Tb_{117}Fe_{54.7}Ge_{112}$ lie between those reported for canonical SG (between 0.0045 and 0.06) [6] and are comparable to those reported for some NMAD concentrated spin glasses like URh_2Ge_2 (0.025) [7], U_2PdSi_3 (0.020) [8] and Ce_2AgIn_3 (0.022) [9], and also that of cluster glass $Pr_{117}Co_{54.5}Sn_{115.2}$ (0.021).

In order to estimate the dynamical parameters used to characterize the SG state of $Tb_{117}Fe_{54.7}Ge_{112}$, two well-known models: the conventional critical slowing down model of spin dynamics, $\tau = \tau_0(T_f/T_{SG} - 1)^{-zv}$, (where T_{SG} is the SG transition temperature determined by the system interaction at $\omega \rightarrow 0$, τ_0 is the shortest relaxation time available to the system and zv is the dynamic critical exponent [10]) and Vogel-Fulcher law [11-14], $\omega = \omega_0 \exp[-E_a/k_B(T_F - T_0)]$ (where ω_0 is characteristic frequency, E_a is activation energy, k_B is the Boltzmann constant, and T_0 is Vogle-Fulcher temperature) are employed to fit the $T_f(\omega)$ data. Since T_{SG} is the infinitely slow cooling value of T_f, we assigned the value of T_{SG} at which the ZFC dc-$\chi(T)$ curve has its maximum (i.e. 38K).

Figure 2 (b) and (c) present the best fits to the data T_f of χ' in the 1-1000 Hz range, showing that the spin glass state can be well described by the two models. Having T_{SG} fixed, the fit using the former equation [solid line in Fig. 2(b)] yields following parameters: $\tau_0 \approx 10^{-9}$ s and $zv = 5.9$. These values compare well with those of well-known spin glasses and cluster glass systems. The value of zv lies between 4 and 12 for different SG systems, such as the cluster glass U_2CuSi_3 [15], and the Ising spin glass $Fe_{0.5}Mn_{0.5}TiO_3$ [16]. Taking $\omega_0 = 1/\tau_0 = 10^9$ Hz, the fit using the latter one [solid line in Fig. 2(c)] yields the activation energy $E_a = 140.8k_B \approx 4.3k_BT_0$, and the Vogle-Fulcher temperature $T_0 \approx 32.8$ K. T_0 can be treated as a measure of the

coupling between the interacting magnetic clusters. [17] $T_0 \ll E_a/k_B$ indicates a weak coupling whereas $T_0 \gg E_a/k_B$ suggests a strong one. For $Tb_{117}Fe_{52}Ge_{112}$, $T_0 \approx 0.23E_a/k_B$, implies a moderate interaction between the magnetic clusters. Moreover, the Tholence criterion [18] of $Tb_{117}Fe_{54.7}Ge_{112}$, $\delta T_{Th} = (T_f - T_0)/T_f \approx 0.17$, is an order of magnitude higher than those of canonical SG systems such as CuMn (≈0.07), but comparable to those observed in cluster glasses (e.g. $La_{0.5}Sr_{0.5}CoO_3$ ≈0.25) [19]. Taken together, all the above evidences support the cluster glass nature of $Tb_{117}Fe_{54.7}Ge_{112}$ system.

To further investigate the SG behavior, we have measured the long-time relaxation of the magnetization. Figure 3(a) shows the isothermal normalized remanent magnetization $M(t)/M(t= 0)$ curves at 5, 15, 30 and 40 K. The measurements were carried out by first zero field cooling the sample from 200 K to the desired temperature, then setting the field to 500 Oe for 1000 seconds before switching it off . The results show that the decay of $M(t)$ at 5 to 30 K is slow and can be represented by a logarithmic time dependence [20]: $M(t)=M_0 - S \ln(t+t_0)$, typically observed in metallic spin glasses. The resultant three fitting parameters are: M_0 = 0.0833, 0.412, and 0.434 emu/g, and S = 0.0038, 0.036, and 0.031emu/g for 5, 15 and 30 K, respectively. The remanent magnetization at 40 K, which is in PM state, is very small and constant in time.

Inset of Figure 3(b) shows the selected $M(H)$ loops measured at different temperatures after zero-field cooling. Both remanent magnetization M_R and coercive field H_C obtained from the $M(H)$ plots decrease as the temperature increases and become almost negligible above freezing temperature, as shown in Fig. 3. The temperature dependence of M_R and H_C values are consistent with that observed in a conventional spin glass system. [21-22]The high H_C in the spin glass state probably results from the frustration of the spin clusters with short range

AFM, as observed in $Pr_{117}Co_{54.5}Sn_{115.2}$. It is noteworthy to point out that the magnetization does not show any tendency to saturation, even in a 70 kOe magnetic field.

The heat capacity $C(T)$ curve of $Tb_{117}Fe_{54.7}Ge_{112}$ measured at zero magnetic field is further evidence for the existence of the spin glass state. It is clear that there is no anomaly associated with magnetic phase transition observed in the $C(T)$ curve at ~40 K, suggesting no long-range magnetic ordering near T_f in $Tb_{117}Fe_{54.7}Ge_{112}$. The first derivative of the heat capacity with respect to temperature (inset of Fig. 4) exhibits a broad peak around ~40 K, indicating a weak contribution from the magnetic cluster state to the heat capacity. Furthermore, the large Sommerfeld coefficient value of 109 (mJ (mole-Tb)$^{-1}$ K^{-2}), which was determined from the C/T vs. T^2 plot, probably originated from cluster glass freezing, and is usually observed in NMAD spin glasses.

Two necessary conditions for formation of a SG state are the existence of randomness and frustration. Interestingly, as determined from the single crystal x-ray analysis, the level of disorder of $Tb_{117}Fe_{54.7}Ge_{112}$ does not provide enough randomness for the formation of the SG state, which is different from $Pr_{117}Co_{54.5}Sn_{115.2}$ possessing an extensive structural disorder. Therefore, we propose that the mechanism of the SG state in $Tb_{117}Fe_{54.7}Ge_{112}$ originates from the large and complex unit cell containing eight symmetrically independent Tb positions resulting in competing interactions. Recently, spin glass behavior was also observed in another compound $Tb_{30}Ru_{6.0}Sn_{29.5}$, a highly complex unit cell presenting low level of disorder. [23]

In summary, the temperature, field and frequency dependent dc and ac magnetic measurements clearly demonstrate the existence of spin glass phase transition at ~38 K. The frequency dependence of the freezing temperature fits well with the critical slowing down

model and the Vogel-Fulcher law, indicating the formation of a cluster glass in $Tb_{117}Fe_{52}Ge_{112}$. The occurrence of a de Almedia-Thouless phase line, the stretched exponential relaxation of remanence and the absence of anomaly near T_f in $C(T)$ data also corroborate the glass nature of $Tb_{117}Fe_{54.7}Ge_{112}$. We believe these behaviors originate from the presence of multiple non-equilibrium sites occupied by R atoms, which leads to competing magnetic interactions between Tb atoms, which is different from mechanisms of traditional spin glass systems. Therefore, the spin glass behavior observed in $Tb_{117}Fe_{54.7}Ge_{112}$ further broadens the classification of spin glass materials.

9.2.5 Acknowledgements

This work was supported by the Office of Basic Energy Science, Division of Materials Sciences and Engineering of the U. S. Department of Energy under Contract No. DE-AC02-07CH11358 with Iowa State University.

9.2.6 References

[1] J. Liu, Y. Mudryk, J. D. Zou, V. K. Pecharsky, K. A. Gschneidner, Jr., submitted.

[2] V. K. Pecharsky, O. I. Bodak, V. K. Bel'skii, P. K. Starodub, I. R. Mokra, E. I. Gladyshevskii, *Kristallografiya*, **1987**, *32*, 334 (in Russian).

[3] P. Salamakha, O. Sologub, G. Bocelli, S. Otani, T. Takabatake, *J. Alloys Compd.* **2001**, *314*, 177.

[4] D. X. Li, S. Nimori, Y. Shiokawa, Y. Haga, E. Yamamoto,Y. Onuki, *Phys. Rev. B* **2003**, *68*, 172405.

[5] J. R. L. de Almeida, D. J. Thouless, *J. Phys. A* **1978**, *11*, 983.

[6] J. A. Mydosh, *Spin Glasses: An Experimental Introduction* Taylor & Francis, London, 1993.

[7] S. Süllow, G. J. Nieuwenhuys, A. A. Menovsky, J. A. Mydosh, S. A. M. Mentink, T. E. Mason, and W. J. L. Buyers, *Phys. Rev. Lett.* **1997**, *78*, 354.

[8] D. X. Li, Y. Shiokawa, Y. Haga, E. Yamamoto, Y. Onuki, *J. Phys. Soc. Jpn.* **2002**, *71*, 418.

[9] T. Nishioka, Y. Tabata, T. Taniguchi, Y. Miyako, *J. Phys. Soc. Jpn.* **2000**, *69*, 1012 (2000)

[10] P. C. Hohenberg, B. I. Halperin, *Rev. Mod. Phys.***1977**, *49*, 435.

[11] H. Vogel, *Phys. Z.* **1921**, *22*, 645.

[12] G. S. Fulcher, *J. Am. Ceram. Soc.* **1925**, *8*, 339.

[13] J. L. Tholence, *Solid State Commun.* **1980**, *35*, 113.

[14] J. Souletie and J. L. Tholence, *Phys. Rev. B* **1985**, *32*, 516(R).

[15] D. Li, S. Nimori, T. Yamamura, and Y. Shiokawa, *J. Appl. Phys.* **2008**, *103*, 07B715.

[16] K. Gunnarsson, P. Svedlindh, P. Nordblad, L. Lundgren, H. Aruga, A. Ito, *Phys. Rev. Lett.***1988**, *61***,** 754.

[17] S. Shtrikman, E. P. Wohlfarth, *Phys. Lett. A* **1981**, *85*, 467.

[18] J. L. Tholence, *Phys. B* **1984**, *126*, 157.

[19] S. Mukherjee, R. Ranganathan, P. S. Anilkumar, P. A. Joy, *Phys. Rev. B* **1996**, *54*, 9267.

[20] D. X. Li, T. Yamamura, S. Nimori, K. Yubuta, Y. Shiokawa, *Appl. Phys. Lett.* **2005**, *87*, 142505.

[21] I. A. Campbell, S. Senoussi, F. Varret, J. Teillet, A. Hamzić, *Phys. Rev. Lett.* **1983**, *50*, 1615.

[22] J. Dho, W. S. Kim, N. H. Hur, *Phys. Rev. Lett.* **2002**, *89*, 027202.

[23] D. C. Schmitt, J. C. Prestigiacomo, P. W. Adams, D. P. Young, S. Stadler, J. Y. Chan, *Appl. Phys. Lett.* **2013**, *103*, 082403.

Appendix III. Summary of failed experiments

1. Co-Zn systems

Loading Composition	Synthesis Process	Results	Series number
$Co_{15.46}Zn_{85.54}$ (Co_2Zn_{11})	1 °C/min to 1000 °C, 1000 °C for 12hrs, 1°C/min to 600 °C, anneal for 3 d. Cool slowly	γ-brass	Wei012; 077
$Co_{18}Zn_{82}$	1 °C/min to 1000 °C, 1000 °C for 12hrs, 1°C/min to 600 °C, anneal for 3 d. Cool slowly	γ-brass	Wei274
$Co_{20}Zn_{80}$	1 °C/min to 1000 °C, 1000 °C for 12hrs, 1°C/min to 600 °C, anneal for 3 d. Cool slowly	γ-brass	Wei273
$Co_{25}Zn_{75}$	1 °C/min to 1000 °C, 1000 °C for 12hrs, 1°C/min to 600 °C, anneal for 3 d. Cool slowly	γ-brass	Wei004
$Co_{30}Zn_{70}$	1 °C/min to 1000 °C, 1000 °C for 12hrs, 1°C/min to 600 °C, anneal for 3 d. Cool slowly	γ-brass	Wei005
$Co_{32.5}Zn_{67.5}$	1 °C/min to 1000 °C, 1000 °C for 12hrs, 1°C/min to 600 °C, anneal for 3 d. Cool slowly	γ-brass + β-Mn	Wei017
$Co_{33.5}Zn_{66.5}$	1 °C/min to 1000 °C, 1000 °C for 12hrs, 1°C/min to 925 °C, anneal for 3 d. Quench.	γ-brass + β-Mn	Wei018; 020
$Co_{35}Zn_{65}$	1 °C/min to 1000 °C, 1000 °C for 12hrs, 1°C/min to 925 °C, anneal for 3 d. Quench.	γ-brass + β-Mn	Wei019
$Co_{40}Zn_{60}$	1 °C/min to 1000 °C, 1000 °C for 12hrs, 1°C/min to 925 °C, anneal for 3 d. Quench.	γ-brass + β-Mn	Wei001; 021; 201
$Co_{45}Zn_{55}$	1 °C/min to 1000 °C, 1000 °C for 12hrs, 1°C/min to 925 °C, anneal for 3 d. Quench.	γ-brass + β-Mn	Wei118
$Co_{50}Zn_{50}$	1 °C/min to 1000 °C, 1000 °C for 12hrs, 1°C/min to 925 °C, anneal for 3 d. Quench.	β-Mn	Wei002; 202

Continued

$Co_{55}Zn_{45}$	1 °C/min to 1000 °C, 1000 °C for 12hrs, 1°C/min to 925 °C, anneal for 3 d. Quench.	β-Mn	Wei117; 121
$Co_{60}Zn_{40}$	1 °C/min to 1000 °C, 1000 °C for 12hrs, 1°C/min to 925 °C, anneal for 3 d. Quench.	β-Mn + Co particle	Wei003; 203
$Co_{65}Zn_{35}$	1 °C/min to 1000 °C, 1000 °C for 12hrs, 1°C/min to 925 °C, anneal for 3 d. Quench.	β-Mn + Co particle	Wei116

2. Co-Zn-M systems to explore β-Mn structure

Loading Composition	Synthesis Process	Results	Series number
$Co_{35}Zn_{60}Ru_5$	1 °C/min to 1000 °C, 1000 °C for 12hrs, 1°C/min to 900 °C, anneal for 3 d. Cool slowly	γ-brass + β-Mn without Ru	Wei029
$Co_{36}Zn_{60}Ru_4$	1 °C/min to 1000 °C, 1000 °C for 12hrs, 1°C/min to 900 °C, anneal for 3 d. Cool slowly	γ-brass + β-Mn without Ru	Wei030
$Co_{37}Zn_{60}Ru_3$	1 °C/min to 1000 °C, 1000 °C for 12hrs, 1°C/min to 900 °C, anneal for 3 d. Cool slowly	γ-brass + β-Mn without Ru	Wei031
$(CoZn)_{95}Ru_5$	1 °C/min to 1000 °C, 1000 °C for 12hrs, 1°C/min to 900 °C, anneal for 3 d. Cool slowly	β-Mn	Wei035
$(CoZn)_{90}Ru_{10}$	1 °C/min to 1000 °C, 1000 °C for 12hrs, 1°C/min to 900 °C, anneal for 3 d. Cool slowly	β-Mn + impurity	Wei036
$(CoZn)_{85}Ru_{15}$	1 °C/min to 1000 °C, 1000 °C for 12hrs, 1°C/min to 900 °C, anneal for 3 d. Cool slowly	β-Mn + impurity	Wei037
$(CoZn)_{80}Ru_{20}$	1 °C/min to 1000 °C, 1000 °C for 12hrs, 1°C/min to 900 °C, anneal for 3 d. Cool slowly	β-Mn + impurity	Wei038
$(CoZn)_{75}Ru_{25}$	1 °C/min to 1000 °C, 1000 °C for 12hrs, 1°C/min to 900 °C, anneal for 3 d. Cool slowly	β-Mn + impurity	Wei039

Continued

$Mg_{50}Ru_{50}$	1 °C/min to 1025 °C, 1025 °C for 12hrs, 1°C/min to 900 °C, anneal for 3 d. Cool slowly	γ-brass + β-Mn	Wei040
$Mg_{60}Ru_{40}$	1 °C/min to 1025 °C, 1025 °C for 12hrs, 1°C/min to 900 °C, anneal for 3 d. Cool slowly	β-Mn	Wei041
Rh_2Zn_3	1 °C/min to 1000 °C, 1000 °C for 12hrs, 1°C/min to 800 °C, anneal for 3 d. Cool slowly	β-brass	Wei042
RhZn	1 °C/min to 1000 °C, 1000 °C for 12hrs, 1°C/min to 800 °C, anneal for 3 d. Cool slowly	β-brass	Wei043
Rh_3Zn_2	1 °C/min to 1000 °C, 1000 °C for 12hrs, 1°C/min to 800 °C, anneal for 3 d. Cool slowly	β-brass	Wei044
Rh_2Zn_{11}	1 °C/min to 1000 °C, 1000 °C for 12hrs, 1°C/min to 800 °C, anneal for 3 d. Cool slowly	γ-brass	Wei045
Rh_1Zn_3	1 °C/min to 1000 °C, 1000 °C for 12hrs, 1°C/min to 800 °C, anneal for 3 d. Cool slowly	β-brass	Wei046
$Co_1Zn_3Mg_2$	1 °C/min to 1000 °C, 1000 °C for 12hrs, 1°C/min to 800 °C, anneal for 3 d. Cool slowly		Wei049
$Co_2Zn_2Mg_2$	1 °C/min to 1000 °C, 1000 °C for 12hrs, 1°C/min to 800 °C, anneal for 3 d. Cool slowly		Wei050
$Co_3Zn_1Mg_2$	1 °C/min to 1000 °C, 1000 °C for 12hrs, 1°C/min to 800 °C, anneal for 3 d. Cool slowly		Wei051
$Co_2Zn_1Mg_2$	1 °C/min to 1000 °C, 1000 °C for 12hrs, 1°C/min to 800 °C, anneal for 3 d. Cool slowly		Wei052
$Co_{40}Mg_{60}$	1 °C/min to 1000 °C, 1000 °C for 12hrs, 1°C/min to 800 °C, anneal for 3 d. Cool slowly	Laves phase	Wei032

Continued

$Co_{50}Mg_{50}$	1 °C/min to 1000 °C, 1000 °C for 12hrs, 1°C/min to 800 °C, anneal for 3 d. Cool slowly	Laves phase	Wei033
$Co_{60}Mg_{40}$	1 °C/min to 1000 °C, 1000 °C for 12hrs, 1°C/min to 800 °C, anneal for 3 d. Cool slowly	Laves phase	Wei034
$Ru_{40}Zn_{60}$	1 °C/min to 1000 °C, 1000 °C for 12hrs, 1°C/min to 800 °C, anneal for 3 d. Cool slowly	$RuZn_6$	Wei022
$Ru_{50}Zn_{50}$	1 °C/min to 1000 °C, 1000 °C for 12hrs, 1°C/min to 800 °C, anneal for 3 d. Cool slowly	$RuZn_6$	Wei023
$Ru_{60}Zn_{40}$	1 °C/min to 1000 °C, 1000 °C for 12hrs, 1°C/min to 800 °C, anneal for 3 d. Cool slowly	$RuZn_6$	Wei024

3. Exploring semi-conductors for thermoelectric materials

Loading Composition	Synthesis Process	Results	Series number
RhSbGa	1 °C/min to 800 °C, 800 °C for 12hrs, 1°C/min to 400 °C, anneal for 3 d. Cool slowly	$RhSb_3$	Wei053
$RhSbGa_2$	1 °C/min to 800 °C, 800 °C for 12hrs, 1°C/min to 400 °C, anneal for 3 d. Cool slowly	$RhSb_3$	Wei054
$RhSb_2Ga_4$	1 °C/min to 800 °C, 800 °C for 12hrs, 1°C/min to 400 °C, anneal for 3 d. Cool slowly	$RhSb_3$	Wei055
$CoMoSb_2$	1 °C/min to 800 °C, 800 °C for 12hrs, 1°C/min to 500 °C, anneal for 3 d. Cool slowly	Mo_3Sb_7	Wei056
$FeMoSb_2$	1 °C/min to 800 °C, 800 °C for 12hrs, 1°C/min to 500 °C, anneal for 3 d. Cool slowly	Mo_3Sb_7	Wei057
$NiMoSb_2$	1 °C/min to 800 °C, 800 °C for 12hrs, 1°C/min to 500 °C, anneal for 3 d. Cool slowly	Mo_3Sb_7	Wei058

Continued

ZnMoSb	1 °C/min to 800 °C, 800 °C for 12hrs, 1°C/min to 500 °C, anneal for 3 d. Cool slowly	Mo_3Sb_7	Wei059
$ZnMoSb_2$	1 °C/min to 800 °C, 800 °C for 12hrs, 1°C/min to 500 °C, anneal for 3 d. Cool slowly	Mo_3Sb_7	Wei060
$ZnMoSb_4$	1 °C/min to 800 °C, 800 °C for 12hrs, 1°C/min to 500 °C, anneal for 3 d. Cool slowly	Mo_3Sb_7	Wei061
Ni_3MoSb_{12}	1 °C/min to 800 °C, 800 °C for 12hrs, 1°C/min to 500 °C, anneal for 3 d. Cool slowly	Mo_3Sb_7	Wei062
Cu_3MoSb_{12}	1 °C/min to 800 °C, 800 °C for 12hrs, 1°C/min to 500 °C, anneal for 3 d. Cool slowly	Mo_3Sb_7	Wei063
$ZnMoSb_6$	1 °C/min to 800 °C, 800 °C for 12hrs, 1°C/min to 500 °C, anneal for 3 d. Cool slowly	Mo_3Sb_7	Wei064
$GaNbSb_6$	1 °C/min to 800 °C, 800 °C for 12hrs, 1°C/min to 500 °C, anneal for 3 d. Cool slowly		Wei065
MoGeTe	1 °C/min to 800 °C, 800 °C for 12hrs, 1°C/min to 500 °C, anneal for 3 d. Cool slowly	Mo_3Te_4	Wei066
Mo_2GeTe	1 °C/min to 800 °C, 800 °C for 12hrs, 1°C/min to 500 °C, anneal for 3 d. Cool slowly	Mo_3Te_4	Wei067
CoGeSn	1 °C/min to 800 °C, 800 °C for 12hrs, 1°C/min to 500 °C, anneal for 3 d. Cool slowly	Co_2Sn	Wei068
Co_2GeSn	1 °C/min to 800 °C, 800 °C for 12hrs, 1°C/min to 500 °C, anneal for 3 d. Cool slowly	Co_2Sn	Wei069
$CrSn_6Zn_2$	1 °C/min to 800 °C, 800 °C for 12hrs, 1°C/min to 600 °C, anneal for 3 d. Cool slowly	ductile	Wei070

Continued

$CrSn_2Zn_2$	1 °C/min to 800 °C, 800 °C for 12hrs, 1°C/min to 600 °C, anneal for 3 d. Cool slowly	ductile	Wei071
$CrSnZn_4$	1 °C/min to 800 °C, 800 °C for 12hrs, 1°C/min to 600 °C, anneal for 3 d. Cool slowly	ductile	Wei072
$CrSn_2Zn_6$	1 °C/min to 800 °C, 800 °C for 12hrs, 1°C/min to 600 °C, anneal for 3 d. Cool slowly	Ductile + several crystals	Wei073
$CrSnZn_2$	1 °C/min to 800 °C, 800 °C for 12hrs, 1°C/min to 600 °C, anneal for 3 d. Cool slowly	ductile	Wei074
$FeSn_6Zn_2$	1 °C/min to 800 °C, 800 °C for 12hrs, 1°C/min to 600 °C, anneal for 3 d. Cool slowly		Wei078
$Fe_3Sn_1Zn_2$	1 °C/min to 800 °C, 800 °C for 12hrs, 1°C/min to 600 °C, anneal for 3 d. Cool slowly	a=b=c=18.137Å	Wei079
$FeSnZn_4$	1 °C/min to 800 °C, 800 °C for 12hrs, 1°C/min to 600 °C, anneal for 3 d. Cool slowly		Wei080
$Fe_1Sn_2Zn_6$	1 °C/min to 800 °C, 800 °C for 12hrs, 1°C/min to 600 °C, anneal for 3 d. Cool slowly		Wei081
$FeSnZn_2$	1 °C/min to 800 °C, 800 °C for 12hrs, 1°C/min to 600 °C, anneal for 3 d. Cool slowly	a=b=c=18.208Å	Wei082

4. Complex intermetallic materials

Loading Composition	Synthesis Process	Results	Series number
$Cr_{224}Sn_{192}Zn_{560}$	1 °C/min to 850 °C, 850 °C for 12hrs, 1°C/min to 600 °C, anneal for 3 d. Cool slowly	$Cr_{22}Sn_{24}Zn_{72}$	Wei083
$Ru_{224}Sn_{192}Zn_{560}$	1 °C/min to 850 °C, 850 °C for 12hrs, 1°C/min to 600 °C, anneal for 3 d. Cool slowly	C2/m	Wei084

Continued

$Fe_{224}Sn_{192}Zn_{560}$	1 °C/min to 850 °C, 850 °C for 12hrs, 1°C/min to 600 °C, anneal for 3 d. Cool slowly		Wei085
$CrBi_2Zn_6$	1 °C/min to 850 °C, 850 °C for 12hrs, 1°C/min to 600 °C, anneal for 3 d. Cool slowly	Ductile	Wei086
$MoBi_2Zn_6$	1 °C/min to 850 °C, 850 °C for 12hrs, 1°C/min to 600 °C, anneal for 3 d. Cool slowly	Ductile	Wei087
$FeBi_2Zn_6$	1 °C/min to 850 °C, 850 °C for 12hrs, 1°C/min to 600 °C, anneal for 3 d. Cool slowly	Ductile	Wei088
$RuBi_2Zn_6$	1 °C/min to 850 °C, 850 °C for 12hrs, 1°C/min to 600 °C, anneal for 3 d. Cool slowly	Ductile	Wei089
$CrInZn_2$	1 °C/min to 850 °C, 850 °C for 12hrs, 1°C/min to 600 °C, anneal for 3 d. Cool slowly	Ductile	Wei090
$MoInZn_2$	1 °C/min to 850 °C, 850 °C for 12hrs, 1°C/min to 600 °C, anneal for 3 d. Cool slowly		Wei091
$FeInZn_2$	1 °C/min to 850 °C, 850 °C for 12hrs, 1°C/min to 600 °C, anneal for 3 d. Cool slowly		Wei092
$RuInZn_2$	1 °C/min to 850 °C, 850 °C for 12hrs, 1°C/min to 600 °C, anneal for 3 d. Cool slowly		Wei093
$MnSnZn_2$	1 °C/min to 850 °C, 850 °C for 12hrs, 1°C/min to 600 °C, anneal for 3 d. Cool slowly		Wei094
$MnInZn_2$	1 °C/min to 850 °C, 850 °C for 12hrs, 1°C/min to 600 °C, anneal for 3 d. Cool slowly		Wei095
$MnBiZn_2$	1 °C/min to 850 °C, 850 °C for 12hrs, 1°C/min to 600 °C, anneal for 3 d. Cool slowly		Wei096

Continued

$Ru_{1.11}Sn_{1.95}Zn_{1.69}$	1 °C/min to 850 °C, 850 °C for 12hrs, 1°C/min to 600 °C, anneal for 3 d. Cool slowly		Wei097
$Mo_7Sn_{12}Zn_{40}$	1 °C/min to 850 °C, 850 °C for 12hrs, 1°C/min to 600 °C, anneal for 3 d. Cool slowly		Wei098
$Ru_4Sn_3Zn_{12}$	1 °C/min to 850 °C, 850 °C for 12hrs, 1°C/min to 600 °C, anneal for 3 d. Cool slowly	Co_2Sn	Wei103
CuCrSb	1 °C/min to 850 °C, 850 °C for 12hrs, 1°C/min to 600 °C, anneal for 3 d. Cool slowly		Wei105
$CuCrSb_2$	1 °C/min to 850 °C, 850 °C for 12hrs, 1°C/min to 600 °C, anneal for 3 d. Cool slowly		Wei106
$Cu_3Cr_2Sb_3$	1 °C/min to 850 °C, 850 °C for 12hrs, 1°C/min to 600 °C, anneal for 3 d. Cool slowly		Wei107
$Cu_2Cr_5Sb_3$	1 °C/min to 850 °C, 850 °C for 12hrs, 1°C/min to 600 °C, anneal for 3 d. Cool slowly		Wei107

5. Exploring Zn-based compounds

Loading Composition	Synthesis Process	Results	Series number
Co_2Zn_2Al	1 °C/min to 800 °C, 800 °C for 12hrs, 1°C/min to 600 °C, anneal for 3 d. Cool slowly		Wei109
$Co_2Zn_1Al_2$	1 °C/min to 800 °C, 800 °C for 12hrs, 1°C/min to 600 °C, anneal for 3 d. Cool slowly		Wei110
Co_2Zn_2In	1 °C/min to 800 °C, 800 °C for 12hrs, 1°C/min to 600 °C, anneal for 3 d. Cool slowly		Wei111
$Co_2Zn_1In_2$	1 °C/min to 800 °C, 800 °C for 12hrs, 1°C/min to 600 °C, anneal for 3 d. Cool slowly		Wei112

Continued

CrCuSn	1 °C/min to 800 °C, 800 °C for 12hrs, 1°C/min to 600 °C, anneal for 3 d. Cool slowly	Wei113
CrRuSn	1 °C/min to 800 °C, 800 °C for 12hrs, 1°C/min to 600 °C, anneal for 3 d. Cool slowly	Wei114
CrCoSn	1 °C/min to 800 °C, 800 °C for 12hrs, 1°C/min to 600 °C, anneal for 3 d. Cool slowly	Wei115

6. γ-brass investigation

Loading Composition	Synthesis Process	Results	Series number
$Co_2Ag_4Zn_7$	1 °C/min to 800 °C, 800 °C for 12hrs, 1°C/min to 600 °C, anneal for 3 d. Cool slowly		Wei122
$Co_2Au_4Zn_7$	1 °C/min to 800 °C, 800 °C for 12hrs, 1°C/min to 600 °C, anneal for 3 d. Cool slowly		Wei123
$Co_2Pd_2Zn_9$	1 °C/min to 800 °C, 800 °C for 12hrs, 1°C/min to 600 °C, anneal for 3 d. Cool slowly		Wei124
$Co_2Pd_1Zn_2$	1 °C/min to 800 °C, 800 °C for 12hrs, 1°C/min to 600 °C, anneal for 3 d. Cool slowly		Wei125
$Co_1Pd_4Zn_8$	1 °C/min to 800 °C, 800 °C for 12hrs, 1°C/min to 600 °C, anneal for 3 d. Cool slowly		Wei126
$Co_2Pd_3Zn_8$	1 °C/min to 800 °C, 800 °C for 12hrs, 1°C/min to 600 °C, anneal for 3 d. Cool slowly		Wei127
$Co_3Pd_2Zn_8$	1 °C/min to 800 °C, 800 °C for 12hrs, 1°C/min to 600 °C, anneal for 3 d. Cool slowly		Wei128
$Co_4Pd_1Zn_8$	1 °C/min to 800 °C, 800 °C for 12hrs, 1°C/min to 600 °C, anneal for 3 d. Cool slowly		Wei129

Continued

$Co_3Pd_2Zn_8$	1 °C/min to 800 °C, 800 °C for 12hrs, 1°C/min to 600 °C, anneal for 3 d. Cool slowly	Wei130
$Co_2Pd_2Zn_9$	1 °C/min to 800 °C, 800 °C for 12hrs, 1°C/min to 600 °C, anneal for 3 d. Cool slowly	Wei131
$Co_2Pd_3Zn_8$	1 °C/min to 800 °C, 800 °C for 12hrs, 1°C/min to 600 °C, anneal for 3 d. Cool slowly	Wei132
$Co_1Pd_1Zn_{11}$	1 °C/min to 800 °C, 800 °C for 12hrs, 1°C/min to 600 °C, anneal for 3 d. Cool slowly	Wei134
$Co_1Pd_2Zn_{10}$	1 °C/min to 800 °C, 800 °C for 12hrs, 1°C/min to 600 °C, anneal for 3 d. Cool slowly	Wei135
$Co_{1.5}Pd_{1.5}Zn_{10}$	1 °C/min to 800 °C, 800 °C for 12hrs, 1°C/min to 600 °C, anneal for 3 d. Cool slowly	Wei136
$Co_2Pd_1Zn_{10}$	1 °C/min to 800 °C, 800 °C for 12hrs, 1°C/min to 600 °C, anneal for 3 d. Cool slowly	Wei137
$Co_1Pd_1Zn_3$	1 °C/min to 800 °C, 800 °C for 12hrs, 1°C/min to 600 °C, anneal for 3 d. Cool slowly	Wei138
$Co_1Pd_2Zn_2$	1 °C/min to 800 °C, 800 °C for 12hrs, 1°C/min to 600 °C, anneal for 3 d. Cool slowly	Wei139
$Co_2Pd_1Zn_2$	1 °C/min to 800 °C, 800 °C for 12hrs, 1°C/min to 600 °C, anneal for 3 d. Cool slowly	Wei140